A Study on Structural Behavior of Historical Brick Masonry Walls under Different Reinforcement Conditions: Through Experiments and Numerical Analysis of General Historical Masonry in Nepal and a Case of Historical Masonry in Japan

ミシュラ, チャビ

https://hdl.handle.net/2324/7182280

出版情報：Kyushu University, 2023, 博士（工学）, 課程博士
バージョン：

A Study on Structural Behavior of Historical Brick Masonry Walls under Different Reinforcement Conditions

– Through Experiments and Numerical Analysis of General Historical Masonry in Nepal and a Case of Historical Masonry in Japan –

BY

CHHABI MISHRA

**A dissertation submitted to the Graduate School of
Human-Environment Studies,
Department of Architecture, Kyushu University
in partial fulfillment of the requirements for the degree of
Doctor of Engineering**

January 2024

Table of Contents

Acknowledgement

I would like to express my utmost appreciation and sincere gratitude to my supervisor, Professor Kentaro Yamaguchi at Kyushu University, whose expertise, understanding, and patience, added considerably to my experience. Many thanks for the fruitful and critical discussions, orientation, and advice. I would like to thank him for checking, revising, and providing valuable comments to improve the quality of the manuscripts. Thank you for being an excellent supervisor and a dedicated researcher who was always approachable and available throughout my studies.

Special thanks to Associate Professor Tomoyuki Koyama at Kyushu University, my dissertation co-supervisor, for his invaluable help and suggestions. Sincere thanks to Professor Tatsuo Kanno at Kyushu University, my dissertation co-supervisor, for his great support and valuable advice. I am also thankful to Professor Masayuki Kuroki at Oita University, my dissertation co-supervisor for his great support and suggestions.

This study was not possible without scholarship from the Program for Leading Graduate Schools, Institute of Decision Science for a Sustainable Society (IDS3), Kyushu University, for Ph.D. studies. The experimental work of a part of this dissertation was supported by JSPS KAKENHI grant number JP16H01825 (Principal Investigator: Professor Toshikazu Hanazato currently at Kanagawa University) and Investigation on the Kyushu University Integrated Relocation Project (Principal Investigator: Professor Toshihiko Ninakawa at Kyushu University and Professor Yamaguchi). The analysis was supported by JSPS KAKENHI grant number JP22K04411 (Principal Investigator: Professor Yamaguchi). These supports are very gratefully acknowledged. In addition, Associate Professor Yohei Endo at Shinshu University and Dr. Manjip Shakya at Khwopa Engineering College made great contributions to the experiments in Nepal.

I am also thankful to all present and past undergraduate, and master’s students of Professor Yamaguchi’s laboratory for their great help and friendly attitude. Especially Mr. Koshi Murakami, Mr. Keisuke Araki, and Mr. Hideki Suehiro shared experimental data with me. And Ms. Tingyun Jing worked with me on numerical analysis.

I would like to express my infinite gratitude to my father Dr. Nagendra Mishra who always motivated me, my mother, Mrs. Krishna Mishra, my siblings, relatives, and friends in Nepal, for all the support and encouragement.

Last but not least, my deep appreciation to my husband Dr. Anand Mishra, and son Ayusman, for their support, love, inspiration, and sacrifice that supported me.

Chhabi Mishra

January 2024

Abstract

Masonry is anisotropic, heterogeneous, and non-linear composite structure that is widely used in rural areas and developing countries. Historical masonry buildings were not built in compliance with building codes; therefore, these buildings are in danger being damaged by an earthquake. The main goal of seismic strengthening unreinforced masonry (URM) buildings is to increase the structure's performance during earthquakes. The choice of reinforcement technique depends on the mechanical behavior of the building, the qualities of the materials utilized, and the direction of loading. In the case of historical buildings minimum reinforcement and reversible reinforcement techniques that do not impair the historical value of the building are required.

The retrofitting of unreinforced brick masonry is necessary to prevent damage to masonry buildings during earthquakes. This study focuses on examining a strengthening technique using timber and steel plates for Nepalese historical brick masonry, and RC wall and steel plates for retrofitting of Japanese historical brick masonry to enhance the structural performance under forces. The proposed technique was examined through a series of experiments. Firstly, experiments to obtain detailed mechanical characteristics of Nepalese and Japanese historical brick masonry were conducted. Further, proposed strengthening techniques were also studied. Lastly, the experimental results are used to simulate the behavior and validate the effectiveness of the techniques through numerical macro modeling approaches.

This dissertation consists of nine chapters. The contents of each chapter are as follows.

Chapter 1 provides a brief introduction to the background of the research, and the aims and objectives of this study. It also provides the flow chart of chapters in this dissertation.

Chapter 2 provides a literature review. The following main topics are described. (1) Major earthquakes around the world and in Nepal. (2) Types of building structures of Nepal and the common failure types during the 2015 Gorkha earthquake. (3) Methods for investigating mechanical characteristics of masonry building materials. (4) Common failure modes of brick masonry structures. (5) Strengthening methods for brick masonry buildings. (6) Numerical modeling approaches for simulating masonry structures.

Chapter 3 describes the mechanical properties of Nepalese historical brick masonry elements and assemblages investigated through an experimental program. Experimental results on the mechanical characteristics of Nepalese historical masonry show that despite the large standard deviations of compressive strength of constituent

materials (unit bricks and mud mortar), the standard deviation of compressive strength of masonry prisms was low.

Chapter 4 describes the tests and procedures adopted to investigate shear strength, shear deformation capacity, and flexural behavior of the URM walls comprised in Nepalese historical masonry buildings. Retrofitting of Nepalese masonry walls shows that timber reinforced masonry and steel reinforced masonry increased the average shear strength by about 2 and 3 fold respectively, compared to unreinforced specimens. Flexural strength increased significantly in ladder and braced type timber reinforced specimens compared to unreinforced specimens.

Chapter 5 presents a macro modeling method for studying the Nepalese historical brick masonry walls. Numerical analysis on three-point bending of test specimen models of Nepalese historical brick masonry shows that the apparent Young's modulus of brick masonry changes depending on the angle of compression struts generated inside the brick masonry, and that if the tensile stress generated in reinforced brick masonry exceeds the tensile strength, its structural behavior can be explained by modeling with slits on the tension side.

Chapter 6 presents the effectiveness of reinforcement with RC walls and steel plates on structural behavior and failure modes of Japanese historical masonry walls. Retrofitting of Japanese historical masonry with RC walls and steel plates shows that RC reinforcement has higher strength, rigidity, and deformation capacity than steel plate reinforcement. In addition, the anchors that penetrate through the masonry could resist the splitting of specimens, and promote integration, and hence higher reinforcement effect could be anticipated.

Chapter 7 presents reinforcement methods for maintaining the first and third headquarters of Kyushu University. Horizontal loading test of Japanese historical brick masonry shows that the maximum load of specimens reinforced with RC walls was about 6 times (one side reinforcement) or 12–14 times (both sides reinforcement) higher than that of unreinforced specimens. In addition, this series of experiments also examined the appropriate amount of anchors and the torsion of the wall when reinforcing one side, providing significant insights for the reinforcing methods.

Chapter 8 presents a macro modeling method for studying the Japanese historical brick masonry (i.e. Kyushu University first and third headquarters). Numerical analysis of Japanese historical brick masonry on diagonal compression test and horizontal loading test models shows that the average Poisson's ratio with respect to the diagonal length of the specimen gave closer analytical results to the experimental results. In addition, these analyses show that the results of diagonal compression experiments are affected by the fact that more stress acts near the center of the cross-section, compared to test specimens for horizontal loading where stress is applied to the entire cross-section.

Chapter 9 discusses the main outcomes and conclusions of this study and the recommendations for future research.

Keywords: Mechanical characterization, Nepalese historical brick masonry, Japanese historical brick masonry, Retrofitting, Timber, RC wall, Steel plates, Horizontal loading test, Macro modeling

Chapter 1: Introduction

1.1 Background

Masonry is anisotropic, heterogeneous, and non-linear composite structure that are widely used in rural areas and developing countries (Wang et al., 2018). About 70% of buildings are brick masonry worldwide (Zamani, 2013). Most masonry structures can withstand compressive forces and vertical loading however they can break easily when subjected to tension forces or lateral loads during earthquakes (Sayin et al., 2019). During earthquake cracks may develop in the building which may propagate throughout the structure and cause irreversible damage. The seismic performance of masonry structures is largely dependent on their foundation, connections, geometry, material qualities, and unit arrangements (Yavartanoo and Kang, 2022).

Older historical masonry buildings were not built in compliance with building codes; therefore, these buildings are in danger of damage during earthquake activity. To get better structural behavior, the cracks must be repaired, especially when brick masonry construction is being done in a seismically active region. Demolition of all these damaged buildings and construction of new seismically safe buildings is not feasible or practical in all cases as it needs huge investment for the construction of new buildings (Shrestha et al., 2016). Strengthening and improving the level of safety of these buildings would be a feasible way to raise the seismic safety standards.

The main goal of seismic strengthening unreinforced masonry (URM) buildings is to increase the structure's performance during earthquake events. The choice of reinforcement technique depends on the mechanical behavior of the building, the qualities of the materials employed, and the direction of loading. Therefore, before choosing any retrofitting technique, designers and engineers must thoroughly examine the structures' performance (Yavartanoo and Kang, 2022). The main ideas behind strengthening and retrofitting techniques are to: (i) increase the masonry structure's integrity; (ii) lessen the impact of external loading; and (iii) improve each element's ability to handle more weight (Bhattacharya et al., 2014). The best strengthening option is selected that not only can improve structural integrity but is also compatible with brick masonry structures in terms of cost, sustainability, accessibility, simplicity of application, mass, and appearance (Abdulla, 2019).

Timber is well recognized for its relatively higher strength-to-weight ratio. In addition, compared to fiber-reinforced polymer (FRP) wrapping and steel bracing systems, it offers good aesthetics and greater shear strength historical (Dauda, 2020). Therefore, timber can be effectively used in the structural retrofit of brick masonry buildings. The seismic performance of timber-framed structures during earthquakes has been reported by Langenbach (2007) and Pan et al. (2016), however, there is little known about the use of timber panels for retrofitting of historical unreinforced masonry buildings. Based on the literature review, if timber-framed structures can withstand earthquakes, then timber panels might potentially be utilized to improve the out-of-plane performance of URM walls was the main source of motivation for using timber panels for retrofitting Nepalese historical brick masonry. Sal wood is commonly grown in the forest of Nepal and was used for retrofitting in this study. Two types of retrofitting were studied namely ladder and brace reinforcement to know their effectiveness for reinforcement on Nepalese historical brick masonry.

For Japanese brick masonry, the surface reinforcement method was employed. The inside faces of the external walls and most of the inner walls of the 1st and 3rd headquarters buildings of the Kyushu University were plastered with cement mortar. The original appearance of buildings did not change when the masonry walls were reinforced from the surface on both the inside faces of external walls and most of the inner walls. Additionally, the thickness of the brick walls for both buildings was larger compared to those of the beams and slabs when they were connected to the reinforcing part with anchors. Therefore, damage could occur and the expected strength of the anchor could not be exhibited. It is more suitable to reinforce walls than beams or slabs. Moreover, it is effective in reinforcing the visible parts of each floor from the inside surface without changing the beams, slabs, and walls of the floors. Furthermore, surface reinforcement is economical and easy to construct.

It takes a lot of time and effort to experimentally test the compressive strength, ultimate shear strength, and failure mechanisms of reinforced and unreinforced masonry walls. An efficient and trustworthy computer simulation of the masonry assemblages test can solve this problem (Hernoune et al., 2020). There are mainly two types of modeling techniques: macro-modeling and micro-modeling (Lourenco, 1998). In the masonry macro model, masonry is simulated as isotropic or anisotropic homogenous material with equivalent mechanical properties. Micro modeling implies separate discretization of mortar and masonry units. In this study, only the macro modeling approach is considered.

1.2 Aims and objectives of this research

The retrofitting of unreinforced brick masonry is necessary to save from damage to masonry buildings during earthquakes; therefore, This study focuses on general historical masonry in Nepal and a case of masonry in Japan for proposing strengthening techniques to enhance the structural performance under seismic forces. This study proceeds with the following steps: Firstly, experimental works were conducted to obtain a detailed mechanical characterization of Nepalese and Japanese historical brick masonry. Further, proposed strengthening techniques were also studied. Lastly, numerical analysis by macro modeling approach was developed and validated using experimental results.

Based on the above aims, the objectives of this research are described as follows:

1. To investigate the material properties and mechanical characterization of Nepalese brick masonry specimens, by using the results from experiments to generate numerical models. The study aims to contribute to a better understanding of the mechanical properties of bricks, mud mortar, and masonry composed of these materials.
2. To experimentally investigate shear strength, shear deformation capacity, and flexural behavior of the URM walls making Nepalese historical masonry buildings. Diagonal compression and three-point bending tests were conducted on masonry specimens with and without reinforcement.
3. To investigate a numerical method that can be used for the analysis of the behavior of Nepalese historical brick masonry walls in the elastic range with low-strength mortar. In addition, the behavior of brick masonry walls reinforced by timber was also investigated through numerical simulation. The macro modeling approach was used in this study.
4. To experimentally investigate seismic reinforcement methods for unreinforced brick masonry buildings to improve the seismic safety of the Kyushu University 1st and 3rd headquarters buildings. The effects of reinforcing on shear strength properties were investigated.
5. To investigate the effect of horizontal loading on retrofitting from the surface on one side or two sides with RC walls of Japanese historical brick masonry. In addition, the evaluation formula for the horizontal strength of brick wall specimens reinforced with RC walls was derived and verified.
6. To investigate a numerical method that can be used for the analysis of the behavior of Japanese historical brick masonry walls in the elastic range. The macro modeling approach was used in this study. The comparison between Nepalese and Japanese historical brick masonry was also investigated in this study.

1.3 Scope and Limitations

In this study, the structural performance of Nepalese historical URM and retrofitted walls under static load conditions only i.e. in-plane and out-of-plane load were studied through experimental and numerical investigations. The mechanical properties of Nepalese historical brick masonry are first characterized via experiments. The shear behavior, along with the flexural behavior, of unreinforced and reinforced Nepalese historical brick masonry were also studied through experiments. A macro modeling method for studying the Nepalese historical brick masonry walls was used in this study. The investigations of the structural performance of unreinforced and reinforced Nepalese historical masonry under cyclic and dynamic load conditions are not covered in this study.

For Japanese historical brick masonry, the structural performance of unreinforced and retrofitted walls was studied under static load conditions only i.e. in-plane and out-of-plane loads were studied through experimental and numerical investigations. The mechanical properties of Japanese historical brick masonry are first characterized via experiments. The shear behavior, along with the flexural behavior, of unreinforced and reinforced Japanese historical brick masonry was also studied through experiments. A macro modeling method for studying the Japanese historical brick masonry walls was used in this study. The investigation of the structural performance of unreinforced and reinforced Japanese historical masonry under dynamic load conditions is not covered in this study. In addition, micro modeling was not covered for both Nepalese and Japanese historical brick masonry in this study.

1.4 Layout of the dissertation

There are nine chapters in this dissertation which are briefly described as follows:

Chapter One provides a brief introduction to the background of the research, and the aims and objectives of this study. It also provides the flow chart of chapters in this dissertation.

Chapter Two provides discussions of major earthquake events. Following this, the types of buildings in Nepal and the causes of damage to buildings due to the 2015 Gorkha earthquake are discussed. The methods related to the mechanical characterizations of brick masonry materials are also presented. In addition, the most common failure mechanisms of masonry structures are presented. Following this, the available existing strengthening techniques for brick masonry structures are reviewed and studied. Finally, the numerical modeling approach and past work related to numerical modeling are discussed.

Chapter Three describes the tests and procedures adopted to produce masonry units and samples. In addition, the mechanical properties of brick masonry samples and assemblages are characterized through an experimental program. The characterizations include compression tests of brick, masonry, and assemblages. The chapter contributes to a better understanding of the mechanical properties of bricks, mud mortar, and masonry composed of these materials.

Chapter Four describes the tests and procedures adopted to investigate shear strength, shear deformation capacity, and flexural behavior of the URM walls making Nepalese historical masonry buildings. Diagonal compression and three-point bending tests were conducted on masonry specimens with and without reinforcement.

Chapter Five presents a macro modeling method for studying the Nepalese historical brick masonry walls. Firstly, a case study on the results obtained in bending experiments of brick masonry that constitutes historical buildings in Nepal is presented. The three-point loading test on the URM prism and reinforced masonry prism with wood (SAL timber) and bolts was performed. Second, for numerical modeling, elastic regions were determined from a graph of flexural stress-deformation angle. The first crack point was identified from experimental data and was also confirmed by basic mechanics theories. Third, numerical analysis was performed on the bending test models. This stage was articulated in two steps, which included (i) validation of the URM prism, and (ii) validation of the retrofitted masonry prism with timber panels.

Chapter Six presents the effectiveness of reinforcement with RC walls and steel plates on structural behavior and failure modes of Japanese historical masonry walls. In addition, the effect of retrofitting with RC walls and steel plates from single and double sides on structural behavior and failure modes was studied. A diagonal compression test was conducted to study the effect of retrofitting on Japanese historical brick masonry walls.

Chapter Seven presents a reinforcement method that could maintain the appearance and reduce the cost of the 1st and 3rd headquarters buildings of Kyushu University was investigated. Surface reinforcement with RC walls was selected for this study because it has higher strength and rigidity than steel plate reinforcement. Brick wall specimens were prepared and reinforced from the surface on one side or two sides with RC walls and a horizontal loading experiment was carried out to confirm the reinforcing effect. In addition, the evaluation formula for the horizontal strength of brick wall specimens reinforced with RC walls was derived and verified.

Chapter Eight presents a macro modeling method for studying the Japanese historical brick masonry (ie Kyushu University 1st and 3rd quarter buildings). Firstly, a case study on the results obtained in horizontal loading experiments of brick masonry that constitutes historical buildings in Japan is presented. Secondly, for numerical modeling, elastic regions were determined from a graph of flexural stress-deformation angle. The first crack point was identified from experimental data. Finally, numerical analysis was performed on URM models by validation of experimental results. In addition, a comparison between Nepalese historical brick masonry buildings and Japanese historical brick masonry was made. The mechanical properties of buildings, effects of retrofitting, and macro modeling approach were also compared with Nepalese historical brick masonry.

Chapter Nine discusses the main outcomes and conclusions of the research and the recommendations for future research.

Figure 1.1 shows the flow of research and the organization of dissertation.

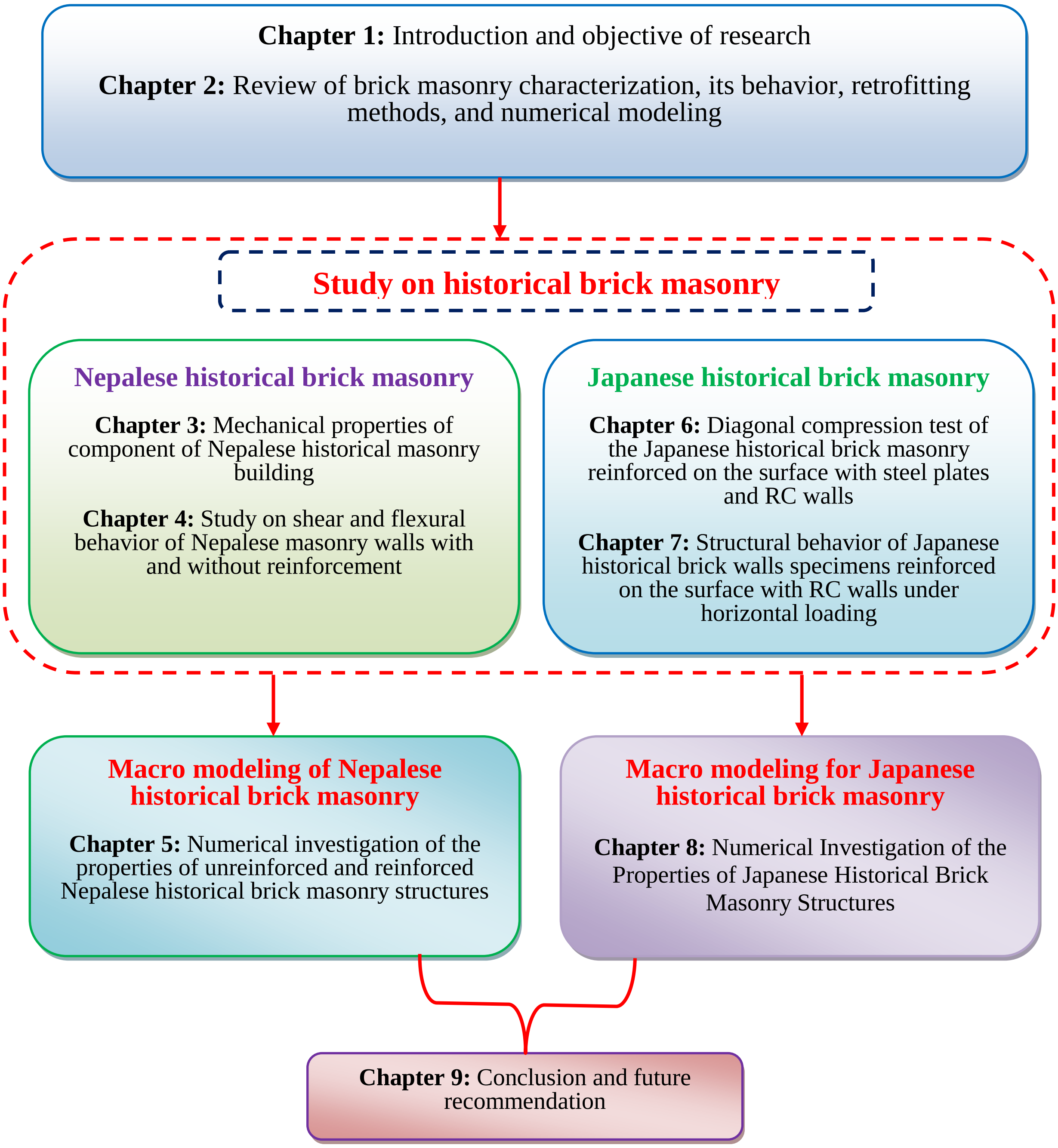

Figure 1.1: Flow of research and organization of dissertation

References

Abdulla, K. F. A. (2019). Innovative Structural Enhancement Techniques for Adobe Masonry Structures, (Doctoral dissertation, The University of Manchester).

Bhattacharya, S., Nayak, S., & Dutta, S. C. (2014). A critical review of retrofitting methods for unreinforced masonry structures. *International Journal of Disaster Risk Reduction*, *7*, 51-67.

Dauda, J. A. (2020). Numerical and experimental investigation of unreinforced masonry wall retrofitted with timber panels (Doctoral dissertation, University of Leeds).

G. Zamani Ahari (2013) Structural In-Plane Behavior of Masonry Walls Externally Retrofitted with Fiber Reinforced Materials, Doctoral Dissertation, Kyushu University, Fukuoka, Japan.

Hernoune, H., Benabed, B., Kanellopoulos, A., Al-Zuhairi, A. H., & Guettala, A. (2020). Experimental and numerical study of behaviour of reinforced masonry walls with NSM CFRP strips subjected to combined loads. *Buildings*, *10*(6), 103.

Langenbach, R. (2007). *From "Opus Craticium" to the "Chicago Frame": Earthquake-Resistant Traditional Construction*. International Journal of Architectural Heritage, 1(1), pp.29-59.

Lourenco, P. (1998). Experimental and Numerical Issues in the Modelling of the Mechanical Behaviour of Masonry. Structural Analysis of Historical Constructions, II.

Pan, Y., Xie, D., Yuan, S., & Wang, X. (2016). Seismic damages of Nepalese cultural heritage buildings and strengthening measures: case studies on three Durbar Squares in Ms 8.1 Gorkha earthquake. *Harbin Gongye Daxue Xuebao/Journal of Harbin Institute of Technology*, *48*(12), 172-182.

Sayin, B., Yildizlar, B., Akcay, C., & Gunes, B. (2019). The retrofitting of historical masonry buildings with insufficient seismic resistance using conventional and non-conventional techniques. *Engineering Failure Analysis*, *97*, 454-463.

Shrestha, H. D., Subedi, J., & Rajbhandari, M. (2016). Seismic retrofitting guidelines of buildings in Nepal. *Kathmandu, Nepal: Government of Nepal, Ministry of Urban Development, Department of Urban Development and Building Construction*.

Wang, C., Sarhosis, V., & Nikitas, N. (2018). Strengthening/retrofitting techniques on unreinforced masonry structure/element subjected to seismic loads: A literature review. *Open Construction and Building Technology Journal*, *12*(1), 251-268.

Yavartanoo, F., & Kang, T. H. K. (2022). Retrofitting of unreinforced masonry structures and considerations for heritage-sensitive constructions. *Journal of Building Engineering*, *49*, 103993.

Chapter 2: Review of Literature

In this chapter, a review of the literature on previous studies is presented as discussed below. The following main topics are described in detail below.

1. Major earthquakes around the world and in Nepal.
2. Types of building structures of Nepal and its common failure types during the 2015 Gorkha earthquake
3. Methods for investigating mechanical characteristics of brick masonry materials and assemblage
4. Common failure modes of brick masonry structures
5. Strengthening methods for brick masonry buildings
6. Numerical modeling approaches for simulating masonry structures

2.1 Major Earthquake Events

2.1.1 Major earthquakes around the world

Earthquakes are natural disasters that cause loss of life and properties. The aftershocks, liquefaction, tsunamis, and landslides can be more dangerous than the earthquake itself. The timeline of the world's major earthquakes in the last two decades is shown in Figure 2.1.

On May 12, 2008, in the Sichuan province of China, an earthquake of 7.8 Mw magnitude hit this region and killed around 87, 600 people. Similarly, on March 11, 2011, an earthquake of 9.0 Mw magnitude hit the Tohoku region of Japan killing about 15,690 people and injuring about 5700 people. Furthermore, on April 25, 2015, an earthquake of 7.8 Mw magnitude hit the Gorkha region of Nepal killing about 9,000 people and disrupting the lives of more than eight million people (Bhagat et al., 2018).

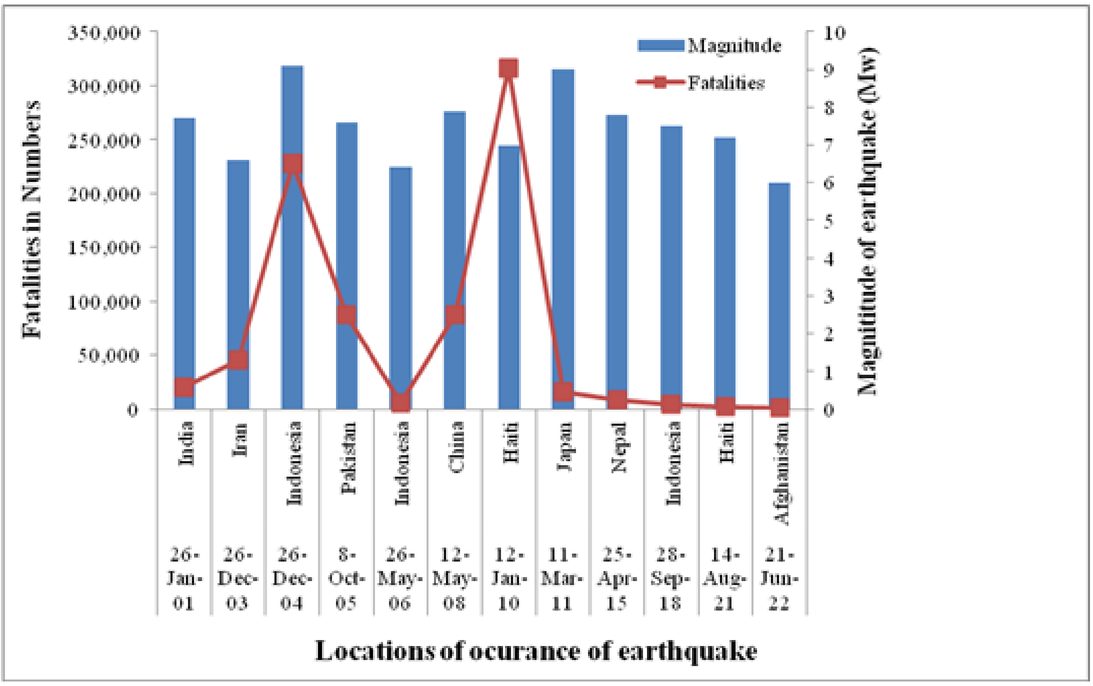

Figure 2.1: World deadliest earthquake around the world

2.1.2 Historic earthquakes and their effect on damages in Nepal

Nepal is a landlocked country and is ranked as the 11th most earthquake-prone country in the world (UNDP, 2009). Many earthquakes occur in Nepal due to the collision of the Indian Subcontinent with Eurasian/Tibetan plates. The major earthquake in Nepal is shown in Figure 2.2. The casualties were caused mainly due to the collapse of infrastructures.

2.1.2.1 Gorkha Earthquake 2015

An earthquake of 7.8 Mw struck Nepal on 25th of April 2015 which affected 31 districts of Nepal, killed around 9000, and 22,302 people were seriously injured. The epicentre of this earthquake was near Barpak, Gorkha which is around 80 km NW from Kathmandu (NPC, 2015). The focal depth was about 8.2 km ± 2.9 km (USGS, 2015). According to USGS, the maximum ground acceleration (PGA) was about 0.35 g and 0.1-0.15 g in the Kathmandu Valley during the 2015 Gorkha earthquake (Bhagat et al., 2018).

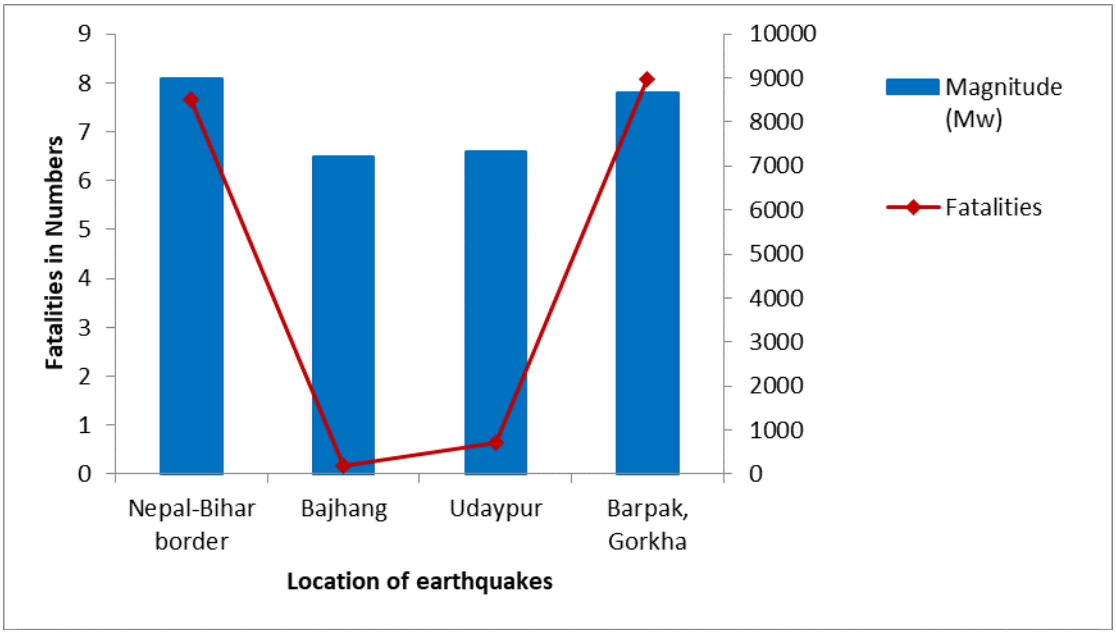

Figure 2.2: Historical earthquake of Nepal

2.2 Housing types in Nepal

In Nepal, reinforced concrete (RC) building structures started only after 1980 and most of the RC walls are found in urban areas of Nepal. About 44.21% of houses are mud-bonded bricks, 24.9% have wooden pillars, cement-bonded structures are about 17.57%, and only 9.94% of buildings are RC construction based on types of structures (Figure 2.3) (CBS, 2012). However, as per the wall systems, mud-bonded brick or stones are 41.38%, cement-bonded brick or stones are 28.7%, bamboo walls are 20.23% and wooden walls are 5.31% (Figure 2.4) (CBS, 2012). In rural areas, wall systems are composed of mud brick or stone, bamboo, and wooden plank walls. Cement-bonded wall types are found in urban areas of Nepal (CBS, 2012). In rural areas of Nepal, galvanized sheets and slate, tile, or straw are extensively used as roofing systems (Figure 2.5). Tile slate covers about 26.68 %, RCC covers about 22.48 % and thatched straw covers about 19.0.3 % which are common types of roofing systems in Nepal (CBS, 2012).

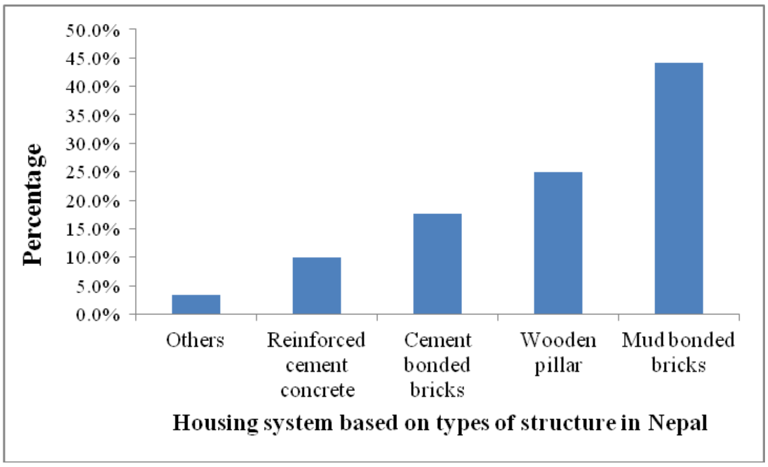

Figure 2.3: Distribution of houses as per types of structure in Nepal

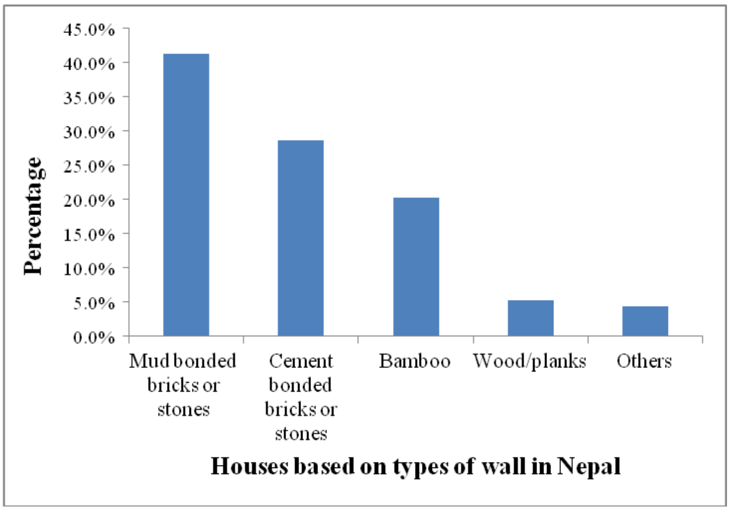

Figure 2.4: Distribution of houses as per types of walls in Nepal

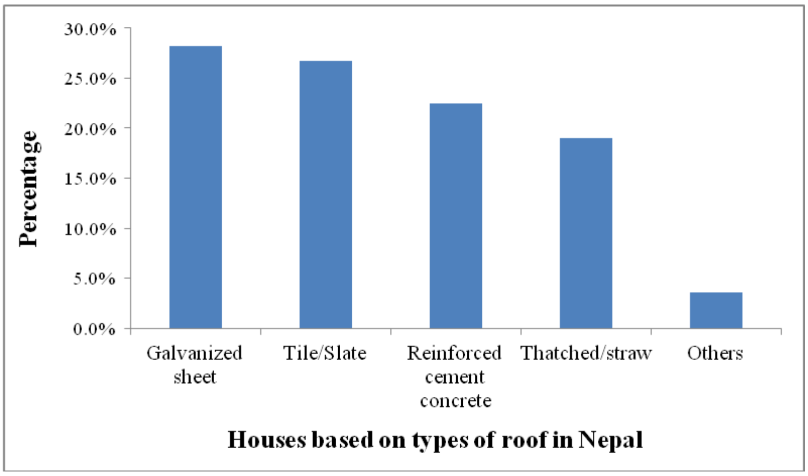

Figure 2.5 Distribution of houses as per types of roofs in Nepal

2.2.1 Building typologies of Nepal before and after of affected area by the Gorkha 2015 earthquake

Figure 2.6 shows a comparison of the building typologies of pre-and post of the 2015 Gorkha earthquake. The variation of housing types across the earthquake-affected area was reported in (HRRP, 2018). The pre-earthquake data was taken from the Central Bureau of Statistics (CBS, 2012), and damage assessment and post-earthquake data were taken from an analysis carried out by HRRP and the Inter-Agency Common Feedback Project (CFP) in May 2018. It shows that mud mortar stone and cement mortar brick houses show to increase in number in post-earthquake (Figure 2.6).

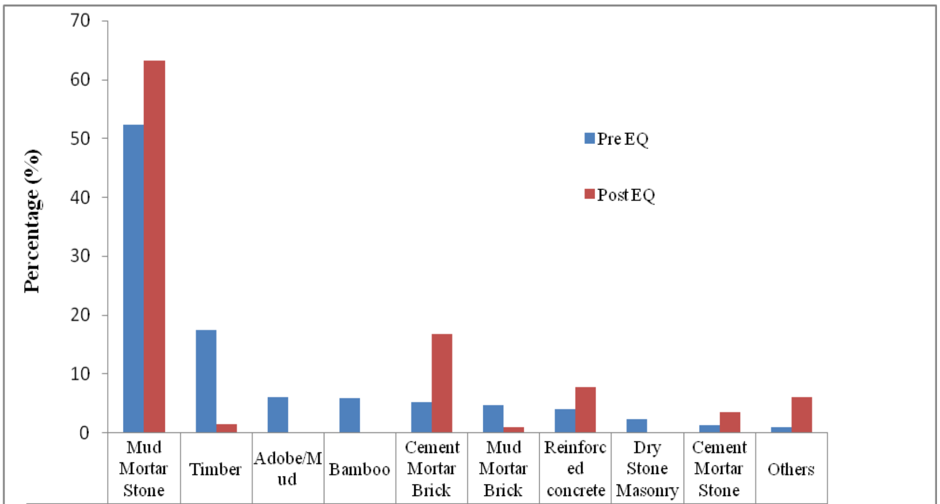

	Mud Mortar Stone	Timber	Adobe/Mud	Bamboo	Cement Mortar Brick	Mud Mortar Brick	Reinforced concrete	Dry Stone Masonry	Cement Mortar Stone	Others
Pre EQ	52.3	17.4	6.1	5.8	5.2	4.7	4	2.3	1.3	1
Post EQ	63.3	1.5	0	0	16.7	0.9	7.8	0	3.5	6

Figure 2.6: Building typologies pre- and post-earthquake

2.2.2 Damages incurred during the 2015 Gorkha Earthquake of Nepal

About 95% of buildings were fully damaged and about 68% of houses were partially collapsed and were low-strength masonry buildings which were mostly constructed with bricks, stone, and mud mortar according to a report published by the Government of Nepal (HRRP, 2018) (Figure 2.7). However, only 4% of buildings were fully collapsed cement-based masonry structures and were made up of brick, concrete blocks, or stone and cement sand mortar (Figure 2.7). Only 1% of buildings were fully collapsed which were reinforced concrete frames (Gautam et al., 2016).

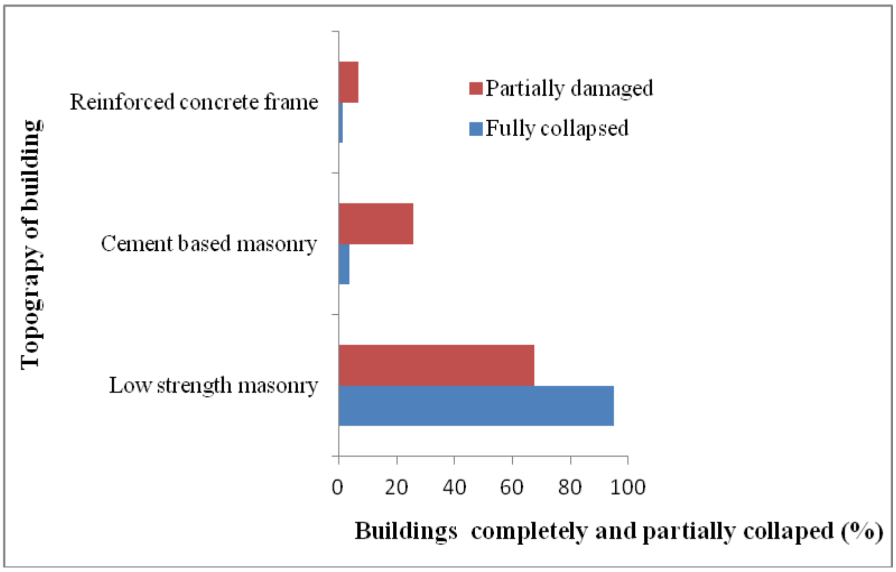

Figure 2.7: Completely and partially collapsed building based on the structural type in the 2015 Gorkha earthquake

2.2.3 Mud masonry house in Nepal

Mud masonry houses are common in rural areas of Nepal which were constructed a long time ago. These houses are constructed by locally available materials such as brick, stones mud, timber, bamboo etc. Unreinforced masonry (URM) is a common type of building in Nepal (Khadka et al., 2020).

Brick is used to construct the walls and foundation of mud masonry houses. Two types of bricks are used in Nepal for the construction of mud masonry houses i.e., sun-dried and burnt bricks. The inner walls or some main walls of old masonry historical buildings are constructed with sun-dried bricks (Khadka and Shakya, 2021). However, these types of brick are rarely used due to low strength. Nowadays, burnt bricks are commonly used for construction purposes. The dimension of sun-dried brick was about 210x105x50 mm for the construction of buildings in Nepal (Khadka et al., 2020).

Lime, mud, and cement are used as mortar. Mud is mostly used as bonding material or for the plastering of walls in old masonry buildings. The quality of mud varies with location and soil type (Khadka et al., 2020).

Timbers are used for the construction of doors, windows, stairs, beams, vertical posts, flooring, and seismic bands in mud masonry houses. Commonly used timber for the construction of houses are Sal (*Shorea Robusta*), Salla (*Pinus Wallichiana*), Utis (*Alnus Nepalensis*), and Gwaisasi (*Schima Wallichi*). Bamboo is also used for the construction of seismic bands, roof battens, floors, and partition walls in mud masonry houses. Roofs are constructed with timber trusses and tiles or light metallic corrugated galvanized iron sheets (Tamrakar, 2018).

2.2.4 Deficiencies in unreinforced masonry buildings in the 2015 Gorkha earthquake

The deficiencies in unreinforced masonry buildings of Nepal during the 2015 Gorkha earthquake have been discussed by many researchers (Tamrakar, 2018; Khadka, 2020; Bhagat et al., 2018; Gautam, 2018; Paudel, 2021). Commonly seen deficiencies during the 2015 Gorkha earthquake are discussed in the following section:

2.2.4.1 Out-plane failure mechanism

During the 2015 Gorkha earthquake, damage from out-of-plane loads was prominent in several masonry buildings. Flexible floor diaphragms, a lack of a seismic band, and a weak connection between return walls are typical characteristics of brick masonry walls (Khadka et al., 2020). During the 2015 Gorkha earthquake common types of out-of-plane behavior were wall bulging, wall buckling, wall splitting, and wall delamination.

2.2.4.2 Delamination of walls

This kind of damage is found in the thick mud mortar of the brick walls. The main reasons for damage or even out-of-plane collapse in masonry walls are when the inner and outer wythes are not connected. This is mostly because the outermost layers of walls are not connected (HRRP, 2018).

2.2.4.3 Short wall out-of-plane damages

Damage of this kind was frequently observed during earthquakes. The walls have insufficient capacity at the wall corners to transfer forces from one wall to another. As a result, the walls at the corner separate. Improper connection between the short wall and the diaphragm may be the cause of this kind of damage (HRRP, 2018).

2.2.4.4 In-plane failure

During the 2015 Gorkha earthquake, shear, tension, compression, and spandrel failure are common types of in-plane failure (HRRP, 2018). Walls with diagonal cracks are indicative of shear collapse. This is mostly because the building lacks seismic bands. Vertical cracks at the corners or ends of walls are observed in tension failure. Lack of anchoring between orthogonal walls is the primary cause of tension failure. Rocking and toe-crushing cracks are seen in compression failure. The main cause of this is the building members' lack of integrity. Flexural cracks, bed joint sliding, and diagonal cracks are seen in spandrel failure. The primary cause of this is the lack of seismic band and spandrel geometries (Khadka et al., 2020).

2.2.4.5 Load path discontinuity

The 2015 Gorkha earthquake caused numerous structural failures due to discontinuities in the load path. According to Khadka et al. (2021), mixed construction practices are the main cause of load path discontinuity. Certain buildings in Nepal are built with cement-bond brick masonry for the top story and mud mortar for the bottom floor. There were reinforced concrete components on the upper stories of some of the buildings. Due to this, the load transfer mechanism may become unbalanced, which could have contributed to the failure during the 2015 Gorkha earthquake (Khadka et al., 2021).

2.2.4.6 Pounding failure

The majority of houses in Nepal are built in rows. The floor heights of the houses are not equal, and there is no space between them. In this type of house, the crack at the return wall, sway of houses, and floor level were observed during the 2015 Gorkha earthquake.

2.2.4.7 Binding materials

The structural integrity of masonry structures depends on the binding material. The low structural integrity could be the result of using low-quality binding material. During the 2015 Gorkha earthquake, it was discovered that the mud mortar used to bind the brick and stone units had already separated and was acting independently (Tamrakar, 2018).

2.2.4.8 Age of building

The earliest kind of building is mud mortar buildings, with the majority having been built more than a century ago. These buildings also lack adequate repair and maintenance. As a result, the structure's strength had declined. The main causes of the failure were inadequate maintenance and lack of strength during the 2015 Gorkha earthquake (Tamrakar, 2018).

2.2.4.9 Roof failure

The weight of the construction is increased by the usage of gable walls and roof tiles. One of the factors contributing to roof failure during the 2015 Gorkha earthquake was an increase in the structure's load at the roofing. The improper joining of the roofing components to the walls is another reason why roofs fail (Tamrakar, 2018).

2.3 Methods for investigating mechanical characteristics of brick masonry materials and assemblage

Masonry is composed of units and joints which is heterogeneous in nature. Masonry has a longer lifespan and can sustain significant compressive weight. Masonry is the oldest building material which is easy to construct. It is defined as the composite of units and mortar. For structural analysis of buildings not only the properties of constituent materials are important but also the properties of composite are important. The types of bricks and mortar used determine the behavior of any masonry. As a result, understanding the characteristics of mortar and brick units is crucial to understanding how masonry behaves. Cement, lime, and clay are utilized as joints, and bricks, blocks, adobes, and stones are regarded as units (Mustafaraj, 2016).

2.3.1 Types of Unreinforced Masonry (URM) walls

The bricks are arranged for the construction of wall in a regular pattern called bond. There are various types of bonds such as Stretcher, Flemish, and English bond (Mustafaraj, 2016). In stretcher bond, all the bricks are laid in length wise direction. However, in the header bond, all the bricks are laid in headers. In English bonds, the bonds are arranged in alternate layers of header and stretchers.

2.3.2 Constituent material properties

The properties of bricks vary widely, depending on the quality of clay or manufacturing processes. Additionally, the mechanical behavior of bricks is not necessarily homogeneous and isotropic.

2.3.3 Unit compressive strength of Brick

The compressive strength of brick is an important material property. The increase in compressive strength of brick also increases the compressive strength and elastic modulus of masonry assemblage. The compressive strength of brick is determined by ASTM C 67 "Method of Sampling and Testing Brick and Structural Clay Tile" (Chin and Petry, 1993). The traction strength of bricks is measured by uni-axial strength and flexural tensile strength. The compressive test arrangement of the brick specimen is shown in Figure 2.8.

Figure 2.8: Compression test on a brick specimen (Bergami, 2007)

Figure 2.9 shows the stress-stain curve for compression in brick proposed by Kaushik et al. (2007).

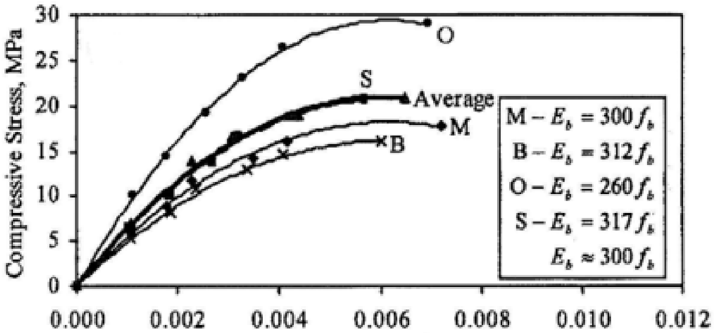

Figure 2.9: Typical stress-strain curve for compression in bricks (Kaushik et al., 2007)

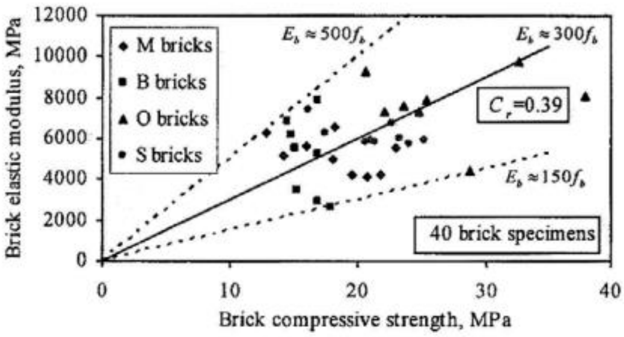

Figure 2.10: Relationship between compressive strength and elastic modulus for bricks (Kaushik et al., 2007)

Figure 2.10 shows the relationship between compressive strength and elastic modulus for brick. Kaushik et al., (2007) reported that for the estimation of the elasticity module (E_b) of clay bricks, a range of values depending on the compression strength of the brick (f_b) was recommended.

These values are given by equation (2.1) below,

$$150*fb \le Eb \le 500*fb \qquad (2.1)$$

2.3.4 Unit compressive strength of Mortar

The unit compressive strength of mortar, bond strength, and elasticity are the mechanical properties that influence the structural performance of masonry. The compressive strength of mortar is determined by ASTM C 270 "Specification for Mortar for Unit Masonry" (ASTM, 2003). Kaushik et al. (2007) proposed a relationship for the estimation of the elasticity module (E_m) of mortar and recommended a range of values depending on the compression strength of the mortar (f_m). The relationship was given by the equation (2.2) below,

$$100 * fm \le Em \le 400 *fm \qquad (2.2)$$

A typical stress-strain curve for compression in mortar is shown in Figure 2.11.

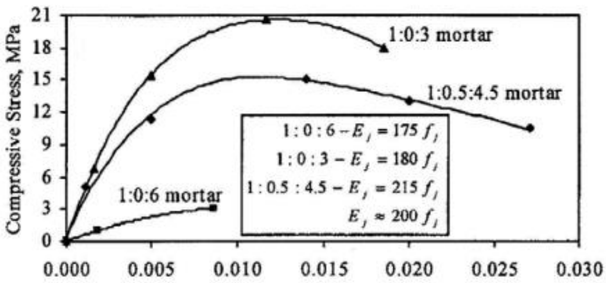

Figure 2.11: Typical stress-strain curve for compression in mortar (Kaushik et al., 2007)

The relationship between compressive strength and modulus of elasticity for mortar is shown in Figure 2.12.

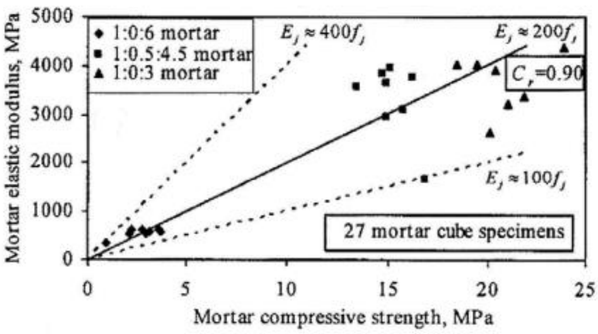

Figure 2.12: Relationship between compressive strength and modulus of elasticity for mortar (Kaushik et al., 2007)

2.3.5 Assemblage Mechanical Properties

Compressive strength of Masonry Unit

The compressive strength of the masonry assemblage is the most important mechanical property in brick masonry design. The compressive strength of the masonry assemblage is determined by prism test.

2.3.5.1 Prism Test Method

Masonry prisms are tested using ASTM C1314 “Standard Test Methods of Compressive Strength of Masonry Prisms” (Alcocer and Klinger, 1994). Three prisms are required for conducting this test and the average value was taken for the determination of compressive strength of the masonry unit. The low strength of prism indicates the poor quality of mortar or mixing error of mortar.

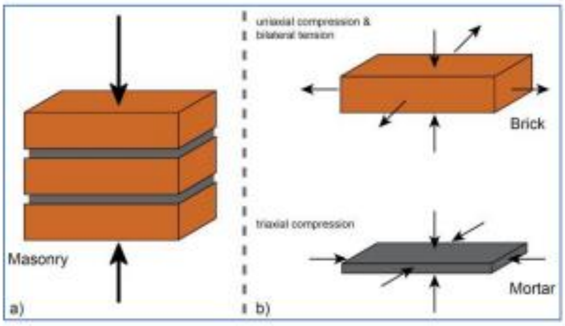

Figure 2.13: a) Compression of masonry prism, b) state of stresses of brick and mortar (Hilsdorf, 1969)

The main reason for the failure of masonry is the difference in the elastic properties of brick and mortar (Hilsdorf, 1969). The compression of the masonry prism and the state of stresses of brick and mortar are shown in Figure 2.13.

Sarangpani et al. (2005) reported that the compressive strength of the prism increased as the grade of mortar increased. Palanisamy and Premalatha (2012) experimented with the compressive strength of clay brick and fly ash brick masonry prisms with three types of mortar. They reported that the compressive strength and elastic modulus of fly ash brick masonry were greater than those of clay brick masonry. Vimala and Kumarasamy (2014) experimented on both the dry and wet state of brick masonry for compressive strength. They found that the dry and wet strength of prism increased with the increasing strength of the mortar. They also confirmed that compressive strength in the dry state was higher compared to that of the wet state.

2.3.5.2 Contact (interface) between brick and mortar

The contact between brick and mortar can be tested by two types of tests; the tensile bond test and the shear bond test. The tensile bond test is used to determine the tensile behavior of brick and mortar. The shear bond test is used to determine the shear-behaviour of the interface between brick and mortar.

2.3.5.3 Flexural Tensile Strength Test

For unreinforced masonry, flexural tensile strength is one of the key design parameters. Flexural tensile strength is the bond strength in flexure. The type of unit, mortar, workmanship, and loading direction all play a role in flexural tensile strength. Prism testing in compliance with ASTM E 518, "Standard Test Method for Flexural Bond Strength of Masonry," and ASTM C 1072, "Standard Test Method for Measurement of Masonry Flexural Bond Strength," is typically used to determine flexural tensile strength (Alcocer and Klinger, 1994).

2.3.5.4 Shear Strength

The shear strength of the masonry assemblage depends on unit and mortar properties. Shear failure of masonry assemblage occurs by splitting of units, steps like cracking in mortar joints, or a combination of both. The unit's compressive strength determines the unit splitting strength. One sort of shear failure that frequently occurs in masonry assemblies is the result of a cracked mortar joint. There are two types of mortar joint failure: separation of head joints and sliding along bed joints. The ASTM E 519 "Standard Test Method for Diagonal Tension (Shear) in Masonry Assemblages" is used to determine the shear strength of a masonry assembly.

Figure 2.14 shows experimental approaches adopted by (Rahman and Ueda, 2014) for determining the shear behavior of joints of brick masonry on couplet, triplet, and prism.

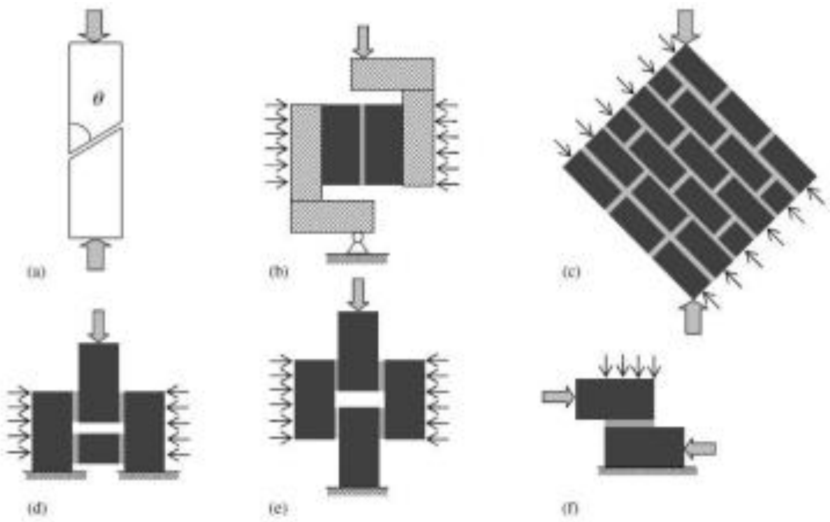

Figure 2.14: Different Types of shear Test Specimens: (a) Nuss Shear Test, (b) Van der Pluijm Test, (c) Diagonal Tension Test, (d) Triplet Test, (e) Meli Test, (f) Direct Shear Test (Rahman and Ueda, 2014)

Crisafulli et al., (1995) and Hendry et al., (1997) suggested that the shear strength of unreinforced masonry is based on the Mohr-Coulomb shear friction expression as expressed in equation (2.3):

$$\tau_m = \tau_0 + \mu * \sigma_n \qquad (2.3)$$

where τ_m: shear strength at the shear bond failure; τ_0: shear bond strength at zero normal stress; μ: internal friction coefficient between brick and mortar; σ_n: normal stress at bed joint.

The most common tests that are used to determine masonry shear strength are couplet or triplet tests which are used to quantify the shear strength parameters.

Shear-compression test: The shear strength is evaluated as the average shear stress of the wall panel subjected to in-plane loading.

Diagonal compression test: Diagonal compression tests were used to evaluate the shear strength and the shear elastic modulus of masonry.

2.3.5.5 Modulus of Elasticity

The modulus of elasticity is the ratio of applied load to corresponding deformation. The modulus of elasticity and moment of inertia of the section determines the stiffness of brick masonry. The modulus of elasticity is proportional to the compressive strength of masonry shown in equation (2.4). The modulus of elasticity of masonry assemblage depends on the mortar type and its unit compressive strength. The Modulus of Elasticity of masonry (E_m) is calculated as the modulus of the chord of the linear part of the masonry compression stress-strain curve, it is generally taken between 5% and 33% of the ultimate masonry compressive strength (f'_m) (ASTM, 2003).

$$E_m = k * f'_m \qquad (2.4)$$

The formula for determination of the modulus of elasticity was proposed by several researchers and standards as shown in Table 2.1 (Mustafaraj and Yardim, 2017).

Table 2.1: Formulas for determining the modulus of elasticity by several researchers and standards

SN	Authors/Standard	Proposed equation
1	Eurocode 6 (CEN, 2005)	$E_m=1000*f'_m$
2	FEMA 273, 1997	$E_m=550*f'_m$
3	Paulay and Prestley, 1992	$E_m=750*f'_m$
4	Tomazeviç,1999	$200f_{cb\leq} \leq Em \leq 2000\ f_{cb}$
5	MSJC (MSJC, 2002	$E_m=700*f'_m$
6	Crisafulli et al., 1995	$E_m=300*f'_m$
7	Drysdale et al.,1994	$E_m=500\text{-}600*f'_m$
8	ASCE, 2007	$E_m=350*f'_m$

Where, E_m is the elastic modulus of masonry, f'_m is the compressive strength of masonry, and f_{cb} is the compressive

2.3.5.6 Shear Modulus of Masonry

The shear modulus of masonry is calculated as the ratio of shear stress to shear strain. It is also known modulus of rigidity (G). It is calculated as the secant modulus up to 33% of the maximum shear stress.

It is calculated by equation (2.5):

$$G = \tau_{1/3} / \gamma_{1/3} \qquad (2.5)$$

where $\tau_{1/3}$ is the shear stress for a load of 1/3rd of the maximum load P_{max} and $\gamma_{1/3}$ is the corresponding shear strain (Milosevic et al., 2013).

The relationship between the Modulus of Elasticity and shear strength is given as follows (Gere and Timoshenko, 1986).

$$G = E / 2(1 + \nu) \qquad (2.6)$$

where "ν" is the Poisson's module of mortar

Various researchers proposed the following relationship for estimations of shear stiffness in terms of Modulus of Elasticity, E_m, or the compressive strength of brick masonry, f'_m as shown in Table 2.2 (Mustafaraj and Yardim, 2017).

Table 2.2: Formulas for determining the shear modulus proposed by researcher and standards

SN	Authors/Standard	Proposed equation
1	Alcocer and Klinger (1994)	$G_m=0.1*E_m$ (for masonry with high-strength brick units); $G_m=0.2*E_m$ (for masonry with low-strength brick units)
2	Paulay and Priestley (1992)	$G_m=400*f'_m$
3	FEMA 273 (1997)	$G_m=0.4*E_m$

where G_m and E_m are shear and elastic modulus, respectively

2.4 Common types of failures in Masonry walls

2.4.1 In-plane failure

In masonry walls, main two types of failures occur in the in-plane loading of walls which are described below.

2.4.1.1 Flexural failure

Due to an increase in shear capacity and high moment in walls, this type of failure occurs. In this type of failure, moderate energy dissipation and low strength degradation occur. If the vertical load imposed on wall is less than the compressive strength of masonry, significant displacement might occur (Salmanpour et al., 2013). Tension cracks in the bed joints are seen due to horizontal loading which results in the crushing of masonry units in the compressed zones (Tomaževič, 1999). The masonry walls rock like a rigid body in this type of failure. On the lower side of the wall toe-crushing normally occurs (Figure 2.15 (a)). Rocking and toe-crushing failure are common types of failure. For non-retrofitted URM walls, Magenes and Calvi (1997) recommend a drift limit of 1%, whereas Cattari and Lagomarsino (2009) recommend a drift limit of 0.8% for flexural failure.

2.4.1.2 Shear failure

Slide failure along bed joints (Figure 2.15 (b)), diagonal cracking through the bed and head mortar joints along a stair-stepped route (Figure 2.15(c)), a straight diagonal route through brick units (Figure 2.15(d)), or a mix of these modes can all be caused by the shear response of the wall. Low-quality mortar might lead to sliding failure. The maximum deflection in the sliding shear failure is high, and a 1% drift limit is advised. Shear failure occurs when the wall is loaded with vertical as well as horizontal forces. Diagonal tension cracking is a common type of failure during earthquakes in masonry walls (Tomaževič, 1999). Shear failure occurs when the principal tensile stresses exceed the in-plane tensile capacity of the wall. According to Tomaževič (1999), diagonal cracks can occur in motor joints in the stair-case-shaped or penetrate through the masonry units. According to Salmanpour et al. (2013), diagonal crack in walls occurs due to poor-quality mortar along the mortar joints, which could lead to the wall's sections sliding apart.

When there is initial cracking, strength and stiffness decrease, and the rate of energy dissipation increases, indicating limited ductility in diagonal shear failure. In cases where shear failure is common in URM walls, Magenes and Calvi (1997) and Cattari and Lagomarsino (2009) suggest a drift limit of 0.5% and 0.4%, respectively.

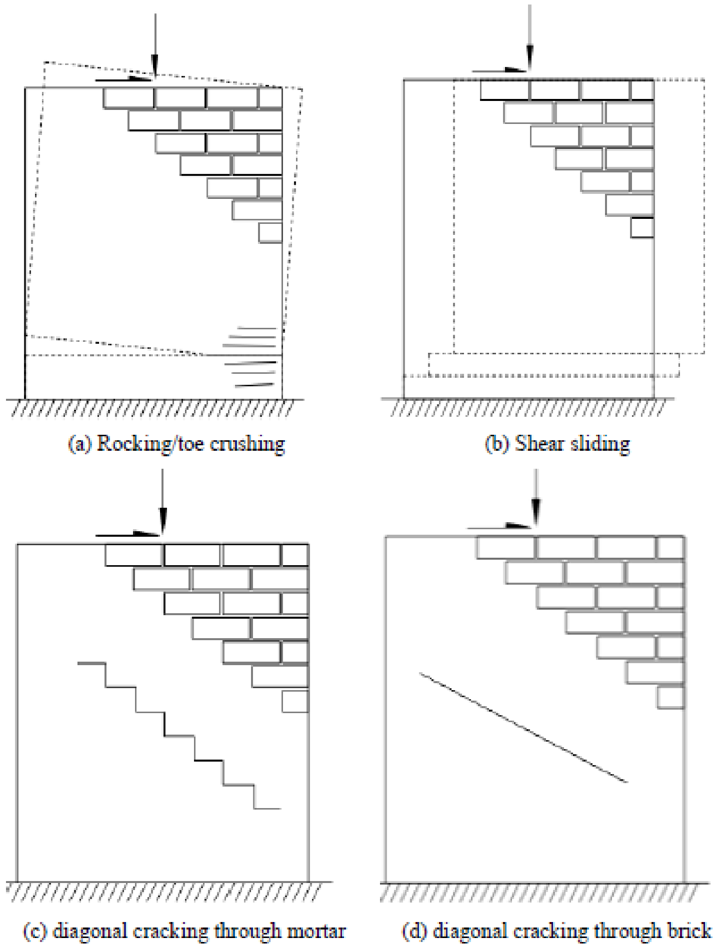

Figure 2.15: In-plane failure response of URM Wall (Calderini et al., 2009)

2.4.2 Response of unreinforced masonry walls in in-plane direction

Stiffness determines the distribution of seismic forces and the overall dynamic behavior of masonry walls. The stiffness of brick masonry depends on the mechanical properties, geometry of structure, and boundary conditions. For in-plane laterally loaded masonry elements, the unit displacements are presented in the following figure (Figure 2.16).

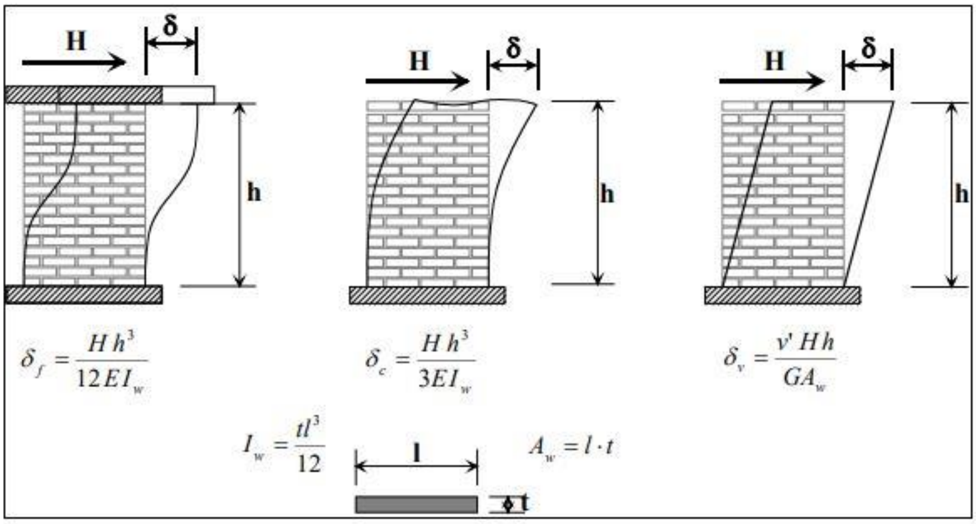

Figure 2.16: Elastic deflections of masonry walls (Bosiljkov et al., 2005)

In the seismic analysis of laterally loaded walls, the deformation δ∑ is calculated as the combination of bending and shear deformation based on elastic beam theory. For the walls with both ends fixed, the δ∑ is equal to the sum of δf and δv, and for cantilever walls δ∑ = δc +δv.

In-plane response (in-plane strength, elastic stiffness, and drift) of URM walls are summarized. The equation (2.7) gives the estimate of the elastic stiffness (Kel) of the wall determined by considering elastic beam theory (Haach et al., 2010; Bosiljkov et al., 2005).

$$K_{el} = \frac{1}{\frac{h^3}{\alpha_K E_m I} + \frac{h}{A_n G_m}} \tag{2.7}$$

where 'h' is the wall height, 'E_m' is Young's Modulus of elasticity of masonry, and 'G' is the shear modulus. Area moment of inertia, $I = tl^3/12$, 'l' and 't' are wall length and thickness, respectively. $An = lt$ is the wall cross-sectional area, α_K is a constant based on the wall geometric boundary conditions ($\alpha_K = 0.83$ for fixed-fixed walls, and $\alpha_K = 3.33$ for cantilever walls).

According to Eurocode, there are three types of failure modes for URM walls under in-plane loading: a) flexural failure (toe-crushing), b) sliding failure, and c) diagonal shear failure.

The in-plane strength during different modes of failure is calculated by equations (2.8), (2.9) and (2.10):

1- Flexural toe-crushing (V_f):

$$V_f = \frac{N \cdot l}{2 \cdot h_0}\left(1 - \frac{N}{0.87 \cdot l \cdot t \cdot f_m}\right) \tag{2.8}$$

where 'N' is the pre-compression load, 'h_0' is the shear span measured from wall base ($h_0 = h$ for cantilever walls and $h_0 = h/2$ for fixed-fixed condition walls), and 'f_m' is the compressive strength of masonry.

2- Sliding failure (V_{sl}):

$$V_{sl} = f_{vk} \cdot t \cdot l' \tag{2.9}$$

where 'l'' is the length of the compressed wall part, and depends on the eccentricity 'e'. The shear strength of the masonry 'f_{vk}' should be less than or equal to 6.5 % of brick compressive strength. It is a function of cohesion of masonry 'f_{vk0}' and pre-compression 'σ_0' and is given as:

$$f_{vk} = \begin{cases} f_{vk0} + 0.4\sigma_0 & ;\textit{if bed and head joints are fully filled with mortar} \\ 0.5f_{vk0} + 0.4\sigma_0 & ;\textit{if vertical joints are not filled with mortar} \end{cases}$$

3- Diagonal Tension (V_{dt}):

$$V_{dt} = \frac{t \cdot l}{b} f_t \sqrt{1 + \frac{\sigma_0}{f_t}} \tag{2.10}$$

where 'f_t' is the tensile strength of masonry obtained from experiments and 'b' is a shape correction factor ($1.0 \leq b = h/l \leq 1.5$).

2.4.3 Force-Displacement Response of In-plane Loaded URM Walls

The actual hysteretic behavior of the wall is converted into an idealized bi-linear curve to determine the elastic stiffness, load capacity, displacement capacity, and ductility factor of walls subjected to in-plane reverse cyclic lateral load (Magenes and Calvi, 1997; Tomaževič, 1999).

The associated deformation and force resistance at the moment when the wall starts to crack for the first time is represented by δ_{cr} and V_{cr} in Figure 2.17. V_{max} indicates the maximum resistance encountered throughout the test, and δ_{Vmax} represents the displacement at this moment. The maximum displacement δ_{max} and the accompanying achieved resistance $V_{\delta max}$ determine the ultimate stage of testing (Tomaževič, 1999) (Figure 2.17).

The equal energy dissipation capacity of the idealized and actual curves, where the area beneath both curves should be equal, was the basis for the development of the bilinear curve. From the prior testing of URM walls, the ultimate resistance V_u of the bi-linear curve was identified, and an average ratio of V_u/V_{max} of 0.9 was selected. The starting slope of the idealized curve, K_{el}, is the elastic stiffness that was determined by dividing V_{cr} by the equivalent displacement, δ_{cr}. The matching point of resistance of $0.8V_{max}$ on the post-peak region of the experimental envelop showed the ultimate displacement point (δ_u) (Howlader, 2020).

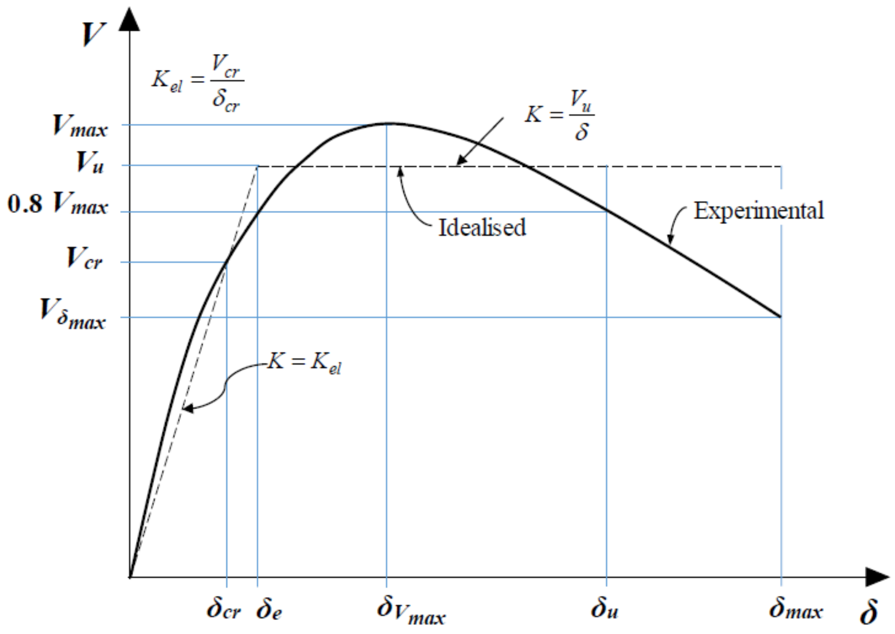

Figure 2.17: Idealized bilinear force-displacement curve (Tomaževič, 1999; Howlader, 2020)

The bi-linearization was defined by Magenes et al. (2008) using Tomaževič's (1999) equivalent energy dissipation approach. The initial cracking point was specified by Magenes et al. (2008) using a load value of 0.70 V_{max}, as shown in Figure 2.18. From this point, it is easy to calculate the elastic stiffness K_{el} and the cracking displacement δ_{cr}. By dividing the value V_u by the elastic stiffness value K_{el}, the displacement at the elastic limit δ_e was determined (Howlader, 2020). The ultimate displacement point (δ_u) matched Tomaževič's (1999) definition.

Magenes et al. (2008) defined the bi-linearization by applying Tomaževič's (1999) equivalent energy dissipation method. As illustrated in Figure 2.18, Magenes et al. (2008) determined the initial cracking point with a load value of $0.70V_{max}$. From this point, the elastic stiffness K_{el} and the cracking displacement δ_{cr} are calculated. The displacement at the elastic limit δ_e was calculated by dividing the value V_u by the elastic stiffness value K_{el}. The ultimate displacement point (δ_u) gave a similar result as that of Tomaževič (1999).

The equivalent energy principle, which states that the areas beneath the bilinear curve and the cyclic envelop curve are equal, was used to calculate the value of V_u in the bilinear curve. The following formulas are used to calculate the areas (Figure 2.18).

The value of V_u in the bilinear curve was determined using the equivalent energy concept, which asserts that the regions beneath the bilinear curve and the cyclic envelop curve are equal. The areas are computed using the following formulas.

$$A_{env} = \sum A_i \tag{2.11}$$

$$A_{bilin} = V_u \times \delta_u - \frac{V_u^2}{2K_{el}} \tag{2.12}$$

$$V_u = \left(\delta_u - \sqrt{\delta_u^2 - \frac{2A_{env}}{K_{el}}} \right) K_{el} \tag{2.13}$$

Where, V_u = yield load, in N; A_{env} = area under the envelop curve from the origin to the δ_u, in N.m; A_i = discrete areas under cyclic envelop curves, in N.m; A_{bilin} = area below the bilinear curve, in N.m; V_{max} = the maximum absolute load in the envelop curve, in N; δ_e = the displacement corresponding to the Vu, in mm; K_{el} = the elastic stiffness, in N/m.

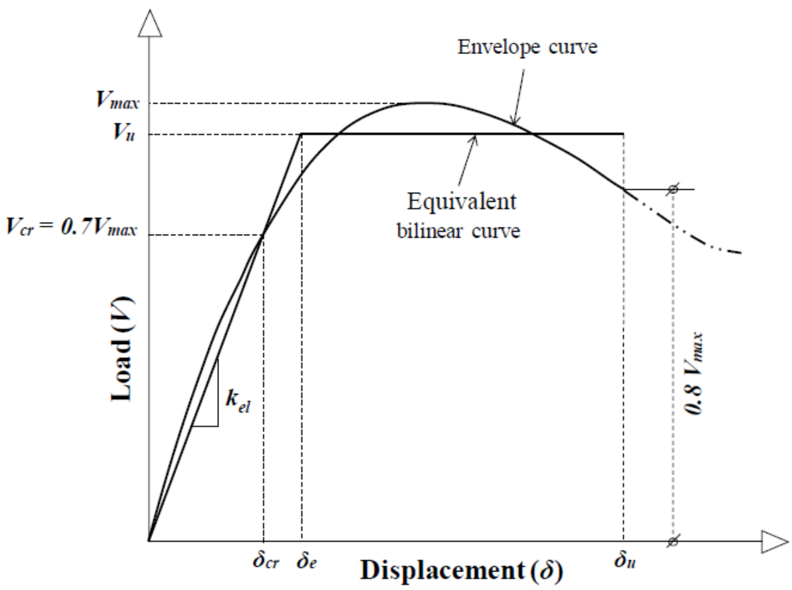

Figure 2.18: Bilinear idealization of the load displacement curve (Magenes et al., 2008; Howlader, 2020)

2.4.4 Past work on In-plane behavior of wall

To understand the seismic behavior of walls, Ashraf et al. (2012) experimented to determine the impact of ferro-cement as a retrofitting material. They tested full-scaled perforated URM walls with apertures for windows and doors in a quasi-static manner.

Before retrofitting, shear cracking was seen in the middle of the pier; however, damage was only visible at the top and bottom of the pier after retrofitting. After retrofitting, there was a 68% and 110% increase in lateral stiffness and strength, respectively.

The impact of Glass Fiber Reinforced Polymers (GFRPs) retrofitting for URM walls with a central opening was investigated by Kalali and Kabir (2012). In this test, walls were subjected to lateral in-plane incremental cyclic loading with constant gravity loadings. Shear failure in the URM wall was visible in the opening's upper and lower corners as well as spreading to the wall's ends. After retrofitting, the GFRP reinforced wall's failure mode shifted to a rocking and sliding mode, confirming the structure's more ductile behavior. Furthermore, compared to unreinforced walls, the in-plane resistance increased significantly by around 2.05 and 4.18 times.

The in-plane shear behavior of URM walls with various brick arrangements in the spandrels and piers was investigated by Vanin and Foraboschi (2012). The testing results demonstrated that the wall's geometry and the brick texture in its pier and spandrel determine the failure mechanism. The findings also demonstrated that variations in brick arrangement had an impact on the wall's ductility and load-resisting capacity.

Allen et al. (2016) conducted in-plane cyclic shear testing of full-scale perforated URM walls by varying the pier-spandrel geometric configuration and the axial pre-compression load. It was observed that at low levels of axial stress, the failure was concentrated mostly in the pier zone but at higher axial load levels the spandrels exhibited extensive combined shear and flexure failures.

Ismail and Ingham (2016) conducted in-plane cyclic testing of pier-spandrel URM substructures by retrofitting with polymer textile-reinforced mortar (TRM). The unreinforced wall displayed diagonal shear failure in the spandrel and rocking failure at the pier's base. The unreinforced wall and the spandrel retrofitting with TRM (FG225) specimens had comparable fracture patterns. Nevertheless, brittle shear failure with diagonal stair-stepped cracking was observed in the pier following the retrofitting of spandrels with higher strength TRM (EF335). The spandrel showed no signs of cracking. When compared to an unreinforced wall, the strength of both TRM types retrofitted in the spandrel was greatly increased.

2.4.5 Out-of-plane failure

The out-of-plane failure is one of the most common types of failure in developing countries for unreinforced masonry (URM) walls. The URM wall can withstand gravity and lateral load. However, URM walls are weak in out-of-plane bending strength is the main cause of failure.

According to Lourenço et al. (2017), the main risk factor for URM structure collapse is the out-of-plane failure of URM walls. The absence of a tensile-resistant element in the URM wall during out-of-plane loading is the main reason for out-of-plane failure.

According to Costa et al. (2014) and Lin et al. (2016), the out-of-plane capacity of URM walls is primarily determined by the wall's thickness, slenderness ratio, and wall-to-diaphragm connections. Failure in the out-of-plane mode might happen parallel to or perpendicular to the bed joints (Figure 2.19). In brick masonry walls, out-of-plane failure happens when the stress is greater than the unit's tensile strength or the mortar's bond strength. This kind of failure happens with weak mortar in masonry.

2.4.6 Effect of retrofitting on out-of-plane behaviors of masonry wall

Strengthening techniques increase the strength and ductility of masonry walls as discussed below.

Various researchers conducted out-of-plane experiments for retrofitted walls as shown in Table 2.3. For example, Nezhad and Kabir (2017) conducted a three-point bending test on the walls retrofitted with GFRP. They reported the flexural strength of the retrofitted wall increased by 2.72 to 6 times compared to the unreinforced sample. Similarly, Kariou et al., (2018) conducted a three-point bending test on the walls retrofitted with textile-reinforced mortar. They reported the flexural strength of the retrofitted wall increased by 1.5 to 2.1 times compared to the unreinforced sample.

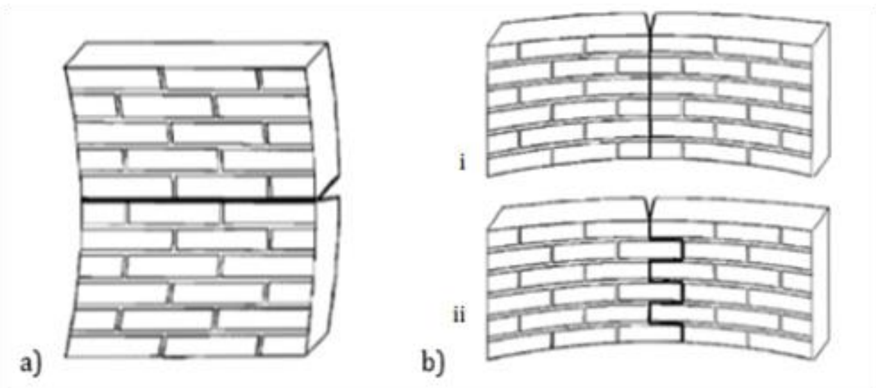

Figure 2.19: Out of plane failure in URM wall: a) parallel to bed joints, b) perpendicular to bed joints (BSI, 1996; Dauda, 2020)

Table 2.3: Out-of-plane experimental test of retrofitting of walls by various researchers

Researchers	Masonry units	Loading type	Strengthing techniques	Flexural strength increment
Banerjee et al., (2020)	Clay and fly ash bricks	Static 4-point loading	Steel wire mesh	2.5 times
Kadam et al., (2015)	Clay brick	Monotonic 4-point loading	Ferrocement overlay	10 times
Padalu et al., (2018)	Clay brick	Monotonic 4-point loading	Welded wire mesh	9.4 times
Padalu et al., (2019)	Clay brick	Static 4-point loading	Basalt fiber-reinforced cement mortar	2-4.1 times
Nezhad and Kabir (2017)	Clay bricks	Static 3-point loading	GFRP	2.72-6 times
Kariou et al., (2018)	Solid clay brick	Static 3-point loading	Textile reinforced mortar	1.5-2.1 times
Shermi and Dubey (2018)	Clay brick	Static 4-point loading	Welded wire mesh	20 times
Anil et al., (2012)	Hollow clay brick	Static 4-point loading	CFRP	9 times

2.5 Methods of retrofitting of unreinforced masonry walls

2.5.1 Steps for seismic retrofitting of historical masonry buildings

It is crucial to preserve culture and tradition by conserving heritage and passing it on to the next generation. Retaining the original aesthetics of historical buildings is usually the primary goal of preservation efforts. Therefore, during the restoration of historical buildings, the retrofitting materials should be selected in such a way that they are compatible with the original masonry substrate (Yavartanoo and Kang, 2022).

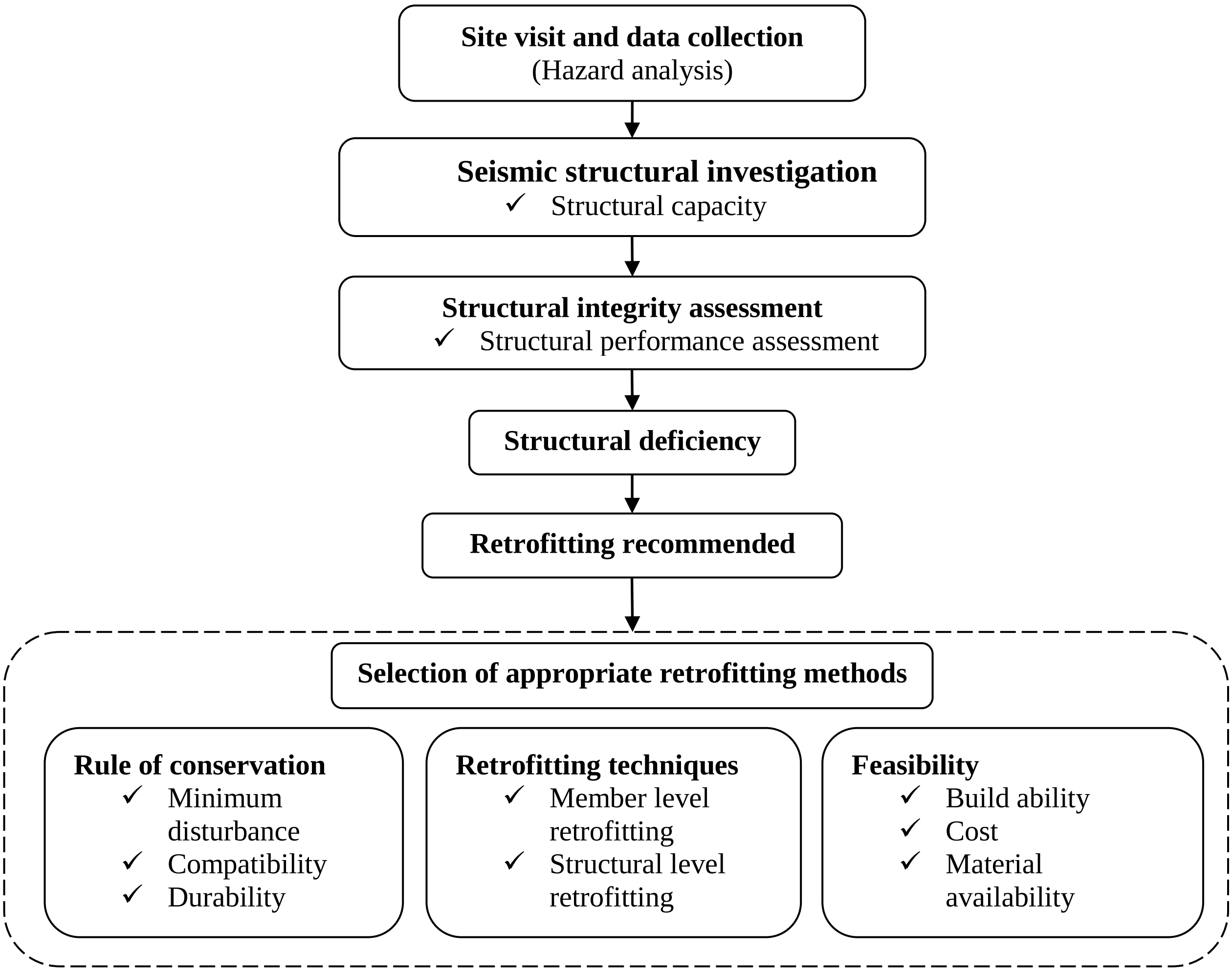

Figure 2.20: Steps for seismic retrofitting of historical masonry buildings (Adopted from (Yavartanoo and Kang, 2022), with modification)

The decision to select a particular technique for retrofitting historical brick masonry depends on many factors and necessitates agreement among practitioners in all relevant disciplines (Yavartanoo and Kang, 2022). The important factors that can guide the practitioners in retrofitting historical brick masonry are shown in Figure 2.20. The flow diagram illustrates the various stages involved in the seismic retrofitting of historical brick masonry buildings. The first step is to visit the site and gather data. Following that, a seismic structural assessment and investigation are completed. Retrofitting is advised if there are structural deficiencies in the structure.

2.5.2 Classification of retrofitting methods

The retrofitting is generally done to URM buildings to increase their collapse time and reduce the loss of lives during earthquakes (Bhattacharya *et al.*, 2014). Retrofitting of building structure helps to increase the structural capacity and ductility of the building (Dauda, 2020). Several retrofit methods have developed over time to increase masonry constructions' ability to withstand extreme out-of-plane loads, such as earthquakes. They are broadly classified into two categories: (i) member level, which involves considering retrofitting specific building elements like the floor, roof, or walls, and (ii) structure level, which involves considering retrofitting the entire building to enhance its overall response and integrity (Izmir and Erberik, 2015; Binda and Cardani, 2015) (Figure 2.21). The member level and structural level retrofitting is further classified as old or modern techniques.

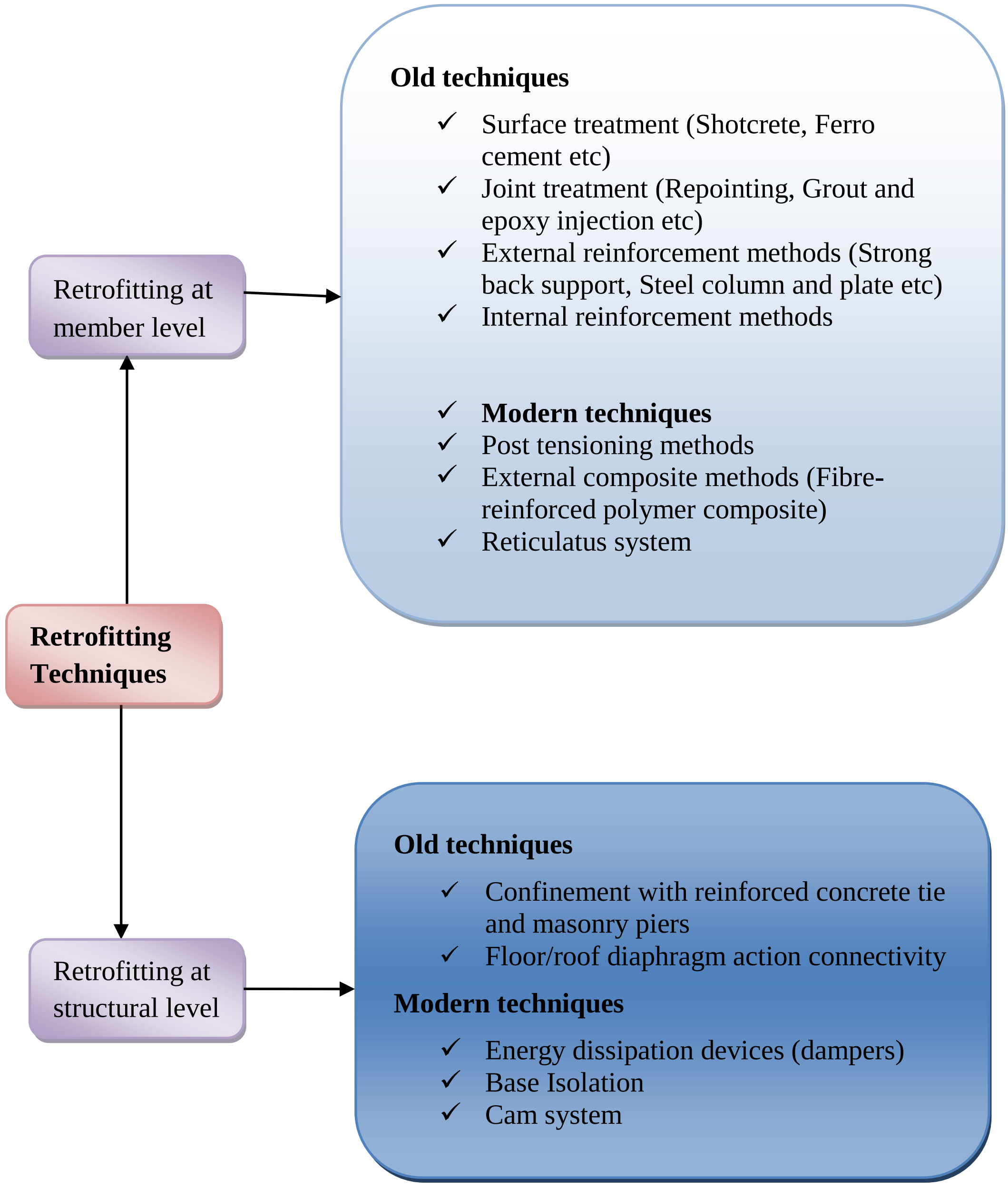

Figure 2.21: Classification of retrofitting techniques (Adopted from (Dauda, 2020), with modification)

2.5.3 Member level retrofitting

2.5.3.1 Surface treatment

The steel or polymer mesh is positioned around the outside of the structure and covered with a coating of high-strength mortar as part of the retrofitting surface treatment process. According to Bhattacharya et al. (2014), the steel reinforcement ratio in this approach ranges from 3 to 8%, depending on the necessary loading resistance. It increases the out-of-plane resistance of masonry buildings. Unskilled labor can perform this less expensive retrofitting procedure.

2.5.3.2 Shotcrete overlays

Shotcrete is the method of applying mortar of thickness of 70 to 150 mm over the wire mesh (Yavartanoo and Kang, 2022). The URM and retrofitted walls with shotcrete overlay walls were evaluated by ElGawady et al. in 2006. There were two approaches to retrofitting walls: in the first, shotcrete was placed from only one side of the wall panel, and in the second, it was applied from both sides (Bhattacharya et al., 2014). A shotcrete retrofitted wall was subjected to the lateral load in increasing order until the wall failed. For both types of reinforcing arrangements, the walls' ultimate lateral load resistance was raised by 3.6 when compared to unreinforced walls (ElGawady et al., 2006). Furthermore, the stiffness at peak load was increased by three times compared to that of unreinforced samples. The efficacy of this retrofitting technique is significantly influenced by the wall's surface smoothness (Wang et al., 2018). When used from both sides, this retrofitting technique can reduce the stress by almost 50%. Tensile stress can be decreased by roughly 33% by applying shotcrete from one side (Karantoni and Fardis, 1992). The use of shotcrete reinforcement increases the ultimate load-carrying capacity of retrofitted walls. Nepal Building Research Institute (NBRI) reported that in the 2015 Gorkha earthquake of Nepal, the buildings retrofitted by this technique performed well (NBRI, 2016). This is low-cost technology for retrofitting of buildings. The disadvantage of this type of reinforcement is that they are time-consuming and also affects the aesthetics of the buildings.

Advantages:

- ✓ Increases the out-of-plane stability of structures
- ✓ Improves the shear and flexural strength of structures
- ✓ Improves ductility of the structure

Disadvantages:

- ✓ Needs skilled workers
- ✓ Affects the architecture of the structure
- ✓ Causes space reduction
- ✓ Time-consuming

2.5.3.3 Ferrocement

In the ferro-cement retrofitting technique, cement mortar is applied to closely space fine rod meshes which are arranged in multiple layers. The mortar thickness varies from 10 to 50 mm. The wall's in-plane behavior is improved by the ferro-cement reinforcing. This method uses a ratio reinforcement that ranges from 3 to 8% (ElGawady, 2006). When compared to an unreinforced specimen, the application of this technique enhances in-plane lateral resistance by 150%, according to Abrams and Lynch's (2001) static test. The out-of-plane strength was increased by approximately 10% by installing 0.29% longitudinal reinforcement. Installing only 0.29% of reinforcement in the longitudinal direction can increase strength in the out-of-plane direction by approximately ten times (Kadam et al., 2015).

Advantages:

- ✓ Increases the lateral resistance, lateral strength, and energy dissipation

Disadvantages:

- ✓ Time-consuming
- ✓ Affects the aesthetic and historical look

2.5.3.4 Stitching and grout/epoxy injection

This method of retrofitting is one of the low-cost technology in which the grout or epoxy is injected into the walls to fill the cracks and voids (Wang et al., 2018). This approach is popular because it is inexpensive to implement, simple to use, and requires less experienced workers to complete the task. Steel ties and mortar can be used to stitch wall cracks to return the wall to its original rigidity (Dauda, 2020). The increase in strength is more influenced by the injection of epoxy compared to stiffness.

Advantages:

- ✓ Restore the initial stiffness and lateral strength of the structure
- ✓ Easy to apply on structure

Disadvantages:

- ✓ No significant increment in initial stiffness is attained
- ✓ Affects the architecture of the structure

2.5.3.5 Re-pointing

This retrofitting technique is suitable for structures with high-quality bricks and lower-quality mortar (Bhattacharya et al., 2014). In this approach, the mortar joint is replaced and filled with new stronger mortar to preserve the wall's integrity (ElGawady et al., 2004). This is a conventional method of building retrofitting that is simple to use and less expensive. According to Wang et al. (2018), this technique is easy to fill the voids for structures made of rubble stone.

Advantages:

- ✓ Restores the initial stiffness and lateral strength of the structure
- ✓ Easy to apply on structure

Disadvantages:

- ✓ No significant increment in initial stiffness is attained
- ✓ Affects the architecture of the structure

2.5.3.6 PP packaging strip mesh reinforcement

One of the simplest and least expensive retrofitting techniques is using PP (polypropylene) band mesh (Wang et al., 2018; Macabuag, 2007). The PP band mesh is installed and drilled into the masonry wall as part of this retrofitting technique. To investigate the effects of diagonal compression, Sathiparan et al. (2005) retrofitted wallets with two distinct arrangements by PP-bands (Figure 2.22). In comparison to an unreinforced specimen, they reported that the strength and deformation capacity rose to 2.5 and 45 times, respectively. The application of PP mesh also improved the frictional resistance. Additionally, it maintains wall integrity, enhances ductility and load resistance, and allows for greater deformation without failure (Macabuag et al., 2012; Meguro et al., 2006).

Nepalese brick masonry was retrofitted with PP meshing and strong shocks were applied artificially in the experiment conducted by (Macabuag et al., 2012). They discovered that brickwork that has been modified with PP mesh is more earthquake-resistant without collapse. It is not advised to retrofit heritage buildings using this technique (Yavartanoo and Kang, 2022).

Advantages:

- ✓ Enhance shear strength and ductility
- ✓ Low cost of construction

Disadvantage:

- ✓ Time-consuming
- ✓ Affects the aesthetic and historical look

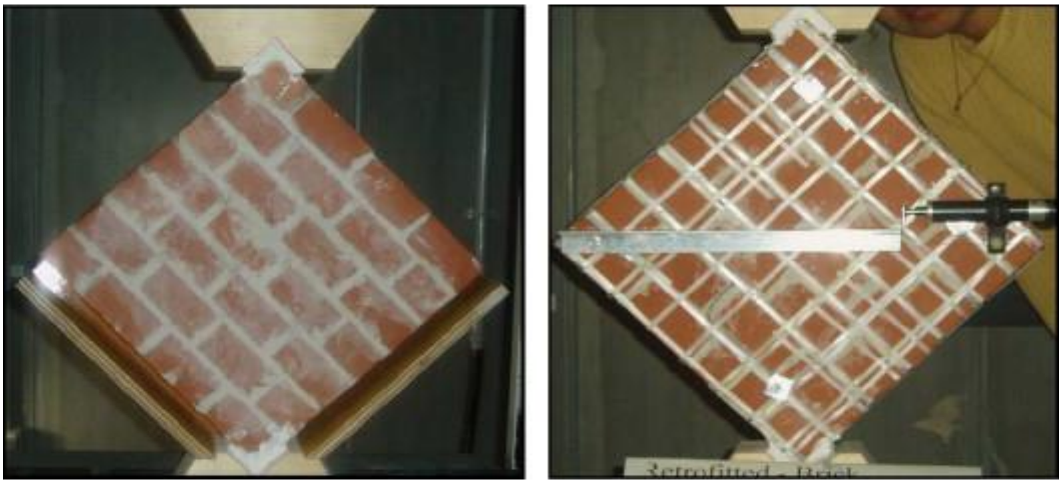

Figure 2.22: Non-retrofitted and retrofitted wall panels with PP retrofitting (Macabuag, 2007)

2.5.3.7 Reticulatus system

Structures made of stone and masonry can be retrofitted using the reticulatus technology. High-strength steel or composite cords are employed as the retrofitting material in this retrofitting approach (Anania et al., 2013). The reticulatus system can significantly enhance the overall integrity, stiffness, compression, shear, and flexural strength of the stone wall (Zampieri et al., 2018; Valvona et al., 2017; Garmendia et al., 2015). The effectiveness of the system highly depends on the reinforcement mesh embedded in the mortar joints and the masonry structure (Figure 2.23).

Figure 2.23: Application of reticulatus system on stone masonry adopted from (Borri et al., 2011)

Advantages:

- ✓ Improves integrity and increases stiffness
- ✓ Improves tensile strength
- ✓ Increase connection between members

Disadvantages:

- ✓ Time-consuming
- ✓ Requires skilled workers for construction

2.5.3.8 Fiber-reinforced polymers (FRP)

This retrofitting technique is becoming popular for URM building reinforcement. According to Alcaino and Santa-Maria (2008) and ElGawady et al. (2004), the strength of URM walls can be increased by 1.1 to 3 times by the use of FRP composites as a retrofitting technique. According to (Mahmood and Ingham, 2011), retrofitting masonry walls with FRP increases their shear resistance by a factor of 3.25. When comparing retrofitted walls to URM walls, the use of FRP as the retrofitting material increases the walls' ultimate load-carrying capability, ductility, and energy absorption (Corradi et al., 2002; Kuzik et al., 2003; Tan and Patoary, 2004). The FRP retrofitting arrangement is shown in Figure 2.24.

The use of FRP as a retrofitting material has several benefits, including less structural disruption, minimal mass addition to the building, and a greater increase in strength. The few disadvantages of using it are that the method is expensive, changes the aesthetic appearance of the building, and requires high skilled workers to retrofit of building (Burgoyne, 2004).

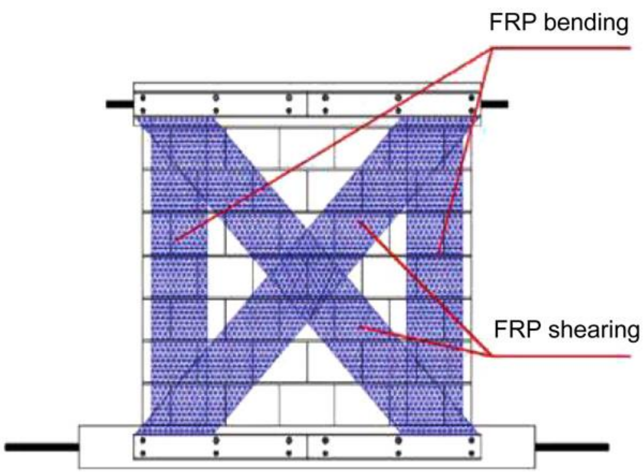

Figure 2.24: Application of FRP, retrofitting technique
(Wang et al., 2018)

Advantages:

- ✓ Enhance shear and flexural strength
- ✓ Creates low disturbance to the structure

Disadvantages:

- ✓ Costly method
- ✓ The skilled worker is required
- ✓ Affects the aesthetic and historical look

2.5.3.9 Engineering cementitious composites (ECC)

Cement, sand, water, fiber, and chemical additives are used in ECC retrofitting. The masonry structures' tensile and flexural resistance is increased by the application of ECC (Dauda, 2020; Ghlomreza, 2013). According to Martins et al. (2015), employing ECC retrofitting to masonry walls increases the ductility of the wall and prevents brittle failure.

Advantages:

- ✓ Enhances the shear strength and out-of-plane behavior
- ✓ Enhances the ductility

Disadvantages:

- ✓ Costly method
- ✓ Affects the aesthetic and historical look
- ✓ The skilled worker is required

2.5.3.10 External reinforcement

The purpose of external reinforcement is to control the spread of cracks and sustain earthquake stresses by installing reinforced elements adjacent to masonry structures (Yavartanoo and Kang, 2022). Applying this retrofitting technique improves the mechanical behavior of the masonry structure (Wang et al., 2018). In this method, the reinforcing materials are bamboo and steel. According to Kuzik et al. (2003), external steel reinforcement enhances the structure's ductility, energy dissipation capacity, and in-plane strength. This retrofitting technique is applied to load-bearing walls that support the floor above (Dauda, 2020). Because bamboo is a locally available material, retrofitting with it is an affordable method. They are very simple to utilize as a reinforcement material. It has little capacity to prevent cracks at low-intensity ground motion however, it increases the collapse time of adobe buildings.

According to Dowling et al. (2005), installing vertical reinforcement on an adobe wall lessens the difficulty of aligning the reinforcement and trimming bricks (Figure 2.25). Additionally, they stated that the displacement intensity was increased by 100% when bamboo and ring beams with horizontal chicken wire mesh were used.

This kind of strengthening is frequently applied to the reinforcement of adobe masonry structures. Josh et al. (2012) used this technique to rural Nepal's non-engineered adobe, they discovered that it helped to preserve the wall's integrity and avoid material loss. (Saleem et al., 2016) reported that retrofitting brick masonry with this technique cannot withstand severe shaking and the method was not too effective for retrofitting brick masonry houses. An adobe house retrofitted with bamboo band meshes increases its input energy by more than double that of the non-retrofitted specimen, according to (Meguro et al., 2012).

Figure 2.25: Bamboo reinforced wall with ring beam extracted   from (Dowling et al., 2005)

2.5.4 Structure Level Retrofit

2.5.4.1 Confinement with Constructional Columns of URM building

This approach uses a construction pier or column made of reinforced concrete to create confinement for already-existing masonry structures (Dauda, 2020). The intersection of the wall and wall corners is where the confinements are located. According to Tomaževič and Klemenc (1997), it enhances the resistance capacity both in-plane and out-of-plane. Furthermore, according to Tomaževič and Klemenc (1997), the technique can increase lateral resistance by approximately 1.5 times and energy dissipation by roughly 50%. The technique is costly and requires skilled man power for its application to the structure.

2.5.4.2 Confinement with Ring Beam of URM Building

The mechanical behavior of masonry constructions is enhanced by the use of reinforced concrete ring-beams (Wang et al., 2018). According to Okail et al. (2016), the ductility and strength of the masonry panel are increased when constructional columns and ring beams are used to confine the masonry constructions. According to Borri et al. (2009), a building's ability to support more weight is increased when its ring beams are strengthened with composite. This method works well with constructional columns and is simple to implement in newly constructed structures (Dauda, 2020).

2.5.4.3 Tie Bars

Masonry structures are strengthened using tie bars to increase their structural stability. According to Darbhanzi et al. (2014), masonry constructions with vertical ties have greater seismic capability, strength, and ductility. They also stated that the strength and ductility of the masonry structure can be enhanced by the vertical ties. While using this retrofitting method, caution should be taken to avoid corrosion in the bar in case of surface treatment.

2.5.4.4 Base isolations

One of the cutting-edge retrofitting techniques used to modify a building's response to an earthquake is base isolation (Wang et al., 2018). The base isolation system is shown in Figure 2.26. By isolating the superstructure from the foundation using isolation devices such as elastomeric bearings, this sort of retrofitting strategy aims to reduce the likelihood of damage or collapse during earthquake events (Matsagar and Jangid, 2008). With this method, the seismic force is not transferred to the superstructure. Retrofitting a masonry building with a combination of steel bracing and dampers helps to disperse a significant amount of seismic energy, excessive cracking, and deformation, according to Gocevski and Petraskovic (2012).

The technique is becoming popular for restoring historic buildings worldwide. Historical buildings such as the San Francisco City Hall, Oakland City Hall, and Salt Lake City hall are retrofitted by base isolators at the foundation level (Melkumyan et al., 2011). Compared to fixed-base constructions, base isolation reduces the inter-story drift in superstructures (Ferraioli et al., 2010).

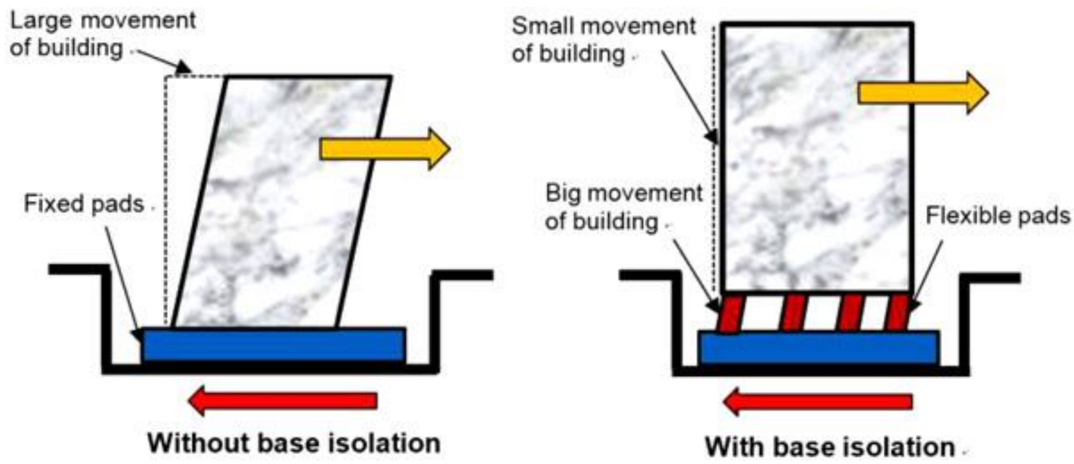

Figure 2.26: The techniques of using base isolation adopted from (Wang el. al., 2018)

Advantages:

- ✓ Minimum effect on building architecture
- ✓ The superstructure is not retrofitted in this method

Disadvantages:

- ✓ Costly method
- ✓ The skilled worker is required

2.5.4.5 Energy- dissipation devices

Seismic dampers, another name for energy dissipation devices, are employed in buildings to lessen the energy generated by earthquakes (Dauda, 2020). Seismic dampers are devices that absorb and release seismic energy during an earthquake, thereby minimizing building damage and deformation. Branco and Guerreiro (2011) investigated the performance of viscous dampers on a 1911 Lisbon building. The researchers concluded that viscous dampers have a beneficial impact through the reduction of the displacements of individual floors. According to Chrysostomou et al. (2015), when dampers are used, URM buildings are less seismically vulnerable than buildings that have been conventionally retrofitted.

Advantages:

- ✓ Improves lateral resistance, energy dissipation
- ✓ Restore the stiffness
- ✓ Can be applied after the earthquake

Disadvantages:

- ✓ Costly method
- ✓ Requires skilled work for the construction of structure

2.5.4.6 Cam system

One of the innovative three-dimensional tying retrofitting approaches is the CAM system, in which the masonry is tied together using a cam system to achieve compaction of masonry parts (Dauda, 2020). Research on applying the CAM method to earthquake-damaged buildings was carried out by Dolce et al. in 2001. They reported that the CAM system's application enhanced the connection between the building's structural elements. Additional tests were carried out by Dolce et al. (2001) to verify the CAM system's efficacy on brick panels. In comparison to an unreinforced masonry panel, they claimed that the strength and dissipation energy had improved by 50% and 60%, respectively. The CAM system is shown in Figure 2.27.

Advantages:

- ✓ Increase strength and ductility
- ✓ Improves connection

Disadvantages:

- ✓ Time-consuming
- ✓ Requires skilled work for the construction of structure

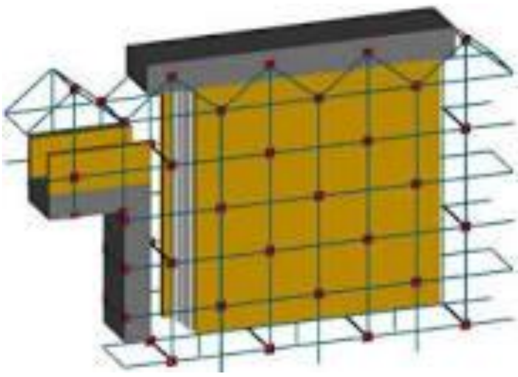

Figure 2.27: CAM arrangement in URM wall adopted from (Dolce el. al., 2001)

2.5.5 Use of timber and RC walls as Reinforcement for unreinforced masonry

This research is to investigate the use of Sal wood timber for reinforcement of Nepalese historical masonry buildings. Furthermore, it also investigates the use of RC walls and steel plates for reinforcement of Japanese historical. The justification for using timber and RC walls for retrofitting Nepalese and Japanese historical brick masonry is comprehensively detailed through experimental and numerical investigations in Chapters 3,4, 5,6,7, and 8 of this dissertation.

2.6 Finite Element Models of Masonry

Masonry structures are one of the oldest types of construction. However, due to the anisotropy nature of masonry, variations in mortar joint thickness, dimension of brick, arrangements of bed and head joints, and the presence of mortar joints, the modeling and analysis are difficult for masonry structures (Lourenco, 1996a). The numerical modeling and analysis of masonry structures is a challenging job for engineers was reported by (Lourenco, 1996a; Maccarini et al., 2018; Portioli, 2020).

Asteris et al., (2015) reported that masonry structures behave as a linear elastic material, and at high load it behaves as a non-linear material. Mostly the joints between the masonry units show non-linear behavior (Lourenço, 1996a). Therefore, studying the behavior of the joints in the masonry is a complex part of the modeling. Asteris et al. (2013) and Lourenço (1996a) reported that there are broadly two types of modeling approaches namely, macro-modeling and micro-modeling on the basics of simplicity and accuracy.

2.6.1 Macro-modeling

The masonry is considered as homogeneous continuum material in the macro-modeling approach. Macro modeling requires less time and memory and the mesh generation is user-friendly (Lourenco, 1996a). This modeling approach can be used for the modeling of large solid walls as well as the modeling of complete buildings with good accuracy. The detailed stress analysis of a small masonry panel, failure modes, and mechanical behavior of the brick-mortar interface cannot be simulated by this modeling approach. This approach is also known as structural level modeling techniques. This modeling technique has been previously adopted by Lourenco (1998) and Pena et al. (2010).

The micro-modeling technique gives accurate results however its analysis is computationally intensive due to the detailed level of refinement (Portioli and Cascini, 2017).

2.6.2 Micro-modeling

In the micro-modeling approach, the units and joints are considered separately. Micro-modeling includes the simulation of units, mortar, and the unit-mortar interface. In this method of analysis, the detailed stress and failure modes of the masonry of small masonry walls with great accuracy can be calculated. There are two types of micro-modeling depending on simplicity and accuracy namely detailed micro-modeling and simplified micro-modeling.

In the detailed micro-modeling, the three-phase material approach is used. The bricks and mortar are represented by continuous elements and are modeled separately, whereas the interface behavior between brick and mortar is shown by discontinuous elements.

Simplified micro-modeling is a two-phase material approach in which the brick units are modeled as expanded units represented by continuous elements and mortar joints and the interface by discontinuous elements and mortar joints are ignored and replaced by interface elements, whose characteristics are based on interface behavior (Lourenço, 1996a).

More accurate results can be obtained by detailed micro-modeling compared to the simplified micro-model. However, the detailed micro-modeling is limited to use for small-scale samples due to being computationally intensive. The computational time required by a simplified micro-model is less. The input parameters for micro-modeling such as the material properties required for units and the interface elements can be determined from experimental testing of the units, joints, and masonry assemblages as described in (Lourenço, 1996a). The other required values for micromodeling can be taken from the literature (Lourenço, 1996a, 2008).

2.6.3 Past works on masonry modeling from the literature

Some previous numerical studies on URM structures are presented below.

A macro-element approach, which is similar to the equivalent frame model, was proposed by Brencich et al. (1998) for the analysis of URM buildings. In this approach, the piers and spandrels were modeled by using the macro-element instead of the beam elements used in the equivalent frame model. This modeling approach can capture the hysteretic dissipation and the damage resulting in better prediction of the lateral resistance and the near collapse failure of the URM buildings. With the development of different computer-aided software in the structural engineering field, more detailed nonlinear finite element modeling approaches of the masonry structure were proposed by Lourenço (1996a) as described above.

Farshchi et al. (2009) studied nonlinear finite element analysis using a micro-modeling approach for simulating the in-plane behavior of plane URM walls. The elastic solid element was used to model brick units and brick failure was estimated by the manual checking using Willam and Warnke’s theory. The numerical simulation shows that the shear and flexural failure modes were in good agreement with the damage patterns of the tested specimens.

Betti et al. (2014) studied the seismic behavior of two storied URM buildings with flexible diaphragms by the FE modeling and analysis. The study used the macro-modeling technique in which masonry assembly was considered homogeneous. In addition, to represent the nonlinear behavior of masonry the smeared crack approach was used. The ultimate load capacity and the crack pattern during the experiment were predicted by the model used.

Zhang et al. (2017) conducted URM modeling using a micro-modeling approach using Abaqus software. Zhang et al. (2017) By comparing the FE result with the experimental in-plane testing, concluded that the element-based cohesive model can capture the nonlinear behavior of the mortar joints with the damage proliferation of the wall.

Allen et al. (2017) conducted micro and macro modeling approaches for the determination of in-plane behaviors of URM perforated walls. Considering the masonry as a homogenous and continuum element the smeared mechanical properties were used in the macro-modelling approach. The crack pattern and load-displacement behavior of the micro modeling and the macro modeling were compared with cyclic in-plane testing results of URM walls. The failure modes were in better agreement with the experimental results for micro-modeling compared to that of the macro-modeling. Finite element analysis shows that the load-displacement behavior was in agreement with the experimental results.

References

Abrams, D. P., and Lynch, J. M. (2001). Flexural behavior of retrofitted masonry piers. In KEERC-MAE joint seminar on risk mitigation for regions of moderate seismicity (pp. 234-243).

Alcaino, P., and Santa-Maria, H. (2008). Experimental response of externally retrofitted masonry walls subjected to shear loading. Journal of composites for construction, 12(5), 489-498.

Alcocer, S. M., and Klinger, R. E. (1994). Masonry Research in the Americas. Masonry in the Americas, 147, 127-169.

Allen, C., Masia, M. J., and Page, A. W. (2016). Experimental Testing of Unreinforced Masonry Walls with Openings Subjected to Cyclic In-plane Shear. Proceedings of the *16th International Brick & Block Masonry Conference (IBMAC)*, Padova, Italy.

Allen, C., Masia, M. J., Page, A. W., Griffith, M. C., and Ingham, J. M. (2017). Nonlinear finite element modeling of unreinforced masonry walls with openings subjected to in-plane shear. Proceedings of the *13th Canadian Masonry Symposium*, Halifax, Canada.

Anania, L., Badala, A., Costa, S., D'AGATA, G., and Giacquinta, C. (2013, September). Experimental investigation of masonry calcareous walls repaired and strengthened by C-FRP. In Proceedings of the Thirteenth East Asia-Pacific Conference on Structural Engineering and Construction (EASEC-13) (pp. H-5). The Thirteenth East Asia-Pacific Conference on Structural Engineering and Construction (EASEC-13).

Anil, Ö., Tatayoğlu, M., & Demirhan, M. (2012). Out-of-plane behavior of unreinforced masonry brick walls strengthened with CFRP strips. *Construction and Building Materials*, *35*, 614-624.

ASCE. (2007). Seismic Rehabilitation of Existing Buildings –SEI/ASCE 41-Reston. VA: American Society of Civil Engineers; 2007. https://doi.org/10.1061/9780784408841

Ashraf, M., Khan, A. N., Naseer, A., Ali, Q., and Alam, B. (2012). Seismic behavior of unreinforced and confined brick masonry walls before and after ferro-cement overlay retrofitting. *International Journal of Architectural Heritage*, *6*(6), 665-688.

Asteris, P., Plevris, V., Sarhosis, V., Papaloizou, L., Mohebkhah, A., Komodromos, P. and Lemos, J. (2015). Numerical Modeling of Historic Masonry Structures. In: P. Asteris and V. Plevris, ed., Handbook of Research on Seismic Assessment and Rehabilitation of Historic Structures. IGI Global, pp.213-256.

ASTM International. (2002). ASTM E519-02, Standard Test Method for Diagonal Tension (Shear) in Masonry Assemblages. West Conshohocken, PA.

ASTM. (2003). ASTM C 270-03, Standard Specification for Mortar for Unit Masonry. West Conshohocken, PA: ASTM International.

Banerjee, S., Nayak, S., & Das, S. (2020). Shear and flexural behavior of unreinforced masonry wallets with steel wire mesh. *Journal of Building Engineering*, *30*, 101254.

Bergami, A. V. (2008). Implementation and experimental verification of models for nonlinear analysis of masonry-infilled RC frames.

Betti, M., Galano, L., and Vignoli, A. (2014). Comparative analysis on the seismic behavior of unreinforced masonry buildings with flexible diaphragms. *Engineering Structures*, *61*, 195-208.

Bhagat, S., Samith Buddika, H. A. D., Kumar Adhikari, R., Shrestha, A., Bajracharya, S., Joshi, R., and Wijeyewickrema, A. C. (2018). Damage to cultural heritage structures and buildings due to the 2015 Nepal Gorkha earthquake. *Journal of Earthquake Engineering*, *22*(10), 1861-1880.

Bhattacharya, S., Nayak, S., and Dutta, S. C. (2014). A critical review of retrofitting methods for unreinforced masonry structures. *International Journal of Disaster Risk Reduction*, *7*, 51-67.

Binda, L. and Cardani, G. (2015). Seismic Vulnerability of Historic Centres: A Methodology to Study the Vulnerability Assessment of Masonry Building Typologies in the Seismic Area. In: P. Asteris and V. Plevris, ed., Handbook of Research on Seismic Assessment and Rehabilitation of Historic Structures. IGI Global, pp.213-256.

Borri, A., Castori, G., and Grazini, A. (2009). Retrofitting of masonry building with reinforced masonry ring-beam. Construction and Building Materials, 23(5), 1892-1901.

Borri, A., Castori, G., Corradi, M., and Speranzini, E. (2011). Shear behavior of unreinforced and reinforced masonry panels subjected to in situ diagonal compression tests. *Construction and Building Materials*, *25*(12), 4403-4414.

Bosiljkov, V. Z., Totoev, Y. Z., & Nichols, J. M. (2005). Shear modulus and stiffness of brickwork masonry: an experimental perspective. Structural Engineering and Mechanics, 20(1), 21-44.

Branco, M. and Guerreiro, L. (2011). Seismic Rehabilitation of Historical MasonrymBuildings. Engineering Structures, 33(5), pp.1626-1634.

Brencich, A., Gambarotta, L., and Lagomarsino, S. (1998). A macroelement approach to the three-dimensional seismic analysis of masonry buildings. Proceedings of the 11th European Conference on Earthquake Engineering, Balkema, Rotterdam.

British Standard Institution (1996). *BS EN 1996-1-1:2005: Eurocode 6 -Design of Masonry Structures - Part 1-1: General Rules for Reinforced and Unreinforced Masonry Structures*. London: British Standards Institution.

Burgoyne, C. J. (2004). Does FRP have an economic future? Proceedings of the 4th conference on advanced composite materials in bridges and structures, Calgary, Alberta.

Cattari, S., and Lagomarsino, S. (2009). Modeling the seismic response of unreinforced existing masonry buildings: a critical review of some models proposed by codes. Proceedings of the *11th Canadian masonry symposium*, Toronto, Ontario.

CBS (2012). National Population and Housing Census 2011 (National Report). Central Bureau of Statistics, Kathmandu, Nepal

CEN. (2005). EN 1996-1-1: Design of masonry structures -Part 1-1: General rules for reinforced and unreinforced masonry structures". Brussels, Belgium: European Committee for Standardization.

Chin, I. R., & Petry, L. (1993). Design and testing to reduce efflorescence potential in new brick masonry walls. ASTM International.

Chrysostomou, C., Kyriakides, N., Roussis, P. and Asteris, P. (2015). Emerging Technologies and Materials for the Seismic Protection of Cultural Heritage. Handbook of Research on Seismic Assessment and Rehabilitation Of Historic Structures, Pp.576-606.

Corradi, M., Borri, A., and Vignoli, A. (2002). Strengthening techniques tested on masonry structures struck by the Umbria–Marche earthquake of 1997–1998. Construction and building materials, 16(4), 229-239.

Costa, A., Arêde, A., Ferreira, T., Gomes, A. and Varum, H. (2014). *Experimental Study of the Out-of-Plane Behaviour of Unreinforced Sacco Stone Masonry Walls: Comparative Analysis of two Different Test Setups.* In: 9th International Masonry Conference.

Crisafulli, F. J., Carr, A. J., and Park, R. (1995). Shear Strength of Unreinforced Masonry Panels. Pacific Conference on Earthquake Engineering, 3, pp. 77-86. Melbourne, Australia.

Darbhanzi, A., Marefat, M. S., and Khanmohammadi, M. (2014). Investigation of in-plane seismic retrofit of unreinforced masonry walls by means of vertical steel ties. Construction and building materials, 52, 122-129.

Dauda, J. A. (2020). Numerical and experimental investigation of unreinforced masonry wall retrofitted with timber panels (Doctoral dissertation, University of Leeds).

Dolce, M., Nigro, D., Ponzo, F. C., and Marnetto, R. (2001). The CAM system for the retrofit of masonry structures. In Proceedings of the 7th International Seminar on Seismic Isolation, Passive Energy Dissipation and Active Control of Vibrations of Structures, Assisi, Italy (pp. 2-5).

Dowling, D., Samali, B., and Li, J. (2005). An improved means of reinforcing adobe walls-external vertical reinforcement. In SismoAdobe2005: international seminar on architecture, construction, and conservation of earthen buildings in seismic areas, Lima, Peru.

Drysdale, R. G., Hamid, A. A., and Baker, L. R. (1994). Masonry Structures, Behavior and Design. Englewood Cliff: Prentice Hall Inc.

"Earthquakes worldwide by Richter Scale gradation 2006-2018". *Statista.com*. Retrieved December 3, 2019.

ElGawady, M. A., Lestuzzi, P., and Badoux, M. (2006). Retrofitting of masonry walls using shotcrete. In 2006 NZSEE Conference, Paper (Vol. 45).

ElGawady, M., Lestuzzi, P., and Badoux, M. (2004). A review of conventional seismic retrofitting techniques for URM. In 13th international brick and block masonry conference (Vol. 4, No. 7).
Farshchi, D. M., Motavalli, M., Schumacher, A., and Marefat, M. S. (2009). Numerical modeling of in-plane behavior of URM walls and an investigation into the aspect ratio, vertical and horizontal post-tensioning, and head joint as a parametric study. *Archives of Civil and Mechanical Engineering, 9*(1), 5-27.
FEMA 273. (1997). NEHRP Guidelines for The Seismic Rehabilitation of Buildings. Washington D.C.
Ferraioli, M., Costanzo, R., and Lavino, A. (2010). Base isolation seismic retrofit of a hospital building in Italy: performance under earthquake strong ground motions. In Proceedings of the Final Conference on COST Action C26: Urban Habitat Constructions under Catastrophic Events (pp. 841-846).
Garmendia, L., Larrinaga, P., San-Mateos, R., and San-José, J. T. (2015). Strengthening masonry vaults with organic and inorganic composites: an experimental approach. Materials & Design, 85, 102-114.
Gautam, D. (2018). Observational fragility functions for residential stone masonry buildings in Nepal. Bulletin of Earthquake Engineering, 16(10), 4661-4673.
Gautam, D., and Chaulagain, H. (2016). Structural performance and associated lessons to be learned from world earthquakes in Nepal after 25 April 2015 (MW 7.8) Gorkha earthquake. Engineering Failure Analysis, 68, 222-243.
Gautam, D., Prajapati, J., Paterno, K. V., Bhetwal, K. K., and Neupane, P. (2016). Disaster resilient vernacular housing technology in Nepal. Geoenvironmental Disasters, 3(1), 1-14.
Gere, J. M., & Timoshenko, S. (1986). Mecánica de Materiales. México: Grupo Editorial Iberoamérica.
Ghlomreza Zamani Ahari. (2013). Structural in-plane behavior of masonry walls externally retrofitted with fiber-reinforced materials (Doctoral dissertation, Kyushu University).
"Global earthquake death toll from 2000 to 2015". Statista.com. Retrieved December 3, 2019.
Gocevski, V., and Petraskovic, Z. (2012). Seismic analysis of existing masonry structures reinforced with "SYSTEM DC90" dampers. In Proceedings of the Earthquake Engineering Conference.
Haach, V. G., Vasconcelos, G., & Lourenço, P. B. (2010). Experimental analysis of reinforced concrete block masonry walls subjected to in-plane cyclic loading.
Hendry, A., Sinha, B., and Davies, S. (1997). Design of Masonry Structures, Load Bearing Brickwork Design, (Third Edition ed.). UK: E&FN Spoon, UK.
Hilsdorf, H. K. (1969). An investigation into the failure of brick masonry loaded in axial compression. In F. B. Johnson (Ed.), Designing, engineering, and constructing with Masonry Products (pp. 34-41). Houston: Gulf Publishing Company.
Howlader, M. L. (2020). In-plane Behaviour of Unreinforced Masonry (URM) Walls with Openings in Australian Heritage Construction. Doctoral thesis, University of New Castle, Australia
HRRP (2018). Housing Typologies: Earthquake Affected Districts. Housing Recovery and Reconstruction Platform.

Ismail, N., and Ingham, J. M. (2016). In-plane and out-of-plane testing of unreinforced masonry walls strengthened using polymer textile-reinforced mortar. Engineering Structures, 118, 167-177.

Izmir, C. and Erberik, M. (2015). A Case Study for Seismic Assessment and Restoration of Historic Buildings: The Arditi Residence. Handbook of Research on Seismic Assessment And Rehabilitation Of Historic Structures.

Josh, M., Ramesh, G., and Bhattacharya, S. (2012). Seismic Retrofitting of Non-Engineered Masonry in Rural Nepal. Proceedings of the ICE-Structures and Buildings.

Kadam, S. B., Singh, Y., & Li, B. (2015). Out-of-plane behavior of unreinforced masonry strengthened using ferro-cement overlay. Materials and Structures, 48(10), 3187-3203.

Kadam, S. B., Singh, Y., and Li, B. (2015). Out-of-plane behavior of unreinforced masonry strengthened using ferro-cement overlay. Materials and Structures, 48(10), 3187-3203.

Kalali, A., and Kabir, M. (2012). Cyclic behavior of perforated masonry walls strengthened with glass fiber reinforced polymers. Scientia Iranica, 19(2), 151-165.

Karantoni, F. V., and Fardis, M. N. (1992). Effectiveness of seismic strengthening techniques for masonry buildings. Journal of Structural Engineering, 118(7), 1884-1902.

Kariou, F. A., Triantafyllou, S. P., Bournas, D. A., & Koutas, L. N. (2018). Out-of-plane response of masonry walls strengthened using a textile-mortar system. Construction and Building Materials, 165, 769-781.

Kaushik, H. B., Rai, D. C., & Jain, S. K. (2007). Stress-strain characteristics of clay brick masonry under uniaxial compression. Journal of materials in Civil Engineering, 19(9), 728-739.

Khadka, B. (2020). Mud masonry houses in Nepal: A detailed study based on entire reconstruction scenario in 31 earthquake-affected districts. In Structures (Vol. 25, pp. 816-838).

Khadka, B., and Shakya, M. (2021). Seismic characteristics of unreinforced mud masonry houses in Nepal: A miserable scenario before and after 2015 Gorkha (Nepal) earthquake. Engineering Failure Analysis, 124, 105308.

Kuzik, M. D., Elwi, A. E., and Cheng, J. R. (2003). Cyclic flexure tests of masonry walls reinforced with glass fiber-reinforced polymer sheets. Journal of Composites for Construction, 7(1), 20-30.

Lin, Y., Lawley, D., Wotherspoon, L. and Ingham, J. (2016). Out-of-Plane Testing of Unreinforced Masonry Walls Strengthened Using ECC Shotcrete. Structures, 7(2016), pp. 33-42.

Lourenco, P. (1998). Experimental and Numerical Issues in the Modelling of the Mechanical Behaviour of Masonry. Structural Analysis of Historical Constructions, II.

Lourenço, P. B. (1996a). Computational strategies for masonry structures. (PhD Thesis), Delft University of Technology (TU Delft), Netherlands.

Lourenço, P. B. (2008). Structural masonry analysis: Recent developments and prospects. Proceedings of the 14th International Brick and Block Masonry Conference, Sydney, Australia.

Lourenço, P., Mendes, N., Costa, A. and Campos-Costa, A. (2017). Methods and Challenges on the Out-Of-Plane Assessment of Existing Masonry Buildings. International Journal of Architectural Heritage, 11(1), pp.1-1.

Macabuag, J. (2007). An introduction to modeling and retrofitting of non-engineered masonry buildings under seismic loading. In MEng Research Report. Oxford University.
Macabuag, J., Guragain, R., and Bhattacharya, S. (2012). Seismic retrofitting of non-engineered masonry in rural Nepal. Proceedings of the Institution of Civil Engineers-Structures and Buildings, 165(6), 273-286.
Maccarini, H., Vasconcelos, G., Rodrigues, H., Ortega, J. and Lourenço, P. (2018). Out-of-Plane Behavior of Stone Masonry Walls: Experimental and Numerical Analysis. Construction and Building Materials, 179, pp.430-452.
Magenes, G., and Calvi, G. M. (1997). In-plane seismic response of brick masonry walls. Earthquake Engineering & Structural Dynamics, 26(11), 1091-1112.
Magenes, G., Morandi, P., and Penna, A. (2008). Test results on the behavior of masonry under static cyclic in-plane lateral loads, ESECMaSE project, Department of Structural Mechanics, University of Pavia, Italy.
Mahmood, H., and Ingham, J. M. (2011). Diagonal compression testing of FRP-retrofitted unreinforced clay brick masonry wallettes. Journal of Composites for Construction, 15(5), 810-820.
Martins, A., Vasconcelos, G., Fangueiro, R., and Cunha, F. (2015). Experimental assessment of an innovative strengthening material for brick masonry infills. Composites Part B: Engineering, 80, 328-342.
Matsagar, V. A., and Jangid, R. S. (2008). Base isolation for seismic retrofitting of structures. Practice Periodical on Structural Design and Construction, 13(4), 175-185.
Meguro, K., Mayorca, P., Guragain, R., Sathiparan, N., and Nesheli, K. N. (2006). PP-Band retrofitting technique: Affordable, acceptable, and feasible method for developing countries.
Meguro, K., Soti, R., Navaratnaraj, S., and Numada, M. (2012). Dynamic testing of masonry houses retrofitted by bamboo band meshes. Journal of Japan Society of Civil Engineers, Ser. A1 (Structural Engineering & Earthquake Engineering (SE/EE)), 68(4), I_760-I_765.
Melkumyan, M., Mihul, V., and Gevorgyan, E. (2011). Retrofitting by base isolation of existing buildings in Armenia and in Romania and comparative analysis of innovative vs. conventional retrofitting. In 3rd International Conf. on Computational Methods in Structural Dynamics and Earthquake Engineering.
Milosevic, J., Gago, A. S., Lopes, M., and Bento, R. (2013). Experimental assessment of shear strength parameters on rubble stone masonry specimens. Construction and Building Materials, 47, 1372-1380. https://doi.org/10.1016/j.conbuildmat.2013.06.036
MSJC. (2002). Building code requirements for masonry structures, ACI 530-02/ASCE 5-02/TMS 402-02". Detroit, Michigan, USA: America Concrete Institute, Structural Engineering Institute of the American Society of Civil Engineers, The Masonry Society.
Mustafaraj, E. (2016). External shear strengthening of unreinforced damaged masonry walls. PhD Thesis, Epoka University, Tirana, Albania.
Mustafaraj, E., and Yardim, Y. (2017). Review of Strengthening Techniques and Mechanical Testing for Unreinforced Masonry. MATTER: International Journal of Science and Technology, 3(2), 33-50.
NBRI (2016). National Building Research Institute (NBRI) – Civil and Environmental Engineering. [online] Cee.technion.ac.il. Available at:

https://cee.technion.ac.il/vision-and-goals/about/research-centers-and-labs/national-building-research-institute-nbri/ [Accessed 10 Aug. 2018].

Nepal, C. B. S. (2012). National population and housing census 2011. National Report.

Nezhad, R. S., & Kabir, M. Z. (2017). Experimental investigation on out-of-plane behavior of GFRP retrofitted masonry panels. Construction and Building Materials, 131, 630-640.

NPC. Post Disaster Need Assessment (PDNA) Government of Nepal (2015). National Planning Commission, Editor. 2015: Kathmandu

Okail, H., Abdelrahman, A., Abdelkhalik, A., and Metwaly, M. (2016). Experimental and analytical investigation of the lateral load response of confined masonry walls. HBRC journal, 12(1), 33-46.

Padalu, P. K. V. R., Singh, Y., & Das, S. (2018). Efficacy of basalt fibre-reinforced cement mortar composite for out-of-plane strengthening of unreinforced masonry. Construction and Building Materials, 191, 1172-1190.

Padalu, P. K. V. R., Singh, Y., & Das, S. (2019). Out-of-plane flexural behavior of masonry wallettes strengthened using FRP composites and externally bonded grids: Comparative study. Composites Part B: Engineering, 176, 107302.

Palanisamy, M., and Premalatha, J. (2012). Experimental study on masonry infill material properties.

Paudel, K. (2021). Structural Suitability of Masonry Structure for Residential Buildings in Rural Areas of Nepal (Masters, Pulchowk Campus).

Paulay, T., and Priestley, M. J. (1992). Seismic design of reinforced concrete and masonry buildings. New York, USA: John Wiley & Sons, . https://doi.org/10.1002/9780470172841

Peña, F., Lourenço, P., Mendes, N. and Oliveira, D. (2010). Numerical Models for the Seismic Assessment of an Old Masonry Tower. Engineering Structures, 32(5), pp.1466-1478.

Portioli F. and Cascini L. (2017). Large Displacement Analysis of Dry-Jointed Masonry Structures Subjected to Settlements using Rigid Block Modelling. Engineering Structures, 148, pp. 485-496, ISSN: 0141-0296, doi: 10.1016/j.engstruct.2017.06.073.

Portioli F.P.A. (2020). Rigid Block Modelling of Historic Masonry Structures using Mathematical Programming: A Unified Formulation for Non-Linear Time History, Static Pushover and Limit Equilibrium Analysis. Bulletin Of Earthquake Engineering, 18 (1), pp. 211-239. doi: 10.1007/s10518-019-00722-0.

Rahman, A., and Ueda, T. (2014). Experimental investigation and numerical modeling of peak shear stress of brick masonry mortar joint under compression. Journal of Materials in Civil Engineering, 26(9), 04014061.

Saleem, M. U., Numada, M., Amin, M. N., and Meguro, K. (2016). Seismic response of PP-band and FRP retrofitted house models under shake table testing. Construction and Building Materials, 111, 298-316.

Salmanpour, A. H., Mojsilovic, N., & Schwartz, J. (2013). Deformation capacity of unreinforced masonry walls subjected to in-plane loading: a state-of-the-art review. International Journal of Advanced Structural Engineering, 5, 1-12.

Sarangapani, G., Venkatarama Reddy, B. V., and Jagadish, K. S. (2005). Brick-mortar bond and masonry compressive strength. Journal of materials in civil engineering, 17(2), 229-237.

Sathiparan, N., MAYORCA, P., NESHELI, K. N., GURAGAIN, R., and MEGURO, K. (2005). Experimental study on in-plane and out-of-plane behavior of masonry wallettes retrofitted by PP-band meshes. Seisan Kenkyu, 57(6), 530-533.

Shermi, C., & Dubey, R. N. (2017). Study on out-of-plane behavior of unreinforced masonry strengthened with welded wire mesh and mortar. Construction and Building Materials, 143, 104-120.

Tamrakar, A., Evaluation of Seismic Behavior of Traditional Brick Masonry Buildings in Nepal, Masters Thesis, Tongji University

Tan, K. H., and Patoary, M. K. H. (2004). Strengthening of masonry walls against out-of-plane loads using fiber-reinforced polymer reinforcement. Journal of Composites for Construction, 8(1), 79-87.

Tomaževič, M. (1999). Earthquake resistant design of masonry buildings (Vol. 1). Imperial College Press, London.1-86094-066-8.

Tomazevic, M. (1999). Earthquake-Resistant Design of Masonry Buildings. In Series on Innovation in Structures and Construction, Masonry Materials and Construction Systems (Vol. 1). Imperial College Press. https://doi.org/10.1142/9781848160835_0002https://doi.org/10.1142/p055

Tomaževič, M., and Klemenc, I. (1997). Seismic behavior of confined masonry walls. Earthquake Engineering & Structural Dynamics, 26(10), 1059-1071.

UNDP. Nepal Country Report-Global Assessment of Risk. ISDR Global Assessment Report on Poverty and Disaster Risk (2009), United Nations Development Programme: Kathmandu, Nepal.

USGS (2015). Available from: https://earthquake. usgs.gov/earthquakes/eventpage/us20002926/origin/detail.

Valvona, F., Toti, J., Gattulli, V., and Potenza, F. (2017). Effective seismic strengthening and monitoring of a masonry vault by using Glass Fiber Reinforced Cementitious Matrix with embedded Fiber Bragg Grating sensors. Composites Part B: Engineering, 113, 355-370.

Vanin, A., and Foraboschi, P. (2012). In-plane behavior of perforated brick masonry walls. Materials and Structures, 45(7), 1019-1034.

Vimala, S., and Kumarasamy, K. (2014). Studies on the strength of stabilized mud block masonry using different mortar proportions. International Journal of Emerging Technology and Advanced Engineering, 4(4), 720-724.

Wang, C., Sarhosis, V., and Nikitas, N. (2018). Strengthening/retrofitting techniques on unreinforced masonry structure/element subjected to seismic loads: A literature review. Open Construction and Building Technology Journal, 12(1), 251-268.

Yavartanoo, F., and Kang, T. H. K. (2022). Retrofitting of unreinforced masonry structures and considerations for heritage-sensitive constructions. Journal of Building Engineering, 49, 103993.

Zampieri, P., Simoncello, N., Tetougueni, C. D., and Pellegrino, C. (2018). A review of methods for strengthening of masonry arches with composite materials. Engineering Structures, 171, 154-169.

Chapter 3: Mechanical Properties of Components of Nepalese Historical Masonry Buildings

Abstract

The historical monuments in Nepal are mostly composed of brick masonry and timber and were seriously damaged in the 2015 Gorkha earthquake. The purpose of this study was to understand the mechanical properties of bricks, mud mortar, and masonry constituting historical buildings of Nepal. The results shows that despite the large standard deviations in results of constituent materials (unit bricks and mud mortar), the standard deviation of compressive strength of masonry prisms was low. The average compressive strength of masonry prism was 1.70 N/mm^2 with a standard deviation of 0.08 N/mm^2. The masonry compressive strength is about 30% of the brick's compressive strength. Furthermore, the average values of shear strength and shear deformation angle of the masonry wall were 0.054 N/mm^2 and, 4.46x10^{-2} rad., respectively. The empirical equation proposed by Euro code gave closer results to our experiment for masonry compressive strength. The results of this study will be good reference for a detailed analysis of historical brick masonry of Nepal.

Keywords: Mechanical properties; Historical brick masonry; Bricks; Mud mortar; Masonry prism

3.1 Introduction

The historical brick masonry is composed of burnt or sun-dried solid brick with mud mortar. Brick masonry structures are commonly seen in developing countries due to the easy availability of materials used for the construction (Knox et al., 2018). Masonry walls are commonly used in most building construction due to low cost, heat insulation properties, and easy availability of materials, and are found in many parts of the world (Kaushik et al., 2007). Masonry with mud mortar is weak in strength and hence vulnerable to earthquakes. During the 2015 Gorkha earthquake, many brick masonry structures were severely damaged or in some cases reached global collapse (Chaulagain et al., 2018).

The compressive strength, shear modulus, and modulus of elasticity are important parameters that are used to analyze and design masonry structures. These parameters have a wide range of adaptability depending on size, the quality of materials, and the workmanship of construction (Phaiju and Pradhan, 2018). Sahlin (1971) reported that the strength of mortar and brick determines the strength of wall strength within practical limits. According to Hilsdrof's theory, the factors affecting the masonry strength are the uniaxial compressive strength of brick, the biaxial tensile strength of brick, failure criteria for a brick under a triaxial state of stresses, the uniaxial compression strength of mortar, the behavior of mortar under triaxial loading and the coefficient of non-uniformities due to joints and brick properties.

Kaushik et al., (2007) conducted the uniaxial monotonic compressive stress-strain behavior of bricks and mortar. They found that the mean values of different bricks used in the study varied from 16.10 MPa to 28.90 MPa. Phaiju and Pradhan (2018) experimented on the mechanical properties of bricks and masonry panels. The results showed that the average value of compression strength of the full brick samples was 11.12 MPa. Bhattarai et al., (2018) experimented on mechanical properties of ancient clay brick of Kathmandu valley using ASTM standards. The experimental results showed that the compressive strength of brick samples was found to be in the range of 5-23 MPa. They also reported that compressive strength of bricks is correlated with their physical properties. The results of mechanical properties conducted by several researchers vary greatly and there are few researches on historical brick masonry therefore this study focuses on historical brick masonry of Nepal.

The purpose of this study was to understand the mechanical properties of bricks, mud mortar, and masonry constituting historical buildings of Nepal. The study would contribute to a better understanding of the mechanical properties of bricks, mud mortar, and masonry composed of these materials.

3.2 Materials and Methods

Uniaxial compression tests were carried out on samples of bricks, mud mortar, and brick masonry to find out the properties such as compressive strength, stress-strain behavior, Young's modulus, and so forth. A diagonal compression experiment was carried out on masonry walls to determine the shear parameters. All the samples were manufactured and tested at the same laboratory of KHWOPA Engineering College, Nepal. The experiments were conducted by the Yamaguchi Laboratory at Kyushu University, Japan to which the author belongs and other collaborators. The author was in charge of analyzing the data obtained from these experiments. The experiment on uniaxial compression test on unit brick, mud mortar cylinders, and masonry prism and diagonal compression test for URM walls were conducted in 2017.

3.2.1 Description of the samples

3.2.1.1 Unit brick compression experiment

The building at least can date back to the 19th century although its exact construction date is not known. It was built in a typical method that prevailed during the Malla Dynasty. Specimens were prepared following the same process as that of the historical masonry buildings of Nepal.

The dimension of brick was about 200-205 mm in length, 115-135 mm in width, and 55-60 mm in height. For the experiment, the brick samples were cut manually from the lengthwise direction making a base of 50mm x 50 mm and a height of 100 mm, approximately as shown in Figure 3.1. 35 brick samples namely UBC 01 ~ UBC 35 were prepared. The dimensions of the bricks are shown in Table 3.1. Figure 1 shows the dimensions of the brick and loading arrangement for the unit brick compression experiment.

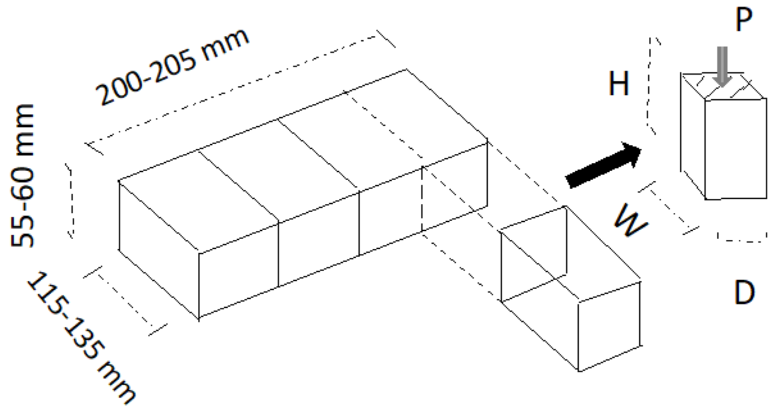

Figure 3.1: Dimensions of bricks and loading arrangement of unit brick compression experiment

Table 3.1: Dimensions of brick samples

Specimen	Width(W), mm	Depth(D), mm	Height(H), mm
UBC 01	48.90	51.77	101.65
UBC 02	51.74	46.60	100.51
UBC 03	50.13	48.57	101.22
UBC 04	50.02	49.56	99.28
UBC 05	49.49	50.12	102.43
UBC 06	51.59	50.45	99.65
UBC 07	52.14	52.10	100.08
UBC 08	49.84	49.23	101.41
UBC 09	50.23	52.00	98.41
UBC 10	50.91	50.18	102.12
UBC 11	46.98	50.13	98.33
UBC 12	51.96	49.91	99.56
UBC 13	49.10	50.25	102.72
UBC 14	48.62	49.47	104.07
UBC 15	46.76	50.99	100.23
UBC 16	48.92	53.03	104.30
UBC 17	50.91	50.76	101.48
UBC 18	50.21	49.46	100.18
UBC 19	50.57	46.94	102.23
UBC 20	51.73	50.13	99.31

UBC 21	48.82	48.48	101.75
UBC 22	51.37	51.50	100.38
UBC 23	50.98	50.50	104.88
UBC 24	50.10	51.00	101.30
UBC 25	50.28	49.65	97.55
UBC 26	51.05	53.90	100.40
UBC 27	50.62	47.72	100.83
UBC 28	50.15	50.22	99.38
UBC 29	50.42	51.62	99.38
UBC 30	48.92	50.87	101.75
UBC 31	51.85	48.02	100.80
UBC 32	48.08	49.78	98.48
UBC 33	50.97	47.88	102.48
UBC 34	47.33	50.22	98.53
UBC 35	48.73	45.88	99.30

Table 3.2: Dimensions of mud mortar cylinders

Specimen	Diameter (D), mm	Height (H), mm	Area (A), mm^2
MMC 1	49.0	73.0	1887.7
MMC 2	47.8	97.8	1796.4
MMC 3	48.8	98.3	1867.2
MMC 4	47.9	99.7	1805.2
MMC 5	47.4	99.1	1765.2

3.2.1.2 Mud mortar compression experiment

Mud mortar was manufactured in February 2017.The mortar was prepared following the same technique as in the wall-making of historical buildings. The sand, silt, clay proportion are 21.4%, 63.3%, 15.3% by weight, respectively. As per Nepalese building code, the sand content in mud mortar should be less than 30% so that the mud mortar can obtain proper cohesiveness. Dry mud was thoroughly kneaded with water for preparing of the dense mud paste (NBC-105, 1994). Five mud mortar cylinders namely MMC 1 ~ MMC 5 were prepared by packing mortar in a plastic mold. The tests were carried out after 134 days of preparation of mud mortar cylinders. The average value of density of the five specimens was 1.50 g/cm^3. The shape and dimensions of mud mortar samples are shown in Figure 3.2 and Table 3.2, respectively.

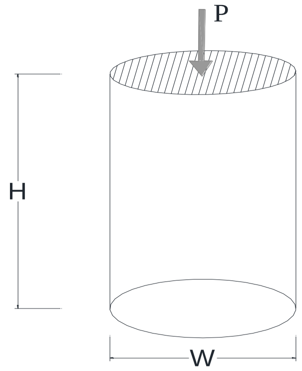

Figure 3.2: Mud mortar sample

3.2.1.3 Masonry prism compression experiment

Three masonry prisms namely C2, C4, and C6 were constructed in February 2017, using the above-mentioned bricks and mud mortar. The width and depth of prism were about 350 mm and 280 mm. Each bricklayer was about 70 mm (including the joint thickness of 10 mm). The top surface of the samples was smoothened and leveled by mud plaster. The tests were carried out after 134 days of preparation of masonry prisms. The shape and dimensions of the prism specimens are presented in Figure 3.3 and Table 3.3, respectively.

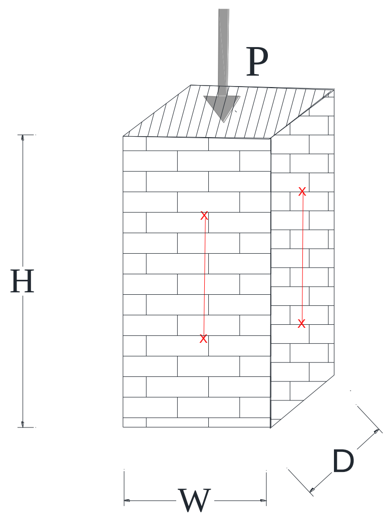

Figure 3.3: Prism sample

Table 3.3: Dimensions of prism specimens

Specimen	Width (W), mm	Depth (D), mm	Height (H), mm
C2	350.5	284.5	869
C4	349.5	279	871
C6	346.5	279.5	846.5

3.2.1.4 Diagonal compression experiment

Using the same bricks and mud mortar as in the compression experiments, two wall panels namely D2 and D6 were constructed. The width of the wall panel was about 1260 mm and the depth of about 280 mm. Each bricklayer was about 70 mm thick (including 10 mm joint thickness). The shape and dimensions of wall specimens are shown in Figure 3.4 and Table 3.4, respectively.

Table 3.4: Dimensions of wall specimens

Specimen	Width (W), mm	Depth (D), mm	Height (H), mm	Area (A), mm^2
D2	1256.5	278.0	1243	3.49×10^5
D6	1268.5	289.5	1262	3.67×10^5

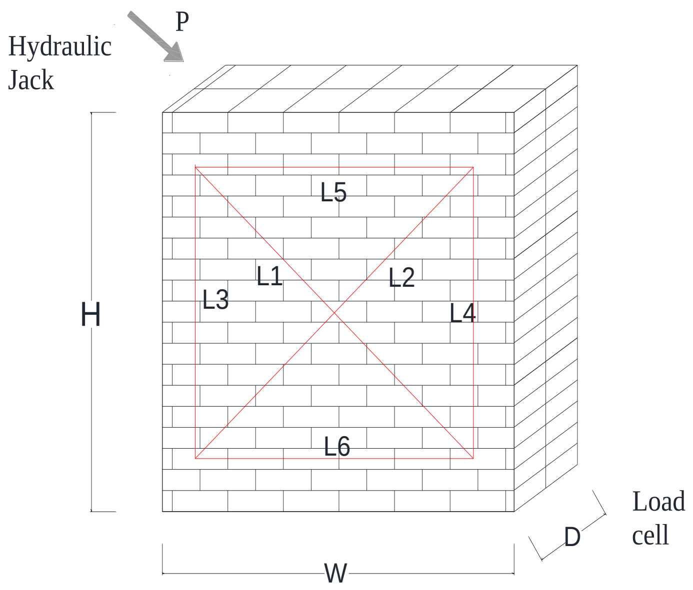

Figure 3.4: Masonry wall specimen

3.2.2 Description of test procedure

3.2.2.1 Unit brick compression experiment

The brick samples were tested by 400 kN universal testing machine and a load cell made in Japan was used. 5 out of 35 specimens (UBC 01~UBC 05) were measured against strain at the time of loading. Four vertical stain gauges and two horizontal strain gauges were used to measure strain. The compressive stress was determined by the ratio of load per unit area of the samples. The experimental set up is shown in Figure 3.5.

Figure 3.5: Uniaxial compression test on unit bricks

3.2.2.2 Mud mortar compression experiment

The mortar cylinders were tested in July 2017. The load was applied by the universal testing machine of 400 kN capacity. Strain in the horizontal and vertical direction was measured at the back and front center of the cylinder. It is noted that for mortar sample MMC1, only the load was measured, as the specimen was broken while removing from the plastic mold. Figure 3.6 shows the compression test on mud mortar cylinders. Compressive loads were applied on mud mortar specimens and the loads versus deformations were recorded. The compressive stress was determined by the ratio of load per unit area of the samples.

Figure 3.6: Uniaxial compression test on mortar cylinders

3.2.2.3 Masonry prism compression experiment

The prism specimens were tested in July 2017. To ensure uniform loading, steel plates of 450 x 400 x 10 mm sizes were set on the top and bottom sides of the prism. The load was applied through 500 kN hydraulic jack. The displacement was measured using displacement transducers at the center of four sides of the prism specimen.

Figure 3.7 shows the compression test conducted on a masonry prism. Compressive loads were applied to the prism and the loads versus displacement were recorded. The compressive stress was determined by the ratio of load per unit area of the samples.

Figure 3.7: Uniaxial compression test on masonry prism

3.2.2.4 Diagonal compression experiment

According to a standard test method for the diagonal compression experiment (ASTM 519), the wall panel is required to be rotated by 45 degrees and the force is applied vertically from the top corner (Knox et al., 2018).

However, in the present study, the wall panel rests horizontally on one side of the wall, and the force is applied diagonally between the two corners as shown in Figure 3.8. In addition, it can also measure the horizontal and vertical displacement of the wall specimen.

For the test set up, the wall panels rest horizontally on a plinth and are positioned so that the load shoe at the bottom corner could be attached to the wall panels. Another load shoe was attached to the diagonally opposite top corner. Two rods on each side of the wall panel connected the two loading shoes with a hydraulic jack and load cell at opposite corners.

The diagonal force was applied through the upper corner by a hydraulic jack and a load cell at diagonally opposite bottom corner measured the load. Displacement was measured with six displacement transducers, two each located in diagonal, vertical, and horizontal directions, respectively.

Figure 3.8: Diagonal compression test on masonry wall

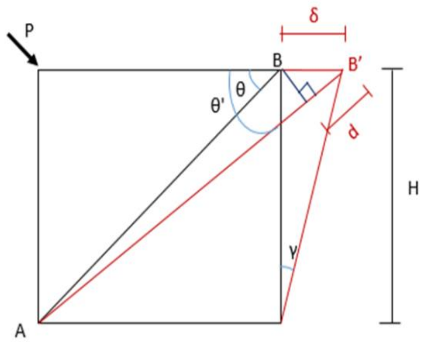

Figure 3.9: Calculation method of deformation angle

In this study, the displacement measured by the displacement meter L2 on the specimen is termed the displacement d on the diagonal tension side. The length of the displacement transducer L4 before the experiment was taken as the test body height H and the shear deformation angle was calculated (Figure 3.9).

Equation (3.1), (3.2), and (3.3) are used for calculating the shear deformation angle.

$\gamma = \tan\gamma = L4$ (3.1)

Where, $\delta = L2' - L2 COS\ \theta$ (3.2)

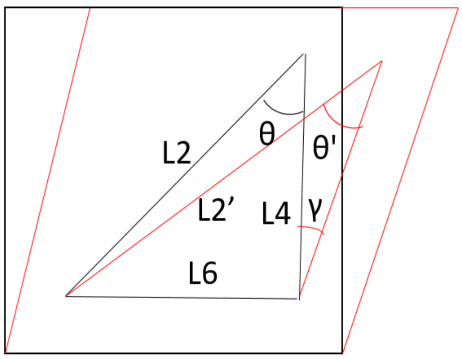

Figure 3.10: Calculation method of deformation angle by using cosine theorem

The Cosine theorem was used to calculate the deformation angle, using the displacement along tensile deformation as shown in Figure 3.10.

$$\gamma = \theta' - \theta \qquad (3.3)$$

3.3 Results and discussion

3.3.1 Unit brick compression experiment

The compressive strength of each brick specimen is shown in Table 3.5. The Average compressive strength of unit bricks was 5.05 N/mm^2 and the standard deviation was 2.55 N/mm^2. The histogram chart in Figure 3.11 indicates the average compressive strength of samples to be 4 N/mm^2.

The deviation in the compressive strength of samples was large. It can be assumed; that the main reason for it can be the uneven specimen samples due to which eccentric load was exerted on specimens instead of uniaxial load. Figure 3.12 shows the stress-strain diagram of 5 specimen samples (UBC 01~UBC 05).

The Young's modulus and Poisson's ratio of each 5 specimens were calculated by taking the linear regression of data up to one-third of the compressive strength. The values of Young's modulus and Poisson's ratio are shown in Table 3.6. Despite eccentric loading in samples, Young's modulus has similar values for all five samples whereas the variation of Poisson's ratio is large. The reason for this can be the existing voids and cracks in the specimens before loading showing few negative values.

Table 3.5: Results of compressive strength of 35 brick samples

Specimen	Compressive strength (N/mm^2)	Specimen	Compressive strength (N/mm^2)
UBC 01	6.17	UBC 19	3.64
UBC 02	3.01	UBC 20	3.93
UBC 03	3.68	UBC 21	7.93
UBC 04	2.66	UBC 22	3.50
UBC 05	4.46	UBC 23	3.47
UBC 06	14.65	UBC 24	5.32
UBC 07	3.20	UBC 25	5.19
UBC 08	2.88	UBC 26	7.61
UBC 09	10.55	UBC 27	8.42
UBC 10	2.90	UBC 28	4.71
UBC 11	4.93	UBC 29	6.61
UBC 12	3.05	UBC 30	4.78
UBC 13	3.92	UBC 31	5.36
UBC 14	2.60	UBC 32	4.80
UBC 15	8.02	UBC 33	4.81
UBC 16	2.96	UBC 34	5.76
UBC 17	3.16	UBC 35	2.54
UBC 18	5.45		

Avg. of UBC 01~UBC 35 = 5.05 N/mm^2; Std. dev. of UBC 01~UBC 35=2.55 N/mm^2

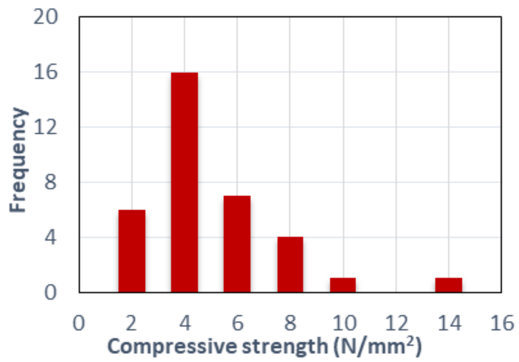

Figure 3.11: Histogram of compressive strength of 35 brick samples

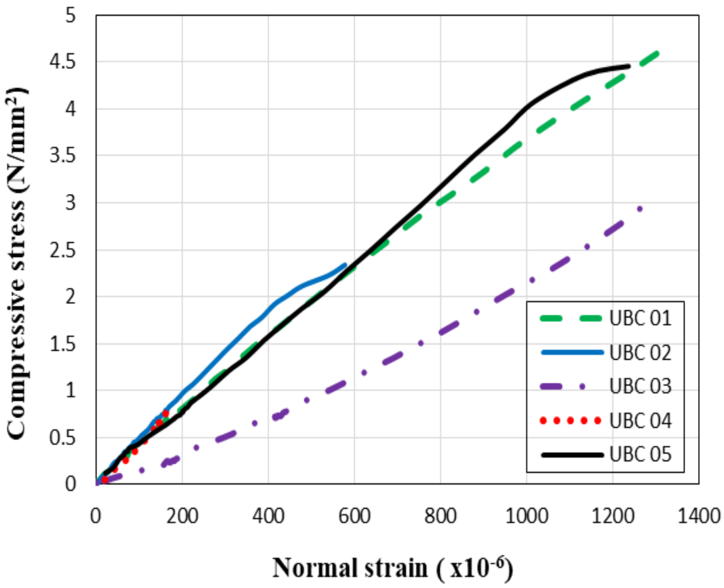

Figure 3.12: Stress-strain diagram for samples UBC01~UBC05

Table 3.6: Young’s modulus and Poisson’s ratio of 5 samples (UBC 01~UBC 05)

Specimen	Young's modulus ($\times 10^3$ N/mm^2)	Poisson's ratio
UBC 01	4.02	0.241
UBC 02	4.86	0.088
UBC 03	1.75*	Negative value *
UBC 04	4.40	Negative value *
UBC 05	3.93	0.384
Average	4.30	0.238

Note: *values are excluded for the calculation of average Young’s modulus and Poisson’s ratio.

3.3.2 Mud mortar compression experiment

The results of the compressive strength for the mud mortar compression experiment are shown in Table 3.7. The average value, the standard deviation, and the coefficient of variation were found to be 1.40 N/mm^2, 0.24 N/mm^2, and 16.4% respectively. The specimen MMC2, MMC4, and, MMC5 were only considered for the calculation of average and standard deviation. MMC1 and MMC3 were excluded as their compressive strength was higher than 3σ. This may be due to the uneven specimen sample used in the experiment test. It can be assumed that due to the voids and cracks present in samples before loading, the variation in results may have occurred. The stress-strain diagram of mortar samples except MMC1 and MMC3 are shown in Figure 3.13.

The Young’s modulus and Poisson’s ratio were calculated by taking linear regression of stress-strain data up to one-third of maximum strength. The Young’s modulus and Poisson's ratio of mud mortar samples are shown in Table 3.8. The Young's modulus of sample MMC 4 was excluded from the average calculation as the value was inadequate. The average value of Young's modulus and Poisson's ratio for mud mortar was 1.17 x 10^3 N/mm^2.

Table 3.7: Compressive strength of mud mortar specimens

Specimens	Compressive strength (N/mm^2)
MMC 1	0.58*
MMC 2	1.67
MMC 3	0.65*
MMC 4	1.30
MMC 5	1.22
Avg.	1.40
Std. dev. (σ)	0.24
CV (%)	16.4

Note: *values are excluded for the calculation of average compressive strength

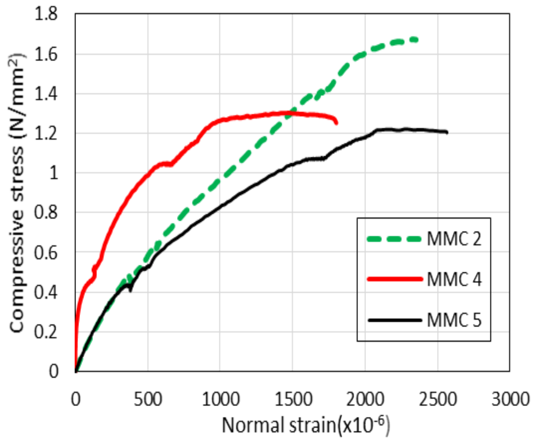

Figure 3.13: Compressive stress-strain diagram of mud mortar specimens

Table 3.8: Young's modulus and Poisson's ratio of mud mortar specimen

Specimens	Young's modulus (x10^3 N/mm^2)	Poisson's ratio
MMC 1	NA	NA
MMC 2	1.20	0.130
MMC 3	0.87	0.193
MMC 4	7.43*	0.167
MMC 5	1.44	0.098
Avg.	1.17	0.147

Note: *values are excluded for the calculation of average compressive strength

3.3.3 Masonry prism compression experiment

The compressive strength and Young's modulus of prism specimens are shown in Table 3.9. The average value and the standard deviation for the compressive strength were found to be 1.70 N/mm^2 and 0.08 N/mm^2. The compressive strength values for all three samples were almost close to each other.

For the prism specimens, a stress-strain relation is shown in Figure 3.14. The Young's modulus was calculated by taking linear regression of stress-strain data up to one-third of maximum strength. The average Young's modulus for prism specimen was 3.10 x 10^3 N/mm^2.

In this study, the compressive strength of brick, mud mortar, and brick masonry was examined by a uniaxial compression test. The relationship between brick unit, mortar and masonry compressive strength is given by the following equation (3.4) as of Euro code 6 (CEN, 2005).

$$f'm = k.\, f'_b{}^{\alpha} .f'_j{}^{ß} \qquad (3.4)$$

where *k, α,* and *ß* are constants and *f'b, f'j* and *f'm* are compressive strengths of brick, mortar, and masonry, respectively. The values of k = 0.5, α = 0.7, and *ß* = 0.3, although α and *ß* has a range of values.

The obtained results are compared with the equation (3.4). The experiment presented the average compressive strength equal to 5.05 N/mm^2, 1.40 $N/mm^{2,}$ and 1.70 N/mm^2 for brick, mortar, and masonry, respectively. Applying the value of brick and mortar obtained by the tests, the equation of Eurocode shows 1.72 N/mm^2 for the compressive strength of the masonry which is very close to our result.

Also, masonry compressive strength varies to about 20-50% of the brick's compressive strength. Such a low value is due to the low mortar strength; the higher mortar strength, the higher the prism's strength (Yardim and Lalaj, 2016).

In this study, the masonry compressive strength is about 30% of the brick's compressive strength.

Table 3.9: Compressive strength of masonry prism

Masonry prism Specimen	Compressive strength (N/mm^2)	Young's modulus (x10^2 N/mm^2)
C2	1.73	3.41
C4	1.61	2.65
C6	1.77	3.26
Avg.	1.70	3.10
Std. dev.	0.08	0.40
CV (%)	5	0.13

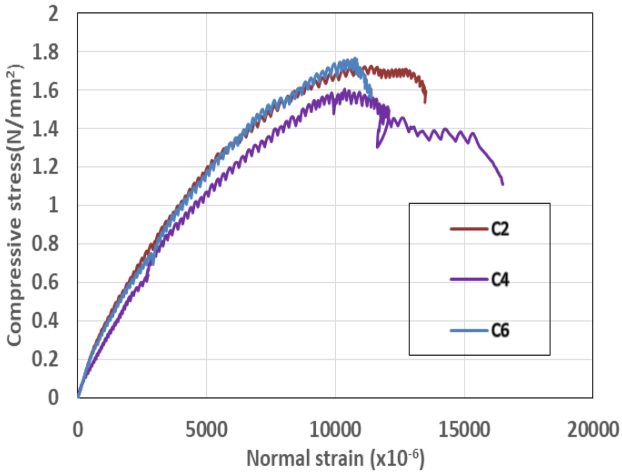

Figure 3.14: Compressive stress-strain diagram of masonry prisms

3.3.4 Comparison of experimental results with an empirical formula

The values of shear stress and shear deformation angle for specimens D2 and D6 are shown in Table 3.10. The average shear strength of the two specimens was found to be 0.054 N/mm^2. The shear Deformation angle was as explained above. The average value of the shear deformation angle calculated was 4.46x10^{-2} rad. Figure 3.15 shows the shear stress-shear deformation angle of the specimens. It can be understood, that although the shear strength is very low, the deformation capacity exceeds 4%which is fairly high.

From the double shear loading test, conducted on the specimens collected from Kyushu University headquarters building 1 and 3 (Japan), the average shear strength of the specimens (OPS 112 and OPS 121) was found to be 1.12 N/mm^2 (Araki et al., 2017).

The average shear strength of specimens in our study was one-twentieth of the average shear strength of specimens from the Kyushu University headquarters building. The possible reasons for it could be the use of mud mortar in our study; while the mortar used in Kyushu University headquarters building was cement mortar of compressive strength 29.5 N/mm^2.Another possible reason might be due to the lower value of the compressive strength of the brick used in our study (5.05 versus 19.2 N/mm^2).

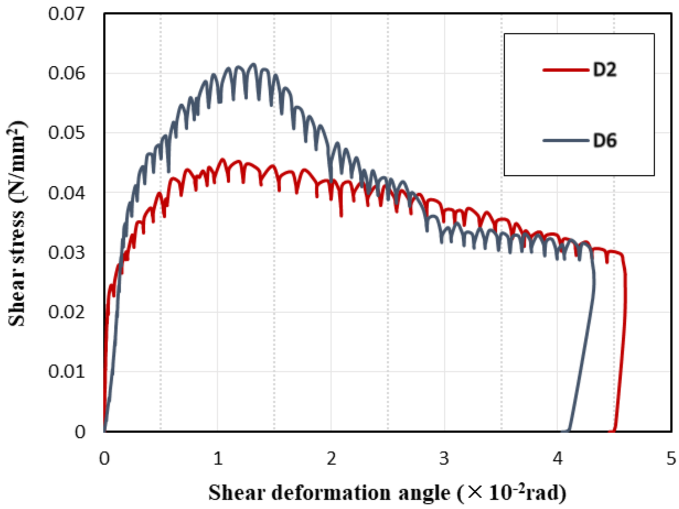

Figure 3.15: Shear stress - shear deformation angle

Table 3.10: Shear strength and deformation angle of samples

Specimen	Shear strength (N/mm^2)	Shear deformation angle ($x10^{-2}$rad.)
D2	0.046	4.60
D6	0.062	4.32
Average	0.054	4.46

3.3.5 Comparison of experimental results with results of other researchers

The comparison of results of mechanical properties of brick units is presented in Table 3.11. The experimental results of this study were close to the results of Parajuli (2012) for mechanical properties of brick units.

Table 3.11: Comparison of results of mechanical properties of brick unit

Brick Unit	Phaiju and Pradhan (2018)	Parajuli et al. (2020)	Parajuli (2012)	Thapa (2011)	This study
Compressive strength (N/mm^2)	11.12	6.4	11.03	9.18	5.05
Youngs modulus (N/mm^2)	3358	N/A	3874	N/A	4300
Poisson’s ratio	N/A	N/A	0.11	N/A	0.238

* N/A= Data not available

Similarly, the mechanical properties of mortar units are presented in Table 3.12. The experimental results of this study were close to the results of Parajuli (2012) for mechanical properties of mortar units.

Table 3.12: Comparison of results of mechanical properties of a mortar unit

Mortar Unit	Phaiju and Pradhan (2018)	Parajuli (2012)	Thapa (2011)	This study
Compressive strength (N/mm^2)	3.8	1.58	1.09	1.4
Youngs modulus (N/mm^2)	2556	33	34	1170
Poisson's ratio	N/A	0.19	N/A	0.147

* N/A= Data not available

Furthermore, the mechanical properties of masonry units are presented in Table 3.13. The experimental results of this study were close to the results of Parajuli (2012) for the mechanical properties of masonry units.

Table 3.13: Comparison of results of mechanical properties of masonry unit

Masonry unit	Phaiju and Pradhan (2018)	Parajuli et al. (2020)	Parajuli (2012)	Thapa (2011)	This study
Compressive strength (N/mm^2)	2.50	0.87	1.82	0.56	1.70
Shear modulus (N/mm^2)	915.1	N/A	204	N/A	49.57
Poissons ratio	0.32	N/A	0.25	N/A	0.048
Shear strength (N/mm^2)	N/A	N/A	0.15	0.135	0.056
Youngs modulus (N/mm^2)	2703	29	509	N/A	310

* N/A= Data not available

3.4 Conclusions

Uniaxial compression tests were conducted on elements of brick masonry and masonry prism. The following conclusions for mechanical characterization of Nepalese bricks were made.

1. Despite the large standard deviations in results of constituent materials (unit bricks and mud mortar), the standard deviation of compressive strength of masonry prisms was low. The average compressive strength of masonry prism was 1.70 N/mm^2 with a standard deviation of 0.08 N/mm^2.
2. In this study, the masonry compressive strength is about 30% of the brick's compressive strength.
3. The empirical equation proposed by Euro code gave similar results to our experiment for masonry compressive strength.

References

Araki, K., Yamaguchi, K., Ninakawa, T., Murakami, K., Ishihara, Y., and Cui, X. (2017). Double shear loading test of brick masonry which constitutes the Kyushu University headquarters building 1 and 3. *Journal of Architecture and Urban Design, Kyushu University*, *31*, 45-52.

Bhattarai, J., Ghale, D. B., Chapagain, Y. P., Bohara, N. B., and Duwal, N. (2018). Study on the physical and mechanical properties of ancient clay brick samples of Kathmandu valley, Nepal. *Tribhuvan University Journal*, *32*(2), 1-18.

Chaulagain, H., Gautam, D., & Rodrigues, H. (2018). Revisiting major historical earthquakes in Nepal: Overview of 1833, 1934, 1980, 1988, 2011, and 2015 seismic events. *Impacts and insights of the Gorkha earthquake*, 1-17.

European Committee of Standardization (CEN) (1996) Eurocode 6： Design of masonry structures Part 1-1: General rules for buildings -Reinforced and unreinforced masonry. Brussels, Belgium.

HILSDORF, H. K. (1969). Investigation into the failure mechanism of brick masonry loaded in axial compression. *Designing engineering and constructing with masonry products*, 34-41.

Kaushik, H. B., Rai, D. C., and Jain, S. K. (2007). Stress-strain characteristics of clay brick masonry under uniaxial compression. *Journal of materials in Civil Engineering*, *19*(9), 728-739.

Knox, C. L., Dizhur, D., and Ingham, J. M. (2018). Experimental study on scale effects in clay brick masonry prisms and wall panels investigating compression and shear-related properties. *Construction and Building Materials*, *163*, 706-713.

Nepal National Building Code (NBC)-105 (1994). Nepal national building code for seismic design of buildings in Nepal, ministry of housing and physical planning, Department of Buildings, Kathmandu, Nepal.

Parajuli, H. R. (2012). Determination of mechanical properties of the Kathmandu World Heritage brick masonry buildings. In *The 15th World Conference on Earthquake Engineering, Lisbon, Portugal*.

Parajuli, R. R., Furukawa, A., and Gautam, D. (2020). Experimental characterization of monumental brick masonry in Nepal. *Structures* (Vol. 28, pp. 1314-1321).

Phaiju S. and Pradhan P. (2018). Experimental work for mechanical properties of brick and masonry panels. Journal of Science and Engineering, 5, 51-57.

Sahlin, S. (1971). Structural Masonry. New Jersey: Prentice Hal.

Thapa, J. B. (2011). Test and simulation of brick masonry walls of historic buildings. Partial fulfillment of the requirements for the Degree of Master of Science in structural engineering. Institute of Engineering.

Yardim, Y., and Lalaj, O. (2016). Shear strengthening of unreinforced masonry wall with different fiber-reinforced mortar jacketing. *Construction and Building Materials*, *102*, 149-154.

Chapter 4: Study on Shear and Flexural Behavior of Nepalese Masonry Walls with and without Reinforcement

Abstract

Masonry with mud mortar is weak in strength and is vulnerable to earthquakes. An earthquake in 2015 caused serious damage to the historical monuments of Nepal. Studies on the URM wall made of mud mortar are still limited for Nepalese historical brick masonry. Thus, the present study was conducted to investigate shear strength, shear deformation capacity, and flexural behavior of the URM walls making historical buildings. A diagonal compression test and three-point bending test were conducted on masonry specimens with and without reinforcement.

For the diagonal compression test, six wall specimens with dimensions of 1250 mm x 1250 mm x 280 mm (W x H x D) were constructed. Among these two were URM, while the other two walls were reinforced with timber (sal wood) (TRM) from both sides of the wall, and the remaining two walls were reinforced with mild steel (SRM) from both sides of the wall. To study the flexural behavior of the wall, six prism specimens with dimensions of 280 mm x 350 mm x 860 mm (B x D x L) were constructed. Among these two were URM, while the other two prisms were reinforced with sal wood with diagonal-type braces, and the remaining two prisms were reinforced with sal wood with ladder-type braces.

Results showed that TRM and SRM increased the average shear strength by 1.98 and 2.78 fold, respectively compared to URM specimens. The shear deformation angle was found to exceed 4% for URM, indicating a high deformation capacity. The average shear strength of the URM in our study was about one-twentieth of the shear strength of Japanese brick masonry. Flexural strength increased significantly in ladder and braced type timber reinforced specimens compared to unreinforced specimens. The failure in the ladder-type reinforced prism was mild and the crack was dispersed equally all over the specimen. The highest flexural strength was found in the diagonal-type braced prism. A drop was observed in the graph when the maximum load was reached due to the sudden split in the reinforcement.

Keywords: Brick masonry; Diagonal compression test; Shear strength; Shear deformation capacity; Flexural strength

4.1 Introduction

In Nepal, brick masonry is one of the most popular building materials (Parajuli, 2012). In 2012, over 20% of structures in Nepal's urban regions were made of reinforced concrete, while the remaining 80% were made of unreinforced stone or brick masonry (CBS, 2012). On April 25, 2015, a powerful earthquake struck Nepal, and several aftershocks were felt (Gautam et al., 2016; Gautam and Chaulagain, 2016). During earthquakes, a large number of brick masonry buildings in Nepal sustain significant damage, and in some instances, they even entirely collapse (Mishra et al., 2018).

The majority of historical buildings in Nepal are constructed of brick, wood, and metal, with roofs composed of tiles or metal. The heritages of masonry are susceptible to seismic risks (Mishra et al., 2018). Mud mortar masonry is weak and susceptible to earthquake events. The two most common failure modes in load-bearing URM walls are an in-plane and out-of-plane failure (Mustafaraj and Yardim 2019). In-plane failure exhibits a diagonal tensile fracture pattern, while out-of-plane failure exhibits cracks along the mortar bed joints. According to Mustafaraj and Yardim (2019), four failure modes might lead to in-plane failure: shear failure, sliding failure, rocking failure, and toe-crushing failure. URM buildings frequently experience shear and sliding failure.

The URM building needs retrofitting work to withstand severe loads and seismic activity. The goal of retrofitting is to increase the building's ultimate strength by strengthening its capacity to withstand inelastic deformation. According to Mustafaraj and Yardim (2019), some traditional retrofitting methods include: i) grouting cracks; ii) stitching major cracks with metallic or brick elements; iii) external or internal post-tensioning with steel ties; iv) shotcrete jacketing; v) ferro-cement; and vi) center core.

Numerous retrofitting techniques are available for unreinforced masonry buildings. The integrity of masonry is increased when timber is used as retrofitting of brick masonry walls with mud mortar (Langenbach, 1989; Endo et al., 2020). According to Vintzileou et al. (2007), timber reinforcement had little influence on the wall's compression strength, but it prevented the wall from disintegration. An experiment was carried out by Moreira et al. (2014) on masonry walls retrofitted with a timber frame. The quasi-static monotonic and cyclic pull-out tests were conducted. The increase in ductility was observed in their experiment due to retrofitting with timber. An experiment was carried out by Borri et al. (2019) on brick masonry walls reinforced with diagonal steel strips that were fastened to the wall's surface using anchor bolts. They found that retrofitting enhanced the walls' shear stiffness without lowering their capacity to deform.

Despite, many other effective methods available, the timber (TRM) and steel reinforcement (SRM) reinforcement were chosen in this study. The Sal wood for strengthening was selected as it is easily available and has higher strength compared to other timbers in Nepal. As per national building code of Nepal Sal wood or any locally available hard wood timber shall be used instead of softwood timber. Sal is a high quality wood which is very strong and durable commonly used for the structural elements like columns, struts and beams. It is also used for making doors and windows. The Sal trees grow up to maximum height of 30 m and are big which allows to use it for various purposes. In addition, in Nepalese historical monuments, timber is widely used for structural as well as aesthetic purposes and can easily embed with the architecture of buildings.

Studies on the URM wall made of mud mortar are still limited for Nepalese historical brick masonry. Thus, the present study was conducted to investigate shear strength, shear deformation capacity, and flexural behavior of the URM walls making historical buildings. Diagonal compression and three-point bending tests were conducted on masonry specimens with and without reinforcement.

4.2 Materials and Methods

4.2.1 Description of samples

Diagonal compression experiments were carried out on masonry walls to determine the shear strength parameters. Similarly, a three-point bending test was conducted to find out the flexural behavior of unreinforced masonry as well as reinforced masonry. All the samples were manufactured and tested at the laboratory of KHWOPA Engineering College, Bhaktapur, Nepal. The experiments were conducted by the Yamaguchi Laboratory at Kyushu University, Japan to which the author belongs and other collaborators. The author was in charge of analyzing the data obtained from these experiments. The experiment on diagonal compression test for steel reinforced masonry and timber reinfored masonry were conducted in 2017. The three point bending test of unreinforced, ladder reinforced and braced reinforced masonry were conducted in 2018.

Bricks were taken from a historical building in Bhaktapur, Nepal. The building is said to be built about 300 years ago although its exact construction date is not known. It was built in a typical method that prevailed during the Malla Dynasty. The dimension of the whole brick was about 200-205 mm in length, 115-135 mm in width, and 55-60 mm in height. The average compressive strength of unit brick, mud mortar, and masonry prism were 5.05 N/mm^2, 1.4 N/mm^2, and 1.70 N/mm^2, respectively (Mishra et al., 2018).

4.2.1.1 Diagonal compression experiment

Six masonry walls, namely D1, D2, D3, D4, D5, and D6 were constructed using the same bricks and mud mortar of our earlier experiment (Mishra et al., 2018). The dimensions of all the specimens are shown in Table 4.1. The front and side view of wall specimens are shown in Figure 4.1 a) and Fig. 4.1 b), respectively.

Each brick layer was about 70 mm thick (including 10 mm joint thickness). Among six wall specimens, D2 and D6 were the unreinforced walls, named D2U1 and D6U2. D1 and D3 were reinforced walls with timber (Sal wood), named D1T1 and D3T2 (TRM) while D4 and D5 were reinforced walls with steel and named D4S2 and D5S1 (SRM). The yield stress of the used steel was 250 MPa.

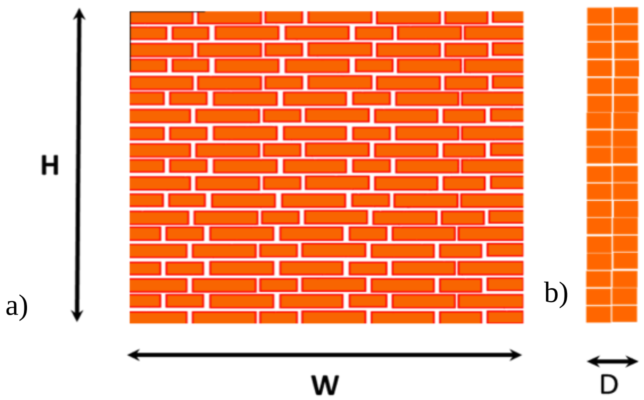

Figure 4.1: a) Front view and b) Side view of the wall specimens

Table 4.1: Dimension of wall specimens

Specimen	W (mm)	H (mm)	D (mm)	A (mm^2)
D2U1	1257	1243	278	3.49×10^5
D6U2	1269	1262	290	3.67×10^5
D1T1	1316	1275	280	3.69×10^5
D3T2	1277	1254	280	3.57×10^5
D5S1	1292	1256	284	3.67×10^5
D4S2	1233	1230	275	3.39×10^5

4.2.1.2 Three-point bending experiment

Six masonry prims, namely B1, B2, B3, B4, B5, and B6 were constructed using the same bricks and mud mortar of our earlier experiment (Mishra et al., 2018). The breadth, width, and length of the masonry prism were about 280 mm, 350 mm, and 860 mm, respectively. The shape of prism for the bending test is shown in Figure 4.2.

The dimensions of all the specimens are presented in Table 4.2. The B5 and B6 were unreinforced specimens named B5U1, and B6U2, while rest of the four specimens were reinforced with Sal wood in two different patterns. Among the reinforced specimens, two of them were reinforced with diagonal brace patterns named B3B1, and B4B2, while the remaining two specimens were reinforced with ladder-type brace patterns named B1L1, and B2L2.

4.2.2 Description of test procedures

4.2.2.1 Diagonal compression experiment

The seismic behavior of URM walls can be experimentally simulated by two kinds of tests: shear-compression test and diagonal compression test. Diagonal compression tests are designed to evaluate the shear strength and the shear elastic modulus of masonry (Mustafaraj and Yardim, 2017; Mustafaraj and Yardim, 2018).

According to a standard test method for the diagonal compression experiment (ASTM 519), the wall panel is required to be rotated by 45 degrees and the force is applied vertically from the top corner.

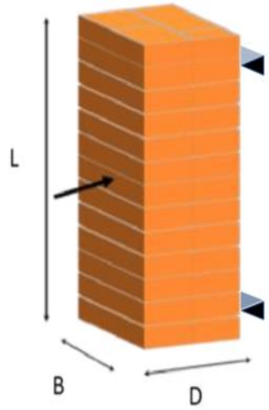

Figure 4.2: Masonry prism specimen for bending test

Table 4.2: Dimension of masonry prism specimen

Specimen	B (mm)	D (mm)	L (mm)
B5U1	282	352	838
B6U2	280	349	858
C1L1	283	352	848
C3L2	281	354	863
C5B1	281	350	847
B4B2	285	355	882

The diagonal shear stress (Ʈs) is calculated as per equations (4.1) and (4.2) (Mustafaraj and Yardim, 2017; Mustafaraj and Yardim, 2018; ASTM (2002, 2010)).

$$Ʈs = (0.707* P)/An \quad (4.1)$$

$$An = ((lw+hw))/(2*bw*n) \quad (4.2)$$

where, P is the force applied,

An is the net area of the wall, lw, hw, and bw are the length, height, and width of the wall, respectively, and n is the solid percent of the gross area of the wall.

The shear strain (γ) of the wall is calculated from equation (4.3),

$$\gamma = (\Delta v + \Delta H)/g \quad (4.3)$$

Where, (Δv – vertical shortening in mm),

(ΔH – horizontal lengthening in mm). For the walls rotated at 45 degrees, the compression strain defined by the ASCE test set-up method is given as

$$\varepsilon c = \Delta short /g,$$

where, Δshort is the change in length parallel to the direction of loading g is the original gauge length, and the tensile strain is defined by

$$\varepsilon t = \Delta long /g,$$

Where, Δlong is the change in length perpendicular to the direction of loading.

The total strain is calculated by equation (4.4):

$$\gamma = \varepsilon c + \varepsilon t \quad (4.4)$$

Equations for shear modulus (G) and Young's Modulus (E) were calculated by equations (4.5) and (4.6), respectively according to ASTM E 519 (2007) and ASTM E 143 (2002).

$$G = 0.707* P/(An * \gamma) \quad (4.5)$$

$$E = 2G (1+v) \quad (4.6)$$

Where, v is Poisson's ratio.

With a slight variation to the ASTM set up, in the present study, the wall panel rests horizontally on one side of the wall, and the force is applied diagonally between the two corners as shown in Figure 4.3. In addition, it can also measure the horizontal, vertical, and diagonal displacement of the wall specimen. For the test set up, the wall panels rest horizontally on a plinth and are positioned so that the load shoe at the bottom corner could be attached to the wall panels. Another load shoe was attached to the diagonally opposite top corner. Two rods on each side of the wall panel connected the two loading shoes with a hydraulic jack and load cell at opposite corners. The diagonal force was applied through the upper corner by a hydraulic jack and a load cell at diagonally opposite bottom corner measured the load. Displacement was measured with six displacement transducers, two each located in diagonal, vertical, and horizontal directions, respectively.

In timber-reinforced masonry (TRM), the Sal wood was used for reinforcement. Anchor bolts were fixed by drilling holes into the brick but not on masonry joints. For TRM, the wooden planks of 10 mm thickness were fixed on all four sides of the wall and one in the middle of the wall height by anchor bolts. For the diagonal side, it was only fixed in the tension diagonal. The reinforcement was done on both faces of the wall. Figure 4.4 a) shows the experimental set up for TRM. The schematic diagram of the diagonal compression test set up for the TRM wall is shown in Figure 4.4 b).

Figure 4.3: Diagonal compression test on unreinforced specimen

a) 

b) 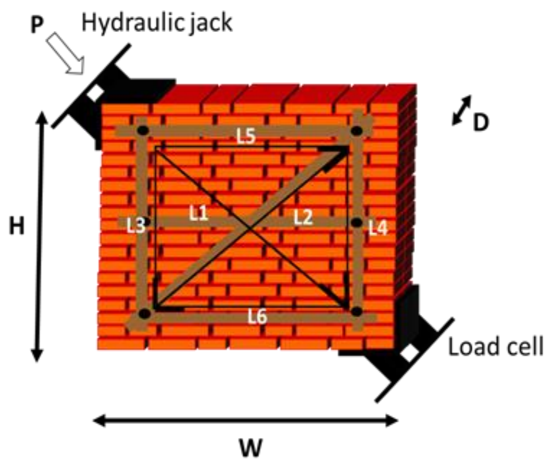

Figure 4.4: a) Diagonal compression test of timber reinforced masonry (TRM) specimen b) Schematic diagram of diagonal compression test set up of TRM specimen

Similarly, for steel reinforced masonry (SRM), the steel plates were used for reinforcement. For SRM, steel plates of 4.5 mm thickness were fixed on all four sides of the wall and one in the middle of the wall height by anchor bolts. For the diagonal side, it was only fixed in the tension diagonal. The reinforcement was on both faces of the wall. The reinforcement was done on both faces of the wall. Figure 4.5 a) shows the experimental set up for SRM. The schematic diagram of the diagonal compression test set up for the SRM wall is shown in Figure 4.5 b).

a)

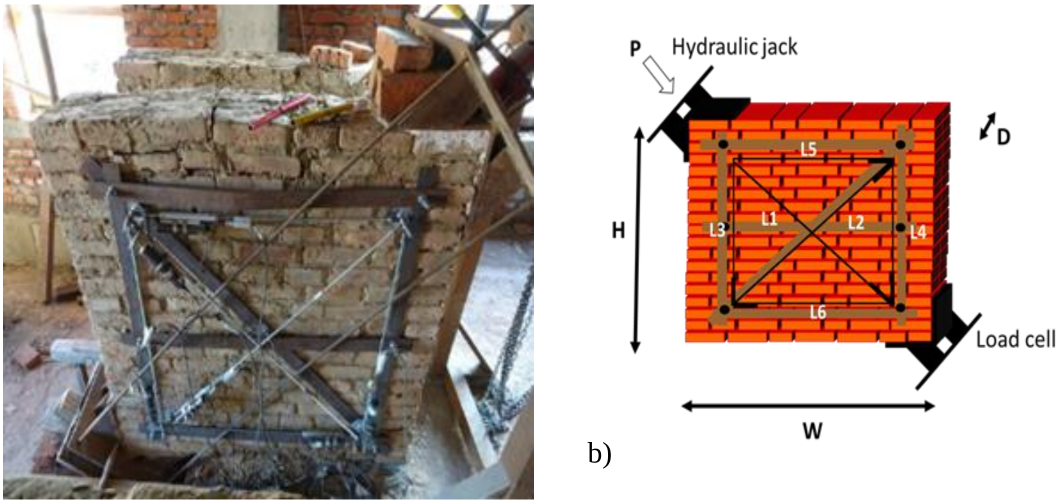

b)

Figure 4.5: a) Diagonal compression test of steel reinforced specimen (SRM) specimen
b) Schematic diagram of diagonal compression test of SRM specimen

The shear strain corresponding to maximum shear stress $\gamma_{\tau max}$ was calculated from the shear stress and shear strain graph.

The shear modulus, G was calculated by equation (4.7).

$$G = \tau_{1/3} / \gamma_{1/3} \tag{4.7}$$

where $\tau_{1/3}$ is the shear stress for a load of one-third of the maximum load and $\gamma_{1/3}$ is the corresponding shear strain.

4.2.2.2 Three-point bending experiment

The test set up for the three-point bending test on unreinforced prism, ladder type reinforced prism, and diagonal braced type reinforced prism, are shown in Figure 4.6, Figure 4.7 a) and Figure 4.7 b), respectively.

Figure 4.6: Bending test on unreinforced prism

a) 

b) 

Figure 4.7: a) Bending test on prism reinforced with ladder type braces b) Bending test on prism reinforced with diagonal braces

The modulus of rupture was calculated using the following equation (4.8),

Modulus of rupture or flexural strength Fr,

$$Fr = (1.5 * P * l) / (B * D^2) \quad (4.8)$$

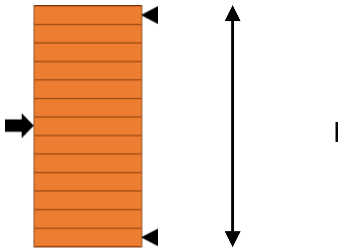

Figure 4.8: Schematic diagram of three point bending test

Where, P= Maximum load taken by specimen

Fr = Modulus of Rupture

L = Support spam of member

B = Width of specimen

D = Depth of specimen

Figure 4.8 shows the schematic diagram of the three-point bending test. It can also be calculated by the ratio of the bending moment at the center of the span to the section modulus of the specimen. The loading arrangement of the three-point bending test on masonry prisms is presented in Figure 4.9.

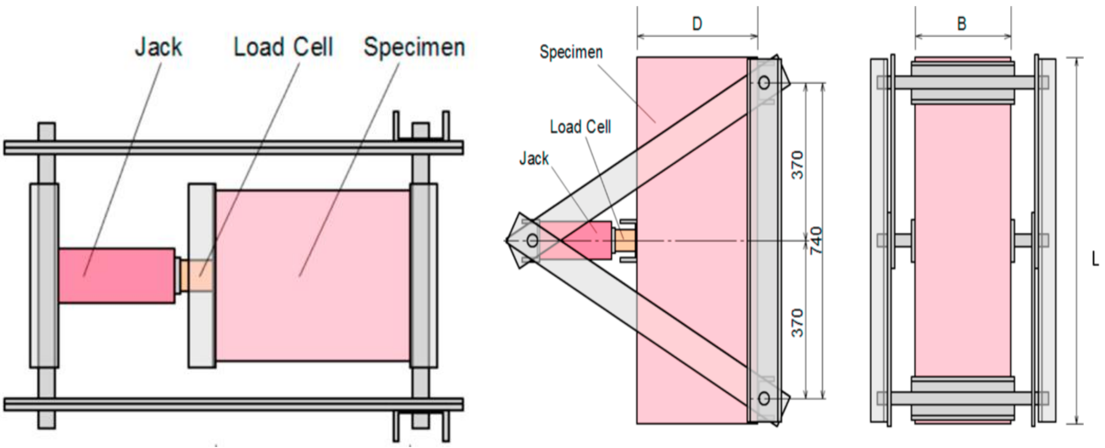

Figure 4.9: Loading arrangement of three-point bending test on masonry prisms (Dimensions are in mm)

4.3 Results and discussion

4.3.1 Diagonal compression experiment

4.3.1.1 Shear strength and shear deformation angle of unreinforced and reinforced specimens

The summary of the mechanical parameters of the tested specimens is shown in Table 4.3. Figure 4.10 shows the shear strength for all specimens. For the unreinforced wall, the average shear strength was 0.054 MPa, with a maximum value of 0.062 MPa for D2U1. For TRM and SRM panels, the average shear strengths were 0.106 and 0.149 MPa, respectively. The average deformation angle was 4.24% for unreinforced specimens. For TRM and SRM, the average deformation angle was 2.04% and 1.59%, respectively (Table 4.3). The TRM and SRM in our study increased the average shear strength by 1.98 and 2.78 folds, respectively compared to unreinforced specimens (Figure 4.11). Mustafaraj and Yardim (2018) also reported an increase in shear strength by reinforcing wall panels with textile-reinforced mortar. The strain corresponding to maximum shear strength increased for the TRM and SRM specimens compared to unreinforced specimens. In addition, the average shear modulus of TRM specimens slightly decreased while for SRM specimens, the average shear modulus increased compared to unreinforced specimens.

4.3.1.2 Failure modes of unreinforced and reinforced specimens

In unreinforced masonry, the failure of the specimen usually occurs with the panel splitting apart parallel to the direction of the load. The development of cracks initially starts at the center and continues mainly along the mortar joints and, in some cases, through the bricks. In our case, at the failure stage, cracks were observed in a step-wise manner along the brick-mortar interface in a compressed diagonal for unreinforced specimens. After reaching the peak shear stress for each wall panel, the reduction in load-carrying capacity was seen and cracks began to form in the stepping pattern. Similar results were reported by Dizhur and Ingham (2013). This might be due to the low ratio of mortar compressive strength to brick compressive strength which was $f_j/f_b=0.28$. For the TRM reinforced specimens, at the failure stage, the buckling was seen on the top horizontal member as well as the top portion of the wall. This might be due to the compressive strain developed in the top horizontal member of the reinforcement. For the SRM-reinforced specimens, at the failure stage, similar pattern of buckling behavior was observed. The possible reason for the buckling of horizontal members might be due to the compressive force developed in the members due to the horizontal force. Furthermore, no buckling was seen in the middle horizontal members. Buckling was also observed at the top of the structure possibly due to the absence of dead load over the wall in both types of reinforcement. The steel-reinforced specimen showed damage concentrated in the specimen, around the bolt than the timber-reinforced specimen. The shear stress- deformation angle for all the specimens is shown in Figure 4.12. For all the wall panels, the graph was approximately linear before crack initiation, followed by a nonlinear portion up to the maximum strength (Figure 4.12). The shear stress-deformation angle curve starts with a steep slope indicating the linear stage of masonry, whereas the second stage indicates the plastic phase which is almost horizontal and usually starts after the cracks.

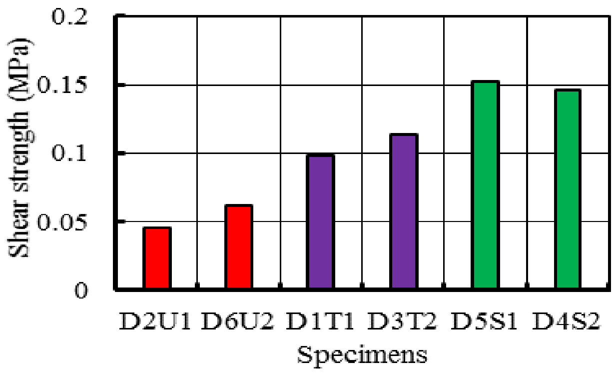

Figure 4.10: Shear strength for all specimens

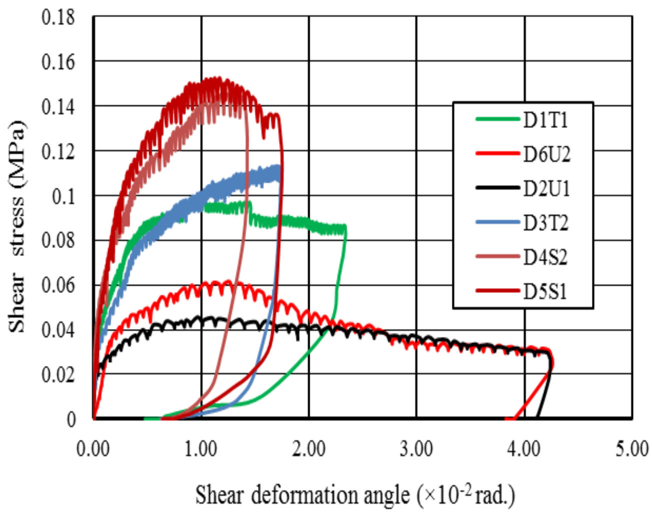

Figure 4.11: Shear stress versus shear deformation angle for all specimens

From the double shear loading test, conducted on the specimens collected from Kyushu University headquarters building 1 and 3 (Japan), the average shear strength of the specimens (OPS 112 and OPS 121) was 1.12 N/mm^2 (Araki et al., 2017). The average shear strength of specimens in our study was one-twentieth of the average shear strength of specimens from the Kyushu University headquarters building. The possible reason might be the use of mud mortar in our study while the mortar used in Kyushu University's headquarters building was cement mortar of compressive strength 29.5 N/mm^2. Another possible reason might be due to the lower value of the compressive strength of the brick used in our study (5.05 versus 19.2 N/mm^2).

Table 4.3: Summary of mechanical parameters of the tested specimen

Specimen	Shear strength τ_{max} (MPa)	Average shear strength (MPa)	Increase in shear strength (%)	Maximum shear deformation angle, γ ($\times10^{-2}$ rad.)	Shear deformation at τ_{max}, $\gamma_{\tau max}$ ($\times10^{-2}$ rad.)	Shear modulus, G ($\times10^{-2}$ GPa)	Average shear modulus, G ($\times10^{-2}$GPa)
D2U1	0.046	0.054	-	4.23	0.97	8.4	5.3
D6U2	0.062		-	4.25	1.26	2.2	
D1T1	0.098	0.106	184	2.34	1.02	5.9	4.6
D3T2	0.113		212	1.74	1.74	3.4	
D5S1	0.152	0.149	285	1.75	1.09	9.7	8.2
D4S2	0.145		272	1.42	1.4	6.7	

4.3.2 Three-point bending test results

4.3.2.1 Flexural strength and deflection angle of unreinforced and reinforced prism specimens

The result of the three-point bending test is summarized in Table 4.4. Figure 4.12 shows the flexural stress versus deflection angle curve for all the test specimens. The flexural strength at a deformation angle of 1x10^{-2}rad. in unreinforced, ladder-type reinforced, and diagonally braced reinforced specimens were 0.025N/mm^2, 0.2N/mm^2, and 0.35 N/mm^2, respectively. The unreinforced specimen was about one-eighth of ladder reinforcement and one-fourteenth of diagonally braced reinforcement. On average the flexural strength for unreinforced specimens was about one-tenth of reinforced specimens when the deformation angle is 1x10^{-2}rad. (Figure 4.12). The ladder and diagonal braced prisms increased the flexural strength by 246% and 465% compared to unreinforced specimens, respectively.

Table 4.4: Summary of test results specimen

Specimen	Maximum flexural load (kN)	Flexural strength (N/mm^2)	Average flexural strength (N/mm^2)	Maximum deflection angle (x10^{-2} rad.)	Average Maximum deflection angle (x10^{-2} rad.)	Mid-point displacement (mm)
B5U1	3.28	0.105	0.126	6.16	6.23	22.78
B6U2	4.46	0.146		6.30		23.30
B1L1	9.73	0.309	0.436	4.99	5.63	18.50
B2L2	17.83	0.563		6.26		23.16
B3B1	22.99	0.743	0.713	7.45	8.20	27.56
B4B2	22.01	0.682		8.95		33.11

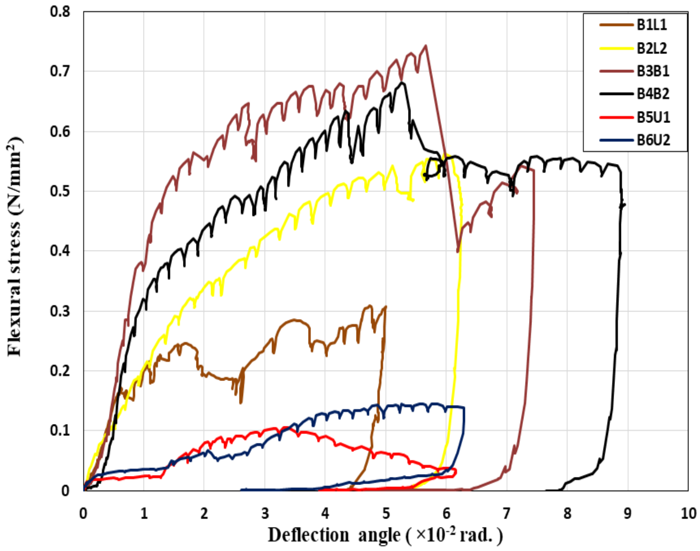

Figure 4.12: Flexural stress versus deflection angle curve for all the specimens

4.3.2.2 Failure modes of unreinforced and reinforced prism specimens

Figure 4.13 a) shows the failure of an unreinforced masonry prism specimen. For the unreinforced specimen, the specimen starts taking load and suddenly decreases when opening starts due to tensile splitting however due to the strut mechanism, the specimen again starts taking load (Figure 4.12, Figure 4.13 a)). The failure and splitting in ladder-type braced specimen is shown in Figure 4.13 b). The flexural strength was increased in reinforced specimens showing the maximum for diagonal type braced prism, however sudden drop was observed in the graph when the maximum load was reached which was also evidenced by the sudden split in the specimen. Among ladder-type reinforced specimens, specimen B1L1 was damaged before loading and as a result, the graph is slightly different than specimen B2L2 which shows a smooth curve. The failure in the ladder-type reinforced prism was mild and dispersed all over the specimen.

a) 

b) 

Figure 4.13: a) Crack pattern in specimen B5U1; b) Crack pattern in specimen B1L1

The failure and splitting in diagonal-type braced specimens are shown in Figure 4.14 a) and Figure 4.14 b), respectively. The flexural strength was increased in reinforced specimens showing the highest for diagonal type braced prism however sudden drop was observed when maximum load was reached (Figure 4.12).

a) 

b) 

Figure 4.14: a) Failure pattern of specimen B4B2 b) Sudden split of timber member for the specimen B4B2

4.4 Conclusions

Diagonal compression experiment and three point bending were conducted for Nepalese historical masonry and following conclusion were made.

1. The average shear strength was 0.054 N/mm^2, 0.106 N/mm^2, and 0.149 N/mm^2 for unreinforced walls, timber-reinforced walls, and steel-reinforced walls, respectively.
2. The shear strength of the unreinforced wall was about one-twentieth of the shear strength of Japanese brick masonry; however, the value of the shear deformation angle was found to exceed 4% for unreinforced masonry, indicating a high deformation capacity. The timber-reinforced masonry (TRM) and steel-reinforced masonry (SRM) increased the average shear strength by 1.98 and 2.78-fold, respectively compared to unreinforced specimens.
3. Flexural strength increased significantly in ladder and braced type timber reinforced specimens compared to unreinforced specimens. The maximum flexural strength was found for the diagonal-type braced prism. A sudden split was observed at maximum load in diagonal type braced prism whereas the failure in ladder type reinforced prism was mild and cracks were dispersed all over the specimen.
4. Reinforcing specimens with timber and steel increased the shear and flexural strength which was confirmed by the diagonal compression and bending tests. Therefore, we concluded that reinforcing with timber and steel on the surface of walls may be an effective retrofitting technique for historical buildings of Nepal composed of brick and mud mortar. However, Sal wood is easily available and can be easily embedded with the architecture of Nepalese historical masonry buildings therefore it can be used in retrofitting methods compared to steel plates. Retrofitting with ladder arrangement performed better compared to the brace arrangement.

References

Araki, K., Yamaguchi, K., Ninakawa, T., Murakami, K., Ishihara, Y., and Cui, X. (2017). Double shear loading test of brick masonry which constitutes the Kyushu University headquarters building 1 and 3. *Journal of Architecture and Urban Design, Kyushu University*, **31**, 45–52 (2017).

ASTM (2002), Standard Test Method for Flexural Bond Strength of Masonry, ASTM, West Conshohocken, PA, 2002.

ASTM (2010), Standard Test Method for Diagonal Tension (shear) in Masonry Assemblages, ASTM, West Conshohocken, PA, 2010.

Borri, A., Corradi, M., Castori, G., & Molinari, A. (2019). Stainless steel strip–A proposed shear reinforcement for masonry wall panels. *Construction and Building Materials*, **211**, 594-604.

Central Bureau of Statistics. (2012). Government of Nepal.

Chaulagain, H., Rodrigues, H., Spacone, E., and Varum, H. (2016). Seismic safety assessment of existing masonry infill structures in Nepal. *Earthquake Engineering and Engineering Vibration*, **15** (2), 251-268.

Dizhur, D., and Ingham, J. M. (2013). Diagonal tension strength of vintage unreinforced clay brick masonry wall panels. *Construction and Building Materials*, **43**, 418-427.

Endo, Y., Yamaguchi, K., Hanazato, T., and Mishra, C. (2020). Characterization of mechanical behavior of masonry composed of fired bricks and earthen mortar. *Engineering Failure Analysis*, **109**, 104280.

Gautam, D., and Chaulagain, H. (2016). Structural performance and associated lessons to be learned from world earthquakes in Nepal after 25 April 2015 (MW 7.8) Gorkha earthquake. *Engineering Failure Analysis*, *68*, 222-243.

Gautam, D., Rodrigues, H., Bhetwal, K. K., Neupane, P., and Sanada, Y. (2016). Common structural and construction deficiencies of Nepalese buildings. *Innovative Infrastructure Solutions*, **1** (1), 1.

Langenbach, R. (1989). Bricks, mortar, and earthquakes. *Apt Bulletin*, *31*(3-4), 31-43.

Mishra, C., Yamaguchi, K., Endo, Y., and Hanazato, T. (2018). Mechanical Properties of Components of Nepalese Historical Masonry Buildings. Proceedings of International Exchange and Innovation Conference on Engineering and Sciences, Interdisciplinary Graduate School of Engineering Sciences, Kyushu University (IEICES, **4**,118-123).

Moreira, S., Ramos, L. F., Oliveira, D. V., and Lourenço, P. B. (2014). Experimental behavior of masonry wall-to-timber elements connections strengthened with injection anchors. *Engineering structures*, **81**, 98-109.

Mustafaraj, E., and Yardim, Y. (2017). Review of Strengthening Techniques and Mechanical Testing for Unreinforced Masonry. *MATTER: International Journal of Science and Technology*, **3** (2).

Mustafaraj, E., and Yardim, Y. (2018). In-plane shear strengthening of unreinforced masonry walls using GFRP jacketing. *Periodica Polytechnica Civil Engineering*, **62** (2), 330-336.

Mustafaraj, E., and Yardim, Y. (2019). Retrofitting damaged unreinforced masonry using external shear strengthening techniques. *Journal of Building*

Parajuli, H. R. (2012). Determination of mechanical properties of the Kathmandu World Heritage brick masonry buildings. In *The 15th World Conference on Earthquake Engineering, Lisbon, Portugal*.

Vintzileou, E., Zagkotsis, A., Repapis, C., and Zeris, C. (2007). Seismic behavior of the historical structural system of the island of Lefkada, Greece. *Construction and Building Materials*, *21*(1), 225-236.

http://www.mbs-architecture.com/nepaltradbuildmat.pdf

Chapter 5: Numerical Investigation of the Properties of Unreinforced and Reinforced Nepalese Historical Brick Masonry Structures

Abstract

Considering the limited strength of traditional masonry structures, retrofitting is essential. The purpose of this study was to discretize a numerical model that can be used to assess the behavior of brick masonry in earth mortar. The behavior of unreinforced brick masonry (URM) and brick masonry reinforced with timber was investigated through numerical simulation. The flexural strength of URM and reinforced masonry prism of size 280 mm x 350 mm x 860 mm (B x D x L) was calculated by three-point bending experiments. For reinforced masonry prism, ladder and diagonal brace reinforcement with timber were studied. From the results, it was observed that the diagonal brace-reinforced prism withstood higher flexural tensile stress compared to the URM and ladder-reinforced prisms. From the uniaxial compression test conducted on the same size of masonry prism, the elastic modulus (E) calculated was 310 MPa. A homogenous macro model was used in ABAQUS software to reproduce a previously performed three-point bending test of a prism built of brick masonry in earth mortar. Material properties such as density, E, and Poisson's ratio were input to the software. The displacement value obtained was very low compared to the experimental result when E of 310 MPa determined from the uniaxial compression test was taken. The reason might be due to the involvement of both tensile and compressive forces in the bending test. In this study, the elastic modulus in tension (E_t) was considered 1/5 of that in compression (E_c) for the URM prism. The numerical model for the URM prism gave closer results to the experimental value when E_c was 41 MPa, which was 1/8 of E determined from the uniaxial compression test (310 MPa). In the uniaxial compression test, the direction of the compressive strut formed was 90 degrees to the bed angle. However, in the three-point bending test, a compressive strut was formed from the point of loading to the supports. For URM and diagonal braced specimen compressive strut formed was 56.3 degrees to the bed angle (θ_{strut}), whereas for ladder reinforced specimen, it was 37.2 degrees. For the ladder and diagonal-braced reinforced model, crack was assumed at the tensile side of the masonry. By trial and error, the numerical result was in good agreement with the experimental value for maximum displacement at the mid-point under the condition that the E of 20.5 MPa and 41.0 MPa was taken for the ladder and diagonal brace model, respectively, with a 70mm crack at the tensile side of masonry. In the analysis, it was observed that for URM and diagonal brace reinforced model, E was greater than for the ladder reinforced model. Namely, with the increase in compressive strut angle (θ_{strut}), there was an increase in the value of E.

Keywords: Historical, Masonry, Numerical modeling, Retrofitting, Sal timber

5.1 Introduction

5.1.1 Masonry in Earth Mortar (Mud Mortar)

5.1.1.1 Mechanical Behavior of Masonry in Earth Mortar

There are a large number of non-engineered constructions still exist in many parts of the world which are mostly constructed with locally available materials such as stones, bricks or adobe joined together with mortar (Ravichandran et al., 2021). About 30% of the world's population lives in earth building (Varum et al., 2014). These buildings are constructed by local masons based on experience and knowledge and are vulnerable to earthquakes (Parisi et al., 2013). Earth construction is widely spread and the oldest type of construction. The historical buildings constructed with brick and mud mortar are vulnerable to earthquakes due to the low strength of materials, poor structural detailing, and lack of seismic design and thus require seismic protection (Arya et al., 2014). Compressive strength, modulus of elasticity, and shear modulus are mechanical properties that are required to analyze and design masonry structures. The value of mechanical properties varies widely depending on the quality of materials, size, and workmanship of construction (Phaiju and Pradhan, 2018). Experimental investigation is needed for understanding the mechanical behavior of earth building properly (Varum et al., 2014; Endo et al., 2020).

5.1.1.2 Strengthening of Masonry in Earth Mortar

Retrofitting of unreinforced masonry (URM) buildings is important as they are vulnerable to damage against in-plane and out-of-plane failure due to limited shear strength, flexural strength, and deformation capacity (Shrestha et al., 2016). Timber panels are used in masonry structures with earthen mortar to enhance the integrity of the masonry walls (Langenbach, 1989). Moreira et al. (2014) reported that ductility was increased by retrofitting the masonry wall with a timber frame in their quasi-static monotonic and cyclic pull-out tests. Sustersic and Dujic (2014) reported that the strength and ductility of URM were increased by retrofitting with Cross Laminated Timber (CLT) panels. The plywood panels can withstand diagonal tension forces compared to timber frames (Maduh et al., 2019). Retrofitting with timber strong-back prevents the out-of-plane failure of masonry walls (Dizhur et al., 2017).

5.1.1.3 Numerical Analysis of Masonry in Earth Mortar

For the reliability and accuracy of the numerical model, the material properties are necessary based on experimental results. Once the model is calibrated, it is possible to vary the desired parameters and verify the effect of each component (Oliveira, 2014). The modeling strategies can be classified as detailed micro-modeling, simplified micro-modeling, and macro-modeling (Dauda et al., 2021). In the micro-modeling technique, the units, mortar, and the unit-mortar interface are modeled separately. In macro modeling, no distinction is made between units and joints, and masonry is modeled as a homogeneous material with equivalent material properties (Parisi et al., 2019). Hence, a macro model which is easy to use for structural design, seismic diagnosis, and retrofitting was used in this study. The purpose of this study was to investigate a numerical method that can be used for the analysis of the behavior of brick masonry walls in the elastic range with low-strength mortar. In addition, the behavior of brick masonry walls reinforced by timber was also investigated through numerical simulation.

5.2 Materials and Methods

5.2.1 Description of the Experiment.

Uniaxial compression experiments were conducted to clarify the basic mechanical properties of elements of brick walls (unit bricks, mud mortar, and masonry prisms) (Mishra et al., 2018). The bulk density of the masonry prism was 1566 kg/m^3, which was calculated from the proportion of brick and mud mortar in a prism. To study the flexural behavior of the wall, six prism specimens with dimensions of 280 mm x 350 mm x 860 mm (B x D x L) were constructed by brick and mortar, namelyB5U1, B6U2, B1L1, B2L2, B3B1, and B4B2, respectively (Endo et al., 2020). In the bending experiment, the B5U1 and B6U2 were unreinforced specimens (Figure 5.1a), while the rest of the four specimens were reinforced with timber (Sal wood). The specimens (B1L1 and B2L2) were reinforced with ladder-type reinforcement (Figure 5.1b), and the other two (B3B1 and B4B2) were reinforced with diagonal-type braces (Figure 5.1c). The cross-section of the timber plate was 50×10mm^{2}and was connected by steel bolts of 12 mm diameter.

The load of 100kN was applied manually by a mechanical jack. The jig system and displacement transducers were also used. Three points bending tests experiment were carried out on prisms that were set vertically and horizontal force was applied at the center of the prism. Supports were fixed at the top and bottom of the prisms. Displacement transducers were set up at the top, middle, and bottom of the prisms. Figure 2 shows the schematic diagram of the loading arrangement.

5.2.2 Calculation of Flexural Strength and Deformation Angle

The flexural strength Fr was calculated using equation (5.1),

$$Fr = \frac{(1.5Pl)}{(BD^2)} \qquad (5.1)$$

where, P is the maximum load taken by the specimen, Fr is the flexural strength of the masonry prism, l is the support span of the member, B is the width of the specimen and D is the thickness of the specimen (Figure 5.2).

To estimate the net displacement in the specimen mid-height, the average value of horizontal displacement at the top and bottom of the specimen was removed from the mean value of the displacement measured at the specimen mid-height. From the displacement measured, the deformation angle was calculated.

Figure 5.1a): URM bending specimen

Figure 5.1b): Ladder type reinforced specimen

Figure 5.1c): Diagonal brace reinforced specimen

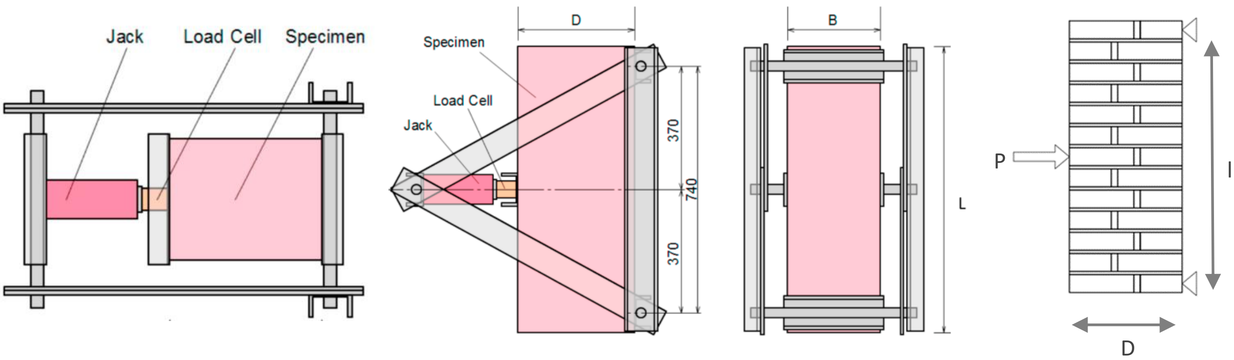

Figure 5.2: Loading arrangement of three-point bending test on masonry prisms (Dimensions are in mm)

5.2.3 Research Methodology

The present research was composed of the following three stages. First, a case study on the results obtained in bending experiments of brick masonry that constitutes historical buildings in Nepal is presented. The three-point loading test on the URM prism and reinforced masonry prism with wood (SAL timber) and bolts was performed. Second, for numerical modeling, elastic regions were determined from a graph of flexural stress-deformation angle. The first crack point was identified from experimental data and was also confirmed by basic mechanics theories. Third, numerical analysis was performed on the bending test models. This stage was articulated in two steps, which included (i) validation of the URM prism, and (ii) validation of the retrofitted masonry prism with timber panels. The numerical models were developed and validated using a macro model elastic analysis. The general-purpose finite element method software ABAQUS was used for the analysis. As the micro model is complicated to use for historical buildings and requires longer time and effort, this research aims to develop an analysis method that can more easily reflect the behavior of actual structures by using macro modeling. In addition, it is not realistic to design structures that cause large deformations in the case of brittle masonry; hence this study mainly focuses on small deformation regions that can be used for safer structural design.

The purpose of the numerical analysis was to propose a macro-model that can best fit with the experimental results of our study. In general, for macro-modeling same Young's modulus of elasticity (E) is assumed for compression and tension. In our study, the flexural modulus of elasticity (E) was 14.816 MPa which was several times lower than the modulus of elasticity (E) under uniaxial compression (310 MPa). Kanno et al. (2001) reported for unreinforced masonry, the compressive modulus of elasticity (E_c) is 5-6 times higher than the tensile modulus of elasticity (E_t). In this study, tensile modulus elasticity (E_t) was assumed $1/5^{th}$ of the compressive modulus of elasticity (E_c). With trial and error, the numerical result was matched with the experimental value for maximum displacement at the mid-point for the tensile side with a lower value of modulus of elasticity ($E_t=1/5^{th} * E_c$). For reinforced masonry, tensile cracks were assumed at the tensile side of masonry at about a depth of 70mm, 90mm, and 130mm. With trial and error, the numerical result was matched with the experimental value for maximum displacement at the mid-point for the crack-introduced model. The calibrated value of E for the diagonal brace-reinforced model was compared to the ladder-reinforced model. The effect of strut angle was also studied.

5.3 Results and Discussion

Figure 5.3 shows the flexural stress versus deformation angle curve for all the test specimens. The values in the graph show the maximum flexural strength of each specimen. The flexural strength was increased in reinforced specimens.

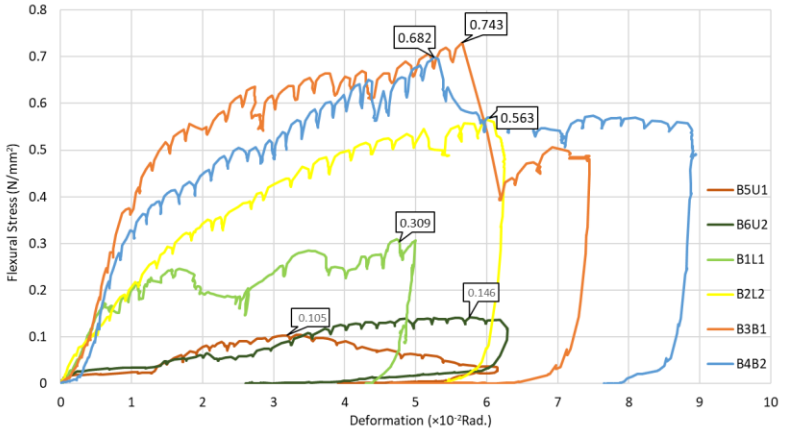

Figure 5.3: Flexural stress versus deformation angle curve for all the specimens

5.3.1 Failure modes of unreinforced and reinforced prism specimens

For the unreinforced specimen, the specimen starts taking load and suddenly decreases when opening starts due to tensile splitting however due to the strut mechanism, the specimen again starts taking load. The flexural strength was increased in reinforced specimens showing the maximum for diagonal braced reinforced prism, however sudden drop was observed in the graph when maximum load was reached which was also evidenced by the sudden split in the specimen, whereas the failure in ladder reinforced prism was mild and cracks were dispersed all over the specimen. Among ladder-reinforced specimens, specimen B1L1 was damaged before loading and as a result, the graph is slightly different from specimen B2L2 which shows a smooth curve.

5.3.2 Calculation of Restoring Force Characteristics

First, the elastic-plastic deformation range was determined. The elastic-plastic range and the deformation angle of each masonry prism for the bending experiment are shown in Table 5.1. First and second crack points A and B were determined as the intersections of linear regressions as shown in Figure 5.4a). The deformation-stress curves of URM, ladder reinforced, and diagonal braced reinforced specimens are shown in Figure 5.4b), 5.4c), and 5.4d), respectively. The deformation-stress curves for all specimens are shown in Figure 5.4e).

Table 5.1: Deformation range of URM and reinforced specimens

Specimens	Elastic deformation ($x10^{-2}$ rad)	Plastic deformation ($x10^{-2}$ rad)
URM (B5U1, B6U2)	0-0.1	0.1-1.33
Ladder (B1L1, B2L2)	0-0.95	0.95-2.00
Brace (B3B1, B4B2)	0-0.75	0.75-2.00

Table 5.2: Calculation of first and second crack points, load, horizontal displacement, and flexural modulus at first crack points

Specimens	First crack point		Second crack point		Stiffness in elastic deformation (N/mm^2)	Stiffness in plastic deformation (N/mm^2)	Load P at first crack (N)	Horizontal displacement at first crack (mm)	Flexural modulus at first crack E_b (MPa)
	Deformation (x10^{-2} rad)	Stress (N/mm^2)	Deformation (x10^{-2} rad)	Stress (N/mm^2)					
URM	0.095	0.02	1.330	0.032	0.2103	0.0099	618	0.352	14.8
Ladder	0.954	0.211	2.000	0.294	0.2214	0.0788	6520	3.533	15.6
Brace	0.804	0.389	2.026	0.549	0.4839	0.1308	12020	2.978	34.1

The bilinear characteristics of restoring force for unreinforced masonry prism were calculated by the first crack point, the second crack point, the elastic deformation, and the plastic deformation. The first crack point was obtained from experimental data when the deformation increased rapidly compared to flexural stress. The elastic deformation is the range from the beginning of the experiment till the first crack point. The URM masonry prism is elastic with a small deformation. The second crack point was obtained from the experimental data when the ratio of change in deformation was less MPa to the increase in flexural stress. The plastic deformation was in the range from the first crack point to the second crack point. The characteristics of restoring force for URM and reinforced masonry specimens were determined as shown in Figure 5.5. Deformation, the stress at the first crack point, the stiffness of the elastic deformation range, and the stiffness of the plastic deformation range are shown in Table 5.2. The stiffness of the elastic deformation of the ladder and diagonal brace reinforced specimens were 1.05 times and 2.30 times greater than the stiffness of the elastic deformation of URM specimens, respectively. However, the stiffness of the plastic deformation range of the ladder and diagonal brace reinforced specimen was 7.96 times and 13.21 times greater than the stiffness of the plastic deformation of the URM specimen. Stiffness reduction from the elastic area to the plastic area of URM, ladder, and diagonal brace reinforced specimen were 0.0471 times, 0.356 times, and 0.270 times, respectively.

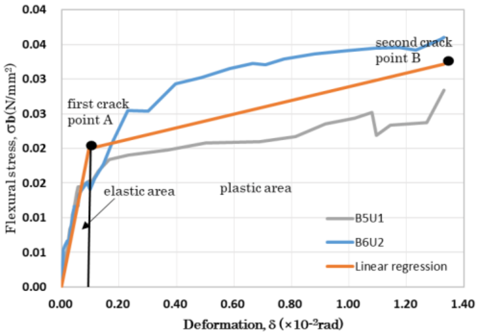

Figure 5.4a): Crack points and elastic-plastic deformations

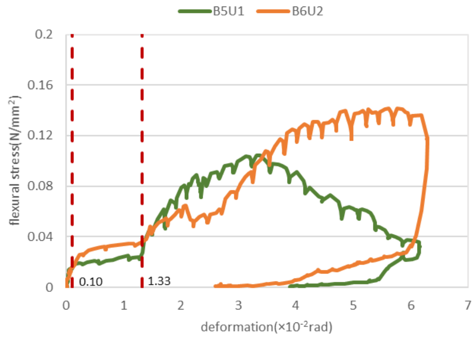

Figure 5.4b): URM specimen

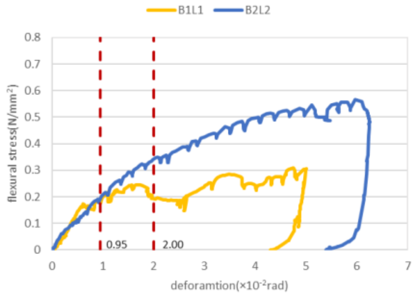

Figure 5.4c): Ladder reinforced specimen

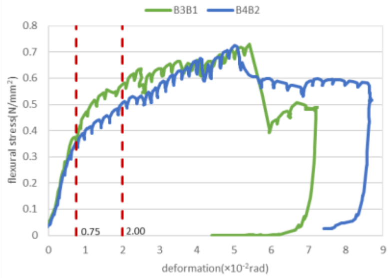

Figure 5.4d): Diagonal brace reinforced specimen

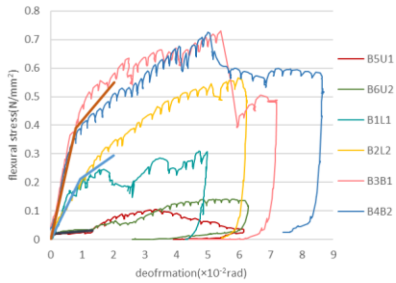

Figure 5.4e): All masonry prisms specimens

Figure 5. 4: Deformation-stress curves of specimens in bending experiment

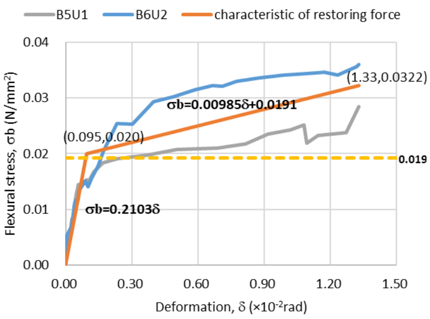

Figure 5.5a: Unreinforced specimen

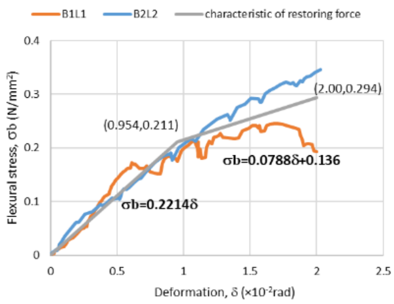

Figure 5.5b: Ladder reinforced specimen

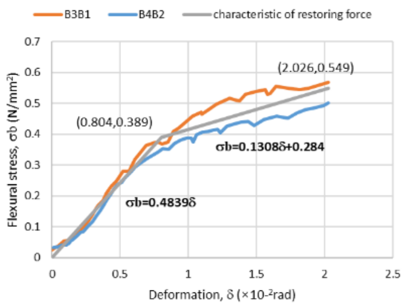

Figure 5.5c: Diagonal brace reinforced specimen

Figure 5.5: Characteristics of restoring force for URM and reinforced specimens

5.3.3 Load Calculation during Rigid Body Rotation of Unreinforced Masonry

The unreinforced masonry prism, subjected to horizontal load applied from a hydraulic jack is shown in Figure 5.6a). The load was calculated from equations (5.2) and (5.3) when the masonry prism began rigid body rotation (Mishra et al., 2021).

$$\sum M_B = Q \times \frac{L}{2} - W \times \frac{D}{2} \qquad (5.2)$$

$$\sum F_x = P - Q - Q = 0 \qquad (5.3)$$

where, Q is the reaction force at the top and bottom supports, W is the self-weight of half of the masonry prism, P is the horizontal force from the hydraulic jack, and D and L are the depth and height of the masonry prism, respectively. The calculated value of horizontal force (P) when rigid body rotation occurred was 609N. At a stress of 0.019 N/mm^2, the URM specimen started rigid body rotation as confirmed by equations (2) and (3) and Figure 5.6a) which was close to the stress in the first crack point of the URM specimen. Figure 5.6b) shows the load at rigid body rotation and load at the first crack point.

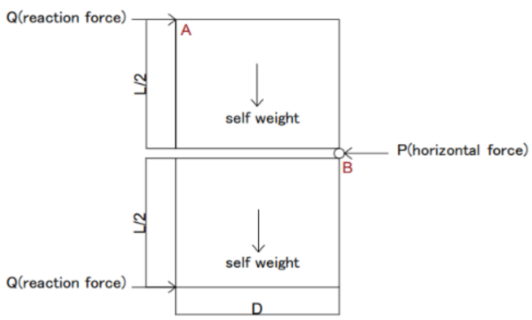

Figure 5.6a): Horizontal and reaction force of bending experiment

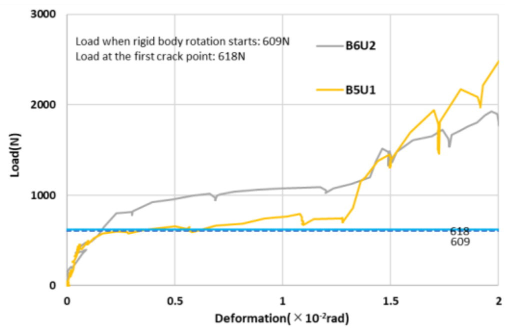

Figure 5.6b): Load at rigid body rotation and load at first crack point

5.3.4 Flexural Modulus for Bending Test

Flexural modulus (Eb) for bending test specimens was determined from equation (5.4) as follows.

$$Eb = \frac{l^3}{4BD^3} \times \frac{\Delta P}{\Delta \delta} \qquad (5.4)$$

where, D is the depth of the masonry prism, B is the width of the cross-section, l is the span of the masonry prism, $\Delta P/\Delta\delta$ is the ratio of the elastic range of load and deflection.

The load, deflection, and flexural modulus at the first crack point of all masonry prisms are shown in Table 5.2. The flexural modulus of masonry prisms calculated from equation (5.4) was less than Young's modulus in the compression experiment (310 MPa) due to the anisotropic behavior of brick masonry with low-strength mortar.

5.3.5 Determination of Poisson's Ratio

Figure 5.7a) shows the shear stress versus tensile/compressive strain of the diagonal compression experiment of D2 and D6 specimens. Poisson's ratio was calculated as the ratio of strain in the tensile direction to the compressive direction as the difference in tensile and compressive strain was large in the diagonal experiment (Figure 5.7a)). Tensile strain is the elongation in the tensile diagonal direction measured by displacement transducer L2 (Figure 5.7b)). Similarly, compressive strain

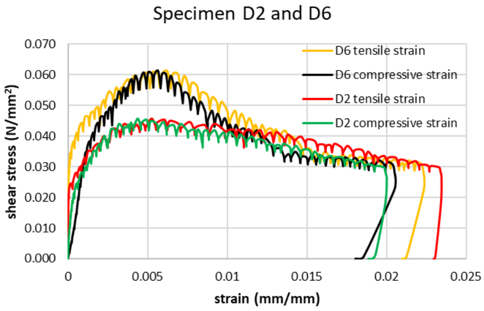

Figure 5.7a): D2 and D6 specimen

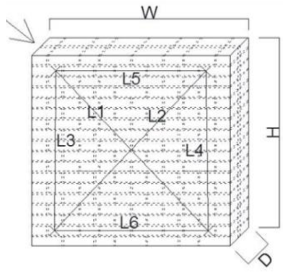

Figure 5.7b): Specimen in diagonal experiment

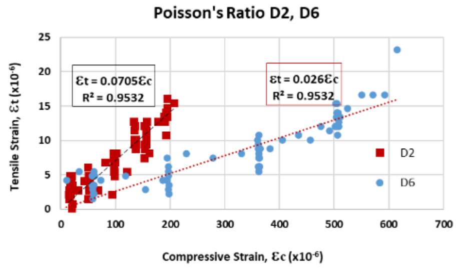

Figure 5.7c): Determination of Poisson's ratio

Figure 5.7: Determination of Poisson's ratio from diagonal compression

is the shortening in the compressive diagonal direction measured by displacement transducer L1 (Figure 5.7b)). Poisson's ratio was calculated by taking linear regression of data up to 33% of maximum load (Figure 5.7c)) (Mishra et al., 2018). The Poisson's ratio of D2 and D6 specimens were 0.0705 and 0.0260, respectively. The average Poisson's ratio was 0.0483.

5.4 Numerical Modeling of URM and Reinforced Masonry Prisms

5.4.1 Numerical Modelling of Masonry Prism

A numerical model of a masonry prism was created using a three-dimensional solid (or continuum) element in ABAQUS finite element software. C3D8R is a hexahedral 8-node linear brick element with reduced integration (one integration point). The integration point of the C3D8R element is located in the middle of the element. C3D8R was selected for mesh generation as it is cost-effective and has enhanced convergence compared to full integration (Dauda et al., 2021).

A mesh size of 30 mm and a friction coefficient of 0.3 was taken in this study (Dauda et al., 2021). The size of URM, ladder-reinforced, and brace-reinforced models was 350mm×280mm×860mm. Masonry was modeled as an isotropic and homogeneous material. The sizes of steel plates used at the top, bottom, and base supports were 280mm×20mm×100mm. In ladder and diagonal brace models, brick masonry prisms were reinforced with timber of cross-section 50mm×10mm. The timber reinforcement was connected to a brick masonry prism with 12 mm bolts by multi-point constraints (MPC). MPC is used to connect the elements between them and to impose constraints between different degrees of freedom of the model. The MPC is a rigid body between two nodes to constrain the displacement and rotation at the first node to the displacement and rotation at the second node. The bolt was considered a one-dimensional element and timber plate and brick masonry were considered as three-dimensional elements. There were three boundary conditions (BC), namely top BC, bottom BC, and base BC in the modeling to replicate the experimental condition (Figure 5.8a)). For URM, ladder reinforced and diagonal brace reinforced specimens load was applied in terms of pressure 0.02207N/mm^2, 0.2329 N/mm^2 and, 0.2329 N/mm^2, respectively. The timber material properties were taken as input to the software (Table 5.3) (Kim et al., 2017). Poisson's ratio and density were also taken as input to the software. Young's modulus of elasticity (E) from the prism compression experiment was taken as the E initial for the first iteration. The trials for different values of Young's modulus of elasticity during modeling were done until the numerical result was in good agreement with the experimental value for maximum displacement at the mid-point.

Table 5.3: Mechanical properties of masonry, steel, and timber

Materials	Young's modulus (MPa)	Poisson's ratio	Density (kg/mm^3)
Masonry	14.8	0.0483	1.57×10^{-6}
Steel	205000	0.3	7.85×10^{-6}
Timber (SAL)	20500	0.4	8.86×10^{-7}

5.4.2 Model Output of URM Model

The 3D model, tensile principal stress, and compressive principal stress contour for the URM model are shown in Figure 5.8a), Figure 5.8b) and Figure 5.8c), respectively. The stress contours show the part under load is in compression, and the part away from the load is in tension, which is in good agreement with the experimental result. The numerical result was in good agreement with the experimental value for maximum displacement (0.352 mm) at the mid-point when E (23MPa) was taken (Table 5.4).

5.4.3 Model Output of Ladder Reinforced Model

The 3D model, tensile principal stress, and compressive principal stress contour for ladder reinforced model are shown in Figure 5.9a), 5.9b), and 5.9c) respectively. The compressive strut in masonry is formed in the ladder-reinforced model as shown in Figure 5.9c). The numerical result was in good agreement with the experimental value for maximum displacement (3.533 mm) at the mid-point when E (16.45MPa) was taken (Table 5.4).

5.4.4 Model Output of Diagonal Brace Reinforced Model

The 3D model, tensile principal stress, and compressive principal stress contour for the diagonal brace reinforced model are shown in Figure 5.10a), 5.10b), and 5.10c) respectively. The numerical result was in good agreement with the experimental value for maximum displacement (1.615 mm) at the mid-point when E (38MPa) was taken (Table 5.4).

In the ladder-reinforced model, E (16.45 MPa) used for best fit was smaller compared to E (24 MPa) for the URM model and E (38 MPa) for the diagonal brace reinforced model. In this study, the strut angle (θ_{strut}) of the ladder-reinforced model was smaller compared to the diagonal brace reinforced model ($\theta_{strut, ladder}$)<($\theta_{strut, brace}$). For the ladder-reinforced model,θ_{strut} was 37.2 degrees, however for the diagonal brace reinforced and URM models θ_{strut} was the same (56.3 degrees). The lower value of E for the ladder-reinforced model compared to URM and diagonal brace-reinforced model might be due to the effect of the angle between the compressive strut formed and the bed angle (Nowak et al., 2021).

5.4.5 Effect of Strut Angle on the Modulus of Elasticity for Reinforced Masonry Model

In this study, the ladder and diagonal brace reinforced specimens take higher loads even after a crack has developed in the masonry. The tensile cracks were assumed at the tensile side of masonry in reinforced specimens at about a depth of 70mm, 90mm, and 130mm (Figure 5.12a) and Figure 5.12b)). The numerical and experimental results by assuming a crack in the tensile side of the masonry of the reinforced model are shown in Table 5.5. In the ladder-reinforced model, after the introduction of a crack of 70mm, 90mm, and 130 mm at the tensile side of the masonry, the numerical result was in good agreement with the experimental value for maximum displacement (3.533 mm) at the mid-point when E of 20.5 MPa, 22.5 MPa, and 27 MPa was taken, respectively. Similarly, in the diagonal brace reinforced model, after the introduction of a crack of 70mm, 90mm, and 130 mm at the tensile side of the masonry, the numerical result was in good agreement with the experimental value for maximum displacement (1.615 mm) at the mid-point when E of 41 MPa, 43 MPa, and 47 MPa were taken, respectively. The numerical result was in good agreement with the experimental value for maximum displacement at the mid-point with an increased value of E for both the ladder and diagonal braced reinforced models compared to the model without cracks. The calibrated value of E for the diagonal brace-reinforced model was greater compared to the ladder-reinforced model. This might be due to the larger strut angle in the diagonal brace reinforcement model compared to the ladder reinforcement model. Nowak *et al*. (2021) also reported that with the increase in the angle formed between the compressive strut developed in the model and the bed angle, there is an increase in the value of E.

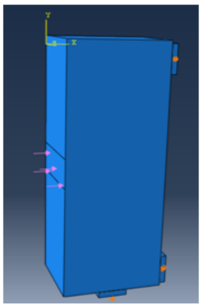

Figure 5.8a): URM model

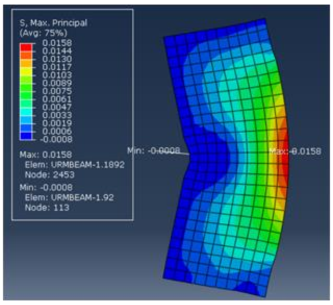

Figure 5.8b): Tensile principal stress of URM model

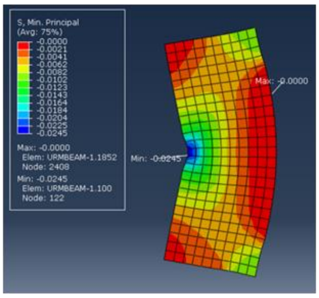

Figure 5.8c): Compressive principal stress of URM model

5.4.6 Effect of Compressive and Tensile Modulus of Elasticity in URM Model

Kanno *et al*. (2001) reported that the tensile modulus of elasticity of URM is in the range of $1/5^{th}$-$1/6^{th}$ of compressive modulus of elasticity as the modulus of elasticity on tension and compression sides differ greatly. Therefore, in this study, the modulus of elasticity in the tension side of the URM model was taken $1/5^{th}$ of the modulus of elasticity of the compression side. The tensile zone in the URM model in this study was chosen so that the compressive strut formation still occurs between the supports and the loading point. With trial and error, the numerical result was in good agreement with the experimental value for maximum displacement (0.352 mm) at the mid-point for the T-shaped area on the tensile side with a lower value of modulus of elasticity ($Et=1/5^{th}$ *Ec) (Figure 5.11). Numerical results matched the experimental value when the compressive modulus of elasticity of 41 MPa and tensile modulus of elasticity of 8.2 MPa were taken for the URM model (Figure 5.11) (Table 5.6). Similarly, for the diagonal braced reinforced model with crack, the numerical result showed the maximum displacement (1.615mm) at the mid-point when the modulus of elasticity of 41 MPa was taken (Table 5.5). This might be due to the angle of the compressive strut (56.3 degrees) being equal for both models (Kanno et al., 2001).

Table 5.4: Numerical and experimental results of displacement at the mid-point of three models

Specimens	Load P (N)	$E_{masonry}$ (MPa)	θ_{strut} (degree)	Num. disp. (mm)	Exp. disp. (mm)
URM model	618	23.0	56.30	0.352	0.352
Ladder model	6520	16.5	37.20	3.533	3.533
Brace model	6520	38.0	56.30	1.615	1.615

Where, $E_{masonry}$ is Young's modulus of elasticity of brick, θ_{strut} is the strut angle, Num. disp. is numerical displacement, and Exp. disp. is experimental displacement

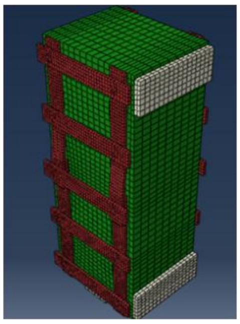

Figure 5.9a): Ladder reinforcement model

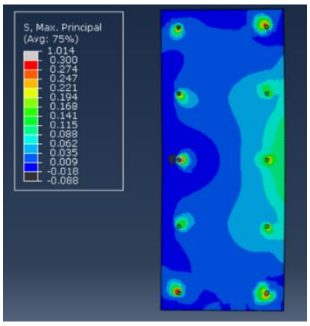

Figure 5.9b): Tensile principal stress for ladder reinforced model

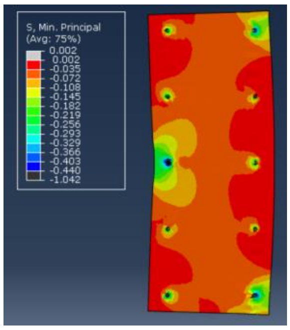

Figure 5.9c): Compressive principal stress for ladder reinforced model

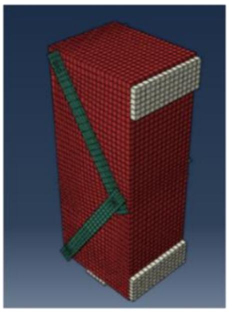

Figure 5.10a): Diagonal brace reinforced model

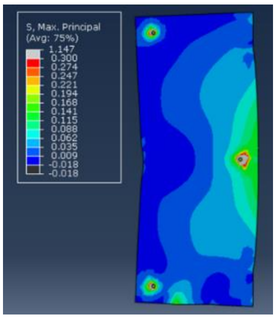

Figure 5.10b): Tensile principal stress for diagonal brace reinforced model

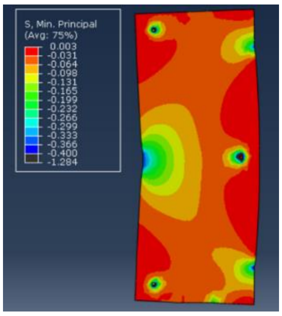

Figure 5.10c): Compressive principal stress of diagonal brace reinforced model

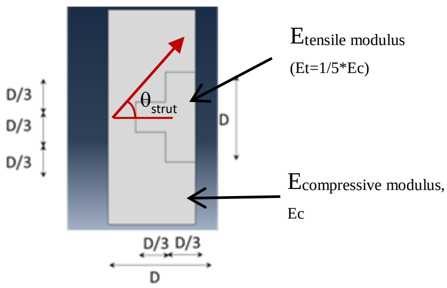

Figure 5.11: Compression and tension side of URM model

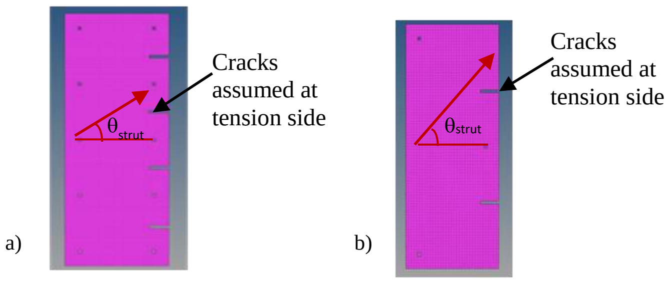

Figure 5.12: Model assuming crack in the tension side of masonry for a). ladder model and b). diagonal brace reinforced model

Table 5.5: Numerical and experimental results of displacement at the mid-point by assuming a crack in the tension side of masonry in reinforced model

Specimens	Load P (N)	$E_{masonry}$ (MPa) with crack (70 mm)	$E_{masonry}$ (MPa) with crack (90 mm)	$E_{masonry}$ (MPa) with crack (130 mm)	θ_{strut} (degree)	Num.disp. (mm)	Exp. disp. (mm)
Ladder model	6520	20.5	22.5	27.0	37.2	3.533	3.533
Brace model	6520	41.0	43.0	47.0	56.3	1.615	1.615

Where, $E_{masonry}$ is Young's modulus of elasticity of brick, θ_{strut} is strut angle, Num. disp. is numerical displacement, and Exp. disp. is experimental displacement

Table 5.6: Numerical and experimental results of the URM model by considering E_t=1/5*E_c

Specimens	Load P (N)	Compressive modulus of elasticity (E_c) (MPa)	Tensile modulus of elasticity (E_t) (MPa)	θ_{strut} (degree)	Num. disp. (mm)	Exp. disp. (mm)
URM model	618	41.0	8.2	56.30	0.352	0.352

Where, θ_{strut} is strut angle, Num. disp. is numerical displacement, and Exp. disp. is experimental displacement

5.5 Conclusions

Numerical analysis on three point bending test specimen models of Nepalese historical brick masonry was conducted and following conclusions were made.

1. A homogenous macro model was used to reproduce a previously performed three-point bending test of a prism built of brick masonry in earth mortar. In this study, the elastic modulus in tension (E_t) was considered 1/5 of that in compression (E_c) for unreinforced brick masonry (URM) prism.
2. The numerical model for the URM prism gave closer results to the experimental value when E_c was 41 MPa which was 1/8 of E calculated from the uniaxial compression experiment (310 MPa).
3. In the uniaxial compression test, the direction of the compressive strut formed was 90 degrees to the bed angle, and E determined was 310 MPa. However, in the three-point bending test, a compressive strut was formed from the point of loading to the supports. For URM and diagonal braced specimens, the compressive strut formed was 56.3 degrees to the bed angle (θ_{strut}) whereas, for ladder-reinforced specimens, it was 37.2 degrees.
4. For the ladder and diagonal-braced reinforced model, crack was assumed at the tensile side of the masonry. By trial and error, the numerical result was in good agreement with the experimental value for maximum displacement at the mid-point under the condition that the E of 20.5 MPa and 41.0 MPa was taken for the ladder and diagonal brace model, respectively, with a 70mm crack at the tensile side of masonry.

5. In the analysis, it was observed that for URM and diagonal brace reinforced model, E was greater compared to ladder reinforced model. Namely, with the increase in compressive strut angle (θ_{strut}), there was an increase in the value of E. This numerical result tends to coincide with the findings of Nowak et al. (2021).

References

Arya, A. S., Boen, T., and Ishiyama, Y. (2014). *Guidelines for earthquake-resistant non-engineered construction*. UNESCO.

Dauda, J. A., Silva, L. C., Lourenço, P. B., and Iuorio, O. (2021). Out-of-plane loaded masonry walls retrofitted with oriented strand boards: Numerical analysis and influencing parameters. *Engineering Structures*, *243*, 112683.

Dizhur, D. Y., Giaretton, M., Giongo, I., & Ingham, J. M. (2017). Seismic retrofit of masonry walls using timber strong-backs. *SESOC Journal*, *30*(2), 30-44.

Endo, Y., Yamaguchi, K., Hanazato, T., and Mishra, C. (2020). Characterization of mechanical behavior of masonry composed of fired bricks and earthen mortar. *Engineering Failure Analysis*, *109*, 104280.

Kanno, T., J. Kino, and T. Furuya (2001). “Applicability of Concrete Structural Analysis Method to Brick Structure.” 56th Annual Conference of the Japan Society of Civil Engineers. Vol. 110, 220-221pp (2 pages) (Japanese)

Kim, S., K. Fujita, and T. Hanazato (2017). “Restoration of seismically-vulnerable historical masonry structures struck by an earthquake Part 3 Micro tremor measurement and damage of multi-storied pagodas by 2015 Nepal Gorkha earthquake.” AIJ conference 31-3 September (2017), Hiroshima, Japan (2 pages) (Japanese).

Langenbach, R. (1989). Bricks, mortar, and earthquakes. *Apt Bulletin*, *31*(3-4), 31-43.

Maduh, U. J., Shedde, D., Ingham, J., and Dizhur, D. (2019, November). In-plane testing of URM Wall Panels Retrofitted Using Timber Strong-Backs. In *Proceedings of the Australian Earthquake Engineering Society 2019 Conference*, *Newcastle*, *Australia* (p. 13).

Mishra, C., K. Yamaguchi, Y. Endo, and T. Hanazato (2018). "Mechanical Properties of Components of Nepalese Historical Masonry Buildings.": Proc. of International Exchange and Innovation Conference on Engineering and Sciences, 4, 1118-123.

Mishra, C., Yamaguch, K., Araki, K., Ninakawa, T., and Hanazato, T. (2021). Structural behavior of brick wall specimens reinforced on the surface with RC walls under horizontal loading. *Journal of Advanced Concrete Technology*, *19*(6), 593-613.

Moreira, S., L. F. Ramos, D. V. Oliveira, and P. B. Lourenço. "Experimental behavior of masonry wall-to-timber elements connections strengthened with injection anchors." *Engineering Structures* 81 (2014): 98-109.

Nowak, R., Kania, T., Derkach, V., Orłowicz, R., Halaliuk, A., Ekiert, E., & Jaworski, R. (2021). Strength parameters of clay brick walls with various directions of force. *Materials*, *14*(21), 6461.

Oliveira, L. M. F. D. (2014) “Theoretical and experimental study of the behavior of vertical interfaces of interconnected structural masonry walls” (Doctoral dissertation, Universidade de São Paulo).

Parisi, F., Balestrieri, C., and Varum, H. (2019). Nonlinear finite element model for traditional adobe masonry. *Construction and Building Materials*, *223*, 450-462.

Parisi, F., Iovinella, I., Balsamo, A., Augenti, N., and Prota, A. (2013). In-plane behavior of tuff masonry strengthened with inorganic matrix–grid composites. *Composites Part B: Engineering*, *45*(1), 1657-1666.

Phaiju, S., & Pradhan, P. M. (2018). Experimental work for mechanical properties of brick and masonry panels.

Ravichandran, N., Losanno, D., and Parisi, F. (2021). Comparative assessment of finite element macro-modeling approaches for seismic analysis of non-engineered masonry constructions. *Bulletin of Earthquake Engineering*, *19*, 5565-5607.

Shrestha, H. D., Subedi, J., & Rajbhandari, M. (2016). Seismic retrofitting guidelines of buildings in Nepal. *Kathmandu, Nepal: Government of Nepal, Ministry of Urban Development, Department of Urban Development and Building Construction*.

Sustersic, I., & Dujic, B. (2014). Seismic strengthening of existing concrete and masonry buildings with cross lam timber panels. In *Materials and joints in timber structures: Recent developments of technology* (pp. 713-723). Springer Netherlands.

Varum, H., Tarque, N., Silveira, D., Camata, G., Lobo, B., Blondet, M., and Costa, A. (2014). Structural behavior and retrofitting of adobe masonry buildings. *Structural rehabilitation of old buildings*, 37-75.

Chapter 6: Diagonal Compression Test of the Japanese Historical Brick Masonry Reinforced on the Surface with Steel Plates or RC Walls

Abstract

This study was conducted on Kyushu University's 1st and 3rd headquarters buildings, built in 1925 to develop and propose a seismic reinforcement method for the unreinforced brick masonry buildings. A diagonal compression test on brick masonry was conducted to clarify the reinforcement effects and mechanical properties of brick masonry reinforced on the surface. The brick masonry was reinforced on the surface with steel plates using anchor bolts or with RC walls using anchor rods from one side or both sides. We investigated the effects of reinforcement on the shear properties and failure modes of each specimen. Results showed that the shear strength increased for all reinforced specimens compared to the unreinforced specimens. The shear strength of double-sided steel reinforcement and double-sided RC reinforcement were about 1.56 and 1.92 times higher than unreinforced specimens, respectively. RC reinforcement had higher strength and rigidity compared to steel plate reinforcement. The initial stiffness of RC double-sided reinforcement was about 1.70 times higher than double-sided steel reinforcement. The shear strength in the case of RC walls decreased gradually with the increase in deformation compared to the steel plate reinforcement. Hence, showed higher deformation capacity in the case of RC wall reinforcement compared to steel plate reinforcement. The anchors could resist splitting of specimens as were fixed by drilling through the masonry body and anchoring rebar to the RC walls on both sides. Hence, a higher reinforcement effect could be anticipated.

Keywords: Diagonal Compression, Brick masonry, RC walls, Steel plates, Shear strength, Shear deformation angle, Anchor rebars

6.1 Introduction

6.1.1 Background of the study

Masonry is regarded as one of the most crucial components for construction and has been utilized as a building material for several thousand years. In recent years, concrete and steel have been used as structural elements in place of brickwork (Wang et al., 2018). The primary application of masonry is as an infill material for steel and reinforced concrete frames. The main causes of unreinforced masonry (URM) building failures include weak out-of-plane loaded walls, insufficient diaphragms or diaphragm-wall connections, or deficient strength of the walls when loaded in-plane (Mahmood and Ingham, 2011).

Depending on the building's orientation and the direction of seismic loading, walls experience a variety of lateral seismic forces during earthquake events. Masonry constructions typically exhibit poor performance due to their brittle nature, making them vulnerable to structural damage during seismic events (Mustafaraj and Yardim, 2018). The following are typical failure modes in in-plane mechanisms: There are four types of failures: shear, slide, rocking, and toe crushing. In URM constructions, shear and slide failures are the most frequent types among them (Mustafaraj and Yardim, 2019).

To enhance the poor structural performance of URM structures under seismic loadings, as well as to raise their tensile and shear strength, a variety of strengthening approaches have been developed (Mustafaraj and Yardim, 2018). The following are a few conventional methods of brick masonry reinforcement: (a) filling cracks and voids by grouting; (b) using metallic or brick elements to stitch major cracks and weak regions; (c) using steel ties for exterior or internal post-tensioning; (d) shotcrete jacketing; (e) ferro-cement; and (f) center core, etc. (Mustafaraj and Yardim, 2018; Mustafaraj and Yardim, 2019; Kalali and Kabir, 2012). Ferrocement jacketing is widely used in both masonry and concrete constructions (Rosenthal, 1986). Ferrocement increases increasing stiffness, load-carrying capacity, and in-plane resistance (Forta Ferro Corporation, 2015) and also improves ductility and crack resistance (Kaushik et al., 1994; Forta Ferro Corporation, 2015).

Modern materials for retrofitting masonry buildings include textile-reinforced mortar (TRM) and fiber-reinforced plaster (FRP). According to Ismail et al. (2011), the various applications of twisted steel bars limit the failure mode of diagonal cracking. Two different failure modes were noted by Turco et al. (2006) in glass and carbon fiber-reinforced polymer retrofitting walls: shear failure of the masonry at the support and debonding of the FRP reinforcement. According to Wang et al. (2006), retrofitting brickwork subjected to in-plane shear loading with GFRP enhanced its load-carrying capacity.

In this study, a seismic reinforcement method was developed and proposed for unreinforced brick masonry buildings to improve the seismic safety of the 1st and 3rd headquarters buildings of Kyushu University built in 1925. Specimens were reinforced with steel plates using anchor bolts and RC wall plates using anchor bars which were subjected to diagonal compression loading experiment to investigate the effects of reinforcing on shear strength.

6.1.2 Overview of Kyushu University 1st and 3rd headquarters building

There were many modern buildings in the old Hakozaki campus of Kyushu University. Among them, Kyushu University's 1st and 3rd headquarters buildings were selected as buildings with a very high heritage value due to their historical importance according to the survey report (Evaluation Report of Modern Buildings at Kyushu University Hakozaki Campus, 2012). The two headquarters buildings were rebuilt in 1925 with bricks and cornerstones of the former main building of the Faculty of Engineering, Kyushu University, which had been destroyed in 1923. It was designed by Ken Kurata, who was the first general manager of Kyushu University and was constructed by Saiki Corporation. After the campus relocation project (February 2016), both the buildings were considered for preservation (Report "Directions for handling modern buildings on the site of the Hakozaki Campus", 2016).

Figure 6.1a) shows the exterior of the Kyushu University 1st headquarters building. It is located in Hakozaki, Higashi-ku, Fukuoka City, which is a two-story brick masonry with a total floor area of 2,881 m^2. The walls are made of unreinforced brick masonry, while the slab on each floor is made of reinforced concrete. It has a small beam and a girder on the top of the wall. Figure 6.1b) shows the exterior of the Kyushu University 3rd headquarters building. The building is made of brick masonry with a basement and 3 floors above ground. The specifications of the walls, floor slabs, and girder are the same as those of the 1st headquarter building.

a)  b) 

Figure 6.1: Kyushu University a) 1st headquarters building b) 3rd headquarters building

In both buildings, masonry bricks appear on the outer wall facing outside (Figure 6.1a)). Plaster finishes such as mortar are made on the surface of the brick wall on both the outer wall facing the inside and most of the inner walls. Therefore, both the outer wall facing the inside and most of the inner wall can maintain the appearance even if they are reinforced from the surface. Hence, the surface reinforcement method was selected in this study. In addition, the thickness of brick walls for both headquarters buildings is larger than the thickness of the beams and slabs. Therefore, it cannot be confirmed whether it can sufficiently be when anchored to the beam or slab. It is effective to reinforce the visible parts of each floor from the indoor side surface without changing the beams and slabs, and the walls or foundations of the upper and lower floors, so the appearance can be maintained. Also, it is economically advantageous and easy to construct.

6.2 Material and Methods

6.2.1 Outline of the experiment

6.2.1.1 Outline of diagonal compression experiment

The experiments were conducted by the Yamaguchi Laboratory at Kyushu University, Japan to which the author belongs. The author was in charge of analyzing the data obtained from these experiments. The experiment on diagonal compression test for Japanese historical brick masonry were conducted in 2015. Figure 6.2a) and 6.2b) shows the shape of the specimen and the schematic diagram of the diagonal compression experiment, respectively. The specimen was rotated by 49 ° vertically from the stacking direction, and jigs were placed on the upper and lower corners for support. Vertical load was applied from the top corner.

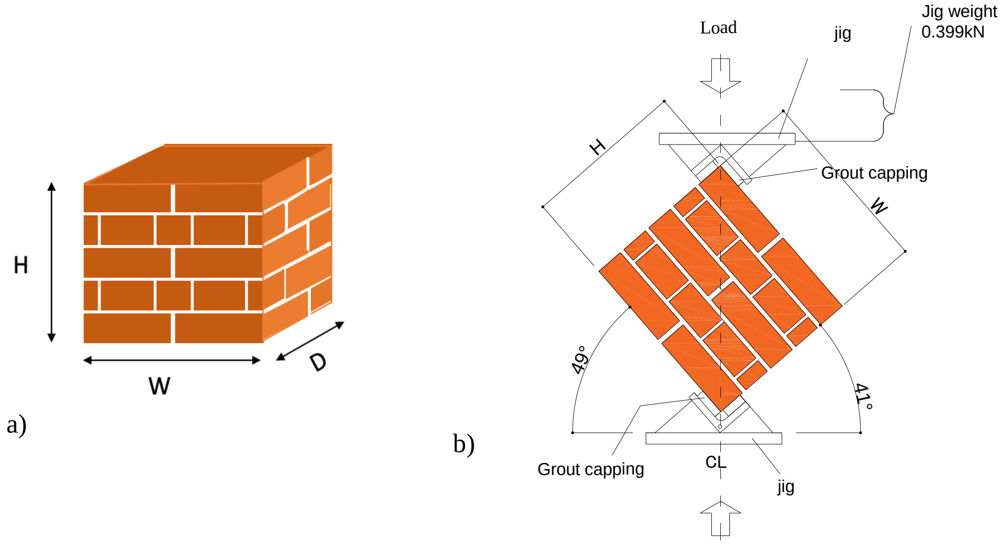

Figure 6.2: a) Specimen shape b) schematic diagram of diagonal compression experiment

6.2.1.2 Description of the test specimens

The bricks used for the specimen were fired solid brick. The average compressive strength of brick was 22.6 N/mm^2 with a dimension of 216mm x 108mm x 63mm. Five types of specimens were prepared namely unreinforced (DUR) specimen, double-sided steel plate reinforced (DSD) specimen, single-sided steel plate reinforced (DSS) specimen, RC double-sided reinforced (DCD) specimen, and RC single-sided reinforced (DCS) specimen. Three samples for each type of specimen were prepared. For all the masonry specimens (unreinforced as well as reinforced), one and a half brick was used in the thickness direction, and five bricks were stacked in the height direction in the English style. In addition, the brick surface of the loading part was capped with grout material for adjustment of the unevenness.

For the reinforced specimens, anchors were embedded in the masonry, and steel plates or RC walls were attached. In the DSD specimens, 140 mm M12 anchor bolts were embedded in the front and back of the masonry, and then 9 mm thick steel plates were attached with bolts. The DSS specimen was given the same reinforcement only on one side (front side) of the masonry. For the DCD specimens, 140 mm D13 anchor bars were embedded in the front and back of the masonry and fixed with adhesive. Afterward, D10 rebars were assembled in a grid and placed so as not to hit the anchors. 100 mm concrete was cast. The bar arrangement is shown in Figure 6.3c). In addition, to secure the cover thickness, the reinforcing part was extended 60 mm beyond the masonry. The DCS specimens were given the same reinforcement only on one side (front side) of the masonry.

For all the reinforced specimens, the embedding depth of the anchor in the masonry was determined by 8 da. or more (where da is the diameter of the anchor), as per the guideline for seismic retrofit design of existing reinforced concrete structures (Japan Architectural Disaster Prevention Association, 2001). Hence, the depth of 106 mm was taken as shown in Figure 6.3.

a)

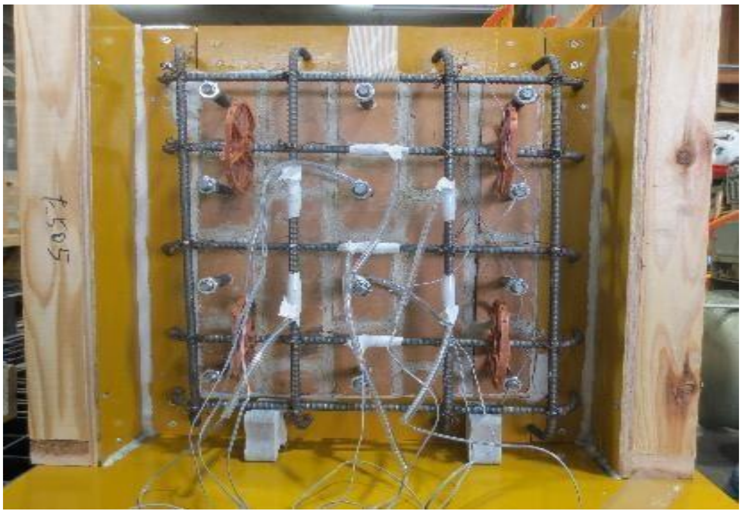

b)

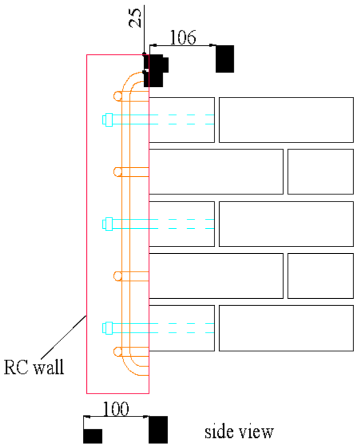

c)

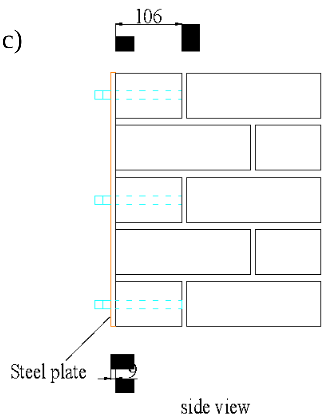

Figure 6.3: Anchor embedding depth in a) RC reinforced specimen b) Steel reinforced specimen c) Bar arrangement for concrete casting

Figure 6.4 shows the anchor placement procedures. In the case of steel plate reinforced specimens (DSD, DSS), holes are drilled in the steel plate in advance with a diameter larger than the bolt diameter so that the anchor bolt can pass through the steel plate. The fixture not only connects the steel plate and anchor bolt but also allows the adhesive to fill the gap between the hole and the bolt.

a)

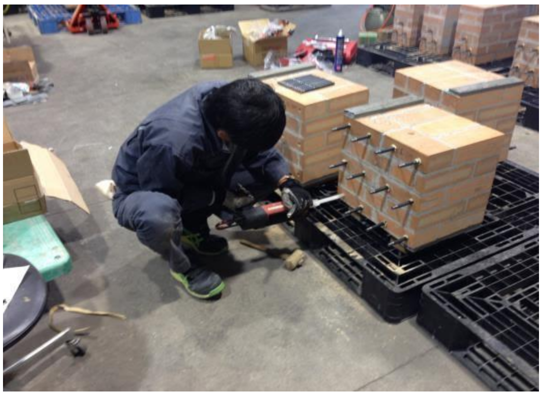

b)

c)

Figure 6.4: Anchor placement procedure a) Cleaning of the anchor hole, b) Injection of adhesive into anchor hole and anchoring of bolt M12 or anchor rod D13, c) Installation of the fixture and (steel plates only)

Table 6.1 and 6.2 shows the size and the material specifications of specimens used in this experiment. The height, weight, and depth of specimens were about 355 mm, 410 mm, and 330 mm, respectively (Table 6.1). The compressive strength of mortar for the DUR specimen was 34.5 (N/mm^2), whereas the compressive strength of mortar for the DCS specimen was 38.3 (N/mm^2). The compressive strength of reinforced concrete for the DCD specimen was 66.6 (N/mm^2), whereas the compressive strength of reinforced concrete for the DCS specimen was 57.4 (N/mm^2).

Table 6.1: Size of the specimens

Specimens		Height H [mm]	Width W [mm]	Depth D [mm]
DUR	501	357	410	331
	502	355	410	331
	503	355	410	332
DSD	510	355	410	332
	511	354	408	332
	516	356	414	331
DSS	505	357	410	331
	507	355	409	332
	508	354	409	330
DCD	512	358	415	331
	517	355	414	331
	518	357	414	331
DCS	504	357	410	330
	506	357	409	330
	509	355	410	331

Table 6.2: Material specification of specimens

Specimens	Mortar		Reinforced concrete		Steel plate
	Compressive strength (N/mm^2)	Young's modulus (N/mm^2)	Compressive strength (N/mm^2)	Young's modulus (N/mm^2)	
DUR	34.5	2.68×10^4	-	-	-
DSD	35.8	2.70	-	-	SS400 356×411×9
DSS	35.8	2.70	-	-	SS400 356×411×9
DCD	38.7	2.24×10^4	66.6	3.82×10^4	-
DCS	38.3	2.08×10^4	57.4	3.88×10^4	-

6.2.1.3 Description of the test setup

Figure 6.5 shows the test setup of the diagonal compression test for all types of specimens. For the DUR diagonal compression test, displacement transducers were installed on each diagonal as well as on four sides of the front surface on both sides of the specimen. The DSS, DCD, and DCS specimens were loaded until the second peak was reached after reaching the maximum load. Figure 6.6 shows the shape and displacement measurement positions for all the specimens.

a) 

b) 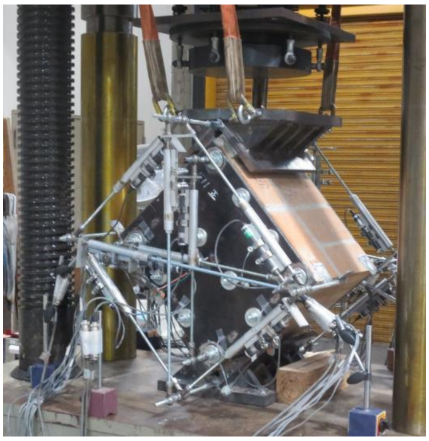

c) 

d) 

e) 

Figure 6.5: Test setup procedures for a) DUR, b) DSD c) DSS, d) DCD, and e) DCS specimens

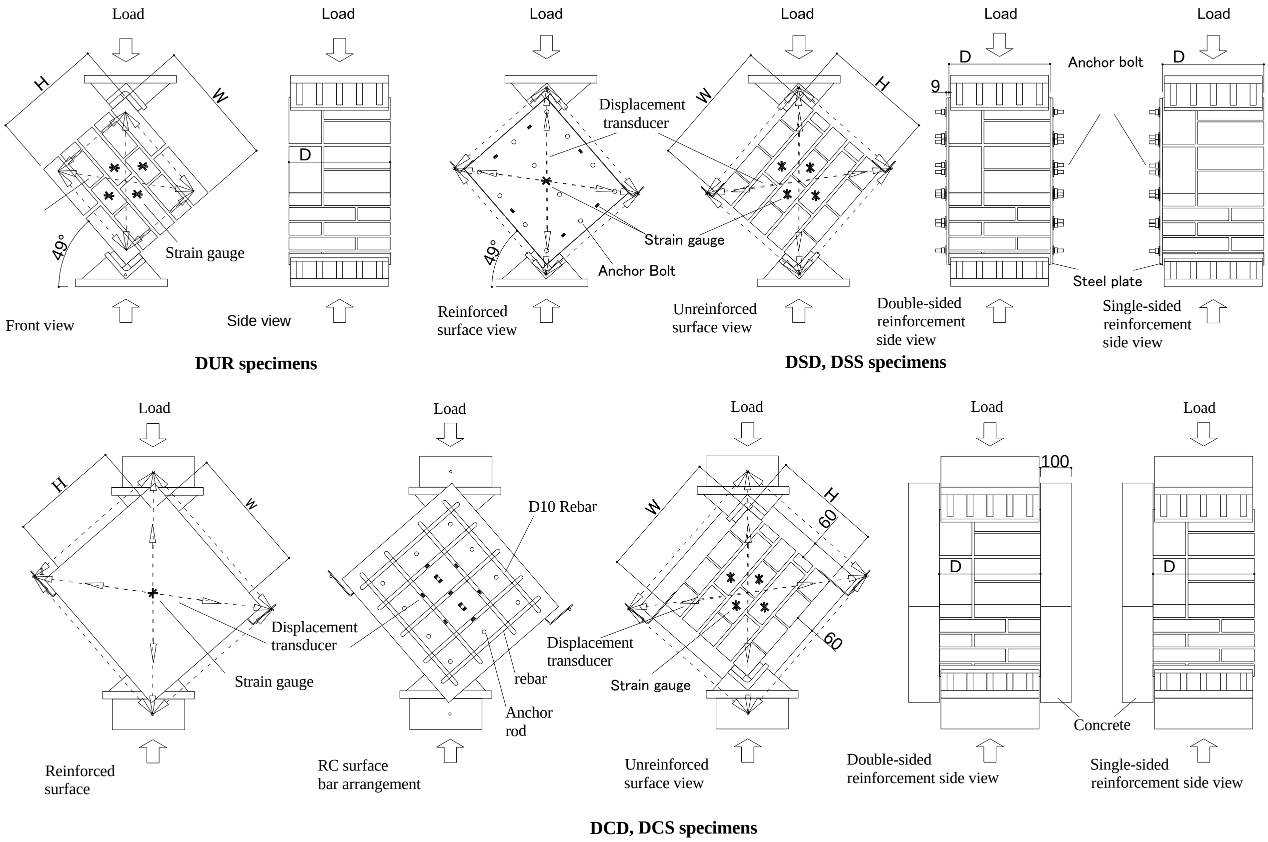

Figure 6.6: Test specimen shape and measurement position of deformation

6.2.1.4 Test procedure

ASTM E 519-02 is used to determine the diagonal tensile or shear strength of 1.2 by 1.2 m masonry assemblages by loading them in compression along one diagonal (Detergents, 2005). This causes a diagonal tension failure, with the specimen splitting apart parallel to the direction of the load. To impart the weight to the specimen, this approach uses two loading shoes positioned on the panel's two diagonally opposed corners.

In this study, the calculation procedure was as follows from the equations (6.1), (6.2), (6.3), (6.4) and (6.5):

$$\tau = P \cos An \qquad (6.1)$$

where: τ= shear stress (MPa); P = load along the compression diagonal (N); An = net shear area of the specimen (mm^2);

$$An = (W+H)*D/2 \qquad (6.2)$$

where: W = width of specimen (mm); H = height of specimen (mm); D = total thickness of specimen (mm);

$$\gamma = \Delta Vgv + \Delta Hgh \qquad (6.3)$$

where: γ is the shear strain or shear deformation angle ($\times 10^{-2}$rad.); ΔV is the vertical shortening (mm);

ΔH is the horizontal extension; gv is the vertical gauge length; gh is the horizontal gauge length

$$G = 0.707 * P/(An * \gamma) \qquad (6.4)$$

$$E = 2G\ (1+v) \qquad (6.5)$$

Where: G= Modulus of rigidity (kN/mm^2), v is Poisson's ratio, E is the modulus of elasticity

6.3 Results and discussion

6.3.1 Shear stress-shear deformation angle responses of specimens

Figure 6.7 shows the relationship between the shear stress and shear deformation angle for each specimen. The DSD 516 specimen was omitted because the behavior of the masonry could not be compared due to the deformation measurement position. Areas where displacement gauges were not measurable and areas, where behavior was negative, were omitted. The shear deformation angle was compared to the value of the diagonal displacement transducer which measured the deformation of the masonry. For the DUR specimen, the average values obtained from each of the four diagonal displacement transducers on the surface were taken. For the DSD and DCD specimens, the values were obtained in the same manner from four diagonal displacement transducers on the side. The DSS and DCS specimens were omitted because the behavior on the reinforcement side was found negative. The deformation obtained from the unreinforced side displacement transducer showed a behavior similar to the DUR specimens. As expected, the DUR specimens reached the maximum load during the stepwise shear failure along the joint. In contrast, the DSD and DCD specimens reached the maximum load after the splitting of side surfaces, and the DCD specimen reached the second peak thereafter. In the DSS and DCS specimens, the second time peak after the maximum load was reached during the stepwise shear failure on the unreinforced surface.

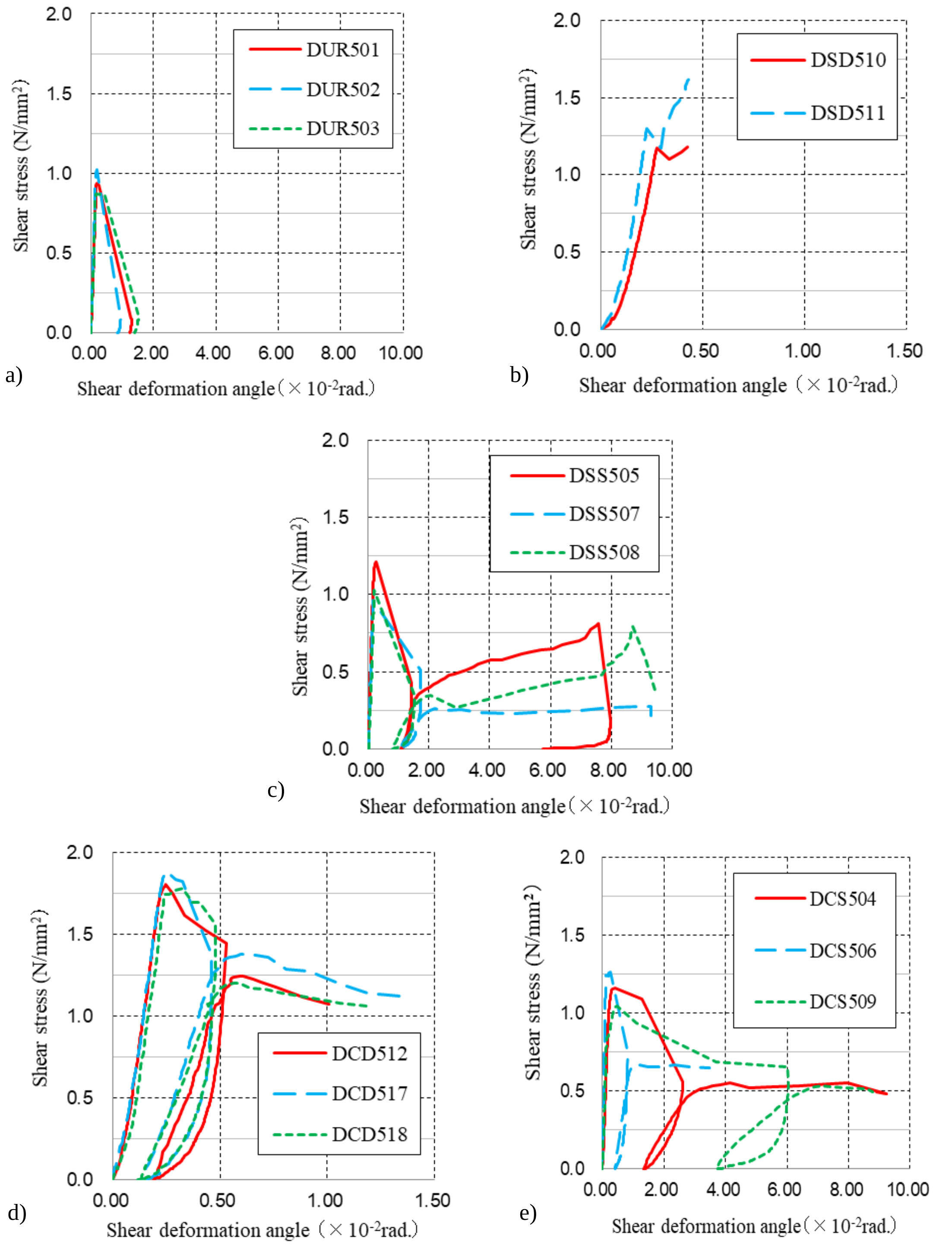

Figure 6.7: Relationship between shear stress and shear deformation angle of a) DUR, b) DSD, c) DSS, d) DCD, and e) DCS specimens

6.3.2 Shear strength and stiffness of specimens

Table 6.3 shows the results of mechanical properties from wallette testing. Figure 6.8 shows the comparison of shear strength for all the specimens. From Table 6.3 and

Figure 6.8, it is evident that the average shear strength of the specimens increased for all types of reinforced specimens compared to the DUR specimens. The average shear strength of DSD and DCD specimens were about 1.56 and 1.92 times higher compared to unreinforced specimens, respectively. The rate of increase in shear strength was higher in RC reinforcement than in the steel plate reinforcement. However, some DSS specimens had lower strength than DUR specimens.

Table 6.3 shows that the average initial shear stiffness of both double-sided reinforcement (DSD and DCD) specimens is lower than that of DUR specimens. This is because the deformation between the upper and lower jigs and the masonry is included in the vertical deformation of the DSD and DCD specimens. DCD specimens have about 1.70 times higher initial stiffness compared to DSD specimens. The average of the initial shear stiffness of the DSS and DCS specimens was higher than that of the DUR specimen. The average of the initial shear stiffness of DCS was higher than the DSS.

From Figure 6.7, it is clear that DCS and DCD specimens show a gradual strength decrease. Overall, it was observed that the shear strength in the case of RC walls decreased gradually with the increase in deformation compared to the steel plate reinforcement. This indicates that the deformation capacity of RC wall reinforcement is higher than that of steel plate reinforcement.

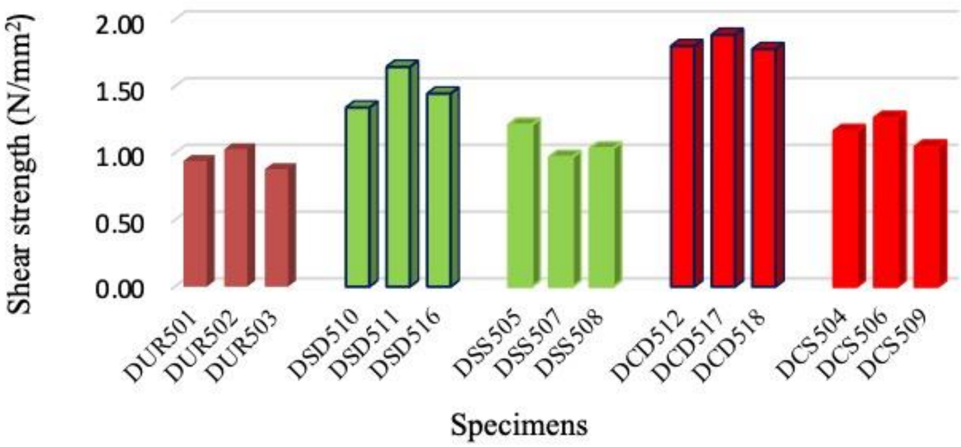

Figure 6.8: Comparison of shear strength of all the specimens

Table 6.3: Summary of results of mechanical properties from wallette testing

Specimens		P_{max} (kN)	τ_{max} (N/mm²)	$\tau_{max.}$ avg. (N/mm²)	$\gamma_{\tau max}$ (×10⁻²rad.)	G (kN/mm²)	G avg. (kN/mm²)	$\gamma_{\tau max}$ (×10⁻²rad.)	G (kN/mm²)	G avg. (kN/mm²)
	501	169.0	0.94					0.17	0.51	
DUR	502	185.0	1.03	0.95 (0.061)	-	-	-	0.19	0.64	0.55
	503	158.5	0.88					0.16	0.51	
	510	241.9	1.34		0.03	0.24				
DSD	511	295.4	1.65	1.48 (0.127)	0.31	0.33	0.29	-	-	-
	516	262.5	1.45		-	-				
	505	218.4	1.21					0.25	0.73	
DSS	507	174.9	0.97	1.07 (0.102)	-	-	-	0.17	0.65	0.61
	508	185.4	1.03					0.20	0.44	
	512	329.0	1.80		0.25	0.50				
DCD	517	343.5	1.89	1.82 (0.046)	0.25	0.56	0.48	-	-	-
	518	323.5	1.78		0.33	0.39				
	504	209.5	1.16					0.40	0.44	
DCS	506	227.0	1.26	1.16 (0.088)	-	-	-	0.27	1.10	0.71
	509	189.0	1.05					0.48	0.57	

P_{max} : maximum load; τ_{max} : maximum shear stress reached; $\gamma_{\tau max}$: shear strain corresponding to maximum stress; G: Shear modulus of rigidity; avg. stands for average

6.3.3 Failure modes of specimens

The unreinforced specimen showed a typical brittle failure showing cracks only in the mortar joints, whereas the reinforced specimen showed a ductile failure. The experimental results showed that the DUR specimen reached its maximum load when a stepwise shear failure occurred along the brick-mortar interface (Figure 6.9a)). In the DSD and DCD specimens, the maximum load was reached when the side masonry was split (Figure 6.9b), Figure 6.9c)), and in the DSS and DCS specimens, the maximum load was reached when the staircase-like shear failure occurred on the unreinforced surface (Figure 6.9d)). In the DSS and DCS specimens, the steel plate and RC did not show any significant damage to the reinforcement at the maximum load. In the DSD and DCD specimens, splitting occurred in the side masonry. This is because the splitting failure occurred due to the elongation in the depth direction of the masonry due to compression before the shear stress was sufficiently transmitted from the masonry to the reinforcement. It was confirmed that all the specimens with splits were cracked at the tip of the embedded anchor (Figure 6.9e)).


a)
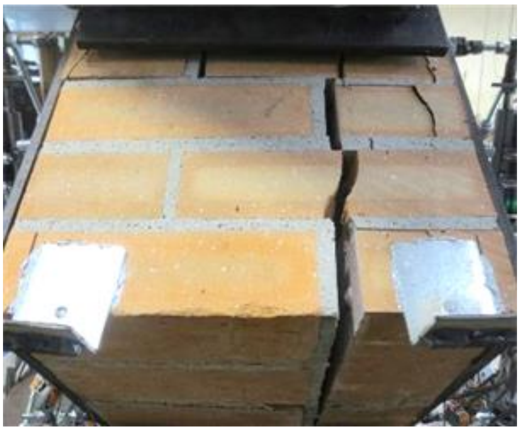
b)

c)
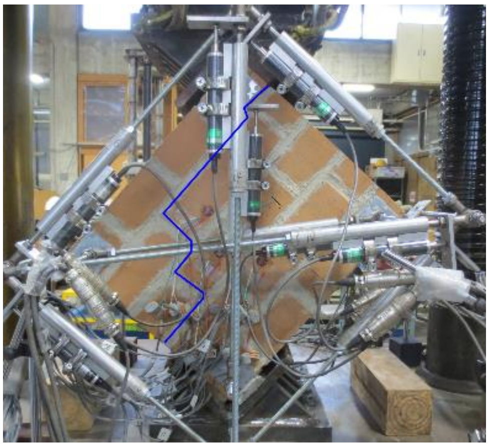
d)
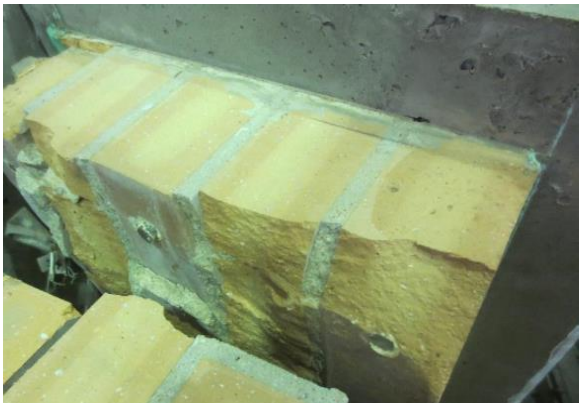
e)

Figure 6.9: a) Shear failure in DUR specimen (DUR503), b) Splitting failure in DSD specimen (DSD 510), c) Splitting failure in DCD specimen, d) Shear failure observed in DSS, DCS (unreinforced side DSS508), e) Splitting of masonry at the tip of embedded anchor in DCD specimens

6.4 Conclusions

In this study, a diagonal compression test of brick masonry was conducted to know the reinforcement effect when the wall of brick masonry was reinforced from the surface. The shear parameters were also investigated. The following findings were obtained.

1. RC reinforcement has higher strength and rigidity than steel plate reinforcement. In addition, in the case of RC walls, the deformation capacity was larger than the steel plate reinforcement.
2. We concluded that anchors that penetrate through the masonry body by drilling anchor rods and fixing rebars on both sides could resist splitting of specimens, promote integration and hence higher reinforcement effect could be anticipated.

References

Detergents, O. (2005). Standard Test Method for Diagonal Tension (Shear) in Masonry Assemblages, ASTM E519-02. *Annual Book of ASTM Standards*, *92*(June), 1-5.

Directions for handling modern buildings on the site of the Hakozaki Campus https://www.kyushu-u.ac.jp/news/file/minkan/kenchiku toriatukai.pdf. In Japanese.

Forta Ferro Corporation, "Forta for Concrete". (2015). Available: www.forta-ferro.com.

Ismail, N., Petersen, R. B., Masia, M. J., & Ingham, J. M. (2011). Diagonal shear behavior of unreinforced masonry wallettes strengthened using twisted steel bars. *Construction and Building Materials*, **25** (12), 4386-4393.

Japan Architectural Disaster Prevention Association: Guide to seismic retrofit design for existing reinforced concrete buildings, pp.262, Table 3.9.1-5, 2001. In Japanese.

Kalali, A., & Kabir, M. Z. (2012). Experimental response of double-wythe masonry panels strengthened with glass fiber reinforced polymers subjected to diagonal compression tests. *Engineering Structures*, **39**, 24-37.

Kaushik, S. K., Singh, K. K., & Prasad, R. (1994). Inelastic buckling of ferro-cement encased columns". In: Ferrocement: *Proceedings of the Fifth International Symposium on Ferrocemen*t UMIST, Manchester, 6-9 Sept. (Nedwell, P. J., Swamy, R. N. (Eds.)). Taylor & Francis e-book.

Mahmood, H., & Ingham, J. M. (2011). Diagonal compression testing of FRP-retrofitted unreinforced clay brick masonry wallettes. *Journal of Composites for Construction*, **15** (5), 810–820. https://doi.org/10.1061/(ASCE)CC.1943-5614.0000209

Mustafaraj, E., & Yardim, Y. (2018). In-plane shear strengthening of unreinforced masonry walls using GFRP jacketing. *Periodica Polytechnica Civil Engineering*, **62** (2), 330-336.

Mustafaraj, E., & Yardim, Y. (2019). Retrofitting damaged unreinforced masonry using external shear strengthening techniques. *Journal of Building Engineering*, **26**, 100913.

Rosenthal, I. (1986) "Precast ferrocement columns". *Journal of Ferrocement,* 16, 273–284.

Study Group on Modern Buildings at Kyushu University Hakozaki Campus: Evaluation Report of Modern Buildings at Kyushu University Hakozaki Campus, pp.26-27, pp.32-33, December 2012. In Japanese.

Turco, V., Secondin, S., Morbin, A., Valluzzi, M. R., & Modena, C. (2006). Flexural and shear strengthening of un-reinforced masonry with FRP bars. *Composites Science and Technology*, **66** (2), 289-296.

Wang, C., Sarhosis, V., & Nikitas, N. (2018). Strengthening/retrofitting techniques on unreinforced masonry structure/element subjected to seismic loads: A literature review. *Open Construction and Building Technology Journal*, *12*(1), 251-268.

Wang, Q., Chai, Z., Huang, Y., Yang, Y., & Zhang, Y. (2006). Seismic shear capacity of brick masonry wall reinforced by GFRP.

Winokur, A., & Rosenthal, I. (1982). Ferrocement in centrally loaded compression elements. *Journal of Ferrocement*, **12** (4), 357-364.

Chapter 7: Structural Behavior of Japanese Historical Brick Wall Specimens Reinforced on the Surface with RC Walls under Horizontal Loading

Abstract

This study aims to develop and propose a seismic retrofitting method for unreinforced brick masonry to improve the seismic safety of the 1st and 3rd headquarters buildings of Kyushu University. Five brick wall specimens representing parts of the walls that were adjacent to the openings in the headquarters buildings were prepared on a 3/4th scale of the actual structure, and they were reinforced on either one or the sides of their surfaces with reinforced concrete (RC) walls. A horizontal loading experiment was conducted to confirm the reinforcing effect. Results indicated that the maximum load of the specimens (CS01, CS02) reinforced on one side with RC walls was 6.1-6.2 times higher than that of the unreinforced specimen. Similarly, the maximum load of the specimens (CD01, CD02) reinforced on both sides with RC walls was 12.6-14.2 times higher than that of the unreinforced specimen. The maximum horizontal strength of specimen CD02 (60 anchors) is approximately 11% lower than that of specimen CD01 (100 anchors). However, the strength was maintained without degradation to a large deformation level. The specimen CS02 reached its maximum load at a smaller deformation angle compared to the specimen CS01 because of the effect of twisting. Additionally, a horizontal strength evaluation formula for brick wall specimens reinforced with RC walls was derived and verified. The values calculated using horizontal strength evaluation formulas were close to the experimental values.

Keywords: Brick masonry, Kyushu University Headquarters Buildings, Horizontal loading experiment, Analytical study

7.1 Introduction

Owing to the heavyweight and brittleness of masonry buildings, they can easily collapse during an earthquake, which causes various casualties and property losses (Bhattacharya *et al*. 2014). Damage to unreinforced masonry (URM) buildings in earthquakes comprises both out-of-plane failures and in-plane failures of the walls (Liu and Crewe, 2020). Owing to the weak out-of-plane behavior of such walls or inadequate diaphragms or diaphragm-wall connections, URM buildings mostly fail when loaded in-plane (Mahmood and Ingham 2011). The out-of-plane failure could be prevented by additional structural elements. However, the overall seismic performance of URM buildings depends on the capacity of in-plane walls to safely transfer the lateral loads to foundations, providing the post-earthquake stability that is required to avoid the collapse of the entire structure (Lourenço, 1996). Shear, sliding, rocking, and toe-crushing failures are common in in-plane mechanisms. Shear and sliding failures are commonly observed in URM structures (Mustafaraj and Yardim 2018). Various strengthening techniques have been used to increase the tensile and shear strength and improve the structural performance of URM structures under seismic loading (Mustafaraj and Yardim 2018; Mustafaraj and Yardim 2019; Kalali and Kabir 2012). Filling cracks and voids by grouting, stitching of large cracks and weak areas with metallic or brick elements, external or internal post-tensioning with steel ties, shotcrete jacketing, ferro-cement, and center core are various conventional reinforcement techniques for brick masonry (Mustafaraj and Yardim 2018; Mustafaraj and Yardim 2019; Kalali and Kabir 2012). The ferro-cement jacketing technique is commonly used in concrete and masonry structures (Winokur and Rosenthal 1982).

In recent years, fiber-reinforced plaster and textile-reinforced mortar have been used for retrofitting of masonry buildings. Wang *et al*. (2006) reported that masonry walls retrofitted with glass-fiber-reinforced plaster increased the load-carrying capacity of masonry walls subjected to in-plane shear loading. Mishra *et al*. (2019), Mishra *et al*. (2020b) and Endo *et al*. (2020) reported that timber reinforcement and steel reinforcement increased the shear strength of URM specimens by 198% and 278%, respectively, compared with the unreinforced specimens in Nepalese masonry buildings.

Reinforced concrete (RC) jacketing is a retrofitting technique that involves the application of single- or double-sided RC walls or coatings (Churilov and Dumova, 2012). This technique is suitable for stone and brick masonry. Alcocer *et al*. (1996), Penazzi *et al*.(2001) and ElGawady *et al*.(2004) reported that RC jacketing improves the lateral capacity of brick masonry. Mishra *et al*. (2020a) reported that the shear strengths of double-sided steel and double-sided RC reinforcement were approximately 1.56 and 1.92 times higher, respectively, than those of the unreinforced specimens. The RC reinforcement exhibited higher strength and rigidity than the steel plate reinforcement. The initial stiffness of the RC double-sided reinforcement was approximately 1.70 times higher than that of the double-sided steel reinforcement (Mishra *et al*. 2020a).

The surface reinforcement method was employed in this study. The inside faces of external walls and most of the inner walls of the 1st and 3rdheadquarterss buildings of Kyushu University were plastered with cement mortar. The original appearance of buildings did not change when the masonry walls were reinforced from the surface on both the inside faces of external walls and most of the inner walls. Additionally, the thickness of the brick walls for both buildings was larger compared to those of the beams and slabs when they were connected to the reinforcing part with anchors. Therefore, damage could occur and the expected strength of the anchor could not be exhibited. It is more suitable to reinforce walls than beams or slabs. Moreover, it is effective to reinforce the visible parts of each floor from the inside surface without changing the beams, slabs, and walls of the floors. Furthermore, surface reinforcement is economical and easy to construct.

The mechanical properties of the unreinforced brick masonry obtained from the actual structures of the 1st and 3rd headquarters buildings of Kyushu University were investigated to obtain basic data to confirm the seismic resistance of the buildings (Koshi *et al*. 2014). Furthermore, a reinforcement method that could maintain the appearance and reduce the cost of the 1st and 3rd headquarters buildings of Kyushu University was investigated. Surface reinforcement with RC walls was selected for this study because it has higher strength and rigidity than steel plate reinforcement (Mishra *et al*. 2020a). Brick wall specimens were prepared and reinforced from the surface on one side or two sides with RC walls, and a horizontal loading experiment was carried out to confirm the reinforcing effect. In addition, the authors derived and verified an evaluation formula for the horizontal strength of brick wall specimens reinforced with RC walls.

7.2 Materials and Methods

7.2.1 Experimental Program

The inner walls of the 1st headquarters building of the University are shown in Figure 7.1a). Figure 7.1b) shows the cross-section of the wall of the actual structure. As shown in Figure 7.2, the specimen has an inverse T-shaped configuration. The upper part of the specimen represents a side of the opening, and the longer lower part is the spandrel wall. The upper part of the specimen is hereinafter referred to as the upper wall and the longer lower part is hereinafter referred to as the spandrel wall.

The bending moment is higher at the upper walls of the 1st headquarters building of Kyushu University, which is nearly double that at the spandrel wall.

A horizontal loading experiment was performed to investigate the effectiveness of the retrofitting method from the surface with RC walls on one or two sides. The experiments were conducted by the Yamaguchi Laboratory at Kyushu University, Japan to which the author belongs. The author was in charge of analyzing the data obtained from these experiments. The experiment on horizontal loading test for Japanese historical brick masonry were conducted in 2016.

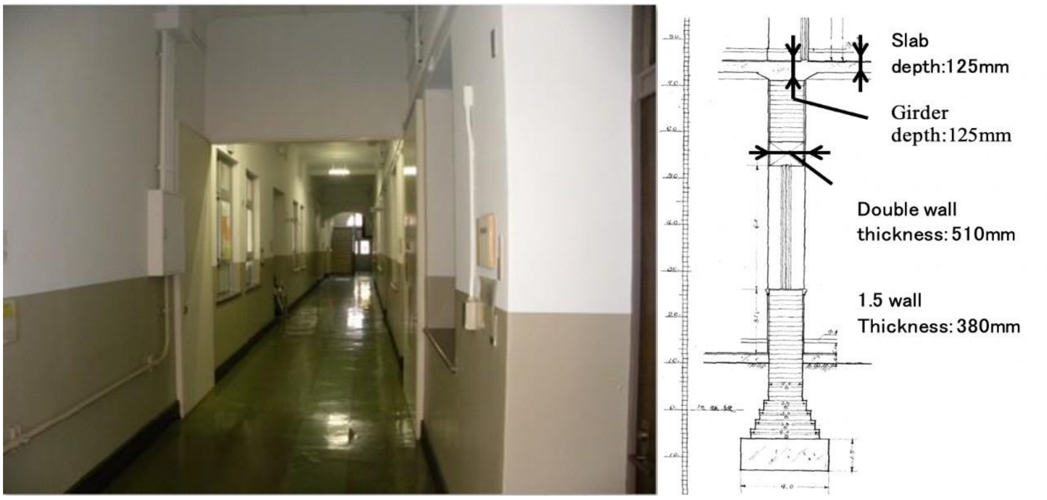

a) Inner wall of existing structure

b) Cross section of a wall of the actual structure

Figure 7.1: Walls of 1st headquarters building of Kyushu University

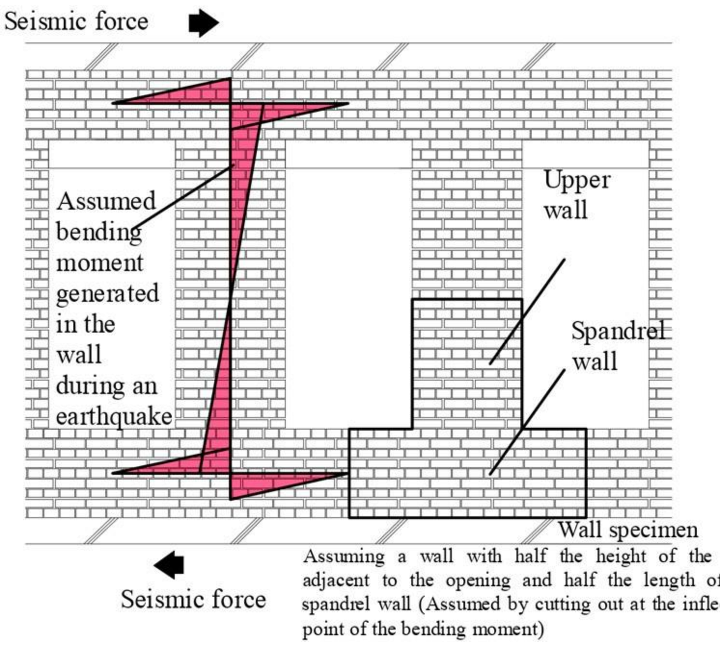

Figure 7.2: Walls around the opening

7.2.2 Mechanical properties of bricks, mortar, and reinforced concrete

The mechanical properties of the brick and mortar used for the brick walls are summarized in Table 7.1. The bricks used were non-perforated fired bricks with dimensions of 216 mm x 108 mm x 63 mm, with an average compressive strength of 22.6 N / mm^2, similar to that of the bricks used in the 1st and 3rdheadquarters buildings of the Kyushu University (Koshi *et al*. 2014). The mortar composition ratio (cement, sand, and water) for the brick wall was 1:3.25:0.614. The composition was determined through estimation and was performed using two trial mixes. For the RC walls, the ordered concrete had a nominal strength of 42 N/mm^2, a slump flow of 60 cm, and a maximum size of coarse aggregate of 13 cm. The concrete for casting the RC walls was of high fluidity. An air-entraining superplasticizer (5.5 kg/m^3) was also added. The water-cement ratio was 60%. Ordinary Portland cement was used in this study. The compressive strength of concrete for all walls was higher than 60 N/mm^2. Additives used in concrete with less water content might have led to such high strength of concrete.

The compressive strengths of mortars and concrete were determined using compression tests on 3-cylinder specimens for each wall. The mechanical properties of the reinforced concrete used for the RC wall are summarized in Table 7.1. The differences in the reinforcement and the loading methods for the five specimens are summarized in Table 7.2. The mechanical properties of the reinforcing bars were determined using tensile tests, and are summarized in Table 7.3.

Table 7.1: Mechanical properties of brick, mortar, and reinforced concrete

Specimen	Brick		Mortar		Reinforced concrete	
	Compressive strength (N/mm^2)	Young's modulus (N/mm^2)	Compressive strength (N/mm^2)	Young's modulus (N/mm^2)	Compressive strength (N/mm^2)	Young's modulus (N/mm^2)
UR01	22.6	0.52×10^4	43.3	2.34×10^4	-	-
CS01	22.6	0.52×10^4	45.1	2.56×10^4	61.6	3.79×10^4
CD01	22.6	0.52×10^4	43.3	2.34×10^4		
CS02	22.6	0.52×10^4	43.4	2.41×10^4	76.2	4.36×10^4
CD02	22.6	0.52×10^4	43.4	2.41×10^4		

Table 7.2: Reinforcement and loading method of specimens

Specimen	Reinforcement part	No.of anchors	Anchor rod ratio (%)	Twist restraint
UR01	No	0	0	Yes
CS01	One side	100	0.56	Yes
CS02	One side	100	0.56	No
CD01	Both sides	100	0.56	Yes
CD02	Both sides	60	0.33	Yes

Table 7.3: Mechanical properties of reinforcing bars

Standard	Young's modulus (N/mm²)	Yield strength (N/mm²)	Tensile strength (N/mm²)	Ultimate elongation (%)
D10(SD345)	1.84×10^5	382	594	19.2
D16(SD345)	1.85×10^5	403	585	17.9
D16(SD345)※	1.84×10^5	401	576	16.9

※ Used for specimen CD02

7.2.3 Description of test specimens

Owing to experimental limitations, all test specimens were scaled down to 3/4th of the original wall. That is, the full scale of the original wall was significantly large for the experiment, and it was difficult to conduct experiments on a full scale. The bricks were not scaled down owing to the limited period of this project and insufficient budget. Five brick wall specimens, which represented the walls around the openings in the actual structure, were prepared. Among them, one was an unreinforced masonry specimen (specimen UR01), two were reinforced by an RC wall on one side (specimens CS01 and CS02), and two were reinforced by RC walls on both sides (specimens CD0 and CD02). All the RC walls had a thickness of 110 mm. The minimum thickness required for the RC walls was 110 mm because of the rebar detailing, anchor layouts, and minimum concrete cover. The brick walls were set on the RC stub, and the reinforcement part was cut off and not embedded in the RC stub (Figure 7.5d)).

7.2.4 Arrangement of rebars and anchors

The URM walls were constructed in the laboratory. The drilling of holes and fixing of anchors on the brick wall specimens were also carried out in the laboratory and are shown in Figure 7.3. In the specimens CS01 and CS02, the anchors were embedded and placed at a depth of 295 mm and through the brick wall in the specimens CD01 and CD02. However, it was necessary to shorten the embedding length slightly because five places were accidentally penetrated when drilling the holes of the specimen CS02 (Figure 7.3c)). The laying of reinforcement and casting of RC walls are shown in Figure 7.4. The rebars were placed on the surface of the brick walls and concrete was cast. Hence, the RC walls were cast in the same laboratory.

The shapes of the rebar arrangements, anchor positions, and strain gauge positions of the five specimens are shown in Figure 7.5. Figure 7.5a) shows the front view of the UR01 specimen. Figure 7.5b) shows the reinforcement diagram of the specimens CS01 and CD01. Figure 7.5c) shows the reinforcement of the specimen CD02 along with the strain gauges attached to rebars. Figure 7.5d) shows the cross-section of the specimens CS01/CS02 (left side) and CD01/CD02 (right side). D13 bars of SD345 type were used for the anchor rods, and epoxy resin was used as an adhesive to fix the anchors. D16 bars of SD345 type were used as main rebars at the ends of the upper walls and the spandrel walls. D10 bars of SD345 type were used as the intermediate rebars in the vertical direction at the center. D10 bars of SD345 type with 90 ° hooks were used as shear reinforcement bars. As the maximum forces are at the sides of the upper walls, where significant displacement could occur, higher-diameter rebars were used as flexural reinforcement. One hundred anchors were placed in each of the specimens CS01, CS02, and CD01. However, only sixty anchors were placed in the specimen CD02. The anchor bar ratio is summarized in Table 7.3. An index showing the anchor amount is defined as the ratio of the cross-sectional area of the anchor bars to the area of the brick wall. Mishra *et al*. (2020a) investigated the behavior of reinforced masonry through the diagonal compression test where the anchor was embedded with a length of one brick edge. During the splitting in all masonry specimens for diagonal compression test, cracks were observed at the tip of the embedded anchor as shown in Figure 7.6. Therefore, in this study, the masonry wall was reinforced by penetrating the anchor rods through the brick masonry.

7.2.5 Description of test procedures

Figure 7.7 shows the loading setup. The shear span to depth ratio of the specimens was 1.20. The arrangement of the twist-restraining device is shown in Figure 7.8. An axial force of 54 kN, which was equivalent to the axial force generated on the second floor of the 1stheadquarters building of Kyushu University, was applied (compressive stress: 0.21 N/mm^2) on the upper surface of the brick masonry wall (excluding RC wall), and it was maintained at a constant level throughout the experiment. The RC wall was connected to the URM brick wall by anchors, but the axial load was not transferred to the RC wall after strengthening. This is because the RC wall is to be added after years of construction of the existing walls. Generally, the slab loads transfer the force directly to the URM brick wall. If additional loads are added after attaching the RC walls, the loads are transferred to the attached RC walls.

In this experiment, the additional load was ignored. An easy reinforcement method was considered in this experiment, wherein only the walls around the openings were strengthened. It is to be noted that, the RC walls are not connected to the RC stub with an anchor and have no support as shown in Figure 7.5d).

a) Wall specimens

b) Anchor hole drilling process

c) Position of five holes where drilling damage occurred

d) Fixing of anchors on wall specimens

e) Anchor rods after application of adhesive

Figure 7.3: Drilling of holes and fixing of anchors on wall specimens

The positions of the relative displacement meter and strain gauge on the tensile rebars are shown in Figure 7.9a) and Figure 7.9b), respectively. Strain gauges were attached to the flexural reinforcement rebars at the lower part of the upper wall, where significant displacement could occur. The loading program and loading method are shown in Figure 7.10 and Figure 7.11, respectively. For the horizontal force, the deformation angles generated at the height from the top surface of the stub to the loading point were ± 0.01, 0.025, 0.05, 0.075, 0.1, 0.2, 0.3, 0.4, 0.5, 0.75, 1.0, 1.5, and 2.0 $\times 10^{-2}$ rad. Three altered loading cycles were carried out for each deformation angle (up to 1.5×10^{-2} rad. for the specimen CS01 and up to 1.0×10^{-2} rad. for the specimen CS02). Specimen CS02 was loaded without restraining the twist in the out-of-plane direction to confirm the performance when affected by twisting. For the other specimens, loading was performed with the twist restrained in the out-of-plane direction. As shown in Figure 7.11, the horizontal load was positive when the compressive force was applied from the jack and negative when the tensile force was applied. The deformation angle was positive when the stub moved to the positive owing to the compressive force of the jack and the deformation angle was negative when the stub was displaced to the negative side by the tensile force of the jack, as shown in Figure 7.11.

Figure 7.4: Laying of reinforcement and casting of RC wall process

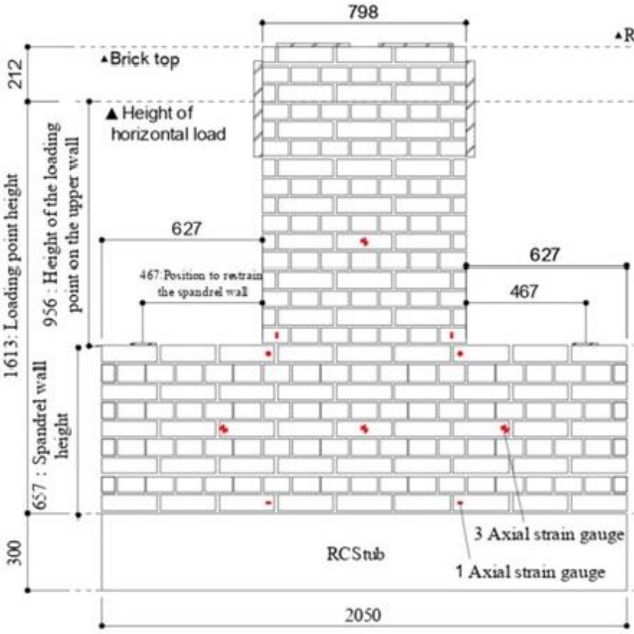

a) Specimen UR01 (front view)
reinforcement diagram

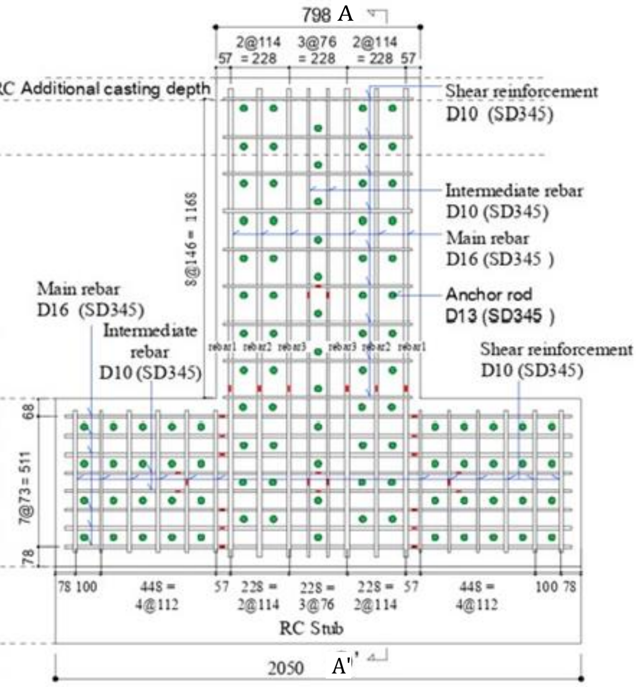

b) Specimen CS01, CD01

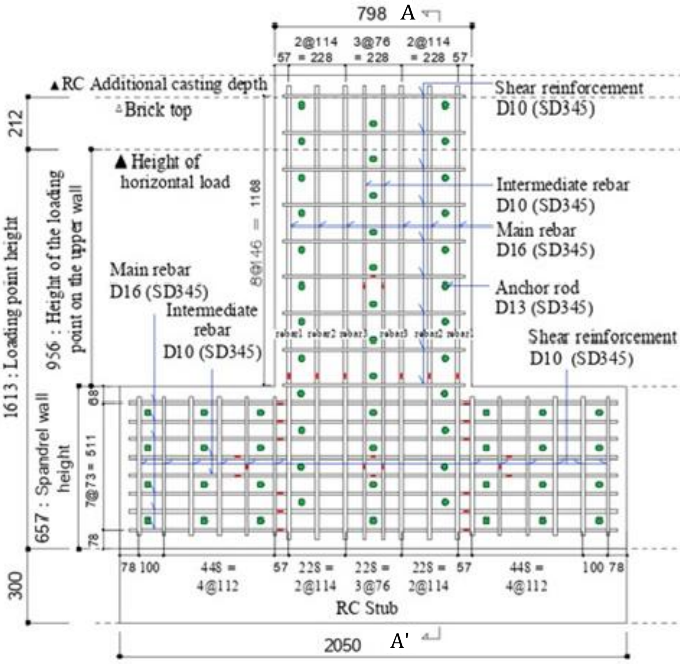

c) Specimen CD02 reinforcement diagram

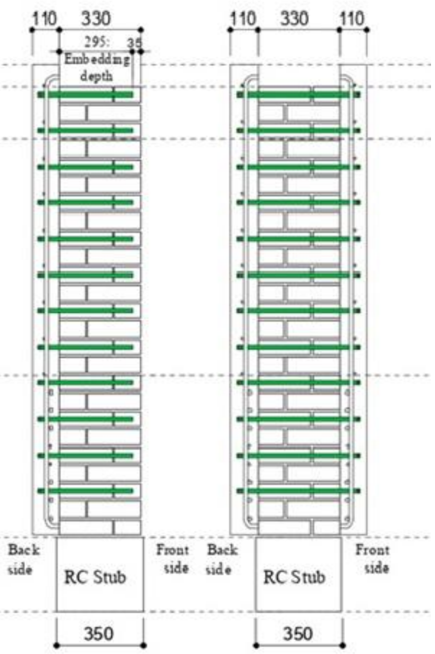

d) Cross section A - A'
(Left CS01/CS02, Right CD01/CD02)

Figure 7.5: Shape, reinforcement diagram, and strain gauge position of wall specimens
(Unit: mm)

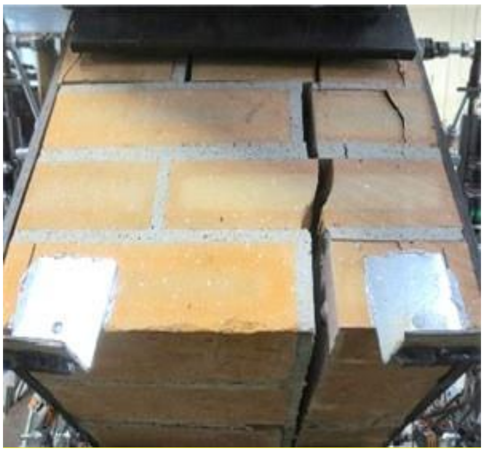

Figure 7.6: Cracks observed at the tip of the embedded anchor

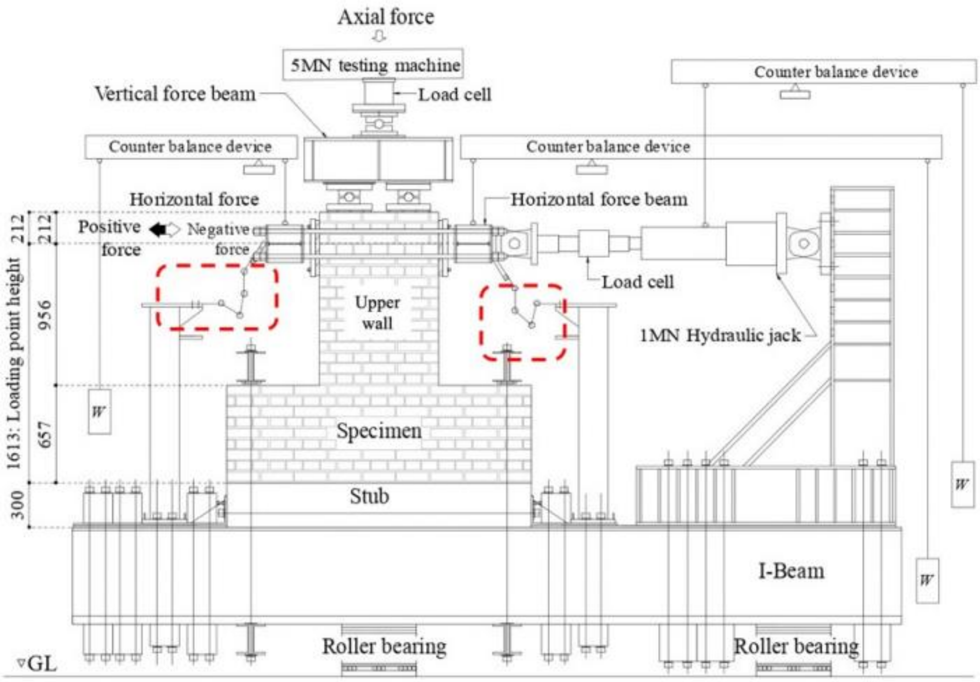

Figure 7.7: Loading setup for wall specimens (Unit: mm). Out-of-plane twisting constrain device shown in red dotted box

Figure 7.8: Twist restraining device

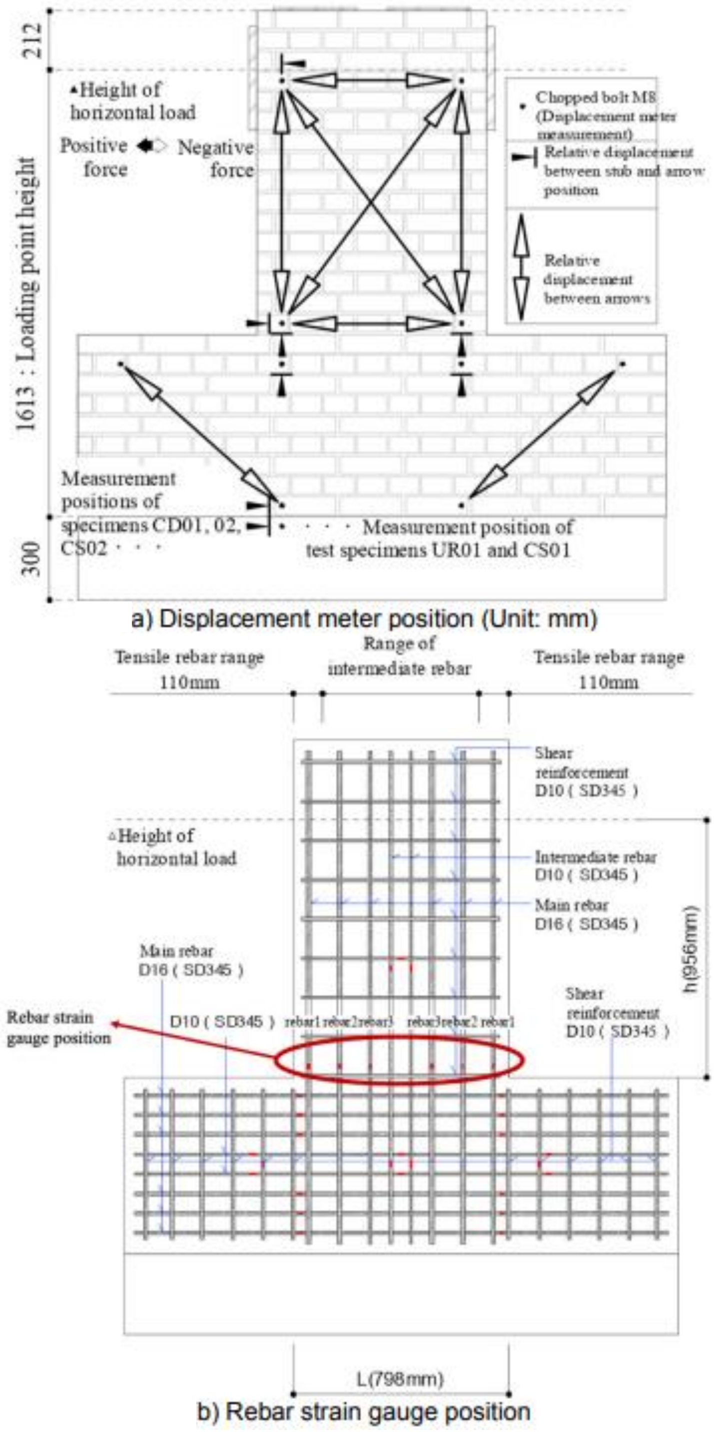

Figure 7.9: a) Displacement meter position and b) Rebar strain gauge position

Table 7.4 summarizes the axial forces before and after the RC wall was added to the 1st headquarters building of Kyushu University. The axial compressive stress summarized in Table 7.4 was obtained from the seismic diagnosis of the building at the maximum axial force position of the walls. The value 0.569 MPa was obtained by dividing the axial force (275 kN) on the cross-sectional area of the brick wall at the maximum axial force position. Higher axial loads were applied to the retrofitted specimens to determine whether the bearing capacity was safe when the retrofitted walls were added, and the weight was increased. The "minimum value of the compressive strength" in Table 7.4 was obtained from the experimental results on masonry prisms taken from some walls of the building (Specimen OPC 111; compressive strength of 6.35 N/mm^2) (Yamaguchi *et al*. 2014). As the foundation of the 1st headquarters building of Kyushu University is composed of similar brick walls whose cross-sectional area is gradually increased along the depth (Figure 7.1) it is expected that the compressive strength is equal to or higher than that of the wall; therefore, the bearing capacity would be sufficient for long-term axial forces.

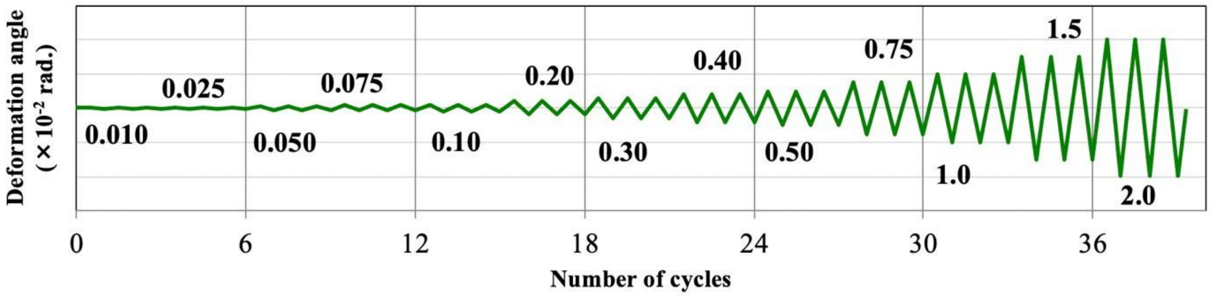

Figure 7.10: Loading program

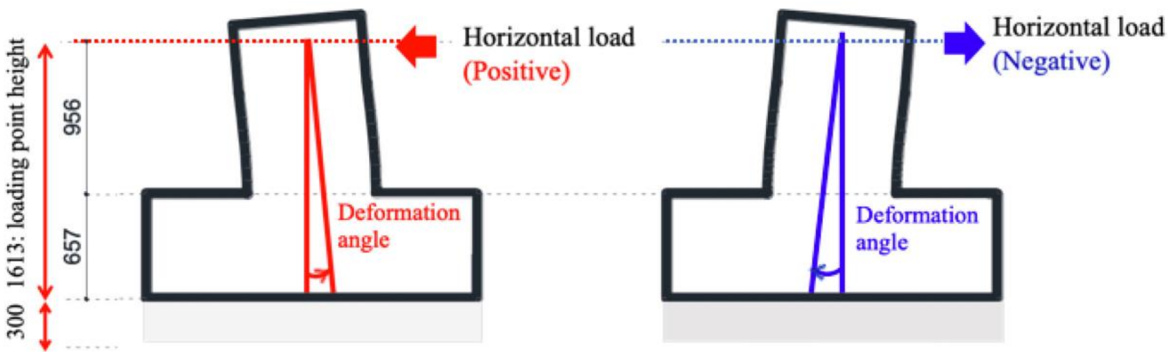

Figure 7.11: Considered deformation angle

7.3 Results and discussion

7.3.1 Experimental observations

This section summarizes the experimental observations of the behavior, crack pattern, and failure mode of the test walls subjected to horizontal cyclic loading. The relationship in terms of the horizontal load-deformation angles of each specimen is shown in Figure 7.12. The marks in the graphs show when the main rebars in the first, second, and third positions from the outside yielded. The states of the specimens after completion of the test are shown in Figure 7.13.

7.3.1.1 Specimen UR01

The maximum load of the unreinforced specimen UR01 was 31.8 kN (at $+0.041\times 10^{-2}$rad.) (Figure 7.12a)). On the positive loading direction of the loading cycle $+0.025\times10^{-2}$ rad., bending cracks occurred in the horizontal joint on the lower surface of the first bricklayer of the upper wall. In the negative direction of the same loading cycle, the bending cracks occurred in the horizontal joint on the upper surface of the first bricklayer. On the positive loading direction of the loading cycle $+0.050 \times 10^{-2}$ rad., the bending cracks occurred in the horizontal joint on the upper surface of the first bricklayer (Figure 7.13a)). In the subsequent larger deformation cycles, the second and higher layers of the wall rotated rigidly around its bottom.

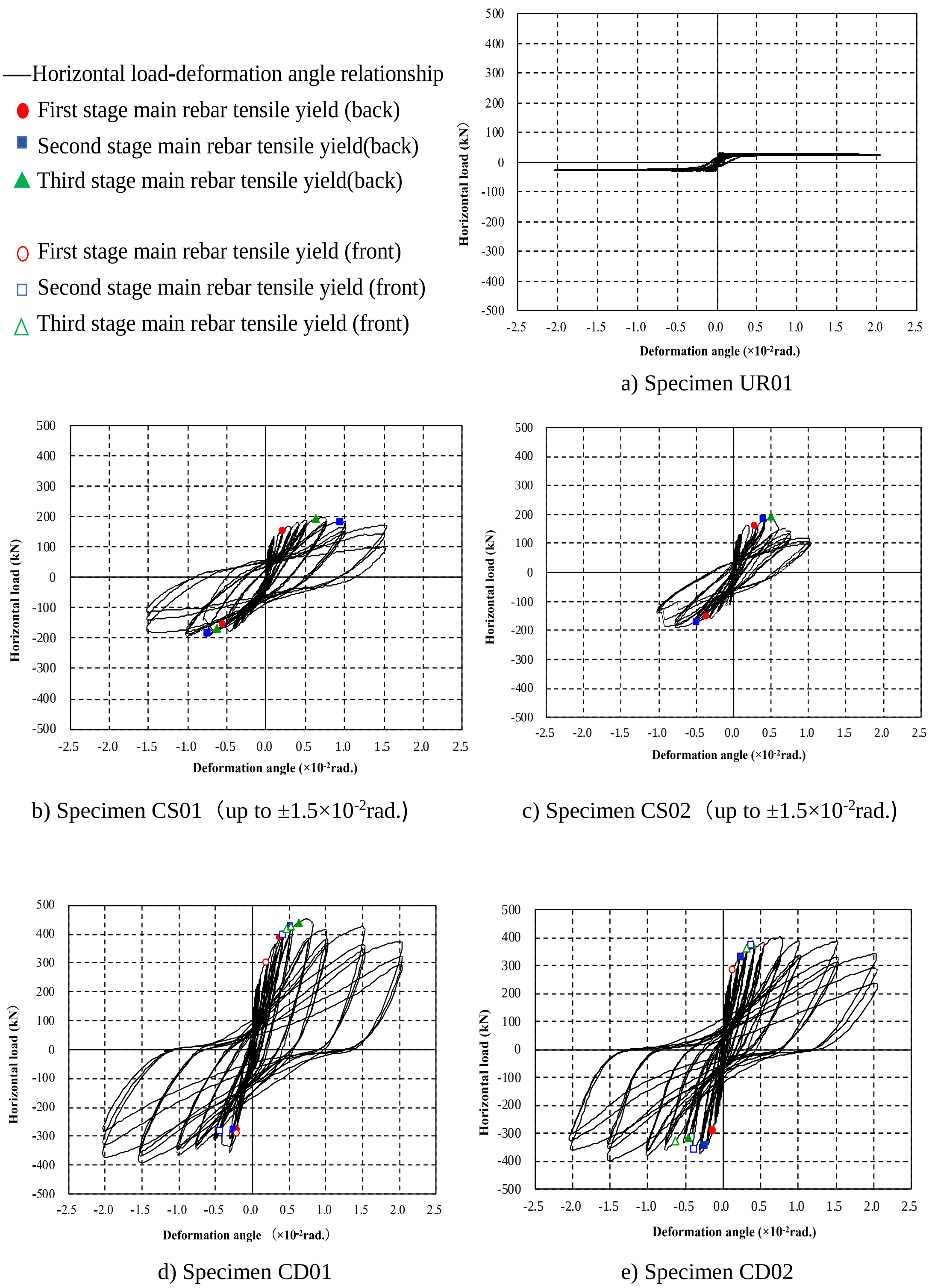

Figure 7.12: Horizontal load-deformation angle relationship of wall specimens

7.3.1.2 Specimen CS01

The maximum load of specimen CS01 was +196 kN (at $+0.71\times10^{-2}$ rad.), which was 6.2 times higher than that of the specimen UR01 (Figure 7.12b)). On the negative loading direction of the loading cycle -0.050×10^{-2} rad., bending cracks occurred on the lower surface of the first brick layer on the unreinforced surface (front) of the upper wall. On the positive loading direction of the loading cycle +0.30×10^{-2} rad., step-like cracks occurred on the surface of the masonry (Figure 7.13b), left side). In addition, bending cracks occurred on the reinforcing surface (back surface) at the bottom of the upper wall. After a cycle of ±0.75to 1.0×10^{-2} rad., bending cracks were developed on the reinforcing surface at the bottom of the upper wall (Figure 7.13b), right side) and diagonal cracks were observed on the reinforcing surface. At ± 1.5 × 10^{-2} rad. cycle, crushing in the concrete at the bottom of the upper wall was observed.

7.3.1.3 Specimen CS02

The maximum load of specimen CS02 was +194 kN (at +0.51 × 10^{-2} rad.), which was 6.1 times higher than that of specimen UR01 (Figure 7.12c)). On the positive loading direction of the loading cycle+0.10 × 10^{-2} rad., the bending cracks occurred on the lower surface of the first brick layer on the unreinforced surface (front) at the bottom of the upper wall. On the positive loading direction of the loading cycle +0.30 × 10^{-2} rad., cracks were observed diagonally on the surface of the masonry (Figure 7.13c), left side). On the positive loading direction of the loading cycle of +0.20 × 10^{-2} rad., bending cracks occurred on the reinforcing surface (back surface) at the bottom of the upper wall; furthermore, cracks progressed after the cycle of ± 0.50 × 10^{-2} rad. (Figure 7.13c), right side).

7.3.1.4 Specimen CD01

The maximum load of specimen CD01 was +453 kN (at +0.88 × 10^{-2} rad.), which was 14.2 times higher than that of specimen UR01 (Figure 7.12d)). On the positive loading direction of the loading cycle +0.20 × 10^{-2} rad., bending cracks first occurred on the reinforcing surface (back surface) at the bottom of the upper wall, and then cracks occurred on the other side and progressed in the subsequent cycles (Figure 7.13d)). In addition, crushing in the concrete was observed at the bottom of the upper wall after a cycle of +0.75 × 10^{-2} rad. The concrete cover at the toe of the upper wall started to fall off, and cracks were observed. However, the spandrel did not crack. This could be because the bending moment in the spandrel wall was nearly half that of the opening wall.

7.3.1.5 Specimen CD02

The maximum load of specimen CD02 was +402 kN (at +0.77 × 10^{-2} rad.), which was 12.6 times higher than that of specimen UR01 (Figure 7.12e)). On the positive loading direction of the loading +0.10 × 10^{-2} rad., bending cracks occurred on the reinforcing surface (front) at the bottom of the upper wall and the cracks continued to expand thereafter. Additionally, after a cycle of $+0.75 \times 10^{-2}$ rad., the concrete was crushed at the bottom of the upper wall (Figure 7.13e)).

a) Specimen UR01

b) Specimen CS01 unreinforced (left) and reinforced surface (right) with twist restraint

c) Specimen CS02 unreinforced (left) and (right)

d) Specimen CD01

e) Specimen CD02 without twist restraint

Figure 7.13: Cracks and failure mode of specimens

7.3.2 Magnitude of the maximum horizontal load for each deformation angle

Figure 7.14 shows the magnitude of the maximum horizontal load for each deformation angle of each specimen. The load of the four reinforced specimens increased even after $+0.041 \times 10^{-2}$ rad. a level at which the maximum load of the unreinforced test specimen UR01 was measured. The main bars of the walls began to yield after the loading cycle $\pm 0.20 \times 10^{-2}$ rad., and the specimens exhibited a large deformation ability until the maximum load was reached.

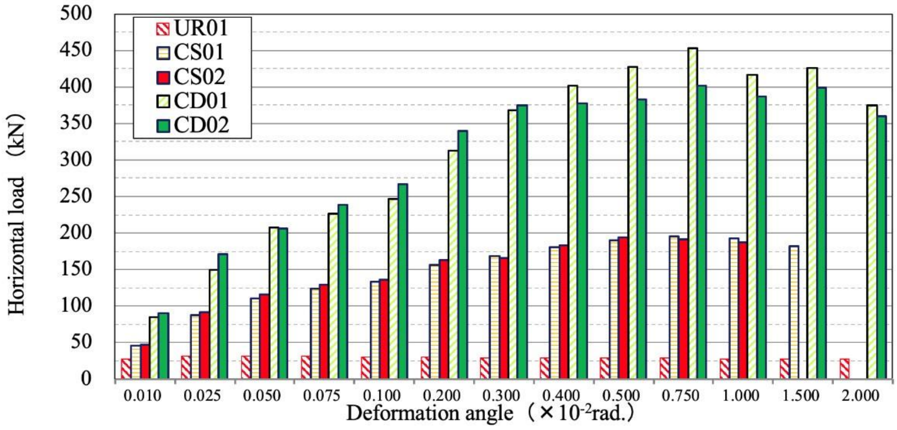

Figure 7.14: Magnitude of the maximum horizontal load for each deformation angle

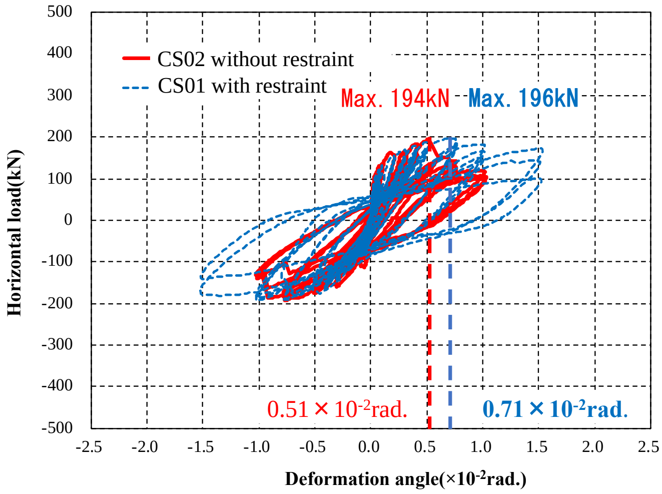

Figure 7.15: Comparison between the load-deformation curves of specimen CS01 (with restraining device) and specimen CS02 (without restraining device)

7.3.3 Effect of twist restrain

A comparison between the load-deformation curves of specimen CS01 (with a restraining device) and specimen CS02 (without a restraining device) is shown in Figure 7.15. The figure shows that the maximum loads of the specimens were similar, but that of the specimen CS02 was reached at a smaller deformation angle than that of the specimen CS01. This was attributed to the effect of twisting.

Figure 7.16 shows a conceptual diagram of the twist of the upper part of the wall. Figure 7.17a) shows the relationship between the twist-overall deformation angles of the upper part of the specimens CS01 and CS02. Figure 7.17b) shows the relationship between the twist-overall deformation angles of the upper part of the specimens CD01 and CD02.

The twist of the upper part of the single-sided reinforced specimen was significant. The upper twists of both specimens were almost similar up to a deformation angle of ± 0.40 × 10^{-2}rad. The twist of the upper part of specimen CS02 increased gradually from a deformation angle of ± 0.50 × 10^{-2}rad. The upper twist of specimen CS01 was approximately 2.2% rad. when the deformation angle of the specimen was +1.0 × 10^{-2} rad. and that of specimen CS02 was approximately 5% rad. Notably, the restraining system was slightly loose, which caused a twist in the restrained specimen (Figure 7.8). However, the twist in the restrained specimen was 2.2% rad. at the end of the experiment, whereas it was 5% rad. at the middle of the experiment.

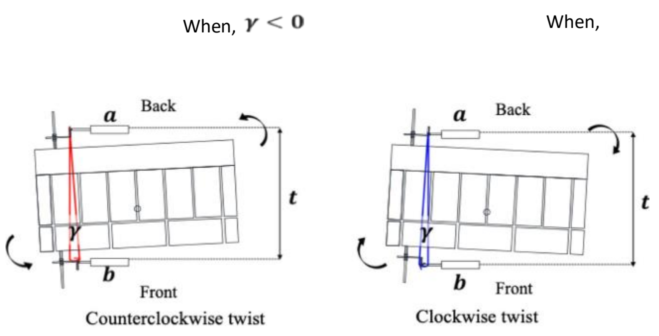

$$\gamma = \frac{a-b}{t}$$

a : : Relative displacement of theupper back

b : : Relative displacement of theupper front

t : : Distance between displacementmeters at the top of the upper wall

γ : : Twist at the top of the upperwall

Figure 7.16: Conceptual diagram of the twist of the upper part of the upper wall

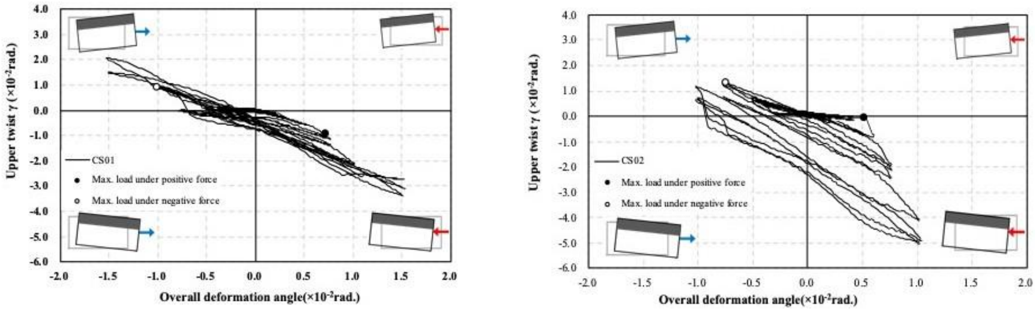

a) Single-sided reinforced specimen

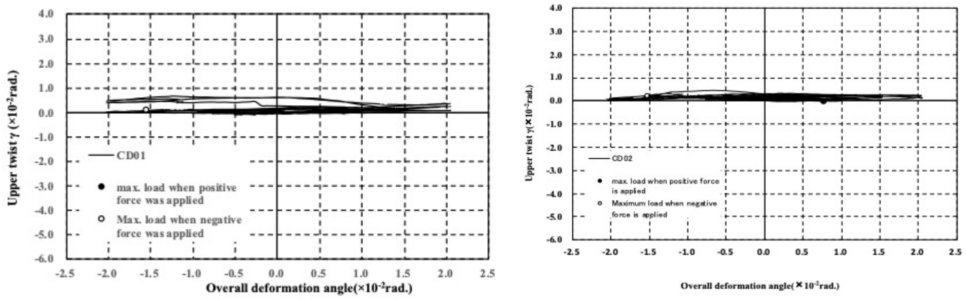

b) Double-sided reinforced specimen

Figure 7.17: Relationship between twist and the deformation angle

7.3.4 Effect of anchor's number

A comparison between the specimens CD01 (100 anchors) and CD02 (60 anchors) is shown in Figure 7.18. Even though specimen CD02 had a maximum strength approximately 11% lower than specimen CD01, it did not show any strength degradation in the deformation region ± 1.50 × 10^{-2} rad.

7.3.5 Shear deformation angle

The shear deformation angle was obtained by calculating the shear deformation from the diagonal relative displacement meters installed on the upper part of the wall. Figure 7.19 and Figure 7.20 show the relationship between the shear deformation angle and the overall deformation angle of the specimens CS02 and CD02. It can be observed that the shear deformation angle of both specimens increases with the increasing deformation angle. Additionally, the relationship horizontal load-deformation angle in Figure 7.12 indicates that the horizontal load decreases with the shear failure.

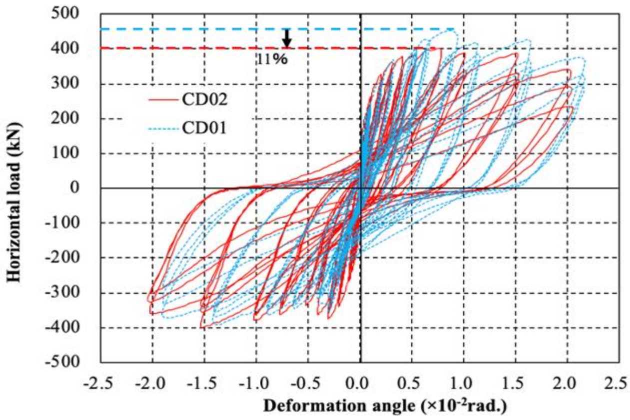

Figure 7.18: Comparison between the specimens CD01 (100 anchors) and CD02 (60 anchors)

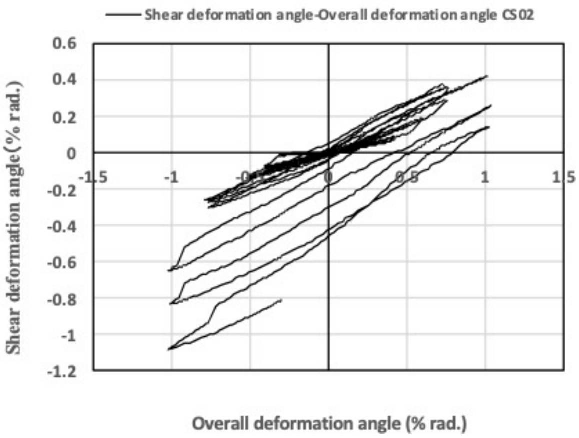

Figure 7.19: Shear deformation angle-overall deformation angle relationship for specimen CS02

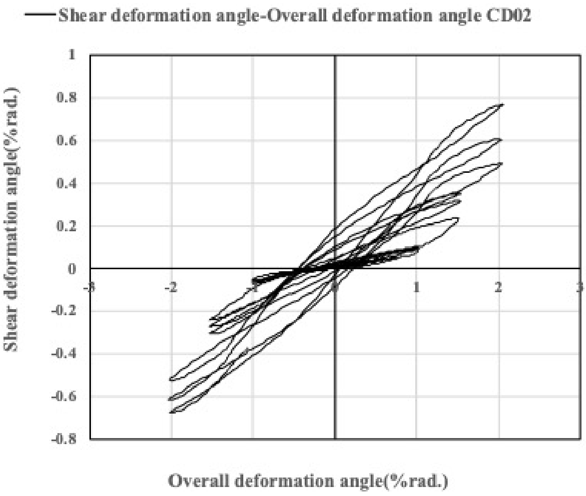

Figure 7.20: Shear deformation angle-overall deformation angle relationship for specimen CD02

7.4 Analytical study

7.4.1 Calculation method of horizontal strength of wall specimens

During the horizontal loading experiment of the wall specimen UR01, it was bent and experienced a fracture at the lower joint of the upper wall, as shown in Figure 7.13 a). Thereafter, the wall rotated as a rigid body. The rotation of the rigid body progressed until loading was completed, and the horizontal bearing capacity during the rotation of the rigid body remained constant. Therefore, the calculated horizontal load capacity (${}_bQ_u$) of the unreinforced brick wall was used as the horizontal load when the wall rotated as a rigid body around the bottom edge of the wall after the lower joint of the upper wall failed. Figure 7.21 shows the positions of the symbols used in Equation (7.1).

$$ {}_bQ_u = (N + w) \cdot L/2h \tag{7.1} $$

where,

N: Axial force acting on the upper surface of the brick masonry

w: Self-weight of the upper wall

L: Length of the upper wall

h: Height from the bottom of the upper wall to the point of application

In this study, the horizontal strength equation of the “summary of seismic diagnostic criteria (SDC) 2017 for existing RC buildings” was applied with necessary modifications.

The horizontal strength (${}_{wc}Q_y$) at the time of bending yield of the brick walls reinforced with RC walls was calculated according to Equation (7.2), based on the SDC. The value was obtained by dividing the moment of bending yield (${}_wM_y$) of the wall by the height, h. The moment ${}_wM_y$ was obtained by accumulating the moments owing to tensile rebar (1st term), intermediate rebars (2nd term), and axial force as well as self-weight of the brick wall (3rd term). Figure 7.22 shows the position of the symbols used in Equations (7.2)-(7.4) and Equation (7.6)-(7.7).

$$ {}_{wc}Q_y = {}_wM_y/h \tag{7.2} $$

$$ {}_wM_y = \left\{\sum ({}_wa_t \cdot {}_w\sigma_y)\right\} \cdot l' + 0.5\left\{\sum ({}_wa_w \cdot {}_w\sigma_{wy})\right\} \cdot l' + 0.5(N + w)l' \tag{7.3} $$

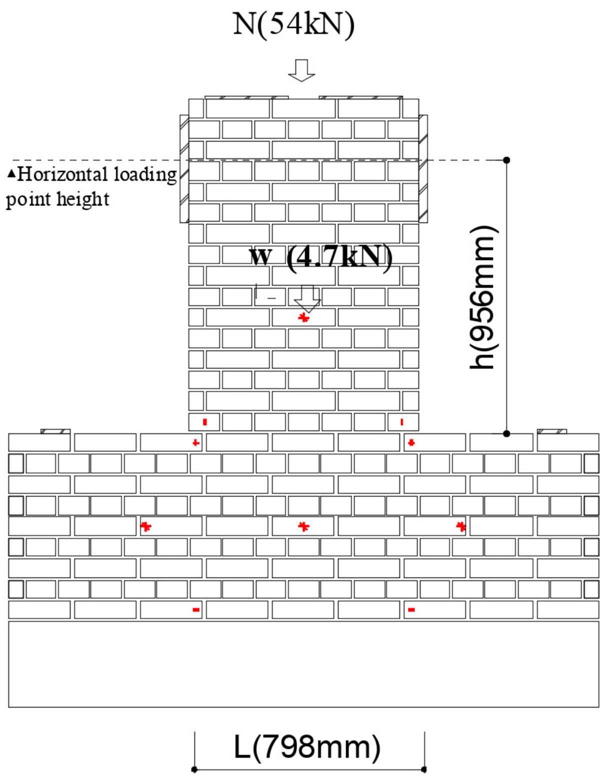

Figure 7.21: Position of symbols in Equation (7.1)

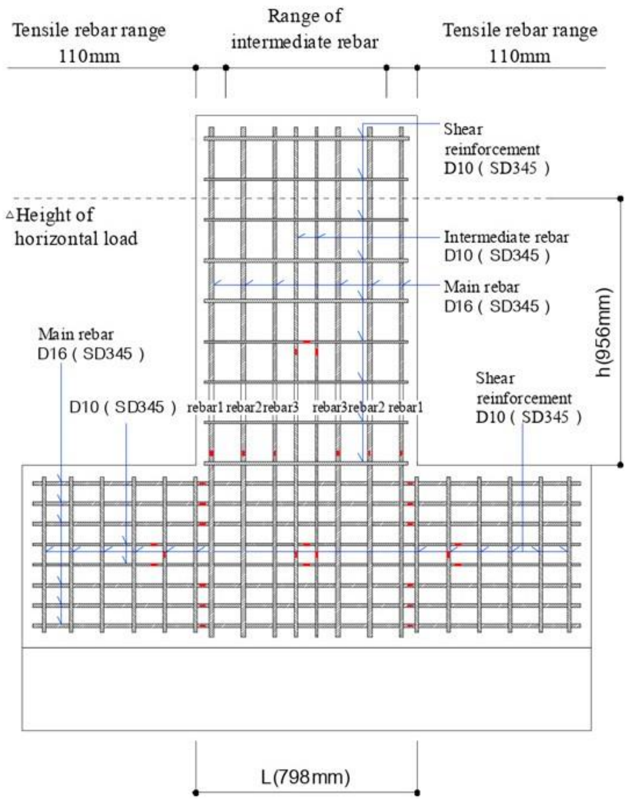

Figure 7.22: Position of symbols in Equations (7.2), (7.3), (7.4), (7.6) and (7.7)

where,

${}_{w}a_t$: The cross-sectional area of the vertical tensile rebars within the range of 110 mm from the end on the tensile side according to the SDC standard.

${}_{w}\sigma_y$: Standard yield strength (345 N/mm^2) of tensile rebars, counted 1.1 times when calculating the ultimate bending moment

l' : 0.9 times the length L of the upper wall

${}_{w}a_w$: Cross-sectional area of intermediate rebars

${}_{w}\sigma_{wy}$: Standard yield strength of intermediate rebars, counted 1.1 times (380 N/mm^2) when calculating the ultimate bending moment

The ultimate bending strength of the brick wall reinforced with RC walls (${}_{wc}Q_u$) was calculated according to Equation (7.4) by dividing the ultimate bending moment of the wall by h.

$${}_{wc}Q_u = {}_{w}M_u/h \tag{7.4}$$

${}_{w}M_u$: Ultimate bending moment of the wall, obtained by counting 1.1 times the standard yield strength of intermediate rebars ${}_{w}\sigma_y$ and ${}_{w}\sigma_{wy}$ in Equation (7.3).

The ultimate shear strength *wQsu* of the wall was calculated using Equation (7.5). As the original equation does not consider openings in the wall, it was slightly modified as presented in Equation (7.5). Notably, this equation is only for RC wall retrofit.

$${}_{w}Q_{su} = \left\{\frac{0.053 p_{te}^{0.23}(F_c+18)}{\frac{M}{(Q.l)}+0.12} + 0.85\sqrt{P_{se}.\sigma_{wy}} + 0.1\sigma_{0e}\right\}.be.je \tag{7.5}$$

Where, $P_{te} = 100a_t / (be \cdot l)$: Equivalent tensile rebar ratio (%)

a_t : Total cross-sectional area of the main rebar of the tension side

be : RC wall thickness

l : Overall length of the wall

$P_{se} = a_h / (be \cdot s)$: Equivalent lateral rebar ratio

a_h, s : Cross-sectional area of one rebar and the pitch of horizontal rebars, respectively

Fc : Compressive strength of concrete

σ_{wy} : Yield strength of the lateral rebar

σ_{0e} : Axial stress ($\sigma_{0e} \leq 8$ N / mm^2)

(In our case, it was taken as zero, as there was no axial stress on the RC wall)

je : Stress center distance i.e. 0.8l

$\frac{M}{(Q.l)}$: Shear span ratio where, $1 \leq M/(Q \cdot l) \leq 3$

Additionally, for comparison, the yield strength obtained by the tensile test of the rebars and summarized in Table 7.3 was used for calculating the ultimate strength according to the SDC standard, as shown in Equation (7.6).

$${}_{cwc}Q_u = {}_{cw}M_u / h \tag{7.6}$$

$${}_{cw}M_u = \sum ({}_w a_t \cdot {}_{tw}\sigma_y) \cdot l' + 0.5 \sum ({}_w a_w \cdot {}_{tw}\sigma_{wy}) \cdot l' + 0.5(N + w) l' \tag{7.7}$$

where,

${}_{tw}\sigma_y$: Yield strength of tensile rebar (Laboratory test result, Table 7.3)

${}_{tw}\sigma_{wy}$: Yield strength of intermediate rebar (Laboratory test result, Table 7.3)

7.4.2 Considerations for the horizontal strength of wall specimens

Table 7.5 summarizes the experimental results for wall specimens, while Table 7.6 summarizes a comparison between the ultimate shear strength and ultimate bending strength. The calculation results indicate that the bending strength was low and, therefore, critical (Table 7.6). Table 7.7 summarizes a comparison between the calculated horizontal strength and the experimental value, while Table 7.8 summarizes the values used to calculate the horizontal strength.

The calculated yield strength at the rotation of the rigid body, which was determined using Equation (7.1) was similar to the experimental value. The yield bending strength calculated using Equation (7.2) was over the experimental value by 22% to 33%. Likewise, the calculated ultimate bending strength using Equation (7.4) was similar to the experimental value; however, the ultimate strength of the single-sided reinforced specimen was over the experimental value by 8 to 11%. Furthermore, the calculated value of the ultimate bending strength using Equation (7.6) was similar to the calculated value using Equation (7.4), although the ratio of the calculated value to the experimental value was large because the stress of the rebar was high. Therefore, the authors concluded that the ultimate strength of the double-sided reinforcement could roughly be obtained by Equation (7.4) and Equation (7.6).

Here, to investigate the difference between the calculated and experimental values, the actual moment during yielding and the ultimate moment due to the tensile rebars and intermediate rebars at the bottom of the upper wall were compared with the corresponding calculated values. The results are summarized in Table 7.9, Table 7.10, and Table 7.11.

In addition, Figure 7.23 and Figure 7.24 show the strain distribution and the axial force distribution at the bottom of the upper wall. For the strain distribution, the value obtained from the strain gauge attached to the rebar at the bottom of the upper wall is presented in Figure 7.9 b); values for the part where the strain gauge was not attached were obtained via linear interpolation. During yielding, the strain at time ② (i.e., during the first tensile yield of the main rebar at the bottom of the upper wall) in Table 7.5 was obtained, and the strain at the maximum load ③ in Table 7.5 was determined for the ultimate. The axial force of the rebar was calculated using the yield strength for all the rebars whose strain exceeded the ultimate yield strain. The experimental moment was calculated as the moment around the center of gravity of the compressive force. The distances between the stress centers listed in Table 7.9, Table 7.10, and Table 7.11 were calculated as the distances at which the sum of the moments of each rebar and the moment of the resultant force were equal, and they were expressed by l'. For those whose neutral axis did not appear at the end owing to the residual strain, the position of the center of gravity of the compressive force, obtained from the distance between the stress centers assumed in the calculation formula, was used. The first term of the tensile rebar in Equation (7.3) tends to underestimate the moment because of the actual tensile rebar during yielding; however, the distance between the stress centers was slightly overestimated (Table 7.9). Moreover, the stress levels of the rebars were underestimated. For the second term of the intermediate rebar in Equation (7.3), the actual distance between the stress centers was larger than that in the calculation formula; however, the moment owing to the actual intermediate rebar during yielding was overestimated by 50% to 157%. The second term of the intermediate rebar in Equation (7.7) was slightly similar to the actual moment because the intermediate rebar was used for double-sided reinforcement; however, it was overestimated by 12% to 19% for the single-sided reinforcement. According to Table 7.11, the ratio of the calculated values to the experimental values increased owing to the higher stress of the rebars in the tensile rebar section (first term) and the intermediate rebar section (second term) in Equation (7.7). This tendency was similar to that indicated by Equation (7.4). For the double-sided reinforcement, almost all the rebars up to the intermediate rebars yield even under the actual stress distribution, and the distance between the stress centers was similar to that in the calculation formula. Therefore, the actual situation could be reflected. However, for the single-sided reinforcement, only a part of the intermediate rebar yields; hence, the calculation formula overestimates the stress of the intermediate rebar.

In conclusion, we established that the calculated value of the bending moment based on the tensile rebar was relatively similar to the bending strength. The effect of the intermediate rebar at the ultimate was greater than its effect on the yield, and the formula overestimates the stress level of the intermediate rebar. The distance between the stress centers was slightly underestimated; for double-sided and single-sided reinforcements, the effects of the intermediate rebars at the ultimate differed slightly.

Table 7.4: Maximum values of axial forces and compressive stresses before and after the addition of RC walls to the URM walls of the 1st headquarters building of Kyushu University

	Current status Maximum value	Reinforced on one side	Reinforced on both sides	Minimum value of compressive strength
Corresponding Axial force (kN)	275	307	339	-
Compressive stress (N/mm^2)	0.569	0.636	0.702	-
Compressive strength (N/mm^2)	-	-	-	6.35

Table 7.5: Results of horizontal loading test of wall specimens

Specimen		① Horizontal load when the opening wall rotates rigidly (kN)	② Horizontal load during the first tensile yield of the main bar of the opening wall (kN)	Deformation angle at the time of the tensile yield (×10^{-2}rad.)	③ Max. load (kN)	Deformation angle at maximum load (×10^{-2}rad.)
UR01	Positive	27.5	-	-	31.8	0.041
	Negative	-28.2			-29.8	-0.087
CS01	Positive	-	157	0.23	196	0.714
	Negative		-160	-0.57	-193	-1.007
CS02	Positive	-	159	0.27	194	0.509
	Negative		-154	-0.37	-192	-0.752
CD01	Positive	-	302	0.18	453	0.879
	Negative		-277	-0.22	-392	-1.394
CD02	Positive	-	280	0.13	402	0.770
	Negative		-288	-0.13	-400	-1.519

Table 7.6: Comparison between the ultimate shear strength Equation (7.5) and ultimate bending strength Equation (7.4)

Specimens	Ultimate shear strength ${}_{w}Q_{su}$ (kN)	Ultimate bending strength ${}_{wc}Q_{u}$ (kN)
CS01	252	212
CS02	252	212
CD01	567	402
CD02	567	402

Table 7.7: Comparison between the calculated horizontal strength and the experimental value

Specimen		$_{b}Q_{u}$ (kN)	$_{b}Q_{u}$ / ① Exp. Value	$_{wc}Q_{y}$ (kN)	$_{wc}Q_{u}$ (kN)	$_{cwc}Q_{u}$ (kN)	$_{wc}Q_{y}$ / ②Exp. Value	$_{wc}Q_{u}$ / ③Exp. Value	$_{cwc}Q_{u}$ / ③Exp. Value
UR01	Positive	24.4	0.89	-	-	-	-	-	-
	Negative		0.87						
CS01	Positive	24.4	-	195	212	223	1.24	1.08	1.14
	Negative		-				1.22	1.10	1.16
CS02	Positive	24.4	-	195	212	223	1.23	1.10	1.15
	Negative		-				1.27	1.11	1.16
CD01	Positive	24.4	-	368	402	424	1.22	0.89	0.94
	Negative		-				1.33	1.03	1.08
CD02	Positive	24.4	-	368	402	422	1.31	1.00	1.05
	Negative		-				1.28	1.01	1.05

Note: Horizontal strength was calculated using Equations (7.1), (7.2), (7.4) and (7.6), For experimental value refer to Table 7.5.

Table 7.8: Values used to calculate the horizontal strength

Specimen	N (kN)	w (kN)	L (mm)	h (mm)	$_{w}a_{t}$ (mm^2)	$_{w}\sigma_{y}$ (N/mm^2)	$_{tw}\sigma_{y}$ (N/mm^2)	$_{w}a_{w}$ (mm^2)	$_{w}\sigma_{wy}$ (N/mm^2)	$_{tw}\sigma_{wy}$ (N/mm^2)
UR01	54.0	4.7	798.0	956.0	-	-	-	-	-	-
CS01	54.0	4.7	798.0	956.0	199.0	345.0	403.0	199,71.3	345.0	382.0
CS02	54.0	4.7	798.0	956.0	199.0	345.0	403.0	199,71.3	345.0	382.0
CD01	54.0	4.7	798.0	956.0	199.0	345.0	403.0	199,71.3	345.0	382.0
CD02	54.0	4.7	798.0	956.0	199.0	345.0	401.0	199,71.3	345.0	382.0

Table 7. 9: Comparison between the calculated value for the moment of the upper wall during yield in Equation (7.3) with the experimental value

Specimen		④ Total moment by tensile rebars (kN-m)	⑤ Total moment by intermediate rebars (kN-m)	④' Eq.(3) first item (kN-m)	⑤' Eq.(3) second item (kN-m)	④' Calculated value / ④Exp. Value	⑤' Calculated value / ⑤Exp. Value	Actual tensile rebar stress center-to-center distance (mm)	Actual distance between intermediate rebar stress centers (mm)	Ave. of the left term
CS01	Positive	55.3	45.3	49.2	116	0.89	2.57	0.96 l'	0.62 l'	0.61 l'
	Negative	52.4	76.3	49.2	116	0.94	1.52	0.91 l'	0.60 l'	
CS02	Positive	56.3	77.3	49.2	116	0.87	1.50	0.98 l'	0.62 l'	
	Negative	55.5	68.0	49.2	116	0.89	1.71	0.97 l'	0.62 l'	
CD01	Positive	105	93.3	98.4	232	0.94	2.49	0.96 l'	0.59 l'	0.63 l'
	Negative	102	101.9	98.4	232	0.97	2.28	0.96 l'	0.65 l'	
CD02	Positive	104	134	98.4	232	0.94	1.73	0.97 l'	0.64 l'	
	Negative	109	120	98.4	232	0.91	1.93	0.96 l'	0.62 l'	

Note:
Equation (7.3) First term $\{\sum({}_{w}a_{t}\cdot{}_{w}\sigma_{y})\}\cdot l'$
Equation (7.3) Second term $0.5\{\sum({}_{w}a_{w}\cdot{}_{w}\sigma_{wy})\}\cdot l'$

Table 7.10: Comparison between the calculated value of the moment of the upper wall at the ultimate point in Equation (7.4) with the experimental value

Specimen		⑥ Total moment by tensile reinforcing rebar (kN-m)	⑦ Total moment by intermediate reinforcing rebars (kN-m)	⑥' first term *wMu* (kN-m)	⑦' second term *wMu* (kN-m)	⑥' Calculated value / ⑥ Exp. Value	⑦' Calculated value / ⑦ Exp. Value	Actual tensile rebar stress center-to-center distance (mm)	Actual distance between intermediate rebar stress centers (mm)	Avg. of the left term
CS01	+ve	55.9	113	54.1	128	0.97	1.13	0.97 l'	0.57 l'	0.61 l'
	-ve*	57.4	111	54.1	128	0.94	1.15	1.00 l'	0.69 l'	
CS02	+ve	56.4	114	54.1	128	0.96	1.12	0.98 l'	0.60 l'	
	-ve	55.2	108	54.1	128	0.98	1.19	0.96 l'	0.59 l'	
CD01	+ve	113	266	108	255	0.96	0.96	0.98 l'	0.53 l'	0.55 l'
	-ve*	115	282	108	255	0.94	0.91	1.00 l'	0.52 l'	
CD02	+ve*	114	257	108	255	0.95	0.99	1.00 l'	0.60 l'	
	-ve*	114	275	108	255	0.95	0.93	1.00 l'	0.54 l'	

* Since the position of the neutral axis is unknown, the position of the center of gravity of the compressive force is used instead.
Note:First term *wMu* $\{\sum({}_{w}a_{t}\cdot{}_{w}\sigma_{y})\}\cdot l'$ Refer to Equation (7.4)
Second term *wMu* $0.5\{\sum({}_{w}a_{w}\cdot{}_{w}\sigma_{wy})\}\cdot l'$ Refer Equation (7.4)
Avg. stands for average

Table 7.11: Comparison between the calculated value of the moment of the opening wall at the ultimate in Equation (7.7) with the experimental value

Specimens		⑧' Eq. (7) first term $\sum ({}_{w}a_{t} \cdot {}_{tw}\sigma_{y}) \cdot l'$ (kN-m)	⑨' Eq. (7) second term $0.5 \sum ({}_{w}a_{w} \cdot {}_{tw}\sigma_{wy}) \cdot l'$ (kN-m)	⑧' Calculated value / ⑥ Exp. Value	⑨' Calculated value / ⑦ Exp. value
CS01	Positive	57.4	134	1.03	1.19
	Negative*	57.4	134	1.00	1.21
CS02	Positive	57.4	134	1.02	1.18
	Negative	57.4	134	1.04	1.25
CD01	Positive	115	269	1.02	1.01
	Negative*	115	269	1.00	0.95
CD02	Positive*	114	268	1.00	1.04
	Negative*	114	268	1.00	0.98

* Since the position of the neutral axis is unknown, the position of the center of gravity of the compressive force is used instead.

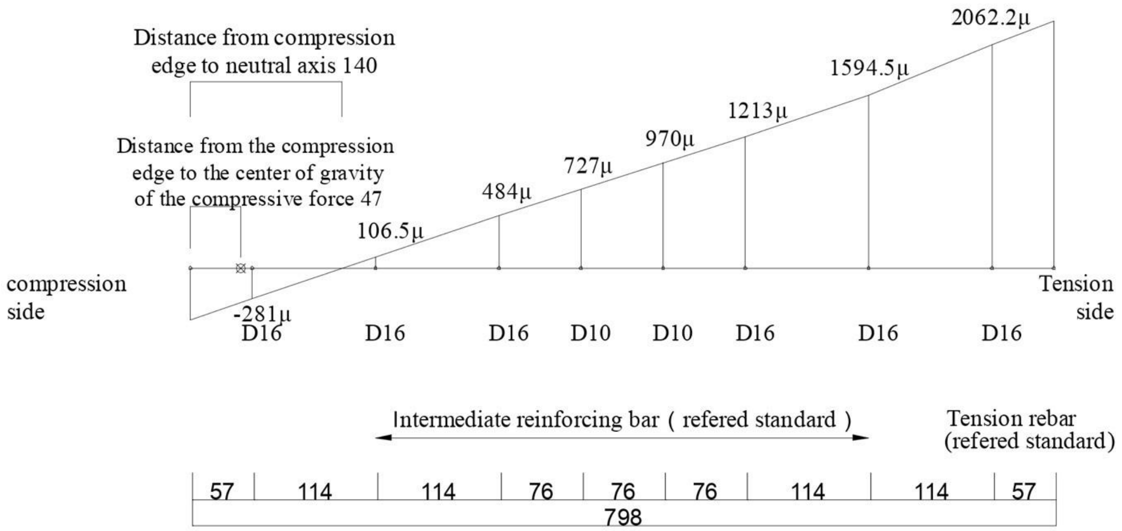

Figure 7.23: Conceptual diagram of strain distribution at the lower part of the upper wall

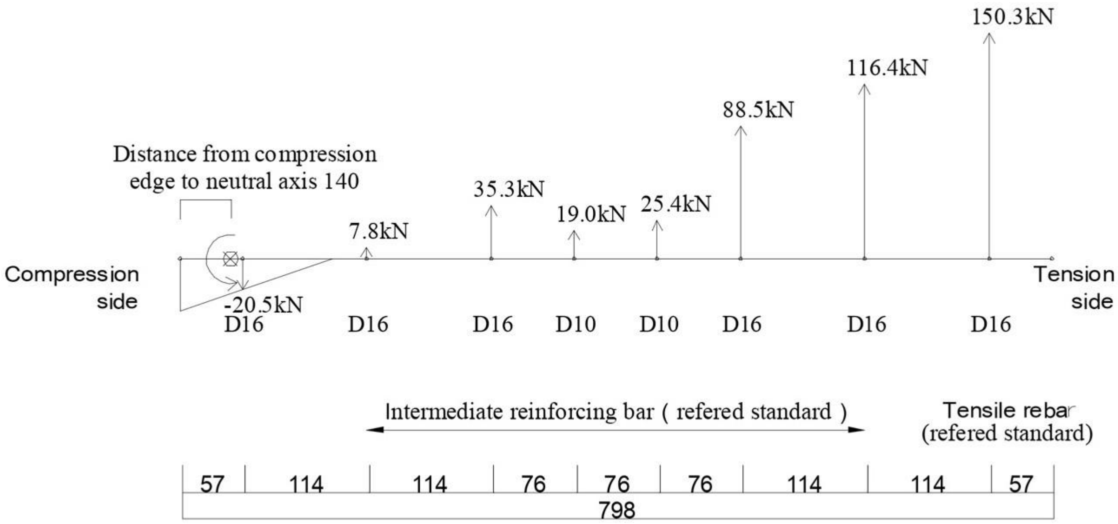

Figure 7.24: Conceptual diagram of axial force distribution
at the lower part of the upper wall

7.4.3 Proposed formula for calculating the horizontal strength of wall specimens

Based on the actual situation, the following points were summarized:

- The calculation formula for tensile rebars was relatively consistent with the actual situation, and using the yield strength affords similar results.
- The effect of the intermediate rebar was greater at the ultimate than at the yield.
- The existing calculation formula overestimates the stress of an intermediate rebar.
- The existing calculation formula slightly underestimates the distance between the stress centers of the intermediate rebars.
- For double-sided and single-sided reinforcements, the influences of the intermediate rebar at the ultimate end differ slightly.

Based on the above calculations, the authors propose a calculation formula that can reflect the actual conditions. The horizontal bearing force (${}_{swc}Q_y$) during the bending yield of the brick wall reinforced with the proposed RC wall was calculated according to Equation (7.8) by using Equation (7.9) for the yield bending moment of the bearing wall.

$$ {}_{swc}Q_y = {}_{sw}M_y / h \tag{7.8} $$

$$ {}_{sw}M_y = \left\{ \sum ({}_{w}a_t \cdot {}_{tw}\sigma_y) \right\} \cdot l' $$

$$ +0.6 \left\{ \sum_{i=1}^{n} ({}_{w}a_w \cdot \alpha_i \cdot {}_{tw}\sigma_{wy}) \right\} \cdot l' + (N + w) \cdot L/2 \tag{7.9} $$

where

α_i : Reduction coefficient of the yield strength of the intermediate rebar in the i-th stage from the tension side when calculating the yield bending moment, based on the actual strain distribution.

n : Number of intermediate rebars.

The distance between the stress centers of the intermediate rebar was considered as 0.6*l'* instead of 0.5*l'*.

As the formula for the bending strength of the wall in the SDC involves obtaining the ultimate strength, it is possible that the stress center distance of 0.5, used in the formula, is determined based on the stress distribution at the ultimate state, where the intermediate rebars also yield. Therefore, we considered adopting a larger value when the rebars at the edge of the wall yield; thus, 0.6 was used for the distance in this study.

In addition, ${}_{swc}Q_u$ during the ultimate bending of the brick wall reinforced with the proposed RC wall was calculated according to Equation (7.10) by using Equation (7.11) for the ultimate bending moment of the bearing wall.

$$ {}_{swc}Q_u = {}_{sw}M_u / h \tag{7.10} $$

$$ {}_{sw}M_u = \left\{ \sum ({}_{w}a_t \cdot {}_{tw}\sigma_y) \right\} \cdot l' $$

$$ +0.5 \left\{ \sum_{i=1}^{n} ({}_{w}a_w \cdot \beta_i \cdot {}_{tw}\sigma_{wy}) \right\} \cdot l' + (N + w) \cdot L/2 \tag{7.11} $$

Where,

β_i : Reduction coefficient of the yield strength of the intermediate rebar in the i-th stage from the tension side when calculating the ultimate bending moment, as shown in Figure 7.25.

β_i is also based on the actual strain distribution. In the equation, the distance between the stress centers of the intermediate rebars (0.5 l') remained constant.

Figure 7.25 shows the graph for obtaining the reduction coefficients α and β, where α denotes the yield and β denotes the ultimate value. Figure 7.25 shows the amount of tensile stress exerted by the intermediate rebar; in the figure, the vertical axis indicates that it has yielded and the horizontal axis represents the location of the rebar. Zero on the left end denotes the position of the tensile rebar at the end of the upper wall. The value of β depends on the RC reinforcement method, i.e., whether single-sided or double-sided reinforcement is employed. When determining the reduction coefficients α and β, the average value of the ratio of the actual stress to the yield strength of the intermediate rebar of each specimen was considered; the average value was employed to determine the reference value, as shown in Figure 7.25. Figure 7.25 shows the actual strain distribution and the strength expression rate of the intermediate rebars.

The coefficient of the stress center distance of the intermediate rebar was determined using the average value of the actual stress center distances listed in Table 7.9 and Table 7.10 as a reference. Table 7.12 summarizes the comparison between the calculated values obtained using the proposed formula and the experimental values. Although the proposed formula underestimated the yield strength of the double-sided reinforcement specimen, it afforded values similar to the experimental values.

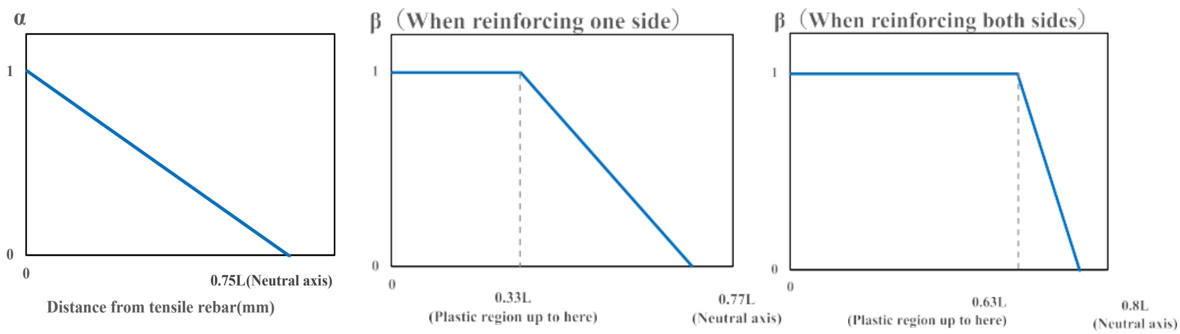

Figure 7.25: Graph for calculating reduction coefficients (α and β)

Table 7.12: Comparison between the calculated value obtained using the proposed formula Equation (7.8) and Equation (7.10) and the experimental value

Specimens		$_{swc}Q_y$ (kN)	$_{swc}Q_u$ (kN)	$_{swc}Q_y$ / ② Exp. Value	$_{swc}Q_u$ / ③ Exp. Value
UR01	Positive	-	-	-	-
	Negative				
CS01	Positive	157	178	1.00	0.91
	Negative			0.98	0.92
CS02	Positive	157	178	0.99	0.92
	Negative			1.02	0.93
CD01	Positive	290	396	0.96	0.88
	Negative			1.05	1.01
CD02	Positive	289	394	1.03	0.98
	Negative			1.00	0.99

7.5 Conclusions

In this study, a loading experiment was carried out to investigate the reinforcing effect on URM walls. In addition, a horizontal strength evaluation formula of a brick wall specimen reinforced with an RC wall was derived and verified. The following conclusions were obtained:

1. The results of the horizontal loading test indicated that the maximum load of specimens reinforced with RC walls from one side was 6.1-6.2 times higher than that of unreinforced specimens. Similarly, the maximum loads of the specimens reinforced with RC walls from both sides were 12.6-14.2 times higher than that of the unreinforced specimen.
2. The maximum loads of the two single-sided reinforced specimens were similar; however, CS02 exhibited a maximum load with a smaller deformation angle than CS01 owing to the effect of twisting.
3. The maximum horizontal strength of specimen CD02 (60 anchors) is approximately 11% lower than that of specimen CD01 (100 anchors). However, the strength was maintained without degradation to a large deformation level.
4. The term of the tensile rebars in the calculation formula based on the SDC standard was relatively consistent with the actual situation, and using the actual yield strength of the steel bars gave closer values to test results.
5. The effect of the intermediate rebar was more significant at the ultimate than at the yield.
6. The calculation formula based on the SDC standard overestimated the stress of the intermediate rebar and slightly underestimated the distance between the stress centers.

7. The strains generated in the intermediate rebars at the ultimate level were larger when both sides were reinforced than those of the intermediate rebars when one side was reinforced.
8. The values calculated using the proposed formula based on the actual strain distribution were highly similar to the experimental values.

References

Alcocer, S. M., Ruiz, J., Pineda, J. A., andZepeda, J. A. (1996). "Retrofitting of confined masonry walls with welded wire mesh." *Proceedings of the Eleventh World Conference on Earthquake Engineering*.

Bhattacharya, S., Nayak, S., and Dutta, S. C. (2014). "A critical review of retrofitting methods for unreinforced masonry structures." *International Journal of Disaster Risk Reduction*, **7**, 51-67.

Churilov, S., and Dumova-Jovanoska, E. (2012). "Analysis of masonry walls strengthened with RC jackets." *15th World Conference on Earthquake Engineering, Lisbon, Portugal*.

ElGawady, M., Lestuzzi, P., and Badoux, M. (2004). "A review of conventional seismic retrofitting techniques for URM." *13th International Brick and Block Masonry Conference* (pp. 1-10).

Endo, Y., Yamaguchi, K., Hanazato, T., and Mishra, C. (2020). "Characterisation of mechanical behavior of masonry composed of fired bricks and earthen mortar."*Engineering Failure Analysis*, **109**, 104280.

Kalali, A., and Kabir, M. Z. (2012). "Experimental response of double-wythe masonry panels strengthened with glass fiber reinforced polymers subjected to diagonal compression tests."*Engineering Structures*, **39**, 24-37.

Koshi, M., Ishihara Y.,Yamaguchi, K., and Ninakawa, T. (2014). "Mechanical properties of brick masonry that composes the headquarters building of Kyushu University, Part 2, Part 3." *Architectural Institute of Japan, Summaries of Technical Papers of Annual Meetings*, **C-2**, 843- 846. (In Japanese)

Liu, Z., and Crewe, A. (2020). "Effects of size and position of openings on the in-plane capacity of unreinforced masonry walls." Bulletin of Earthquake Engineering, 18 (10), 4783-4812.

Lourenço, P. B. (1996). "Computational strategies for masonry structures." PhD Thesis. Delft University of Technology, Delft, Netherlands.

Mahmood, H., and Ingham, J. M. (2011). "Diagonal compression testing of FRP-retrofitted unreinforced clay brick masonry wallettes*." Journal of Composites for Construction*, **15**(5), 810-820.

Mishra, C., Yamaguchi, K., Araki, K., and Ninakawa, T. (2020a). "Diagonal Compression Test of the Brick Masonry Reinforced on the Surface with Steel Plates or RC Walls."*Proceedings of the Sixth International Conference on Construction Materials*, 1244-1255.

Mishra, C., Yamaguchi, K., Endo, Y., and Hanazato, T. (2019). "Shear Strengthening of Unreinforced Masonry Wall Constituting Nepalese Historical Buildings with Steel and Timber." *Architectural Institute of Japan Conference, Summaries of Technical Papers of Annual Meetings*, **C-2**, 229-232.

Mishra, C., Yamaguchi, K., Endo, Y., Hanazato, T., and Shakya, M. (2020b). "Study on Shear and Flexural Behavior of Nepalese Masonry Walls with and without

Reinforcement." *Proceeding of the 17th World Conference on Earthquake Engineering, Sendai, Japan*, **2i**-0199.
Mustafaraj, E., and Yardim, Y. (2018). "In-plane shear strengthening of unreinforced masonry walls using GFRP jacketing." *Periodica Polytechnica Civil Engineering*, **62** (2), 330-336.
Mustafaraj, E., and Yardim, Y. (2019). "Retrofitting damaged unreinforced masonry using external shear strengthening techniques."*Journal of Building Engineering*, **26,** 100913.
Penazzi, D., Valluzzi, M. R., Saisi, A., Binda, L., and Modena, C. (2001). "Repair and strengthening of historic masonry buildings in seismic areas. *International Congress, more than two thousand years in the history of architecture safeguarding the structure of our architectural heritage, Bethlehem, Palestine*, (pp. 1-6).
The Japan Building Disaster Prevention Association/ Seismic Repair Support Center, the Minister of Land, Infrastructure, Transport and Tourism. (2017). "Standard for Seismic Evaluation of Existing Reinforced Concrete Buildings." (pp. 271-285). (In Japanese).
Wang, Q., Chai, Z., Huang, Y., Yang, Y., and Zhang, Y. (2006). "Seismic shear capacity of brick masonry wall reinforced by GFRP." *Asian Journal of Civil Engineering*, 7 (6), 563–580.
Winokur, A., and Rosenthal, I. (1982). "Ferrocement in centrally loaded compression elements."*Journal of Ferrocement*, **12** (4), 357-364.
Yamaguchi, K., Koshi, M., Ishihara Y. and Ninakawa, T. (2014). "Mechanical Characteristics of Brick Masonry which Constitutes the Kyushu University Headquarters Buildings, Part 1. Compressive Loading Test of Brick Masonry Specimens Extracted from Kyushu University Headquarters Building 1 and 3", *Architectural Institute of Japan Conference, Summaries of Technical Papers of Annual Meetings*, (pp.841-842). (In Japanese).

Chapter 8: Numerical Investigation of the Properties of Japanese Historical Brick Masonry Structures

Abstract

The purpose of this study was to discretize a numerical model that can be used to assess the behavior of brick masonry with cement mortar. The behavior of unreinforced brick masonry (URM) was investigated through numerical simulation. A homogenous macro model was used in ABAQUS software to reproduce a previously performed diagonal compression test and horizontal loading test of a wall built of brick masonry with cement mortar. Material properties such as density, E, and Poisson's ratio were input to the software. The objective of this study was to confirm Young's modulus and Poisson's ratio so that it can used in macro modeling. To confirm Young's modulus and Poisson's ratio the numerical modeling of diagonal compression test and horizontal loading test were conducted. The Poisson's ratio obtained from transducers gave closer analytical results to experimental results compared to Poisson's ratio obtained from Rosette's strain gauge. From the numerical analysis of diagonal compression model and from contours in the model, it was observed that most of the compressive forces pass through the centre of the specimen and are only concentrated in the area directly under the load rather than distributing to the whole cross-sectional area of the specimen. The highest value of the modulus of elasticity (E = 6870 MPa) was obtained for samples loaded perpendicularly to horizontal joints (θ_{strut}=90°). For the horizontal loading test, the value of E = 5700 MPa was obtained from the analysis (θstrut = 67.43°). The values of shear modulus G (calculated from the diagonal transducers in diagonal compression test) are within the range of 8–17% of the value of modulus of elasticity E (prism compression test) for Nepalese and Japanese historical brick masonry. In either case, the values of shear modulus were not close to 40% of E, as recommended by Eurocode 6.

Keywords: Historical brick masonry, Numerical modeling, Diagonal compression model, Horizontal loading model, Rosette's Poisson's ratio

8.1 Introduction

Brick masonry is one of the earliest and most widely utilized types of construction in the world. Depending on their geometric configurations, arrangement, and mechanical properties, brick units and mortar combine to construct various masonry walls (Ma et al., 2022; Abdulla et al., 2017). Moderate to strong earthquakes resulted in partial damage or complete collapse of the Unreinforced reinforced masonry (URM) structures due to cracking, resulting in significant financial losses and a high death toll (Penna et al., 2014; Kouris and Triantafillou, 2018).

URM structures are load-bearing type structures and their compressive capacity is noticeably greater than that of tension, shear, and bending. Under external forces such as earthquakes, and wind load, URM structures are susceptible to macro fractures, which lead to successive failure and damage. URM walls frequently exhibit horizontal, vertical, and diagonal cracks when subjected to seismic action (Sun et al., 2009).

For experimental research on the seismic performance of masonry walls, numerical simulations offer a workable substitute approach that can mimic both the linear and nonlinear behaviors of masonry (Mojsilović et al., 2013; Roca et al., 2010). Furthermore, numerical simulation can employ either macro modeling techniques which are typically used to simulate structural performance, or micro modeling techniques, which are based on the needed degree of accuracy and model size (Holler et al., 2004; Hu et al., 2023). Based on the findings of experiments, the material properties are required for the accuracy and dependability of the numerical model. It is feasible to alter the intended parameters and confirm the impact of each component after the model has been calibrated (Oliveira, 2014).

Various methods have been developed for analyzing the behavior of masonry structures. Lourenço stated that the modeling techniques fall into three main categories: macro-modeling, simplified micro-modeling, and detailed micro-modeling (Lourenco, 1998). The simulation of units, mortar, and the unit-mortar interface are all included in micro-modeling. It works well for examining the structural behavior of small masonry components, but it takes a lot of CPU time for models with a large number of elements (Annecchiarico et al., 2010). However, the macro-modeling approach requires less computing power and is the preferred method in use today. Masonry is considered a continuous material and there is no differentiation between units and joints in the macro-modeling approach. The masonry was considered an isotropic, homogeneous continuum in this approach. Units and mortar in the joints were taken into consideration in the case of the simplified micro-modeling approach, but no interface element was taken into consideration (Annecchiarico et al., 2010).

This study used a macro model that is simple to use for seismic analysis and structural design. This work aimed to explore a numerical technique for the analysis of the behavior of brick masonry walls in the elastic range. Furthermore, through numerical simulation, the behavior of brick masonry walls for diagonal compression test and horizontal loading test for Japanese historical brick masonry was also examined through a macro modeling approach. This study also gives insight into the structural behavior of historical brick masonry subjected to horizontal loading. This study also confirms Young's modulus and Poisson's ratio of Japanese historical masonry so that it can be used in macro modeling analysis.

8.2 Materials and Methods

8.2.1 Description of the Experiment

Uniaxial compression experiments were conducted to clarify the basic mechanical properties of elements of brick walls (unit bricks, mud mortar, and masonry prisms). From the three specimens of the masonry prism, average compressive strength and Young's modulus E for Japanese masonry were determined. From the diagonal compression experiment, the shear strength and shear modulus G were determined. Also, a horizontal loading test was done to determine the load-displacement characteristics and stiffness of the Japanese wall.

For the diagonal compression experiment load was applied and displacement transducers measured the compressive shortening and tensile elongation of the specimen. Horizontal loading tests were carried out on an inverted T-shaped specimen where a pre-compressive load of 0.21 N/mm^2 was applied and horizontal loads were applied in positive and negative directions to the wall. Displacement transducers were set up to measure the shear deformation, bending deformation, and horizontal displacement. Figure 8.1a) shows the prism compression test setup. Figure 8.1b) shows the diagonal compression test setup and 8.1c) shows a schematic diagram of the loading of the diagonal compression test. Figure 8.2a) shows the horizontal loading test setup and Figure 8.2b) shows the position of transducers on the specimen. Figure 8.3a) shows the diagonal compression test specimen showing the transducer's position and Figure 8.3b) shows the diagonal compression test specimen showing Rosette's strain gauges.

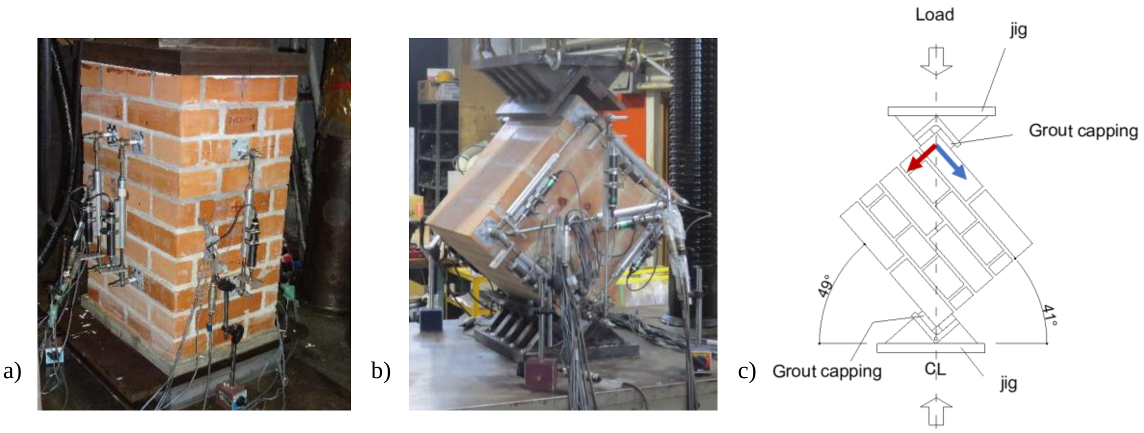

Figure 8.1: a) Prism compression test b) diagonal compression test c) schematic diagram of loading of diagonal compression test

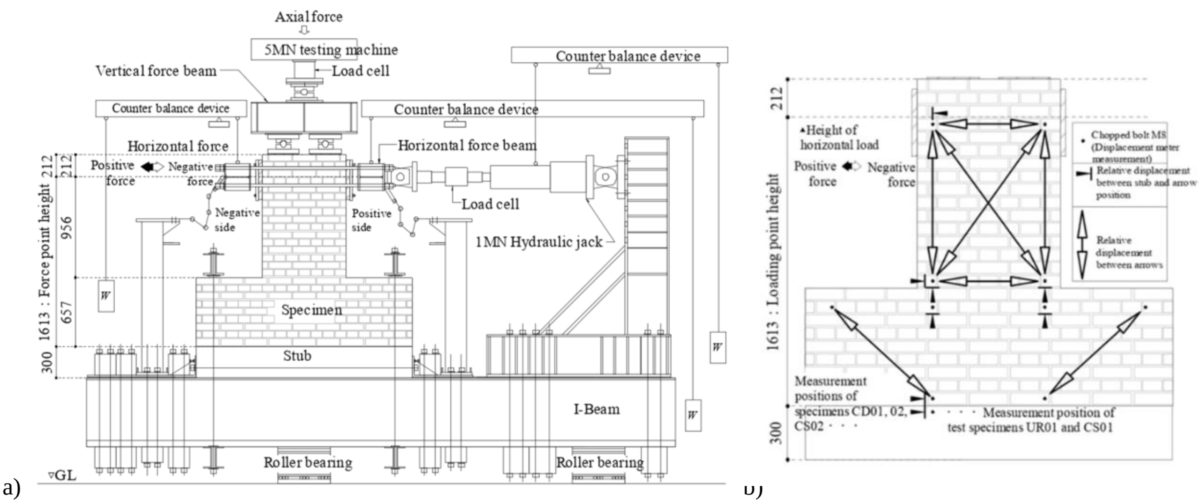

Figure 8.2: a) Horizontal loading test setup b) Position of transducers on the specimen

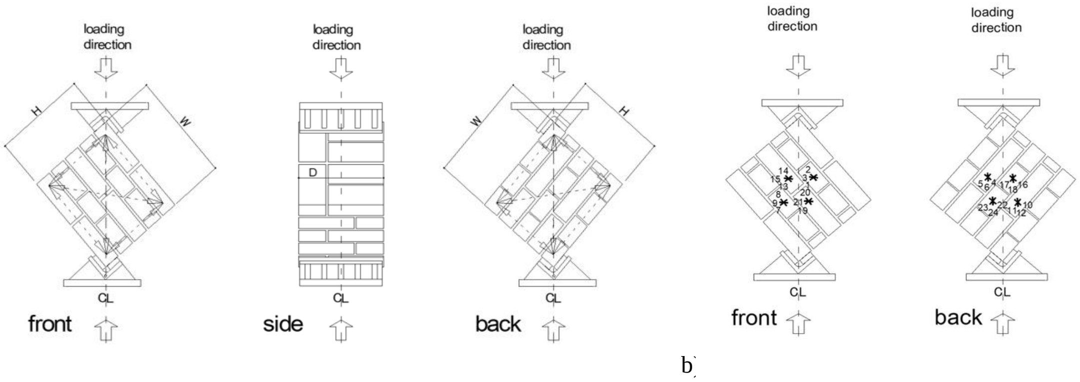

Figure 8.3: a) Diagonal compression test specimen showing transducers position
b) Diagonal compression test specimen showing Rosette strain gauges

8.2.2 Research Methodology

A case study on the results obtained in various experiments of brick masonry that constitutes Japanese historical buildings was conducted. Firstly, the mechanical properties from the experimental results were determined. Secondly, for numerical modeling, load-deformation relationships from experimental results were also confirmed. From the Diagonal compression test, the shortening and elongation of diagonal transducers before crack propagation were noted. For the horizontal loading test, the first crack point observed was at approximately 75% of the maximum load. The first crack point was identified from experimental data by using hysteresis and envelope curves. Shear deformation from diagonal transducers, bending deformation from vertical transducers, and horizontal displacement before the crack point were also noted. Thirdly, numerical analysis was performed on the diagonal compression model and horizontal loading test models. This stage was articulated in two steps, which included (i) validation of the diagonal compression model to confirm Poisson's ratio, and (ii) validation of the horizontal loading test model. The numerical models were developed and validated using a macro model elastic analysis. The analysis was conducted using the general-purpose finite element method software, ABAQUS. Since applying the micro model to historical buildings is more difficult and time-consuming, the goal of this research is to create an analysis technique that uses macro modeling to more accurately depict the behavior of real structures. Furthermore, when designing structures using brittle masonry, it is not practical to create huge deformations. For this reason, the majority of this work concentrates on minor deformation regions that can be utilized to create safer structural designs.

The discretization of a numerical model for evaluating brick masonry behavior was the aim of this study. Numerical simulation was used to study the behavior of Japanese URM walls. The material properties for macro modeling in any FEM software are Young's modulus of elasticity and Poisson's ratio which are important parameters for macro modeling in the elastic range. Masonry is heterogeneous and anisotropic in nature due to brick units and mortar. However, in macro modeling masonry is considered isotropic and homogenous where the software automatically calculates shear modulus (G) from the values of Young's modulus (E) and Poisson's ratio (v). For the confirmation of value of Poisson's ratio for macro modeling, a numerical analysis of the diagonal compression model was carried out. After confirming the value of v, the numerical analysis on the horizontal loading test model was carried out to confirm the value of Young's modulus (E) in the elastic range.

8.3 *Results and Discussion*

8.3.1 Determination of Poisson's ratio (from transducers)

Poisson's ratio was calculated as the ratio of strain in the tensile direction to the compressive direction as the difference in tensile and compressive strain was large in the diagonal experiment. Tensile strain is the elongation in the tensile diagonal direction measured by a horizontal displacement transducer. Similarly, compressive strain is the shortening in the compressive diagonal direction measured by the vertical displacement transducer. Poisson's ratio was calculated by taking linear regression of data up to 33% of maximum load (Figure 8.4). The Poisson's ratio of DUR 501, DUR 502, and DUR 503 specimens were 0.0348, 0.0535, and 0.0584, respectively. The average Poisson's ratio was 0.0489.

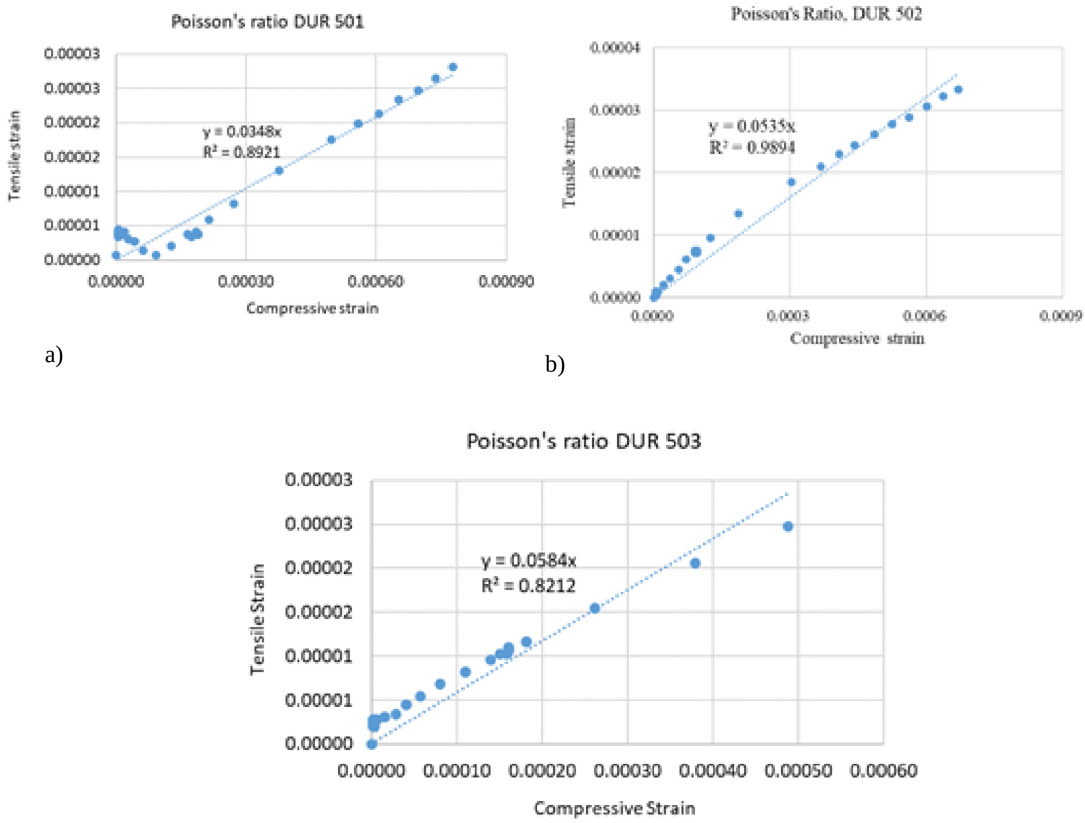

Figure 8.4: Poisson's ratio determined by diagonal transducers for a) DUR 501, b) DUR 502, and c) DUR 503 specimens

8.3.2 Determination of Poisson's ratio by Rosette method (from strain gauges)

The principal compressive strain was calculated by equation (8.1). The principal tensile strain was calculated by equation (8.2) and shear strain was calculated by equation (8.3). Where, ε1 is the strain in the horizontal direction, ε2 is the strain in the vertical direction, and ε3 is the strain in the diagonal direction of the Rosette strain gauge. The Poisson's ratio was calculated from the Rosette method as a ratio of tensile strain to compressive strain. The Poisson's ratio was calculated by linear regression of data up to 33% of maximum load as shown in Figure 8.5. The average Poisson's ratio was determined from all three specimens which was 0.312.

$$\varepsilon_{min} = \frac{1}{2}\left[\varepsilon_1 + \varepsilon_2 - \sqrt{2\{(\varepsilon_1 - \varepsilon_3)^2 + (\varepsilon_2 - \varepsilon_3)^2\}}\right] \quad (8.1)$$

$$\varepsilon_{max} = \frac{1}{2}\left[\varepsilon_1 + \varepsilon_2 + \sqrt{2\{(\varepsilon_1 - \varepsilon_3)^2 + (\varepsilon_2 - \varepsilon_3)^2\}}\right] \quad (8.2)$$

$$\gamma_{max} = \sqrt{2\{(\varepsilon_1 - \varepsilon_3)^2 + (\varepsilon_2 - \varepsilon_3)^2\}} \quad (8.3)$$

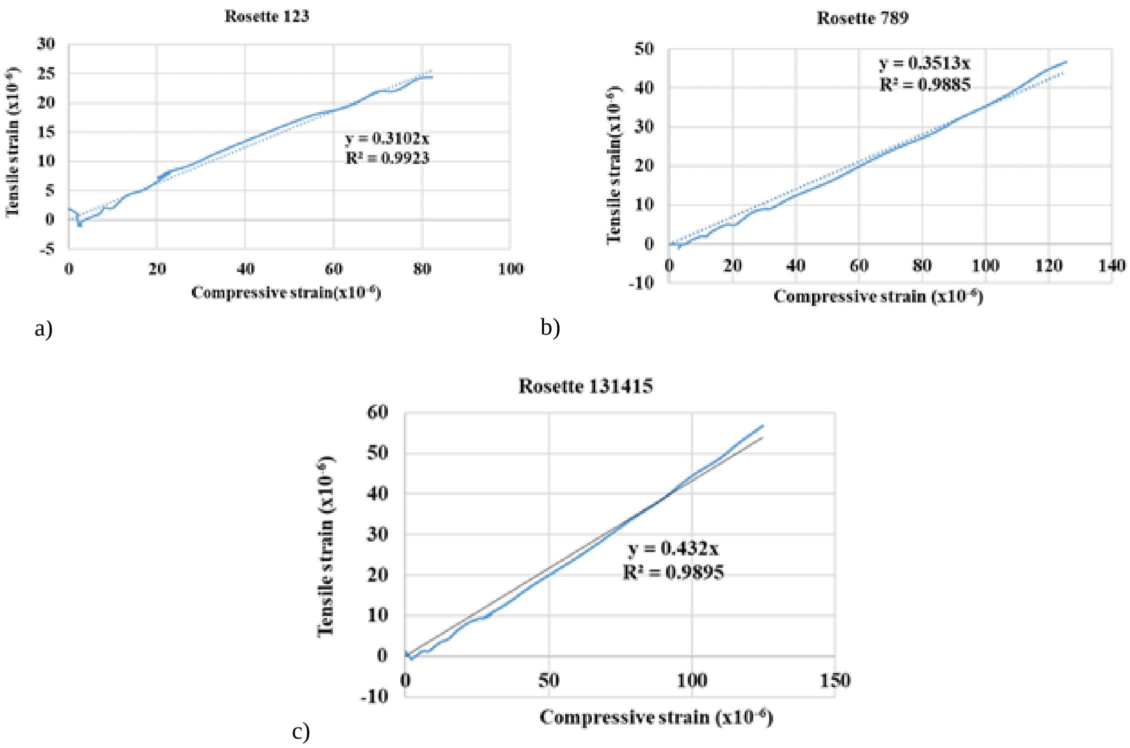

Figure 8.5: Poisson's ratio by Rosette method for a) DUR 501, b) DUR 502, and c) DUR 503 specimens

8.3.3 Material properties from prism compression test

The dimensions of masonry prisms are shown in Table 8.1. Table 8.2 shows the results of prism compression test. The compressive strength of the brick was 19.2 N/mm^2 (Mishra et al., 2020; Mishra et al., 2021).

Table 8.1: Dimensions of masonry prism and its component properties

Specimen	Height H	Width W	Depth D	Mortar	
				Compressive strength (N/mm^2)	Young's Modulus (N/mm^2)
PPC 101	690.3	345.0	464.8		2.42×10^4
PPC 102	689.3	345.5	464.5	29.0	2.43×10^4
PPC 103	689.5	345.0	464.8		2.42×10^4

Table 8.2: Results from prism compression test

Experiment	Prism average compressive strength (MPa)	Average Young's modulus of masonry prism (MPa)	Density of brick (Kg/m^3)
Prism compression test	15.8	6870	1566

8.3.4 Material properties of diagonal compression test

The size of diagonal compression test specimen is shown in Table 8.3. The results from diagonal compression test are shown in Table 8.4. The average shear strength of wall was 0.95 MPa, the average shear modulus (G) was 553 MPa, the average Poisson's ratio (v) was 0.0489, and Young's modulus of elasticity from the equation E = 2(1+V) *G was 1160.083, respectively.

Table 8.3: Size of the specimens

Specimens		Height [mm]	Width [mm]	Depth D [mm]
	501	357	410	331
DUR	502	355	410	331
	503	355	410	332

Table 8.4: Results from diagonal compression test

Experimental Results	Shear strength of wall (MPa)	Shear Modulus, G (MPa)	Poisson's ratio from transducers, v	Poisson's ratio from Rosette method, v	E = 2(1+V) xG
Diagonal Compression	0.95	553	0.0489	0.312	1160

8.3.5 Determination of shear modulus by considering the shear deformation due to compressive diagonal and tension diagonal transducers

Shear modulus (G) was calculated as the ratio of shear stress and shear deformation angle. For the calculation of shear deformation angle, the average deformation of compressive and tensile diagonals was considered. However, the shear deformation calculated from shortening of compressive diagonal and elongation in tensile diagonal have large variations in values. Therefore, shear modulus due to compressive diagonal (Gc) and shear modulus due to tensile diagonal (Gt) were calculated separately. The shear modulus was calculated by taking the linear regression of experimental data up to 33% as shown in Figure 8.6.

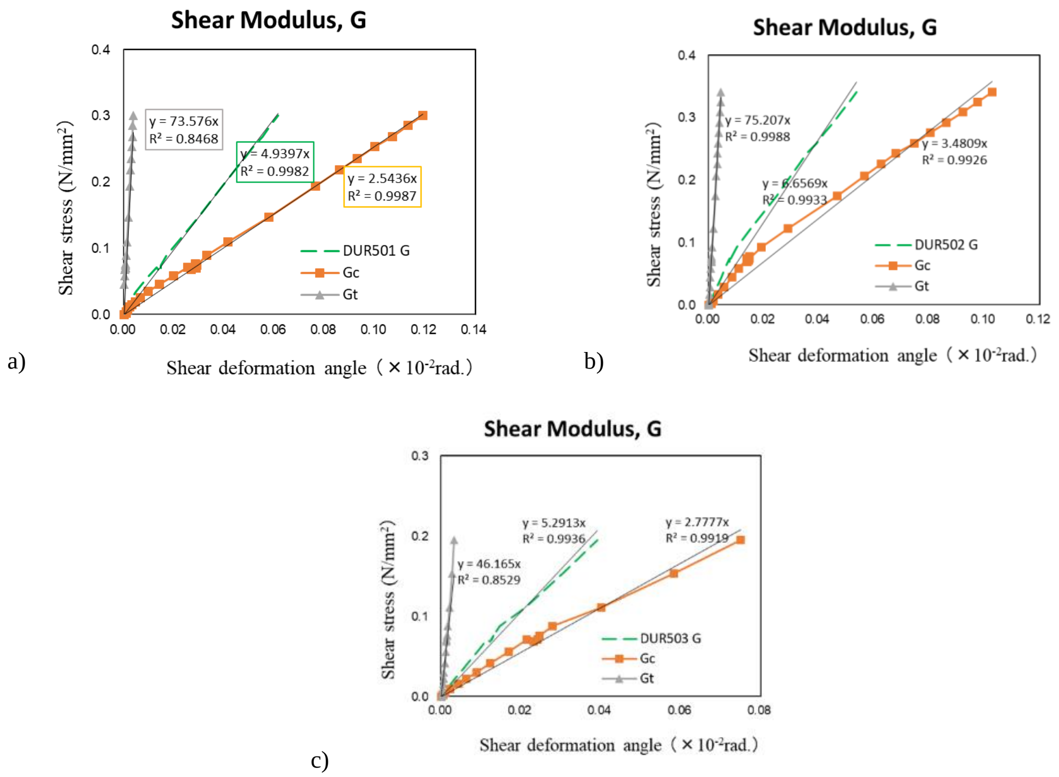

Figure 8.6: Shear modulus determination for a) DUR 501, b) DUR 502, and c) DUR 503 specimens

Table 5 shows the results of shear modulus, shear modulus considering only compressive diagonal, and shear modulus considering only the tensile diagonal.

Table 8.5: Results of shear modulus for URM specimens

Specimens		(G) [N/mm^2]	(Gc) [N/mm^2]	(Gt) [N/mm^2]
DUR	501	493.9	254.3	7358
	502	635.9	348.0	7521
	503	529.1	277.7	4617
Average		553.0	293.4	6498

Where G is shear modulus, Gc is shear modulus considering only the compressive diagonal, Gt is shear modulus considering only the tensile diagonal

8.4 Numerical Modeling of Unreinforced Masonry Walls

A numerical model of a URM wall was created using a three-dimensional solid (or continuum) element in ABAQUS finite element software. C3D8R is a hexahedral 8-node linear brick element with reduced integration. The integration point of the C3D8R element is located in the middle of the element. C3D8R was selected for mesh generation as it is cost-effective and has enhanced convergence compared to full integration (Dauda et al., 2021). A mesh size of 30 mm was used. Masonry was modeled as an isotropic and homogeneous material. Elastic modulus (E) from the prism compression experiment was taken as the E initial for the first iteration.

Using a three-dimensional solid (or continuum) element in ABAQUS finite element software, a numerical model of a URM wall was produced. The element C3D8R is a reduced integration linear brick element with hexahedral eight nodes. The center of the C3D8R element is where its integration point is situated. Because it is more affordable and has better convergence than full integration, C3D8R was chosen for mesh generation (Dauda et al., 2021). A 30 mm mesh size was employed. Masonry was represented as a homogenous, isotropic material. Poisson’s ratio and density were also taken as input to the software. For the first iteration, elastic modulus (E), obtained from the prism compression experiment, was used as the initial E. The trials for different values of E during modeling were done until the numerical result was in good agreement with the experimental value.

8.4.1 Numerical Modeling of Diagonal Compression Model

There were two boundary conditions, the bottom base was fixed in the y-direction and the center of base was pinned in the modeling to replicate the experimental condition of the diagonal compression test (Figure 8.7). The load was applied from the top which was uniformly distributed all over the loading shoe.

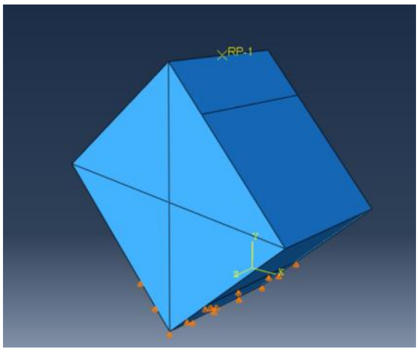

Figure 8.7: 3D Abaqus model of diagonal compression test

Table 8.6 shows the results of numerical analysis of diagonal compression model. Three cases were considered in this study. For case 1, results from the diagonal compression test were taken (G and v) and E was calculated from the equation E = 2(1+V) G. In this case, the v was calculated from transducers. The values v and E were used as input to software during numerical analysis.

For case 2, the same value of E as that of case one was taken and v calculated from the Rosette`s strain gauge was used as input to software during numerical analysis.

For case 3, E was calculated from the equation E = 2(1+V) G by taking v from the Rosette`s strain gauge was used as input to software during numerical analysis.

In this study, Case one gives the least error for both compressive shortening and tensile elongation. However, for tensile elongation, the error % was irrelevant as the tensile elongation was much less compared to compressive shortening.

Table 8.6: Results of numerical analysis of diagonal compression test

Number of cases	E (N/mm^2)	ν	Experimental Results		Analysis results from Abaqus			
			Compressive shortening (mm)	Tensile elongation (mm)	Compressive shortening (mm)	% Increase or decrease	Tensile elongation (mm)	% Increase or decrease
Case 1	1160	0.0489			0.232	-11.0	0.035	327.0
Case 2	1160	0.3126	0.2616	0.0082	0.219	-16.0	0.081	888.0
Case 3	1452	0.3126			0.173	-34.0	0.064	680.0

Figure 8.8a) shows the displacement contour in a vertical direction and Figure 8.8b) shows the displacement contour in a horizontal direction. Figure 8.9a) shows the principal compressive strain and Figure 8.9b) shows the principal tensile strain. The contours show that the part under load was in compression, and the part perpendicular to the load was in tension, which was in good agreement with the experimental results.

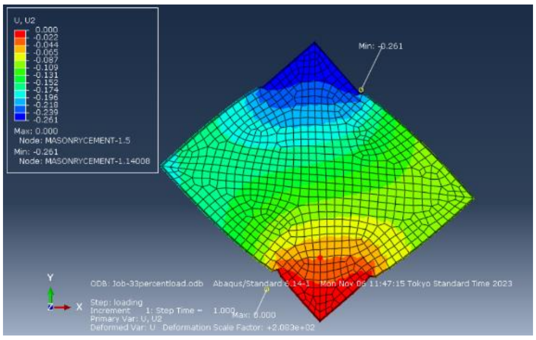

a)

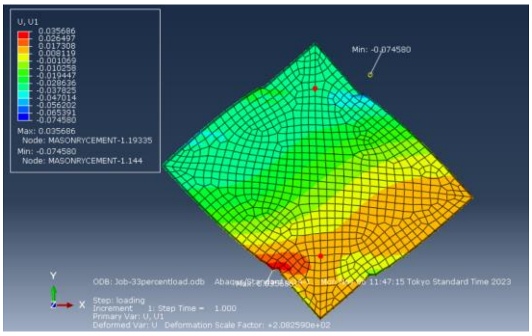

b)

Figure 8.8: Displacement contour in a) vertical direction b) horizontal direction

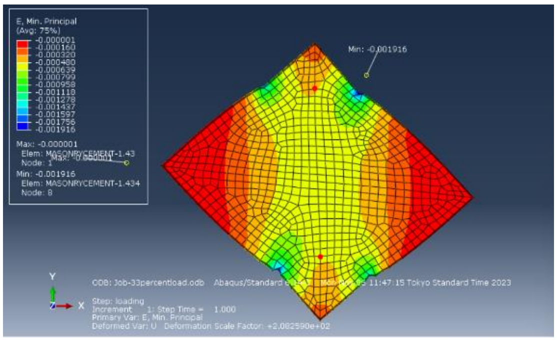

a)

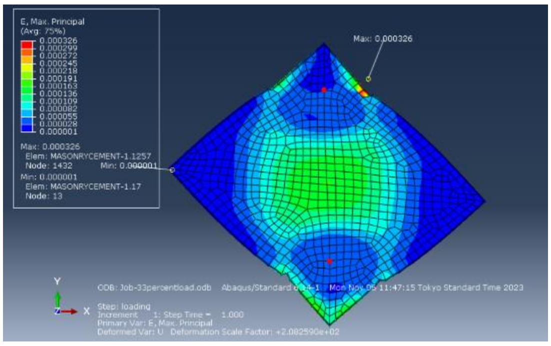

b)

Figure 8.9: a) Principal compressive strain b) Principal tensile strain

8.4.2 Selection of best-fit value of Poisson's ratio from numerical modeling of diagonal compression test

The Poisson's ratio obtained from transducers gave closer results compared to Poisson's ratio obtained from Rosette's strain gauge. This might be due to the Rossette's strain gauge being only attached to brick whereas the transducers included the deformation of bricks and mortar together.

From the stress contour in numerical analysis (Figure 8.9a) and b)), it is clear that the compressive strut is formed under the loading shoe (169 mm) and the effective area for compression is load shoe length times the specimen depth (A=55939 mm^2).

Also, from the relation of σ = E*εc where E is the young's modulus of elasticity (1160.083 N/mm^2) and εc is the compressive strain from the experimental results, the effective area in the specimen was determined as 59977 mm^2. Most of the compressive forces pass through the center of the specimen and are only concentrated in the area directly under the load rather than distributed to the whole cross-sectional area of the specimen. The tensile force also concentrates on a small area rather than distributing to the whole cross-sectional area. This might be the reason for the higher % error for tensile elongation.

The ratio of load shoe length to the total diagonal length multiplied by tensile elongation obtained from analysis gives the actual tensile elongation. This ratio of actual tensile elongation to the compressive shorting obtained from analysis was Poisson’s ratio which was close to the value of Poisson’s ratio obtained from transducers. Therefore, we selected Poisson’s ratio obtained from transducers for further analysis.

8.4.3 Horizontal loading test

Figure 8.2a) shows the loading arrangement of horizontal load test and Figure 8.2b) shows the positions of transducers to measure the shear and bending deformation. From the load-displacement behavior, the hysteresis or all loading cycles were plotted. The envelope curve of URM wall was developed from the hysteresis curve. From experimental data and envelope curve, the first crack point was determined and the corresponding displacement was also determined. The first crack point was at approximately 75% of the maximum load as shown in Figure 8.10. The load-displacement behavior of the horizontal wall test is shown in Table 8.7. The stiffness was 147.87 KN/mm. At the first crack point, the shear deformation and bending deformation were noted from experimental data.

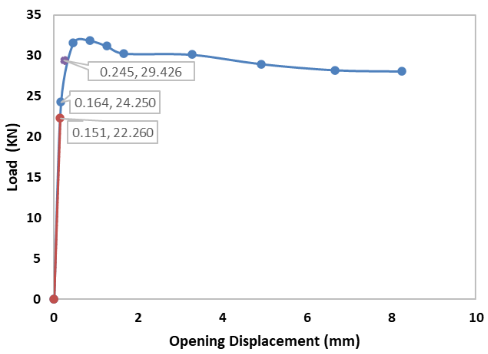

Figure 8.10: Envelope curve obtained from hysteresis curve of horizontal wall test

Table 8.7: Load displacement behavior of horizontal wall test

Crack load, H (KN)	Displacement, d (mm)	Stiffness, K=H/d (KN/mm)
24.25	0.164	147.87

8.4.4 Numerical modeling of horizontal loading test

There were three boundary conditions. First was half of the bottom of the RC base fixed in the y-direction, the second was the plate fixed on the RC stub base side which was fixed in the x-direction and third was the spandrel restrained in the y-direction on the left side of the opening wall (Figure 8.11). The pre-compression load of 0.21 N/mm2 was applied as a uniformly distributed load. The horizontal load was applied from the left side of the specimen and the model was run. From the analysis results, the deformation in compressive diagonal and tensile diagonal were also verified with the experimental results. Similarly, the left vertical and right vertical transducers were also verified with the experimental results. Finally, the top horizontal displacement was also verified with the horizontal loading test experimental data.

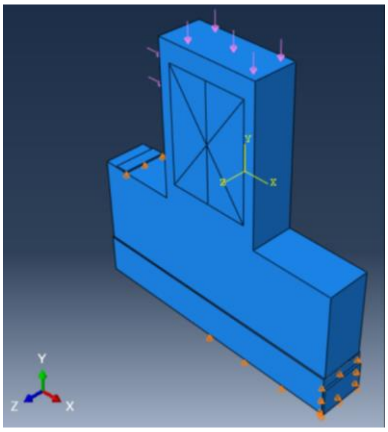

Figure 8.11: 3D Abaqus model of horizontal loading test

Table 8.8 shows the results of numerical analysis of the horizontal loading test for shear deformation and Table 8.9 shows the results of horizontal loading test for bending deformation. Three cases were studied. Table 8.8 and 8.9 show that when the value of E from the diagonal compression test was input to the software, the results deviated far away from the experimental results. When Young's modulus from prism compression test E=6870 N/mm^2 was taken as input to the software along with previously calibrated Poisson's ratio, v, the results were closer to the shear deformation (Table 8.8). However, the bending deformation % error was higher (Table 8.9). When Young's modulus of E = 5700 N/mm^2 (from trial and error) was taken as input to the software along with previously calibrated Poisson's ratio (v), the numerical results were closer to the experimental values of shear and bending deformation (Table 8.8 and 8.9).

Table 8.8: Results of numerical analysis of horizontal loading test for shear deformation

Cases	E (N/mm^2)	ν	Experimental Results (Shear deformation)		Analysis results from Abaqus			
			Compressive shortening (mm)	Tensile elongation (mm)	Compressive shortening (mm)	% Increase or decrease	Tensile elongation (mm)	% Increase or decrease
Case 1	1160				0.17	541.5	0.14	500.9
Case 2	6870	0.0489	0.0265	0.0233	0.0277	4.5	0.0233	0.0
Case 3	5700				0.0329	24.2	0.028	20.2

Table 8.9: Results of numerical analysis of horizontal loading test for bending deformation

Cases	E (N/mm^2)	ν	Experimental Results (Bending deformation)		Analysis results from Abaqus			
			Left vertical elongation (mm)	Right vertical shortening (mm)	Left vertical elongation (mm)	% Increase or decrease	Right vertical shortening (mm)	% Increase or decrease
Case 1	1160				0.165	368.0	0.158	348.2
Case 2	6870	0.0489	0.0353	0.0353	0.028	-20.6	0.0270	-23.4
Case 3	5700				0.033	-6.4	0.0320	-9.2

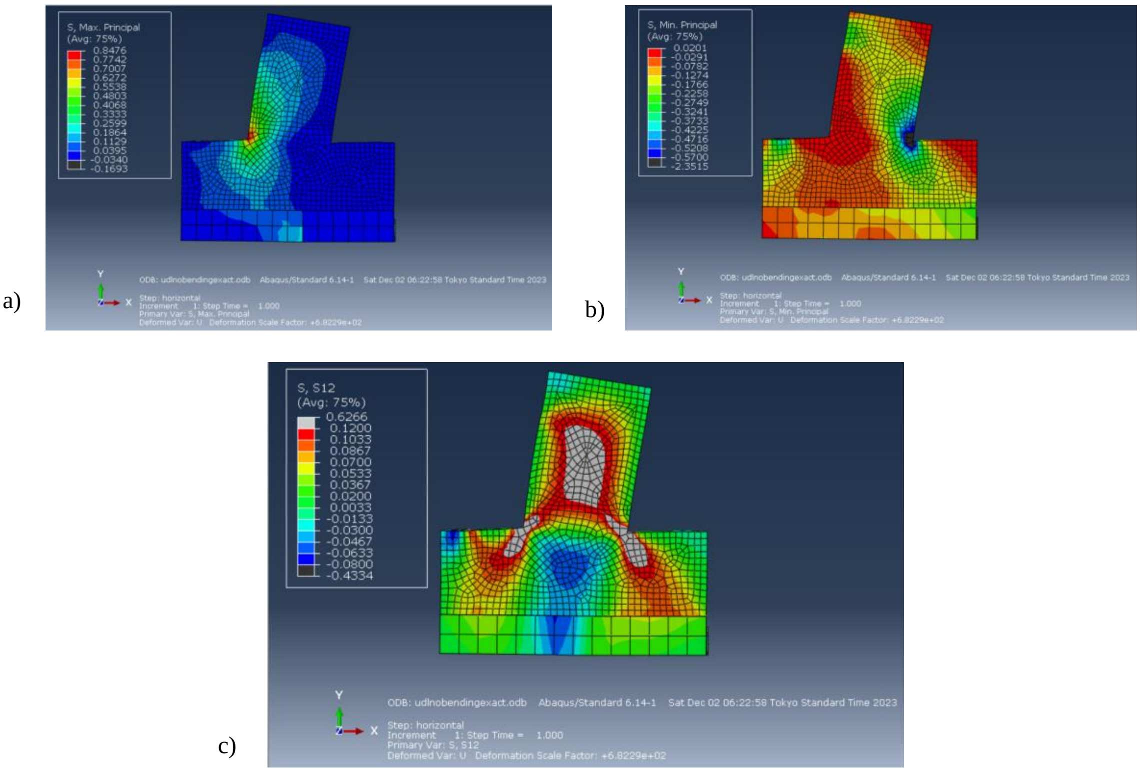

Figure 8.12: a) Principal tensile stress b) Principal compressive stress c) Shear stress (xy)

Figure 8.12 a) shows principal tensile stress b) shows principal compressive stress and c) shear stress (xy) for the horizontal loading test model.

8.4.5 Changes in Young's modulus with the angle of the compressive strut with bed joint (θstrut)

The highest value of the modulus of elasticity (E = 6870 MPa) was obtained for samples loaded perpendicularly to horizontal joints (θstrut = 90°). For the horizontal loading test, the value of E = 5700 MPa was obtained from the analysis (θstrut = 67.13°). The lowest value of E = 1160 MPa was obtained for the samples with angle θstrut = 41° (Table 8.10). The lowest value of the coefficient E_θ/E_{90} has been obtained for samples with joints rotated at an angle θ = 49° for the diagonal compression test. Nowak et al. (2021) and Mishra et al. (2023) reported similar results. It has been noted that depending on the angle of the compressive stress trajectory, the anisotropy of the brickwork greatly affects the wall's ability to support loads (Nowak et al., 2021). The analysis made it possible to calculate the masonry strength when the load was applied at various angles to the bed joints.

Table 8.10: Changes in Young's modulus with the angle of the compressive strut with bed joint (θstrut)

Experiments	Bed angle	θstrut	E (Mpa)	E_θ/E_{90}
Prism compression experiment	0°	90°	6870	-
Horizontal loading test	0°	67.43°	5700	0.83
Diagonal compression experiment	49°	41°	1160	0.20

8.4.6 Comparison of results of Nepalese and Japanese historical brick masonry

Table 8.11 shows the comparison of G/E ratio for Nepalese and Japanese historical brick masonry. In the case of Nepalese historical brick masonry, the G/E ratio found was 16% (Mishra et al., 2020) while in Japanese historical brick masonry G/E ratio was 8%. The values of shear modulus are within the range of 8–16% of the value of modulus of elasticity E for Nepalese and Japanese historical brick masonry. In either case, the values of shear modulus were not close to 40% of E, as recommended by Eurocode 6. Tomaževič (2009) also reported that the actual values of G are within the range of 6–13% of the value of modulus of elasticity E. Experimental results of this study also collaborates with the findings of (Tomaževič, 2009)

Table 8.11: Comparison of G/E ratio for Nepalese and Japanese historical brick masonry

Brick masonry	Prism compression	Diagonal compression	Ratio
Type of buildings	E (MPa)	G (MPa)	G/E (%)
Nepalese	310	53	17.0
Japanese	6870	553	8.0

Where, G is the shear modulus and E is the modulus of elasticity

8.5 Conclusions

Numerical analysis was conducted on diagonal compression test and horizontal loading test models and following conclusions were made.

1. The Poisson's ratio obtained from transducers gave closer analytical results to experimental results compared to Poisson's ratio obtained from Rosette's strain gauge.
2. From the numerical analysis of diagonal compression model and from contours in the model, it was observed that most of the compressive forces pass through the centre of the specimen and are only concentrated in the area directly under the load rather than distributing to the whole cross-sectional area of the specimen.
3. The highest value of the modulus of elasticity (E = 6870 MPa) was obtained for samples loaded perpendicularly to horizontal joints (θ_{strut}=90°). For the horizontal loading test, the value of E = 5700 MPa was obtained from the analysis (θstrut = 67.43°).
4. The values of shear modulus G (calculated from the diagonal transducers in diagonal compression test) are within the range of 8–17% of the value of modulus of elasticity E (prism compression test) for Nepalese and Japanese historical brick masonry. Similar findings were reported by Tomaževič (2009). In either case, the values of shear modulus were not close to 40% of E, as recommended by Eurocode 6.

References

Abdulla, K. F., Cunningham, L. S., and Gillie, M. (2017). Simulating masonry wall behavior using a simplified micro-model approach. *Engineering Structures, 151*, 349-365.

Annecchiarico, M., Portioli, F., and Landolfo, R. (2010). Micro and macro finite element modeling of brick masonry panels subject to lateral loadings. In *Proc., COST C26 Action Final Conf* (pp. 315-320).

Dauda, J. A., Silva, L. C., Lourenço, P. B., & Iuorio, O. (2021). Out-of-plane loaded masonry walls retrofitted with oriented strand boards: Numerical analysis and influencing parameters. *Engineering Structures*, *243*, 112683.

Holler, S., Butenweg, C., Noh, S. Y., and Meskouris, K. (2004). Computational model of textile-reinforced concrete structures. *Computers & structures*, *82*(23-26), 1971-1979.

Hu, Y., Ma, P., and Yao, J. (2023). Effects of aspect ratios and vertical loads on in-plane seismic behavior of unreinforced masonry walls: A numerical simulation. *Plos one*, *18*(3), e0282430.

Kouris, L. A. S., and Triantafillou, T. C. (2018). State-of-the-art on strengthening of masonry structures with textile-reinforced mortar (TRM). *Construction and Building Materials*, *188*, 1221-1233.

Lourenço, P. B. (1998). Experimental and numerical issues in the modeling of the mechanical behavior of masonry.

Ma, P., Yao, J., and Hu, Y. (2022). Numerical Analysis of Different Influencing Factors on the In-Plane Failure Mode of Unreinforced Masonry (URM) Structures. *Buildings*, *12*(2), 183.

Mishra, C., Yamaguchi, K., Endo, Y., Hanazato, T., & Shakya, M. (2020). Study on shear and flexural behavior of Nepalese masonry walls with and without reinforcement. In *Proceedings of the 17th World Conference on Earthquake Engineering, Sendai, Japan* (pp. 13-18).

Mishra, C., Yamaguch, K., Araki, K., Ninakawa, T., and Hanazato, T. (2021). Structural behavior of brick wall specimens reinforced on the surface with RC walls under horizontal loading. *Journal of Advanced Concrete Technology*, *19*(6), 593-613.

Mishra, C., Yamaguchi, K., Araki, K., and Ninakawa, T. (2020). Diagonal compression test of the brick masonry reinforced on the surface with steel plates or RC walls. In *Proc. 6th International Conference on Construction Materials, Fukuoka, Japan* (pp. 27-29).

Mishra, C., Yamaguchi, K., Jing, T., Hanazato, T., Endo, Y., and Shakya, M. (2023). Numerical Investigation of the Properties of Unreinforced and Reinforced Nepalese Historical Brick Masonry Structures. In *International Conference on Structural Analysis of Historical Constructions* (pp. 125-139). Cham: Springer Nature Switzerland.

Mojsilović, N., Kostić, N., and Schwartz, J. (2013). Modeling of the behavior of seismically strengthened masonry walls subjected to cyclic in-plane shear. *Engineering structures*, *56*, 1117-1129.

Nowak, R., Kania, T., Derkach, V., Orłowicz, R., Halaliuk, A., Ekiert, E., and Jaworski, R. (2021). Strength parameters of clay brick walls with various directions of force. *Materials*, *14*(21), 6461.

Oliveira, L. M. F. D. (2014). Theoretical and experimental study of the behavior of vertical interfaces of interconnected structural masonry walls. (Doctoral dissertation, Universidade de São Paulo).

Penna, A., Morandi, P., Rota, M., Manzini, C. F., Da Porto, F., and Magenes, G. (2014). Performance of masonry buildings during the Emilia 2012 earthquake. *Bulletin of Earthquake Engineering*, *12*, 2255-2273.

Roca, P., Cervera, M., Gariup, G., and Pela', L. (2010). Structural analysis of masonry historical constructions. Classical and advanced approaches. *Archives of computational methods in engineering*, *17*, 299-325.

Sun, A., Hou, S., and Lin, C. (2009). Failure mode analysis of buildings in Dujiangyan in Wenchuan earthquake. *Journal of Dalian University of Technology*, *49*, 731-738.

Standard, B. (2005). Eurocode 6-Design of masonry structures—. *British Standard Institution. London*, (2005).

Tomaževič, M. (2009). Shear resistance of masonry walls and Eurocode 6: shear versus tensile strength of masonry. *Materials and structures*, *42*, 889-907.

Chapter 9: Conclusions and Recommendations for Future Studies

This dissertation study is on strengthening with timber, RC walls, and steel plates for Nepalese and Japanese historical brick masonry. The effectiveness of the suggested strengthening technique in improving the structural performance of adobe masonry subjected to horizontal forces has been investigated using both numerical and experimental techniques. It was necessary to characterize the mechanical properties of both the rope and adobe materials to fully comprehend them, to add more specific information to the body of existing literature, and to supply the input data needed for numerical analyses. The conclusions and suggestions for future research are provided in the sections that are as follows.

9.1 Conclusions

9.1.1 Mechanical Properties of Components of Nepalese Historical Masonry Buildings

Uniaxial compression tests were conducted on elements of brick masonry and masonry prism. The following conclusions for mechanical characterization of Nepalese bricks were made.

- Despite the large standard deviations in results of constituent materials (unit bricks and mud mortar), the standard deviation of compressive strength of masonry prisms was low. The average compressive strength of masonry prism was 1.70 N/mm^2 with a standard deviation of 0.08 N/mm^2.
- In this study, the masonry compressive strength varies to about 30% of the brick's compressive strength.
- The empirical equation proposed by Euro code gave similar results to our experiment for masonry compressive strength.

9.1.2 Study on Shear and Flexural Behavior of Nepalese Historical Masonry Walls with and without Reinforcement

Diagonal compression experiment and three point bending were conducted for Nepalese historical masonry and following conclusion were made.

- The average shear strength was 0.054 N/mm^2, 0.106 N/mm^2, and 0.149 N/mm^2 for unreinforced walls, timber-reinforced walls, and steel-reinforced walls, respectively.

- The shear strength of the unreinforced wall was about one-twentieth of the shear strength of Japanese brick masonry, however, the value of the shear deformation angle was found to exceed 4% for unreinforced masonry, indicating a high deformation capacity. The timber-reinforced masonry (TRM) and steel-reinforced masonry (SRM) increased the average shear strength by 1.98 and 2.78 fold, respectively compared to unreinforced specimens.
- The flexural strength was increased in reinforced specimens. The maximum flexural strength was found for the diagonal-type braced prism. A sudden split was observed at maximum load in diagonal type braced prism whereas the failure in ladder type reinforced prism was mild and cracks were dispersed all over the specimen.
- Reinforcing specimens with timber and steel increased the shear and flexural strength which was confirmed by the diagonal compression and bending tests. Therefore, we concluded that reinforcing with timber and steel on the surface of walls may be an effective retrofitting technique for historical buildings of Nepal composed of brick and mud mortar. However, Sal wood is easily available and can be easily embedded with the architecture of Nepalese historical masonry buildings therefore it can be used in retrofitting methods compared to steel plates. Retrofitting with ladder-type arrangement performed better compared to the brace type arrangement in this study.

9.1.3 Numerical Investigation of the Properties of Unreinforced and Reinforced Nepalese Historical Brick Masonry Structures

Numerical analysis on three point bending test specimen models of Nepalese historical brick masonry was conducted and following conclusions were made.

- A homogenous macro model was used to reproduce a previously performed three-point bending test of a prism built of brick masonry in earth mortar. In this study, the elastic modulus in tension (E_t) was considered 1/5 of that in compression (E_c) for unreinforced brick masonry (URM) prism.
- The numerical model for the URM prism gave closer results to the experimental value when E_c was 41 MPa which was 1/8 of E calculated from the uniaxial compression experiment (310 MPa).
- In the uniaxial compression test, the direction of the compressive strut formed was 90 degrees to the bed angle, and E determined was 310 MPa. However, in the three-point bending test, a compressive strut was formed from the point of loading to the supports. For URM and diagonal braced specimens, the compressive strut formed was 56.3 degrees to the bed angle (θ_{strut}) whereas, for ladder-reinforced specimens, it was 37.2 degrees.

- For the ladder and diagonal-braced reinforced model, crack was assumed at the tensile side of the masonry. By trial and error, the numerical result was in good agreement with the experimental value for maximum displacement at the mid-point under the condition that the E of 20.5 MPa and 41.0 MPa was taken for the ladder and diagonal brace model, respectively, with a 70mm crack at the tensile side of masonry.
- In the analysis, it was observed that for URM and diagonal brace reinforced model, E was greater compared to ladder reinforced model. Namely, with the increase in compressive strut angle (θ_{strut}), there was an increase in the value of E. This numerical result tends to coincide with the findings of Nowak et al. (2021).

9.1.4 Diagonal Compression Test of the Japanese Historical Brick Masonry Reinforced on the Surface with Steel Plates or RC Walls

In this study, a diagonal compression test of brick masonry was conducted to know the reinforcement effect and the mechanical properties when the wall of brick masonry was reinforced from the surface. The shear parameters were also investigated. The following findings were obtained.

- RC reinforcement has higher strength and rigidity than steel plate reinforcement. In addition, in the case of RC walls, the deformation capacity was larger than the steel plate reinforcement.
- We concluded that anchors that penetrate through the masonry body by drilling anchor rods and fixing rebars on both sides could resist the splitting of specimens, and promote integration and hence higher reinforcement effect could be anticipated.

9.1.5 Structural Behavior of Japanese Historical Brick Wall Specimens Reinforced on the Surface with RC Walls under Horizontal Loading

In this study, a loading experiment was carried out to investigate the reinforcing effect on URM walls. In addition, a horizontal strength evaluation formula of a brick wall specimen reinforced with an RC wall was derived and verified. The following conclusions were obtained:

- The results of the horizontal loading test indicated that the maximum load of specimens reinforced with RC walls from one side was 6.1–6.2 times higher than that of unreinforced specimens. Similarly, the maximum loads of the specimens reinforced with RC walls from both sides were 12.6–14.2 times higher than that of the unreinforced specimen.

- The maximum loads of the two single-sided reinforced specimens were similar; however, CS02 exhibited a maximum load with a smaller deformation angle than CS01 owing to the effect of twisting.
- The maximum horizontal strength of specimen CD02 is approximately 11% lower than that of specimen CD01. However, the strength was maintained without degradation to a large deformation level.
- The term of the tensile rebars in the calculation formula based on the SDC standard was relatively consistent with the actual situation, and using the actual yield strength of the steel bars gave closer values to test results.
- The effect of the intermediate rebar was more significant at the ultimate than at the yield.
- The calculation formula based on the SDC standard overestimated the stress of the intermediate rebar and slightly underestimated the distance between the stress centers.
- The strains generated in the intermediate rebars at the ultimate level were larger when both sides were reinforced than those of the intermediate rebars when one side was reinforced.
- The values calculated using the proposed formula based on the actual strain distribution were highly similar to the experimental values.

9.1.6 Numerical Investigation of the Properties of Japanese Historical Brick Masonry Structures

Numerical analysis was conducted on diagonal compression test and horizontal loading test models and following conclusions were made.

- The Poisson's ratio obtained from transducers gave closer analytical results to experimental results compared to Poisson's ratio obtained from Rosette's strain gauge.
- From the numerical analysis of diagonal compression model and from contours in the model, it was observed that most of the compressive forces pass through the centre of the specimen and are only concentrated in the area directly under the load rather than distributing to the whole cross-sectional area of the specimen.

- The highest value of the modulus of elasticity (E = 6870 MPa) was obtained for samples loaded perpendicularly to horizontal joints (θ_{strut}=90°). For the horizontal loading test, the value of E = 5700 MPa was obtained from the analysis (θstrut = 67.43°).

- The values of shear modulus G (calculated from the diagonal transducers in diagonal compression test) are within the range of 8–17% of the value of modulus of elasticity E (prism compression test) for Nepalese and Japanese historical brick masonry. Similar findings were reported by Tomaževič (2009). In either case, the values of shear modulus were not close to 40% of E, as recommended by Eurocode 6.

9.2 Recommendations for Future Studies

Based on this study, the following recommendations are presented below for future studies to add more insights into the structural performance of brick masonry structures and the efficiency of the proposed timber and RC wall reinforcement technique.

- The effectiveness of timber reinforcement was investigated experimentally and numerically in this study under monotonic horizontal loads. Experimental work on the cyclic behavior of the Nepalese historical brick masonry was not conducted in this study. Therefore, a cyclic experiment on Nepalese historical brick masonry was suggested for future research.

- The suggested strengthening technique by timber might work well for low-rise historical masonry buildings. To investigate this further, research work needs to be done in the future for experimental and numerical analysis of low-rise historical brick masonry buildings.
- In this study, the retrofitting by timber for Nepalese historical brick masonry was done from both sides, the impact of one-side retrofitting should be examined as well in the future. This is due to two-sided retrofitting might not be feasible due to the issues with applicability in some real construction cases.

- This study only focuses on the macro modeling approach for both Nepalese and Japanese historical brick masonry. In future studies, the micro modeling should be conducted to understand how wall joints behave in different loading conditions.